Beyond the Surface of Mudrocks:

Probing Texture, Porosity and Rock-Fluid Interactions at the Nano-Scale

Von der Fakultät für Georessourcen und Materialtechnik
der Rheinisch-Westfälischen Technischen Hochschule Aachen

zur Erlangung des akademischen Grades eines

Doktors der Naturwissenschaften

genehmigte Dissertation

vorgelegt von

Timo Seemann, M.Sc.

Berichtende: **Univ.-Prof. Dr. rer. nat. Helge Stanjek**
Univ.-Prof. Dr. rer. nat. Ralf Littke

Tag der mündlichen Prüfung: 05.07.2024

Diese Dissertation ist auf den Internetseiten der Universitätsbibliothek online verfügbar

To Teresa, Aurel & Camillo

Acknowledgements

I extend sincere gratitude to my PhD supervisor, Helge Stanjek, for unwavering guidance and commitment to excellence throughout this research journey. He gave me the opportunity to flourish as an assistant under his scientific guidance and follow up my own interests in every possible direction. His expertise and encouragement have been invaluable in shaping the outcome of this thesis. I hope that he and his wife experience a wonderfully fulfilling retirement.

Special thanks to Ralf Littke for accepting the task of being co-examiner and providing me with the opportunity to work with him and his research team at the Institute for Geology and Geochemistry of Petroleum and Coal for a year on interesting topics.

I am deeply grateful to Nicolai Thuens, my long-time student and PhD companion. Sharing an office, discussing X-ray diffraction, and creating lasting memories with our families and friends have been highlights of this academic journey. His camaraderie has been a source of motivation and joy. A heartfelt appreciation goes to Hannes Claes, whose engaging discussions on scientific and cultural topics, along with memorable beer tastings, added a unique and enjoyable dimension to my doctoral experience. Our shared moments of intellectual exchange will be cherished.

Acknowledgment to Bernhard Hoffmann for sharing knowledge of inorganic chemistry and his great patience and enthusiasm for distracting me momentarily from my primary work with discussions on politics, culture and Switzerland. Heartfeld thanks to Christiane Finken for her assistance with administration and our delightful conversations about chickens, pigs, and kids over coffee breaks.

A genuine thank you to Pieter Bertier for sparking my interest in science and imparting valuable lessons on scientific work and life. His encouragement to have an open mind and explore beyond the confines of one's field has been truly inspiring which I will keep up my whole life and teach my son. Much appreciation to Christian Weber for consistently providing critical and honest opinions about the scientific work and the scientific method over phone calls and beers. His insights have been crucial in refining the rigour of my view on research.

Further appreciation goes to Prof. Andreas Busch, Amirsaman Rezaeyan, Leon Leu and Dirk Prinz for interesting talks about mudrocks, coal, sorption and small angle neutron scattering, sparking innovative ideas for future research. Thanks are due to Garri Gaus, Sebastian Grohmann and Saeed Khajooie for their assistance with Petrophysical measurements, Rock Eval analysis and great discussion over soups and excursions. Sincere thanks to Prof. Florian Amann for generously giving me time to finish this thesis and opening up the possibility to broaden my scientific expertise in the field of rock mechanics.

In expressing my gratitude to those mentioned earlier in this acknowledgement, I must also acknowledge the indispensable role played by my family. Their love, understanding, and encouragement have been the bedrock upon which my academic pursuits have flourished. My deepest gratitude goes to my wife Teresa and our son Aurel, who are the greatest blessings in my life. Teresa and I have shared more than half of our lives, and her unwavering support in every matter has been the cornerstone in my achievements. I am profoundly thankful for her patience along this challenging journey and for playfully teasing me over the finish line. Aurel's presence has been the source of immense joy and inspiration, making every effort worthwhile. I extend heartfelt thanks to my parents and my sister for providing me with every opportunity to develop without constraints. Their support and belief in my endeavours have been instrumental in shaping my academic path. I am grateful for the foundation they laid and the encouragement they provided.

To Teresa, Aurel, my parents, and my sister this achievement is as much yours as it is mine.

Yours truly,

Timo

Abstract

The scientific and economic interest in fine-grained, argillaceous mudrocks has persisted for several decades because of their crucial role in socio-economic developments related to the oil and gas industry, the recent shift towards a carbon-neutral industry, and their consideration for storage of toxic and nuclear waste. The unique physico-chemical and petrophysical properties of these mudrocks, attributed to their intricate pore network primarily build by clay minerals at the nano scale, include the capacity to impede fluid- and solute transport as well as self-healing capabilities associated with volumetric expansion upon exposure to aqueous solutions. Conventional analytical techniques such as imaging techniques often struggle to provide reliable information about the pore structure of nanoporous media. Conversely, gas and vapour sorption, primarily driven by van der Waals forces, cover transport- and storage relevant scales down to the molecular level. Despite that, specific interactions between adsorptive and surface groups can complicate interpretations and the pore structure characterisation. However, the complementary employment of various adsorptives enables scrutiny of fluid-rock interactions, providing insights into its mechanisms and controls at the pore scale. This is of particular significance and interest in water-mudrock systems, given water's omnipresence in subsurface, its physico-chemical properties and its effects on transport, storage, and rock mechanical properties. To study the above, a diverse suite of mudrocks, clay minerals and their mixtures as well as engineered analogues were investigated by a combination of argon, nitrogen, carbon dioxide and water sorption alongside compositional analysis.

Argon physisorption, recommended by the International Union of Pure and Applied Chemistry for its apolar character related to its symmetrical electron configuration, has emerged as a practical and reliable tool for microporosity analysis, instead of the traditionally used, slightly polar nitrogen. Comparative analysis of Ar and N_2 physisorption isotherms revealed qualitatively similar isotherms with significant differences in the submonolayer range, with N_2 underestimating micropore volumes by an average of 15%. Differences varied randomly, independent of the sorbent class but causes remained unclear. While specific surface areas were concluded to be equivalent, microporosity was only reliably assessed by argon physisorption. Yet, Gurvich total pore volumes and mesopore size distributions highlight saturation pressure offsets, induced by atmospheric pressure fluctuations, as a primary factor of uncertainty of physisorption measurements. The effect scaled with p/p^0, hence its negative impact was more severe for pore volume- and pore size calculations at high p/p^0.

Shifting the focus to water-mudrock interaction, with a particular emphasis on the distribution of water in the pore network of mudrocks, its controls, and the fundamental mechanisms of hysteresis, emphasised the constitutive control of (expandable) clays on water uptake in those types of rocks.

Correlation analysis of textural properties from differently saturated, immature mudrocks highlighted the predominant influence of smectite content and exchangeable cations on water distribution, explaining 89 to 99.5% of the variance in water uptake. The remaining discrepancies were linked to differences in microstructure. This implied that the fundamental processes of smectite hydration are the dominant sorption mechanisms in mudrocks: (i) exchangeable cation hydration and (ii) interlayer hydration via heterogeneous intercalation of mixed-water layers accompanied by crystalline swelling. Swelling was determined as one factor contributing to the prevalent imbalance of presorbed water and total pore volume loss, which was resolved by a mixing model that combined

clay hydration with capillary condensation, alongside swelling-induced pore network modification. Differences in textural parameters, obtained from ad- and desorption conditioned mudrocks, were low, but the hysteretic character of water sorption isotherms was detectable in all textural parameters. Major impacts of presorbed water concentrated in pores below 20 nm, with mudrock-specific pore occlusion occurring primarily at 97%RH.

Scrutiny of water vapour sorption hysteresis revealed multiple hysteresis mechanisms. General causes, such as tightly bound water by polar surface groups, exchangeable cations or molecule-sized micropores, and kinetic hysteresis, contributed to low-pressure hysteresis. Specific hysteresis was linked to crystalline swelling for smectite-bearing mudrocks, and for non-swelling mudrocks (Cu-Triethylentetramin exchanged samples, with a locked interlayer space, were considered as analogues of such) to the variation in ad- and desorption mechanisms. Scanning isotherms provided evidence for capillary condensation above $p/p^0 = 0.4$ (adsorption), while evaporation occurred freely down to $p/p^0 \approx 0.45$; below this pressure, cavitation controlled desorption in form of spinodal evaporation. From that a coherent, condensation-, hysteresis- and cavitation critical neck size of 2.2 to 2.5 nm was determined.

In summary, this scientific contribution aimed to advance the understanding of complex fluid-mudrock systems by capturing the unique pore structure and highlighting mechanisms of the complex interplay of fluid-rock interaction.

Zusammenfassung

Tonsteine stehen seit Jahrzehnten im Zentrum des wissenschaftlichen und sozioökonomischen Interesses, bedingt durch ihre Bedeutung als Barrieregesteine in der Öl- und Gasindustrie, ihrer Rolle bei der Energiewende und der CO_2-Neutralität sowie ihrer Nutzung für die Lagerung von giftigen und nuklearen Abfällen. Zu ihren einzigartigen physiko-chemischen und petrophysikalischen Eigenschaften zählen unter anderem die Fähigkeit den Flüssigkeits- und Lösungstransport zu behindern, sowie ihre Selbstheilungsfähigkeit, beruhend auf ihrem Quellvermögen.

Im Gegensatz zu herkömmlichen Analysetechniken wie Bildgebungsverfahren bietet die Gas- und Dampfsorption die Möglichkeit transport- und speicher relevante Skalen bis hinunter auf die molekulare Ebene abzudecken. Physisorption ist dominiert durch van der Waals Kräfte, jedoch können spezifische Wechselwirkungen zwischen Adsorptiv und funktionellen Oberflächengruppen die Interpretation der Porenstruktur erschweren. Die komplementäre Anwendung unterschiedlicher Adsorptive ermöglicht die Untersuchung von Fluid-Gesteins Wechselwirkungen auf der Porenskala und bietet Einblicke in grundlegende Mechanismen. Für die Untersuchung der Fluid-Gesteins-Wechselwirkungen wurde eine Reihe von Tonsteinen, Tonmineralen, deren Mischungen sowie technisch hergestellte Analoga mittels Ar-, N_2-, CO_2- und H_2O-Sorption in Verbindung mit einer detaillierten Zusammensetzungsanalyse untersucht. Das Wasser-Tonstein-System ist dabei von besonderem Interesse aufgrund der spezifischen physiko-chemischen Eigenschaften von Wasser und seines komplexen Einflusses auf Transport, Speicherung und gesteinsmechanische Eigenschaften.

Argon-Physisorption, empfohlen durch die „International Union of Pure and Applied Chemistry“, hat sich als praktisches und zuverlässiges Werkzeug zur Charakterisierung der Mikroporenstruktur nanoporöser Festkörper erwiesen, anstelle des traditionell verwendeten, leicht polaren Stickstoffs. Ar- und N_2-Isothermen erwiesen sich als qualitativ ähnlich im Hinblick auf Isothermen- und Hysteresetypus. Texturelle Unterschiede der Sorbentien waren unabhängig von ihrer Festkörperklasse und variierten unsystematisch. Signifikante Unterschiede beschränkten sich auf den „Submonolayerbereich“. Während die spezifischen Oberflächen als gleichwertig betrachtet werden können, konnte eine zuverlässige Bewertung der Mikroporosität nur durch die Ar-Physisorption stattfinden. Das Mikroporenvolumen wurde von N_2 im Mittel um 15% unterschätzt und Porenverteilungen konnten nicht ermittelt werden. Die Ursache für die unterschiedlichen Mikroporenvolumina ist nach wie vor unklar. Des Weiteren erwiesen sich Sättigungsdampfdruckschwankungen, hervorgerufen durch Luftdruckschwankungen, als primärer Unsicherheitsfaktor bei Physisorptionsmessungen. Der Einfluss ist proportional zum Partialdruck und entsprechend hoch waren die Auswirkungen auf die Gesamtporenvolumenbestimmung und die Berechnung der Mesoporenverteilungen.

Zusätzlich zur Analyse der texturellen Charakterisierung wurden Wasser-Tonstein Wechselwirkungen näher betrachtet. Der Schwerpunkt lag auf der Verteilung von Wassermolekülen im Porennetzwerk von Tonsteinen und den grundlegenden Hysteresemechanismen. Die Korrelationsanalyse textureller Parameter unterschiedlich gesättigter, unreifer Tonsteine zeigte den vorherrschenden Einfluss des Smektitgehaltes und der austauschbaren Kationen auf die Wasserverteilung. Beide Parameter konnten 89-99,5% der Varianz der Wassersorption erklären und der verbleibende Unterschied wurde mit der Mikrostruktur in Verbindung gebracht. Demnach sollten die Sorptionsmech-

anismen in Tonsteinen den primären Prozessen der Smektithydratation entsprechen: (i) Hydration austauschbarer Kationen und (ii) Einlagerung von Mischwasserlagen in Zwischenschichträume begleitet durch kristallines Quellen. Die Volumenexpansion des Smektits trug entscheidend zu dem beobachteten Ungleichgewicht zwischen sorbiertem Wasser und N_2-detektiertem Porenvolumenverlust bei. Die Diskrepanz der Massenbilanz konnte durch ein Mischungsmodell angenähert werden, das die Tonhydratation mit der Kapillarkondensation kombinierte unter Berücksichtigung der Modifikation des Porennetzwerks durch Quellung. Die Konditionierungspfad-Abhängigkeit der Texturparameter war gering, aber die Hysterese der Wasserdampf Isothermen spiegelte sich in den berechneten Texturparametern wieder. Die Hauptauswirkung des sorbierten Wassers konzentrierte sich im Porenraum unterhalb 20 nm und eine Porenfüllung trat hauptsächlich bei einer Feuchtekonditionierung von 97% auf. Die maximal gefüllte Porengröße war Tonstein-spezifisch.

Die Untersuchung der Hysterese von Wasserdampf Isothermen ergab mehrere Erzeugungsmechanismen, die sich in allgemeine und spezielle Ursachen unterteilen ließen. Zu den allgemeinen Ursachen zählen die starke Bindung von Wassermolekülen (durch funktionelle Oberflächengruppen, austauschbare Kationen oder Mikroporen) sowie kinetisch bedingte Hysterese. Beide Mechanismen tragen maßgeblich zur Niederdruckhysterese bei. Spezifische Hysteresemechanismen beinhalten kristallines Quellen, sofern quellfähige Minerale vorhanden sind, sowie die klassischen Ursachen unterschiedlicher Ad- und Desorptionsmechanismen. Letztere wurden primär bei Cu-Triethylentetramin ausgetauschten, nicht-quellfähigen Proben mit verriegeltem Zwischenschichtabstand festgestellt, die als Analoga für nicht-quellfähige Tonsteine gewertet wurden. “Hystere-Scanning” nicht-quellender Materialien (Cu-Trien) lieferte Beweise für Kapillarkondensation oberhalb von $p/p^0 = 0,4$ während der Adsorption. Die Desorption erfolgte durch freie Verdampfung bis zu $p/p^0 \approx 0,45$, darunter kontrollierte Kavitation (spinodale Verdampfung) die Desorption. Folglich konnte eine kohärente, kondensations-, hysterese- und kavitationskritische Porenhalsgröße im Bereich 2,2 bis 2,5 nm abgeleitet werden.

Zusammenfassend erweitert dieser wissenschaftliche Beitrag das Verständnis der komplexen Fluid-Tonstein-Systeme, indem die einzigartige Porenstruktur aufgeschlüsselt und Mechanismen des komplexen Zusammenspiels der Fluid-Gesteins-Wechselwirkung beleuchtet werden.

Contents

Acknowledgements

Abstract **I**

Zusammenfassung **III**

Contents **V**

List of Figures **IX**

List of Tables **XIX**

Glossary **XXIII**

1 ***Introduction*** **1**

2 ***Argon Physisorption for Pore Analysis of Mudrocks, Clays and Engineered Analogues:***
Argon a better Choice than Nitrogen and Carbon dioxide? **11**

Abstract 12

2.1 Introduction 13

2.2 Materials & Methods 14

2.2.1 Sample materials 14

2.2.2 Sample preparation for physisorption measurements 16

2.2.3 Nitrogen and carbon dioxide physisorption 16

2.2.4 Argon physisorption 17

2.3 Primary experimental results 18

2.3.1 Argon, nitrogen and carbon dioxide physisorption isotherms 18

2.4 Quantitative evaluation of isotherms and discussion 23

2.4.1 Equilibrium tests 24

2.4.2 Reproducibility and precision of Ar physisorption measurements 26

2.4.3 Factors of uncertainty and the importance of saturation pressure 27

2.4.4 Comparison and characterisation of N_2, Ar and CO_2 isotherms 30

2.4.5 Micropore volume 32

2.4.6 Specific surface area . . . 35
2.4.7 Gurvich pore volume and porosity . . . 37
2.4.8 Micropore size distributions of porous materials . . . 39
2.4.9 Mesopore size distribution of porous materials . . . 43
2.4.10 Compositional control on differences in Ar, N_2 and CO_2based micropore volumes . . . 49
2.4.11 Note on sorption mechanism . . . 51
2.5 Conclusion . . . 53

Appendices **55**
A.1 Background information on Materials . . . 56
A.2 Adsorptive Properties . . . 56
A.3 Statistical data of textural parameters of repetitive Ar physisorption measurements . . . 57
A.4 Comparison of micropore volumes DA-theory and α_s method . . . 57
A.5 Statistical thickness models . . . 58
A.6 Textural parameter collection for argon physisorption isotherms . . . 59
A.7 Textural parameter collection for nitrogen physisorption isotherms . . . 60
A.8 Textural parameter collection for carbon dioxide physisorption isotherms . . . 61

3 *Insights into Sorbed Water in Mudrocks: Investigating Distribution Patterns, Controls & Mechanisms* **65**
Abstract . . . 66
3.1 Introduction . . . 67
3.2 Theory and concepts of water sorption . . . 69
3.3 Materials & Methods . . . 72
3.3.1 Sample materials . . . 72
3.3.2 Sample preparation . . . 73
3.3.3 X-ray diffraction . . . 73
3.3.4 Cation exchange capacity . . . 73
3.3.5 Rock-Eval pyrolysis . . . 74
3.3.6 Dynamic water vapour sorption . . . 74
3.3.7 Low-pressure nitrogen physisorption . . . 74
3.3.8 Low-pressure argon and carbon dioxide physisorption . . . 75
3.3.9 Textural analysis strategy . . . 75
3.4 Results . . . 76
3.4.1 Composition of mudrocks . . . 76
3.4.2 Dynamic and static water vapour sorption isotherms of mudrocks . . . 77
3.4.3 Nitrogen physisorption isotherms of dry and moist mudrocks . . . 78
3.4.4 Secondary results and isotherm evaluation of moist mudrocks . . . 81
3.4.5 Reproducibility . . . 86

3.5 Discussion . . . 89
3.5.1 Reproducibility of physisorption measurements on moist mudrocks . . . 89
3.5.2 Controls on water sorption . . . 90
3.5.3 Compositional and textural influence on water sorption . . . 92
3.5.4 Water distribution and pore filling . . . 97
3.5.5 The 97%RH conundrum and the issue of equilibrium . . . 100
3.5.6 Mass-volume balance . . . 102
3.5.7 Experimental limitations and critical perspectives . . . 105
3.5.8 Mechanistic implications for the interpretation of water vapour sorption isotherms 107
3.6 Conclusion . . . 110

Appendices **111**
B.1 Carbon dioxide and argon physisorption isotherms of dry mudrocks . . . 112
B.2 Compilation of textural parameters of nitrogen physisorption isotherms of dry and moist mudrocks . . . 113
B.3 Validation of statistical treatment . . . 115
B.4 Validation of textural differences . . . 116
B.5 Compositional control on microstructure . . . 117
B.6 Normalised static water vapour sorption isotherms of mudrocks . . . 118

4 ***Hysteresis in Water Sorption Isotherms of Mudrocks: Origins and Mechanisms*** **121**
Abstract . . . 122
4.1 Introduction . . . 123
4.2 Materials and Methods . . . 126
4.2.1 SWy2 montmorillonite (source clay) . . . 126
4.2.2 Ypresian Clay mudrocks . . . 126
4.2.3 Cu-triethylenetetramine exchange . . . 127
4.2.4 Water vapour sorption . . . 127
4.2.5 Physisorption measurements (N_2, Ar) . . . 127
4.2.6 X-ray diffraction . . . 128
4.2.7 Cation exchange capacity . . . 128
4.2.8 Total (in-) organic carbon content . . . 129
4.3 Results . . . 129
4.3.1 Mineralogical composition . . . 129
4.3.2 Pore structure characterisation . . . 133
4.3.3 Water vapour sorption isotherms . . . 134
4.3.4 Scanning isotherms of Cu-Trien-exchanged materials . . . 135
4.4 Discussion . . . 137
4.4.1 Tightly bound water and low-pressure hysteresis . . . 137
4.4.2 Kinetic hysteresis . . . 140
4.4.3 Sorbent swelling and geometrical deformation . . . 143

4.4.4 Hysteresis in Cu-Trien-exchanged materials 144
4.4.5 Mechanisms of water sorption in non-swelling geomaterials 147
4.5 Conclusion 151

Appendices **152**
C.1 Textural parameters of mudrocks and clays 153

5 *Outlook and concluding remarks* **157**
5.1 Traditional and advanced physisorption protocols 157
5.2 The future of water vapour sorption in mudrocks 162
5.3 Future prospects and developments of (physi-) sorption 164

Bibliography **169**

List of Figures

Chapter 2: ***Argon Physisorption for Pore Analysis of Mudrocks, Clays and Engineered Analogues:***
Argon a better Choice than Nitrogen and Carbon dioxide? **11**

2.1 Ar, N_2 and CO_2 physisorption isotherms measured on the mudrock sample set at operational temperature of the adsorptive (a to i). The molar uptake is recalculated to liquid basis, assuming bulk liquid density of the respective fluid (cf. section A.2 Table A.2 in the appendix) for better comparison. The higher uptake of N_2 relative to Ar at $p/p^0 \ll 0.1$ shifts N_2 isotherms above those of Ar in the micropore range. CO_2 physisorption isotherms are either lower or equal to Ar physisorption isotherm on liquid basis. 20

2.2 Ar, N_2 and CO_2 physisorption isotherms measured on mudrocks, clay minerals and clay mixtures at operational temperature of the adsorptive (a to i). Further explanation is found in Figure 2.1. 21

2.3 Ar, N_2 and CO_2 physisorption isotherms measured on engineered materials, silicas and Fe-oxides at operational temperature of the adsorptive (a to i). Further explanation is found in Figure 2.1 22

2.4 Ar and N_2 physisorption isotherms measured on the Fe-oxides at operational temperature of the adsorptive (a & b). Further explanation is found in Figure 2.1. 23

2.5 (a) Ar physisorption isotherm (87 K) of Opalinus Clay (OCM) and Longmaxi(a) (LM(a)) mudrock measured as a function of equilibration time (pressure drop of 81 Pa for 1 to 13 min and 2 to 10 min), respectively; (b) Plots of characteristic parameters (A_{BET}, V_0, V_{GV}) of OCM and LM(a) mudrocks as function of equilibration time. Error bars show 2 standard deviations obtained from repetitive measurements at 5 min equilibration time (OCM) or interpolation (LM(a)). 25

2.6 (a) Ar physisorption isotherms measured at 87 K at 5 min and 60 min equilibration time on the YPC-Kortemark mudrock. The inlay shows a zoom into the low-pressure region ($p/p^0 < 10^{-1}$); (b) Characteristic parameters (A_{BET}, V_0, V_{GV}) plotted as function of equilibration time including 2 standard deviations obtained from uncertainty interpolation. The Gurvich volume decrease of the 60 min sample is attributed to a saturation pressure offset (cf. section 2.4.3). 25

2.7 Ar physisorption isotherms (87 K) of repetitive measurements on (a) the SiAl pellets (n=10) and on (b) the Haynesville mudrock (n=5); The precision is represented by two standard deviations (2σ) shown for individual data points. 27

2.8 (a) Saturation pressure (p^0) fluctuations recorded during N_2 physisorption measurements performed on five (n = 5) porous and non-porous samples on a *Gemini VII 2340*; (b) Ar (p^0 offset) and N_2 physisorption isotherms of the Boom Clay sample plotted on a molar basis. The inset shows a zoom into the high partial pressure region; (c) Cumulative BJH-PSDs (adsorption branch) computed from Ar and N_2 physisorption isotherms measured on the Boom Clay sample. 29

2.9 Characteristic energies of adsorption (E_0) calculated using DA-theory from N_2 (77 K), Ar (87 K) and CO_2 (273 K) physisorption isotherms of representative mudrocks (Bossier(a), Opalinus Clay), clays (SWy2-CuTrien, YPC-CF-E) and engineered materials (VY-COR cpg-20nm; SiAl pellets). 31

2.10 (a) Cross-plot of V_0 obtained from N_2 and Ar physisorption isotherms measured at normal boiling point temperature, respectively. Error bars represent two standard deviations and were obtained from interpolation of repeated measurements of representative mudrocks and the SiAl pellets; (b) Cross-plot of V_0 obtained from CO_2 and Ar physisorption isotherms measured at normal boiling point temperature (Ar) and 273 K (CO_2), respectively. No error bars are assigned because data for CO_2 isotherms are missing. The dashed line indicates unity. 33

2.11 (a) Cross-plots of A_{BET} calculated from N_2 and Ar physisorption isotherms measured at normal boiling point temperatures, respectively. Error bars represent two standard deviations and were obtained from interpolation of repeated measurements of representative mudrocks and the SiAl pellets; (b) BET areas of this dataset combined with literature data ($n_{tot} = 70$) (Payne et al., 1973, Thommes et al., 2002a,b, Klank, 2021, Sotomayor et al., 2018). Dashed lines indicate unity. 36

2.12 Cross plot of V_{GV} obtained for a pore size of 250 nm from N_2 and Ar physisorption isotherms measured at normal boiling point temperature, respectively. Error bars represent two standard deviations and were obtained from interpolation of repeated measurements of representative mudrocks and the SiAl pellets. The dashed line indicates unity. Gurvich pore volumes of the non-porous (np) silicas and Fe-oxides are only shown for completeness but not considered in the analysis for reasons outlined in section 2.4.7. 38

2.13 (a) Differential micropore size distributions (µPSD) of mudrocks computed using DA-theory from Ar physisorption isotherms. G(I) to G(III) represent the grouping of mudrocks according to their primary pore size; (b) Ar DA-plots of selected mudrocks. Data points represented by a cross (x) were not used for numerical fitting due to an instrumental step as explained earlier; (c) Ar α_s-plots of selected mudrocks using the reduced isotherm published by Kruk & Jaroniec (2000). α_s-plots displayed two linear ranges indicated by black and green regression lines. 40

2.14 Meso- and macro pore size distributions calculated from the adsorption (a, c) and desorption (b, d) branch of Ar and N_2 isotherms using BJH-theory in combination with a thickness curve from Kruk & Jaroniec (2000) : a) PSD obtained for Bossier(a) mudrock from the adsorption branch, b) PSD obtained for Bossier(a) mudrock from the desorption branch c) PSD obtained for Opalinus Clay from the adsorption branch, d) PSD obtained for Opalinus Clay from the desorption branch. The differential pore size distributions are shown as inserts, respectively. 45

2.15 As Figure 2.14, but for a) PSD obtained for the Kaolinite from the adsorption branch, b) PSD obtained for the Kaolinite from the desorption branch c) PSD obtained for the Montmorillonite from the adsorption branch, d) PSD obtained for the Montmorillonite from the desorption branch. 46

2.16 As Figure 2.14, but for a) PSD obtained for the VYCOR cpg-20nm from the adsorption branch, b) PSD obtained for VYCOR cpg-20nm from the desorption branch c) PSD obtained for SiAl pellets from the adsorption branch, d) PSD obtained for the SiAl pellets from the desorption branch. 47

2.17 DA micropore volumes (V_0) calculated for Ar, N_2 and CO_2 physisorption isotherms and percentage difference of V_0(Ar and N_2) normalised to the Gurvich (total) pore volume (V_{GV}) plotted as function of (a) total organic carbon content (TOC), (b) cation exchange capacity (CEC), (c) total clay content, (d) mixed layer clay minerals including illite, smectite and muscovite (here: I/S). 50

A.1 Differential PSD of SiAl reference material calculated based on different statistical thickness curves. The mean pore size is 8.54 ± 0.08nm ($CV \approx 1\%$). The exact equations can be found in the manual of Micromeritics *Microactive*. 58

Chapter 3: *Insights into Sorbed Water in Mudrocks: Investigating Distribution Patterns, Controls & Mechanisms* **65**

3.1 X-ray powder diffraction patterns of bulk mudrocks; Boom Clay (black), Callovo Oxfordian argillite (pink), Opalinus Clay (orange), and Tournemire argillite (green). 76

3.2 (a) Dynamic water vapour sorption isotherms measured at 303 K on dry mudrocks; (b) Static water sorption isotherms determined by weighing of individual subsamples of the respective mudrock. Error bars indicate standard deviations obtained from reproducibility measurements of mudrock subsamples conditioned at 97%RH in desorption mode. 78

3.3 N_2 physisorption isotherms measured at 77 K on dry and moist mudrocks in ad- and desorption conditioning: (a) N_2 isotherm collection of Boom Clay; (b) N_2 isotherm collection of Callovo Oxfordian argillite, adsorption (11 to 97%RH) data of COx were taken from Lahn et al. (2020); (c) N_2 isotherm collection of Opalinus Clay, adsorption (11 to 97%RH) data of OCM were taken from Lahn et al. (2020); (d) N_2 isotherm collection of Tournemire argillite. 80

3.4 DA micropore pore volumes (V_0) calculated from N_2 physisorption isotherms measured on moisture conditioned mudrocks (ad-, desorption) plotted as a function of gravimetric water uptake. Closed symbols represent adsorption conditioning and open symbols refer to desorption conditioning. Connecting lines serve as guides to the eye. Error bars represent 95% confidence intervals calculated based on the relative standard deviations obtained from repetition measurements performed for the Opalinus Clay (97%RH desorption conditioning). 81

3.5 BET specific surface areas (A_{BET}) calculated from N_2 physisorption isotherms measured on moisture conditioned mudrocks (ad-, desorption) plotted as a function of gravimetric water uptake. Rouquerol plots were employed to constrain fitting intervals (Rouquerol et al., 2007). Closed symbols represent adsorption conditioning and open symbols refer to desorption conditioning. Connecting lines serve as guides to the eye. Error bars represent 95% confidence intervals calculated based on the relative standard deviations obtained from repetition measurements performed for the Opalinus Clay (97%RH desorption conditioning). 82

3.6 Gurvich (total) specific pore volumes (V_{GV}) calculated from N_2 physisorption isotherms measured on moisture conditioned mudrocks (ad-, desorption) plotted as a function of gravimetric water uptake. V_{GV} were obtained at maximum experimental partial pressure ($p/p^0 \approx 0.995$). Closed symbols represent adsorption conditioning and open symbols refer to desorption conditioning. Connecting lines serve as guides to the eye. Error bars represent 95% confidence intervals calculated based on the relative standard deviations obtained from repetition measurements performed for the Opalinus Clay (97%RH desorption conditioning). 83

3.7 Cumulative pore size distributions (BJH) obtained from the adsorption branch of N_2 physisorption isotherms (77 K) measured on dry (reference curve) and moist mudrocks obtained from ad- and desorption conditioning; (a) PSDs of Boom Clay; (b) PSDs of Callovo Oxfordian argillite; (c) PSDs of Opalinus Clay; (d) PSDs of Tournemire argillite. 85

3.8 Normalised cavitation volume ($V_{\mathrm{c,n}}$) at hysteresis loop closure of moisture conditioned mudrocks in ad- and desorption mode plotted as a function of relative humidity. The cavitation volume was converted to fluid volume by assuming the bulk liquid density of nitrogen ($\rho = 0.808$ g/mL) at 77 K and normalised to the cavitation volume of the dry mudrocks. Closed symbols represent adsorption conditioning and open symbols indicate desorption conditions. Connecting lines serve as guides to the eye. 86

3.9 (a) N_2 physisorption isotherm determined from 5 repetitions measured on subsamples of the Opalinus Clay equilibrated at 97%RH along the desorption pathway; (b) Corresponding BJH PSD calculated from 5 repetitive N_2 physisorption isotherms. Error bars indicate one standard deviation in (a) and (b). 87

3.10 (a - c) V_0, A_{BET} and V_{GV} of SiAl reference material, Opalinus Clay in dry (0%RH) and moist conditions (56%RH adsorption; 97%RH desorption); Error bars indicate coefficients of variations computed from at least 5 reproducibility tests; (d) Coefficients of variation of Gurvich specific pore volume (V_{GV}), BET area (A_{BET}) and DA micropore volume (V_0) calculated from reproducibility measurements of N_2 physisorption isotherms of dry mudrocks. 88

3.11 Correlation matrix of compositional and textural parameters vs. static water uptake as a function of relative humidity. Sub-matrices are highlighted for composition + texture and static water uptake (SVS) (red squares). The strongest correlations are indicated by blue and peach shades. Numerical values in the upper triangle indicate the correlation coefficients (r) of parameter pairs. Circles (lower triangle) visualise the strength of correlation by circle size and colour (colour bar on the right). Nc = sum of non-clay minerals, TC = sum of clay minerals, Kao = kaolinite quantity, Chl = chlorite quantity, Sm = smectite quantity, I = sum of illite and muscovite quantities, MLM = sum of illite, muscovite and smectite quantities, CEC = cation exchange capacity, A_{BET} = BET specific surface area, V_0 = DA micropore volume, V_{GV} = Gurvich (total) specific pore volume. 91

3.12 Overview of compositional parameters (TOC, T_{max}, smectite content, CEC) plotted against water uptake as a function of relative humidity (11 to 97%RH) in ad- and desorption conditioning. Red lines represent linear regression lines of numerical fits of water uptake at 97%RH. The remaining correlation lines are omitted for reasons of visual clearance. 92

3.13 (a) Linear regression of smectite content vs. cation exchange capacity (CEC) of the investigated mudrocks; (b,c) Smectite content and CEC normalised water vapour sorption isotherms obtained from dynamic vapour sorption measurements of the investigated mudrocks. 94

3.14 Overview of dynamic water vapour sorption isotherms of mudrocks and scaled sodium and calcium montmorillonite (SWy2) and a natural clay mixture. Original water vapour sorption isotherms of the montmorillonites and the clay mineral mixture were scaled based on the smectite content of mudrocks estimated by Rietveld refinement of XRD powder patterns. Plum coloured isotherms represent the desorption branch obtained from XRD profile modelling of water equilibrated sodium saponite (layer charge = 0.4) from Ferrage et al. (2010). 96

3.15 Fractional change of differential pore volume accessible to nitrogen after moisture conditioning. Relative changes were obtained by normalising the differential pore volume obtained from N_2 isotherms at a specific pore size (W = 5 nm, 20 nm and 50 nm) to their respective differential uptake of the dry sample. PSDs were computed by a combination of DA-theory and BJH-theory from the adsorption branch. The secondary x-axis (top) shows the corresponding pore width theoretically filled by water at the given relative humidity (primary x-axis) obtained from the Kelvin equation modified by the t-curve of Hagymassy et al. (1969). The vertical, red-dashed line indicates the relative humidity at which the targeted pore size (W_{mK}) is theoretically filled by water according to the modified Kelvin equation. 98
3.16 (a) Image of centimetre sized (d = 30 mm) mudrock core (top view) equilibrated at 97%RH using a saturated K_2SO_4 solution at room temperature ($T \approx 298$ K) exemplifying macroscopic condensation/ droplet formation on the outer surface of the cylinder, (b) Example of temperature fluctuations over the course of several days of a saturated K_2SO_4 solution; (c) Saturation pressure of water plotted as a function of temperature calculated via the Antoine equation obtained from NIST (2023). . . . 101
3.17 Comparison of presorbed water volumes and Gurvich pore volume loss at equivalent BJH pore width: (a) Boom Clay, (b) Callovo Oxfordian argillite, (c) Opalinus Clay, (c) Tournemire argillite. Unity is presented as a solid black line and adsorption conditioning is indicated by closed symbols whereas desorption conditioning is represented by open symbols. Plum coloured symbols represent the linear mixing model (Equation 3.1). 102
B.1 (a) Argon physisorption isotherms measured at 87 K on dry mudrocks; (b) Cumulative pore size distributions were obtained from the adsorption branch of the isotherms of the dry mudrocks. PSDs were computed by a combination of DA-theory and BJH-theory. 112
B.2 Comparison of V_0, A_{BET} and V_{GV} determined for ad- and desorption conditioning at 97%RH for Boom Clay, Callovo Oxfordian argillite, Opalinus Clay and Tournemire argillite. Error bars represent 95% CIs calculated from standard deviations of 5 repetitive isotherm measurements on Opalinus Clay (equilibration at 97%RH). . . . 116
B.3 Cross plot of smectite content (x-axis), BET specific surface area (left y-axis) and DA micropore volume (right y-axis). Linear regression curves are shown for each parameter pair including regression equations and the coefficient of determination (R^2). 117
B.4 Static water vapour sorption isotherms (gravimetric) normalised to (a) smectite content determined by XRD and (b) cation exchange capacity (CEC) measured by the Cu-Trien method (Stanjek & Künkel, 2016). 118

Chapter 4: *Hysteresis in Water Sorption Isotherms of Mudrocks: Origins and Mechanisms* **121**

4.1 X-ray diffraction powder patterns of the original and Cu-Trien-exchanged Ypresian Clay mudrock. The samples were measured with (0.2 g/g α-Al_2O_3) and without (0 g/g α-Al_2O_3) internal standard. The black line (original) and the green line (Cu-Trien) represent XRD powder patterns of samples infused with internal standard and the pink (original) and lilac (Cu-Trien) patterns represent samples measured without internal standard. The inset shows a zoom-in of the lower 2°θ range of the original and Cu-Trien-exchanged materials indicating the shift in the 001 reflection of the smectite. 130

4.2 (a) Diffraction patterns of the oriented samples of the clay fraction (<2 µm) of the Ypresian Clay mudrock including the original material, the glycerol expanded material (glass carrier) and the heated materials (673 K and 823 K; ceramic carrier); (b) Diffraction patterns of the oriented SWy2 montmorillonite showing the Na- and Cu-Trien-exchanged material. 131

4.3 X-ray diffraction powder patterns of the separated clay fraction (Atterberg treatment) of the Ypresian Clay mudrock. The original material is presented by a blue line and the Mg-exchanged material is represented in pink. The inlet shows a zoom-in of the higher 2°θ range (lower *d*-spacing) to discriminate di- and trioctahedral smectites based on the position of the 060 reflection. 132

4.4 (a) Overlay of molar Ar physisorption isotherms measured at 87 K of untreated and Cu-Trien-exchanged SWy2, YPC, and YPC-CF; (b) Semi-logarithmic plot of Ar physisorption isotherms in the ultra-low pressure region ($p/p^0 \leq 0.1$) of untreated and Cu-Trien-exchanged SWy2, YPC and YPC-CF; (c) Micropore size distributions calculated according to Medek (1977) based on DA theory; Isotherms of SWy2-Na, SWy2-CuTrien, YPC-CF and YPC-CF-CuTrien were collected from *Chapter 2* since the identical sample material was used for the presented study. 133

4.5 (a) Overlay plot of molar N_2 physisorption isotherms measured at 77 K of untreated and Cu-Trien exchanged SWy2, YPC and YPC-CF; (b) Cumulative pore size distributions calculated by BJH theory in the meso/ macropore range obtained from the adsorption branch of the nitrogen isotherms; Isotherms of SWy2-Na, SWy2-CuTrien, YPC-CF and YPC-CF-CuTrien were collected from *Chapter 2* since the identical sample material was used for the presented study. 134

4.6 Water vapour sorption isotherms (303 K) measured on untreated and Cu-Trien-exchanged samples of the SWy2 montmorillonite, the YPC mudrock and the clay fraction (YPC-CF) of the Ypresian Clay mudrock. Isotherms were measured gravimetrically using the dynamic vapour sorption method. 135

4.7 (a, c) Descending and (b, d) ascending water scanning isotherms of Cu-Trien-exchanged SWy2 (a, b) YPC-CF (c, d) measured by the DVS method with a time-based equilibrium criterion ($\mathrm{d}m/\mathrm{d}t = 5\,\mathrm{h}$). During the first sub-cycle measured on the SWy2-CuTrien the apparatus over-generated the target humidity and a maximum p/p^0 of 0.97 was reached instead of the target p/p^0 of 0.94. Therefore, the first cycle exceeds the enveloping water vapour isotherm. 136

4.8 Sketch of a theoretical water vapour sorption isotherm (black solid line) of a mudrock; special hysteresis features (low-pressure hysteresis and attempted hysteresis closure) and specific sorption mechanisms separated for ad- ($M1_{\mathrm{ads}}$ to $M2_{\mathrm{ads}}$) and desorption ($M1_{\mathrm{des}}$ to $M3_{\mathrm{des}}$) are indicated. The relative pressure range of the particular sorption mechanisms is indicated by the black dashed envelop lines. Strong retention capacity (Q_{SRC}) and Gurvich specific pore volume (V_{GV}) are shown at zero p/p^0 and maximum p/p^0, respectively. The directions of ascending (pale blue, dashed line) and descending (pale red dashed line) scanning isotherms are shown and discussed in detail in the main text. The mechanisms are based on the data analysis presented in the main text. The specific role of crystalline swelling (p/p^0 dependent on actual cation type) and osmotic swelling ($p/p^0 >$ threshold p/p^0 of capillary condensation) has not been indicated. 137

4.9 Normalised time-mass plots of untreated and Cu-Trien-exchanged samples obtained at the final desorption stage ($p/p^0 = 0$); dashed lines indicate linear regression fits of the final 100 min of the stage time illustrating the sample-specific slope of time-mass data. The qualitative trend remains valid when the calculation is performed over shorter times like 30 min. The mass at the beginning of the p/p^0 stage ($t = 0$) was used for normalisation. 138

4.10 Areal hysteresis index (AHI) of Cu-Trien-exchanged materials and the Ypresian Clay bulk rock measured by the DVS method with different equilibration criteria (mass-based vs. time-based). The AHI was calculated after Tang et al. (2017). 142

4.11 (a) Overlay of gravimetric water vapour sorption isotherms (303 K) of the Cu-Trien-exchanged Ypresian Clay mudrock, its clay fraction, and the montmorillonite; (b) Hysteresis width ($\Delta Q(p/p_{\mathrm{i}}^0)$) of Cu-Trien-exchanged SWy2, YPC mudrock, and YPC-CF calculated according to Equation 4.2. 145

Chapter 5: *Outlook and concluding remarks* **157**

5.1 (a) Argon physisorption isotherms of a random lower Jurassic mudrock outgassed at $P < 5\,\mathrm{Pa}$ and $P < 13\,\mathrm{mPa}$ at $T = 378\,\mathrm{K}$ for 24 h; (b) Bar plots of micropore volume and specific surface area; error bars represent uncertainties of the fit. 159

5.2 (a) Argon physisorption isotherms of Cu-Trien exchanged montmorillonite outgassed at $P < 5\,\mathrm{Pa}$ and $P < 13\,\mathrm{mPa}$ at $T = 378\,\mathrm{K}$ for 24 h; (b) Bar plots of micropore volume and specific surface area; error bars represent uncertainties of the fit. 159

5.3 (a) Argon physisorption isotherms of a lower Jurassic mudrock measured with (isotherm incomplete due to empty dewar) and without helium removal at elevated temperature ($T = 378\,\mathrm{K}$) prior to the physisorption measurement; (b) Bar plots of micropore volume and specific surface area; error bars represent uncertainties of the fit; (c) Pore size distributions calculated via BJH theory. 161
5.4 (a) Argon physisorption isotherms of Cu-Trien exchanged montmorillonite measured with and without helium removal at elevated temperature ($T = 378\,\mathrm{K}$) prior to the physisorption measurement; (b) Bar plots of micropore volume and specific surface area; error bars represent uncertainties of the fit; (c) Pore size distributions calculated via BJH theory, severely affects by low argon levels during measurement. 161
5.5 Amount adsorbed as a function of time, measured (open circles) at constant partial pressure, on the Boom Clay (a) and Tournemire argillite (b). The dashed lines represent fits to the data points, of the analytical solution of Fick's Law (1000 summation terms) for the weighted dual diffusion model, for diffusion into a sphere ($r = 300\,\mu\mathrm{m}$). The apparent diffusion coefficients (D) are shown for the individual fits. 163

List of Tables

Chapter 2: ***Argon Physisorption for Pore Analysis of Mudrocks, Clays and Engineered Analogues:***
Argon a better Choice than Nitrogen and Carbon dioxide? **11**

2.1 Collection of general mineralogy obtained by XRD and Rietveld refinement. Qtz: quartz, Fsp: feldspar, Cb: carbonate minerals, Clays: illite + smectite + I/S + muscovite + kaolinite + chlorite, Traces: pyrite, gypsum, anhydrite, rutile, anatase, apatite, sphalerite; (...) = sum of illite and smectite with no differentiation of mixed-layer contribution. Total organic carbon (TOC) and cation exchange capacity (CEC) were measured for this study on all samples; * = literature data collected from Seemann et al. (2017), Lahn et al. (2020), Hu et al. (2021). 16

A.1 Geological background information of studied mudrocks including references to studies in which similar or identical samples are used; * = +Louisiana; (-) = no info. . . 56

A.2 Collection of physical properties of CO_2, N_2 and Ar collected from Sircar (2006). . . 56

A.3 Statistical data (X_{mean}, σ: standard deviation, CV: coefficient of variation) of textural parameters (V_{GV}= Gurvich specific pore volume, A_{BET} = BET specific surface area and V_0 = DA micropore volume) of SiAl-pellets and selected mudrocks (BCM, HM, OCM) calculated from repeated Ar physisorption isotherms (87 K); *The Gurvich specific pore volume of the BCM has been obtained from p^0-offset isotherms. . . 57

A.4 Ar and N_2-based micropore volumes of mudrocks calculated from DA theory and α_s-plots using a macroporous LiChrosphere-Si1000 as reference solid. [x_i(Ar) | x_j(N_2)]; - = negative intercept; * = intercept statistically zero; V_0(DA) = micropore volume obtained from DA theory; V_{α_s}(t,mic) = total micropore volume obtained from α_s-plots; V_{α_s}(u, mic) = ultra-micropore volume obtained from α_s-plots; V_{α_s}(s, mic) = super-micropore volume obtained from α_s-plots. 57

A.5 Textural properties of mudrocks obtain by physisorption analysis of Ar sorption isotherms measured at 87 K; V_{GV} = Gurvich (total) pore volume calculated at p/p^0 = 0.9916 (at W_{BJH} = 250 nm), A_{BET} = BET specific surface area, Q_{mono} = BET monolayer capacity, C = BET energy constant, V_0 = DA micropore volume, Q_0 = DA limiting micropore capacity, E_0 = DA characteristic energy of system, n = DA exponent. 59

A.6 Textural properties of mudrocks obtain by physisorption analysis of N_2 sorption isotherms measured at 77 K; V_{GV} = Gurvich (total) pore volume calculated at p/p^0 = 0.9923 (at W_{BJH} = 250 nm), A_{BET} = BET specific surface area, Q_{mono} = BET monolayer capacity, C = BET energy constant, V_0 = DA micropore volume, Q_0 = DA limiting micropore capacity, E_0 = DA characteristic energy of system, n = DA exponent. 60

A.7 Textural properties of studied materials obtain by physisorption analysis of CO_2 sorption isotherms measured at 273 K; Isotherm analysis is restricted to application of DA theory; V_0 = DA micropore volume, Q_0 = DA limiting micropore capacity, E_0 = DA characteristic energy of system, n = DA exponent. 61

Chapter 3: *Insights into Sorbed Water in Mudrocks: Investigating Distribution Patterns, Controls & Mechanisms* **65**

3.1 Mineralogical composition, cation exchange capacity (CEC), total organic carbon content (TOC) and temperature of maximum hydrocarbon generation rate (T_{max}; maturity indicator). * = semi-quantitative phase quantities; MLM = sum of mixed-layer minerals (smectite + illite + muscovite (=Musc)). 77

3.2 Selection of petrophysical data collected from literature and personal communication or calculated based on measurements performed in this study. ρ_{gr} = grain density [g/mL], ϕ_{He} = helium porosity [-], ϕ_{N_2} = nitrogen porosity [-], ϕ_{H_2O}(SVS) = water porosity [-] from static vapour sorption measurements, ϕ_{H_2O}(DVS)= water porosity [-] from dynamic vapour sorption measurements. The grain density and helium porosity were obtained from literature and personal communication. 104

B.1 Textural properties of dry mudrocks by physisorption analysis of Ar and CO_2 physisorption isotherms measured at 87 K and 273 K, respectively; x_i(Ar) ; x_j(CO_2); V_{GV} = Gurvich (total) specific pore volume calculated at maximum pore size (W_{BJH}) assessed [µL g^{-1}], A_{BET} = BET specific surface area [m^2 g^{-1}], Q_{mono} = BET monolayer capacity [mmol g^{-1}], C = BET energy constant [-], V_0 = DA micropore volume [µL g^{-1}], E_0 = DA characteristic energy of system [kJ mol^{-1}], n = DA exponent [-], D = mean micropore size [nm]. 113

B.2 Textural properties of Boom Clay, Callovo Oxfordian argillite, Opalinus Clay, and Tournemire argillite equilibrated at different relative humidity in adsorption mode obtain from N_2 physisorption isotherms measured at 77 K; RH = relative humidity [%], Q_{H2O} = gravimetric water content [µL g^{-1}], V_{GV} = Gurvich (total) specific pore volume calculated at given pore width (W_{BJH}) [µL g^{-1}], A_{BET} = BET specific surface area [m^2 g^{-1}], Q_{mono} = BET monolayer capacity [mmol g^{-1}], C = BET energy constant [-], V_0 = DA micropore volume [µL g^{-1}], E_0 = DA characteristic energy of system [kJ mol^{-1}], n = DA exponent [-]. 114

B.3 Textural properties of Boom Clay, Callovo Oxfordian argillite, Opalinus Clay and Tournemire argillite equilibrated at different relative humidity in desorption mode obtain from N_2 physisorption isotherms measured at 77 K; For parameter description cf. Table B.2 114

Chapter 4: ***Hysteresis in Water Sorption Isotherms of Mudrocks: Origins and Mechanisms*** **121**

4.1 Mineralogical composition obtained by XRD and Rietveld refinement using bulk powder preparation (YPC) and oriented samples of the separated clay fraction (YPC-CF, Atterberg treatment) and the purified montmorillonite (SWy2); d. = detected not quantified; n.d. = not detected; n.m. = not measured. 130

4.2 Collection of descriptive isotherm parameters obtained from the H_2O vapour sorption isotherm of the YPC mudrock, its clay fraction (YPC-CF) and the purified Wyoming montmorillonite (SWy2); Gurvich volumes (V_{GV} [µL/g]) were calculated at p/p^0 = 0.94 assuming bulk liquid density of water (ρ = 1 g/mL); The strong retention capacity of water (Q_{SRC} [mmol/g]) was obtained from the residual moisture after desorption to zero p/p^0; the hysteresis loop closure range (attempted H-loop closure) was established by the step range in the desorption branch. 135

C.1 Textural properties of mudrocks obtain by physisorption analysis of Ar sorption isotherms measured at 87 K; V_{GV} = Gurvich (total) pore volume calculated at p/p^0 = 0.9916 (W_{BJH} = 250 nm) [µL g^{-1}], A_{BET} = BET specific surface area [m^2 g^{-1}], Q_{mono} = BET monolayer capacity [mmol g^{-1}], C = BET energy constant [-], V_0 = DA micropore volume [µL g^{-1}], Q_0 = DA limiting micropore capacity [mmol g^{-1}], E_0 = DA characteristic energy of system [kJ mol^{-1}], n = DA exponent [-]. Textural data of SWy2-Na, SWy2-CuTrien, YPC-CF, and YPC-CF-CuTrien were taken from *Chapter 2*. 153

C.2 Textural properties of mudrocks obtain by physisorption analysis of N_2 sorption isotherms measured at 77 K; V_{GV} = Gurvich (total) pore volume calculated at p/p^0 = 0.9923 (W_{BJH} = 250 nm) [µL g^{-1}], A_{BET} = BET specific surface area [m^2 g^{-1}], Q_{mono} = BET monolayer capacity [mmol g^{-1}], C = BET energy constant [-], V_0 = DA micropore volume [µL g^{-1}], Q_0 = DA limiting micropore capacity [mmol g^{-1}], E_0 = DA characteristic energy of system [kJ mol^{-1}], n = DA exponent [-]. Textural data of SWy2-Na, SWy2-CuTrien, YPC-CF, and YPC-CF-CuTrien were taken from *Chapter 2*. 153

Chapter 5: ***Outlook and concluding remarks*** **157**

Glossary

sign	description	unit
A_{BET}	BET specific surface area	[m^2/kg]
C	BET constant	—
De	Deborah number	—
E_0	DA characteristic energy	[kJ/mol]
P	Absolute pressure	[Pa]
Q	Sorbed amount	[mol/kg]
Q_0	DA limiting micropore capacity	[mol/kg]
Q_{SRC}	Strong retention capacity	[mol/kg]
Q_{mono}	BET monolayer capacity	[mol/kg]
R	Molar gas constant	[J/K/mol]
T	Absolute temperature	[K]
T_{max}	Temperature of maximum hydrocarbon generation rate	[K]
TPV	Total specific pore volume	[m^3/kg]
T_{c}	Critical temperature of the bulk fluid	[K]
T_{hc}	Hysteresis critical temperature of the bulk fluid	[K]
V_0	DA limiting micropore volume	[m^3/kg]
V_{GV}	Gurvich specific pore volume	[m^3/kg]
V_{c}	Cavitation specific pore volume	[m^3/kg]
V_{m}	Liquid molar volume of gas	[m^3/mol]
W	Pore width	[m]
W_{cav}	Caviation critical pore width	[m]
W_{c}	Condensation critical pore width	[m]
W_{hc}	Hysteresis critical pore width	[m]
W_{mK}	Modified Kelvin pore size	[m]
W_{pb}	Pore body width	[m]
W_{t}	Pore throat width	[m]
ΔV_{GV}	Loss of Gurvich specific pore volume	[m^3/kg]
Γ	Gamma function	—
κ	Electrical conductivity	[S/m]

sign	description	unit
ϕ	Porosity	[m^3/m^3]
ρ_{gr}	Grain density	[g/mL]
σ	Standard deviation of the mean	—
θ	Contact angle	[°]
d_m	Adsorptive molecular diamete	[m]
k	Interaction constant of the adsorptive	[kJ nm^3/mol]
n	DA-exponent	—
p/p^0	Partial pressure	[Pa/Pa]
p/p^0_{cav}	Cavitation critical partial pressure	[Pa/Pa]
p^0	Saturation pressure	[Pa]
r_K	Kelvin radius	[m]
r_e	Equivalent micropore radius	[m]
r_c	Capillary condensation critical pore radius	[m]
AHI	Areal hysteresis index	—
BCM	Boom Clay mudrock	—
BET	Brunauer Emmett Teller theory	—
BIB-SEM	Broad ion beam scanning electron microscopy	—
BJH	Barrett Joyner Halenda	—
BM(a)	Aliquote "a" of Bossier mudrock	—
BM(b)	Aliquote "b" of Bossier mudrock	—
CCS	Carbon capture and storage	—
CEC	Cation exchange capacity	[mol(+)/kg]
CI	Confidence interval	—
COx	Callovo Oxfodrian Argillite	—
Cu-Trien	Cu-triethylenetetramine complex	—
CV	Coefficient of variation =(RSD)	—
DA	Dubinin Astakhov theory	—
DFT	Density functional theory	—
DVS	Dynamic vapour sorption	—
FIB-SEM	Focused ion beam scanning electron microscopy	—
FTIR	Fourier transformed infrared spectroscopy	—
GCMC	Grand canonical Monte Carlo simulation	—
HCCR	Hydrocarbon reservoir caprock	—
HM	Haynesville mudrock	—
IUPAC	International Union of Pure and Applied Chemistry	—
LM(a)	Aliquote "a" of Longmaxi mudrock	—
LM(b)	Aliquote "b" of Longmaxi mudrock	—
LOD	Limit of detection	—
LOQ	Limit of quantification	—

sign	description	unit
LPH	Low pressure hysteresis	—
MICP	Mercury intrusion porosimetry	—
nCT	Nano computer tomography	—
NLDFT	Non-local density functional theory	—
NMR	Nuclear magnetic resonance spectroscopy	—
NWR	Nuclear waste repository	—
OCM	Opalinus Clay mudrock	—
OM	Organic matter	—
PSD	Pore size distribution	—
QSDFT	Quenched solid density functional theory	—
SANS	Small angle neutron scattering	—
SAXS	Small angle x-ray scattering	—
SEM	Scanning electron microscopy	—
SVS	Static vapour sorption	—
SWy2	Wyoming montmorillonite	—
SWy2-CuTrien	Cu-Trien-exchanged Wyoming montmorillonite	—
SWy2-Na	Sodium Wyoming montmorillonite	—
TGA	Thermogravimetric analysis	—
TIC	Total inorganic carbon	—
TM	Toarcian "Tournemire" mudrock	—
TOC	Total organic carbon	—
UHCR	Unconventional hydrocarbon reservoir	—
VYCOR cpg	VYCOR controlled pore glass	—
XRD	X-ray diffraction	—
XRF	X-ray fluoresence	—
YPC	Ypresian Clay Elveringe mudrock (Mccroned bulk sample)	—
YPC-A	Ypresian Clay Aalbeke mudrock	—
YPC-CF	Clay fraction of Ypresian Clay Elverdinge mudrock with original cation occupation	—
YPC-CF-CuTrien	Cu-Trien exchanged clay fraction of Ypresian Clay Elverdinge mudrock	—
YPC-CF-E	Clay fraction of Ypresian Clay Elverdinge mudrock	—
YPC-CuTrien	Cu-Trien exchanged Ypresian Clay Elverdinge mudrock	—
YPC-E	Ypresian Clay Elverdinge mudrock	—
YPC-K	Ypresian Clay Kortenmark mudrock	—
µCT	Micro computer tomography	—
µPSD	Micropore size distribution	—

Chapter 1

Introduction

Geological barrier units have been pivotal for the socioeconomic development of human societies since their instrumental role as seals of oil and gas reservoirs during the era of fossil fuels, as a central element for subsurface climate mitigation measures (carbon capture and storage) and for the energy transition towards climate-friendly energy carriers such as hydrogen intended to be stored underground (Miocic et al., 2023). Moreover, geological seals take a central part in the long-term storage of hazardous, high-level nuclear waste (Tournassat et al., 2015b, Fink et al., 2019). Barrier units are required to provide application-adequate retention capacities with respect to pressure- and concentration-driven — i.e. advective and diffusive — transport including the ability to restrict free ion migration, especially in the framework of nuclear waste disposal. Furthermore, self-sealing properties are considered favourable for long-term storage applications in order to avoid excessive loss through fracture migration. Besides ductile and low-permeable salt formations, argillaceous mudrocks are excellent and effective barriers and seals, because of their low permeability and diffusivities and their potential to adsorb ions. Permeabilities of mudrocks can span up to ten orders of magnitude and even three orders of magnitude at a single porosity value depending on the particular lithology and its burial history (Neuzil, 1994, Yang & Aplin, 1998, Dewhurst et al., 1999). But permeabilities of caprocks can be as low as 10^{-19} to $10^{-24}\,\mathrm{m}^2$ with gas capillary breakthrough pressures up to 30 MPa (Hildenbrand et al., 2020, Amann-Hildenbrand et al., 2015a). Likewise, gas diffusivities are variable, spanning about three orders of magnitude ($10^{-10}\,\mathrm{m}^2/\mathrm{s}$ and $10^{-12}\,\mathrm{m}^2/\mathrm{s}$ Amann-Hildenbrand et al. (2015a) (*collection therein*)). Savoye et al. (2011) reported effective isotope diffusion coefficients of Na-22, Cl-36 and Cs-137 for the Callovo Oxfordian argillite in a similar range than the given gas diffusivities ranging from 1.83×10^{-10} to $3 \times 10^{-12}\,\mathrm{m}^2/\mathrm{s}$ at 353 K. This is at least an order of magnitude lower than free ion diffusion in pure water. A collection of cation and anion diffusivities is presented by Bourg & Tournassat (2015).

Globally, mudrocks are the most common sedimentary rock type, making up approximately 60% of the sedimentary column (Potter et al., 1977). Potter (2003) defines mudrocks as fine-grained, argillaceous sedimentary rocks deposited in low-energy depositional environments, most abundant in marine and lacustrine realms. With respect to their mineralogical composition, mudrocks are qualitatively not substantially different from other sedimentary rocks, yet their grain/particle size is smaller and the relative contribution of specific minerals is distinctly different (Milliken &

Hayman, 2019). Mudrocks are composed predominantly of silt-sized ($< 62.5\,\mu m$) and clay-sized particles ($< 2\,\mu m$). Mineralogically, detrital and authigenic clay minerals dominate the mudrock composition; often far above 0.5 g/g (e.g., Yang & Aplin, 1998, Dewhurst et al., 1999, Potter, 2003). Clay minerals endow mudrocks with their distinct petrophysical and geomechanical properties like strength, fracture toughness, cohesion, plasticity, ductility, brittleness or elasticity (Rutter et al., 2017). The clay mineralogical composition and the clay mineral fabric in mudrocks can be highly variable in terms of clay mineral type and structure, but the most common types are smectites, illites, mixed-layer illite-smectite, kaolinite and sometimes chlorite (Tournassat et al., 2015a).

Fundamental structural units of these (hydrous) phyllosilicates constitute sheets of corner-sharing tetrahedral sheets ($X_{Tet}O_4$, here: X_{Tet} = Si or substituted by Al) and edge-sharing octahedral sheets ($X_{Oct}O_6$; here (X_{Oct} = Al, Fe, Mg etc.) linked via apical oxygen atoms, together forming elemental particles (Tournassat et al., 2015a). Clay minerals include the following structural types based on the stacking combination of layer types: 1:1 (T-O) clay minerals (e.g. kaolinite), non-expandable to expandable 1:2 (T-O-T) clay minerals (e.g. illite and smectites) and 1:3 clay minerals such as chlorites which incorporate an additional sheet of octahedrally coordinated Al, Fe or Mg (Worden et al., 2020). Depending on the cation occupation of the octahedral sheet, dioctahedral (2/3 sites occupied by trivalent cations) or trioctahedral (3/3 sites occupied by divalent cations) are distinguished (Brigatti et al., 2006). According to Tournassat et al. (2015a) Al-occupied dioctahedral clay minerals are most abundant in sedimentary rocks. Besides their *cis-* or *trans-vacant* structure, imposed by the location of the octahedral vacancies, some 2:1 clay minerals possess a negative layer charge because of isomorphic substitution of cations in the tetra- and/or octahedral position by lower charged cations or octahedral vacancies (Tournassat et al., 2015a). The negative layer charge might not be uniformly distributed, yet it is typically balanced by alkali and alkaline earth metals most commonly Na^+, K^+, Ca^{2+} or Mg^{2+} (Tournassat et al., 2015a). The balancing cation population, however, depends on the local mineralogy and the availability of cations. Moreover, the negative layer charge gives rise to the clay minerals' ability to exchange cations with solutions (Brigatti et al., 2006) and the charge-balancing cations provide expandable clays like smectites with their unique water-interaction properties. This includes, for example, the intercalation of up to four discrete water layers into the interlayer space resulting in crystalline- and osmotic swelling controlled by the type of interlayer cation (e.g., Likos & Lu, 2006). The reader is referred to the *Handbook of clay science* by Bergaya & Lagaly (2013) for an in-depth review of clay minerals, their structure and properties and to the scientific compilation of Tournassat et al. (2015b) for an overview of clays within the framework of natural barriers.

Besides clay minerals, mudrocks can contain variable amounts of detrital mica, framework silicates (quartz, feldspars), various carbonates (calcite, dolomite/ankerite, siderite), and accessories like (hydro-) oxides (hematite, magnetite, goethite, rutile, anatase etc.) or biogenic silica like opal (Potter, 2003). Diagenetic pyrite, anhydrite and gypsum are also common (Rutter et al., 2017). Additionally, mudrocks can comprise a relevant amount of organic matter (about 0.05 g/g) in the form of kerogen and bitumen (Potter, 2003, Rutter et al., 2017). Depending on the depositional setting, mudrocks can even contain several tenth percent of organic matter like the Alum shale (25%), the lacustrine black shales of the Batateira beds (> 30%) or the Kimmeridge clay with

above 40% of organic matter, classifying them as *Black shales* and sources for fossil fuels when thermally mature enough (Schieber, 2003, Gasparik et al., 2012, Li & Krooss, 2017, Claes et al., 2021).

The variability in transport properties is closely related to lithological properties like mineralogy, pore size distribution and degree of compaction (Dewhurst et al., 1998, 1999, Yang & Aplin, 1998, 2007). The pore network of mudrocks is witness to an intricate entanglement of depositional setting, mineralogy and burial history, making the development of the pore network as well as its transport- and storage properties highly variable and heterogeneous. Following Loucks et al. (2012), pores and pore networks of mudrocks display multiple stages of evolution. Fundamentally, the pore network is shaped by several key factors: mineralogy, sedimentary fabric (the architectural arrangement of crystallites and their aggregates), the size and geometry of grains, aggregates, and crystallites, as well as the presence of organic matter and its response to burial. Furthermore, turbostratic stacking disorder is another factor coming into play for smectites and mixed-layer phases involving smectitic layers (Moore & Reynolds, 1989, Michot & Villiéras, 2006, Kaufhold et al., 2010, Tournassat et al., 2015b, Michot, 2018, Schoonheydt et al., 2018). As a result of their small crystallite size, platy geometry, spatial organisation, and assemblage architecture (fabric), clay minerals share major responsibility in forming tightly interwoven pore networks. Their structural arrangement contributes to broad pore size distributions and high specific surface areas. Środoń & MaCarty (2008), Michot & Villiéras (2006), Michot (2018) as well as Ziemiański et al. (2020) emphasise the key role of clay minerals in the architectural shaping of the microstructure of mudrocks, especially their contribution to microporosity and specific surface area. This yields microstructures in the range of Angstrom to hundreds of nanometres and even micrometric structures. As outlined by Kaufhold et al. (2010) and Schoonheydt et al. (2018), the micro- and mesoporosity[1] of clayey materials is primarily governed by the arrangement of crystallites and the degree of turbostratic disorder — specific to smectites and mixed-layer phases containing smectitic layers (cf. Moore & Reynolds (1989)) — which results in slit-shaped micropores. Additionally, the organisation of aggregates (assemblage architecture) plays a key role in forming interparticle mesoporosity. Moreover, the aggregate's internal arrangement of crystallites (regular laminar vs. chaotic card house) influences the microstructure, particularly in the mesopore range (Kaufhold et al., 2010). Hereby, it should be noted that an alignment of clay minerals perpendicular to the principal stress is common upon burial, but not always observed (Aplin et al., 2006).

While the elemental and compositional analysis of mudrocks are complex but straightforward with respect to a methodology involving, for example, X-ray fluorescence (XRF), thermogravimetry (TGA), and X-ray diffraction (XRD) combined with organic petrology and (Rock-Eval) pyrolysis, the microstructural examination is at least equally challenging. Conventional methods applied to sandstones often fail or are insufficient in resolution for the pore-scale of mudrocks.

Anovitz & Cole (2015) and Busch et al. (2017) presented a comprehensive review of (petrophysical) methods, in relation to their assessed pore size scale, that are frequently applied to mudrocks for microstructural analysis. These authors have categorised the techniques commonly applied to mudrocks into: fluid invasion, scattering and imaging methods.

[1] Porosity associated with pore widths of ≤ 2 to 50 nm, respectively.

Fluid invasion methods include mercury intrusion porosimetry, helium pycnometry, thermoporometry, imbibition, and gas/vapour sorption techniques (Schlömer & Krooss, 1997, Dewhurst et al., 1999, Schlömer & Krooss, 2004, Chalmers & Bustin, 2007, 2008, Clarkson & Solano, 2016, Fink et al., 2018, Hildenbrand et al., 2020, Hu et al., 2021). Mercury intrusion porosimetry is a regularly used technique, but its data suffer from sample compression and overestimation of smaller pores, especially for ductile mudrocks (Anovitz & Cole, 2015). In contrast, helium pycnometry and imbibition by capillary action provide merely grain density, specific pore volume and porosity, while thermoporometry is restricted to a narrow pore size range below 50 nm (Majda et al., 2018).

Scattering techniques such as small angle X-ray- and neutron scattering (SAXS, SANS) involve delicate and hardly accessible instrumentation, but they allow microstructure quantification from the nano- to micrometre scale (Clarkson et al., 2013, Leu et al., 2016, 2019, Busch et al., 2018, Rezaeyan et al., 2023, 2024).

Contrastingly, imaging techniques such as focused or broad ion beam scattering electron microscopy (FIB-SEM, BIB-SEM) or computer tomography (e.g. nCT and µCT) often suffer from limited resolution and representative elementary volume issues for mudrocks (Klaver et al., 2012, Keller et al., 2013, Desbois et al., 2016).

Bertier et al. (2016) and Busch et al. (2017) performed a comparison of microstructural quantities including porosity (ϕ), specific surface area (BET area) and pore size distributions (PSD) obtained from different petrophysical techniques for Opalinus Clay. These authors demonstrated the inherent method dependency of these microstructural parameters and partially attributed the observed differences to variations in accessible pore space and pore scale. However, inaccessibility cannot quantitatively explain the variations (Bertier et al., 2016).

A by now frequently used and cost-effective technique is low-pressure gas/vapour (physi-) sorption (Rouquerol et al., 2014).[2] Sorption relies on the principle of adsorption, defined as the exothermal accumulation of molecules at an interfacial layer; for the given case: the gas/solid interface (Lowell et al., 2006). According to the International Union of Pure and Applied Chemistry (IUPAC), the system of concern is divided into three components: the solid termed *sorbent*, the gaseous phase referred to as *adsorptive* and the adsorbed phase defined as *adsorbate* which distinguishes itself by a higher density, typically assumed to be liquid-like and with less mobility (Thommes et al., 2015). One discriminates chemi- and physisorption based on the energy involved in sorption processes. Chemisorption is irreversible and limited to a monolayer, since it occurs by means of "permanent" chemical bonding, involving high enthalpies of adsorption (Lowell et al., 2006). In contrast, physisorption emerges whenever gaseous molecules come into contact with a solid surface, and it releases substantially less energy. Such fluid-solid interaction is fully reversible and primarily governed by van der Waals forces, specifically London dispersion forces and short-range Born repulsion, resulting in non-specific molecular interactions (Thommes, 2007). Specific interactions rise when polar adsorptives and/or surfaces are involved (Thommes, 2007).

Physisorption measurements provide isotherms representing the adsorbed amount (Q) plotted as a function of partial pressure (p/p^0), defined as the absolute pressure (P) normalised to the fluids' saturation pressure (p^0) at constant operating temperature (T). Hence, the adsorbed

[2]Here, sorption is strictly understood as adsorption. Absorption, defined as the incorporation of a substance into the structure of another, is not considered.

quantity at equilibrium is a function of pressure, absolute temperature and interaction energy, the latter being specific with respect to the fluid-solid combination (Lowell et al., 2006). The shape of the isotherm essentially reflects the strength of the fluid-solid and fluid-fluid interaction and it is determined by the pore network structure (pore size distribution and disorder) of the solid (Lowell et al., 2006). Furthermore, operating temperature, representing the differences in thermodynamic state and stability of the confined and bulk fluid (e.g. shift in critical point), and surface-chemical heterogeneity influence the sorption isotherms (Thommes, 2004, 2007). The covered pore size range ($\approx 0.35\,\mathrm{nm}$ up to $> 100\,\mathrm{nm}$) falls within the range of what has been observed for mudrock porosity (Yang & Aplin, 1998, Clarkson et al., 2012, Clarkson & Haghshenas, 2013). Therefore, the pore size classification of the IUPAC is commonly adapted by geoscientists distinguishing pores based on their size (W) into micropores ($W < 2\,\mathrm{nm}$), mesopores ($2\,\mathrm{nm} < W < 50\,\mathrm{nm}$) and macropores ($W > 50\,\mathrm{nm}$). Further, a great number of *best-practice* guides and recommendations exist for physisorption measurements and data evaluation that aid to obtain high-quality data (e.g., Thommes et al., 2015, Cychosz & Thommes, 2018, Schlumberger & Thommes, 2021, etc.). Data processing can involve traditional theories like the Brunauer Emmett Teller (BET) theory as well as more sophisticated models based on statistical mechanics (e.g. density functional theory (DFT)) or molecular simulations (e.g., Monte-Carlo simulations) describing the fundamental sorption processes and mechanisms, while they deliver a multitude of microstructure information ranging from microporosity, over the specific surface area and pore size distribution to a fingerprint of the adsorptive-accessible specific pore volume termed Gurvich pore volume. However, the theories must be suitable for the studied sorptive-sorbent system; i.e. inherent physical processes, chemical and geometrical assumptions about the solid and its porosity should capture the true system as closely as possible; otherwise accurate and reliable texture data are not obtained, despite good numerical fits like for DFT models (Thommes et al., 2015, Bertier et al., 2016). To acquire such data, an isotherm measurement requires a fairly small amount of material which can be taken in compliance with a proper sampling strategy from a large and representative batch sample broken down to an appropriate aggregate size (e.g., 200 to 400 µm; cf. Lahn et al. (2020)). A detailed description and thermodynamic derivation of the adsorption process is given in Rouquerol et al. (2014), Lowell et al. (2006) and Tóth (2002).

Internationally accepted standard adsorptives are nitrogen (N_2 at 77 K), carbon dioxide (CO_2 at 273 K) and argon (Ar at 87 K) for which high-resolution experimental protocols and recommendations exist (Thommes et al., 2015). Despite IUPACs recommendation to employ argon physisorption at its normal boiling point temperature, only 2% of all physisorption measurements involved Ar, whereas N_2 and CO_2 isotherms shared 64% and 33% of all physisorption measurements performed in the geoscience community (Kr = 1%; Medina-Rodriguez & Alvarado, 2021). Moreover, data quality and data interpretation are found to vary (e.g., Chen & Xiao, 2014, Cao et al., 2015, Zhang et al., 2023). Recently, there has been an increased interest in the use of water as a probe molecule in the geoscience community, in order to study surface chemistry and pore structure in mudrocks (e.g., Li et al., 2016a,b, Tang et al., 2017, Feng et al., 2018, Sang et al., 2019, Lahn et al., 2020, Hou et al., 2021, Zhang et al., 2022, Xie et al., 2023). The reason for that is the omnipresence of water in the subsurface and its substantial influence on transport (e.g. multi-phase flow), storage

(e.g. blockage of sorption sites) and rock mechanical properties like a loss in compressive strength with increasing water content. Yet, systematic and mechanistic studies of water vapour sorption are mostly restricted to pure clay minerals because of their (clay mineral type dependent) affinity to take up water. From a "sorption" perspective water vapour sorption is appealing because (i) H_2O vapour sorption can be performed in a wide temperature range including room temperature, (ii) H_2O is sensitive to surface chemistry because of its permanent dipole, and (iii) the kinetic diameter of H_2O ($\sigma = 0.28\,\mathrm{nm}$) is smaller than that of $\mathrm{Ar}, \mathrm{N_2}$ and $\mathrm{CO_2}$ allowing entrance to smaller pores (Thommes et al., 2013). However, the interpretation of experimental water vapour sorption isotherms is not straightforward due to competing effects of surface chemistry and pore structure, leading to no direct correlation of p/p^0 and a particular sorption mechanism (Thommes et al., 2012, 2013). The influence of surface chemistry is particularly complex because physisorption theories used in the interpretation of $\mathrm{Ar}, \mathrm{N_2}$ and $\mathrm{CO_2}$ isotherms do not necessarily account for that and may therefore not apply to water vapour sorption isotherms in heterogeneous materials like mudrocks (Seemann et al., 2017). This is especially true for geological materials containing swelling clays which expand through the intercalation of water into the interlayer space (e.g. Mooney et al., 1952a, Norrish, 1954, Bérend, 1995, Cases, 1997, Ferrage et al., 2005, Lindholm et al., 2019). While an ample body of work is available for clay-water interaction, the application of water vapour sorption to mudrocks is scarcer and oriented more towards application- and saturation-related questions. Furthermore, it often remains on a qualitative level, especially when it comes to the mechanistic understanding and the often uncritical application of physisorption theories. In consequence, there is a need for a revision of the application and interpretation of gas- and water vapour sorption in geoscience, in particular when it comes to mudrocks.

Organisation of thesis

The following contribution is organised into four independent chapters, each of which is intended to answer basic questions on the application and interpretation of physisorption isotherms of different gases and vapours such as argon, nitrogen, carbon dioxide and water with a specific focus on mudrocks and clay minerals. Earlier works of Seemann et al. (2017) and Lahn et al. (2020) provided the basis for a more detailed analysis of specific phenomena and features associated with water vapour sorption on mudrocks which are followed up on in this scientific contribution.

Chapter 2 presents a systematic comparison of argon, nitrogen and carbon dioxide physisorption isotherms focusing on the microstructural interpretation of physisorption isotherms and the potential difference of textural descriptors. The study restricts itself to the most commonly used physisorption theories employed in Geoscience including microporosity evaluation via Dubinin-Astakhov theory (DA theory, Dubinin & Astakhov (1971)) and α_s method (Sing & Williams, 2005), specific surface area quantification via Brunauer Emmett Teller theory (BET theory, Brunauer et al. (1938)), pore size distribution analysis by Barrett Joyner Hallenda theory (BJH theory, Barrett et al. (1951) and total specific pore volume assessment via Gurvich rule (Gurvich, 1915). According to the IUPAC recommendation (Thommes et al., 2015), Ar physisorption should be preferred over N_2 and CO_2 because specific adsorptive-sorbent interaction is absent. The study did not reveal any systematic differences between textural parameters obtained from Ar, N_2 or CO_2 physisorption isotherms related to specific interactions except in the micropore range. Differences in specific surface area and Gurvich specific pore volume were small and a controlling parameter could not be identified. However, saturation pressure has emerged as the largest factor of uncertainty in this investigation, whereas reliable microporosity data could only be provided by Ar physisorption measurements.

The chapter is the published version of the present author's publication: Seemann T, Weber C, Bertier P, Claes H, Stanjek H. Argon physisorption for pore analysis of mudrocks, clays, and engineered analogues: is argon a better choice than nitrogen and carbon dioxide? Clays and Clay Minerals. 2025;73:e2. doi:10.1017/cmn.2024.3.

Chapter 3 is concerned with the distribution and controls of sorbed water in the disordered pore network of organic-lean mudrocks including the Boom Clay, the Callovo Oxfordian argillite, the Opalinus Clay, and the Tournemire argillite; formations highly considered in the context of nuclear waste disposal. The study is a direct continuation of the works of Seemann et al. (2017) and Lahn et al. (2020) who investigated the distribution of water upon adsorption conditioning. Here, the distribution of sorbed water was extended towards ad- and desorption conditioning and the differences were analysed. After a brief summary of principles and theories of water vapour sorption in engineered materials and pure clay minerals, constitutive water-sorption controls are identified for mudrocks and basic sorption processes are inferred. The water uptake could be tied to the quantity of smectite and the exchangeable cation capacity of the mudrocks, independent of the conditioning history. It was deduced that similar sorption mechanisms like in smectite should prevail in mudrocks containing swelling clays. This involved hydration of exchangeable cations (clustering),

interlayer hydration accompanied by crystalline swelling and likely capillary condensation. The textural modification encountered by nitrogen physisorption measurements on moisture-conditioned mudrocks was interpreted as a combination of capillary water uptake and heterogeneous smectite swelling. Finally, implications for the interpretation of water vapour sorption isotherms are outlined with respect to mudrocks and clayey materials and limitations of the experimental approach are discussed.

This chapter is a longer version of the current author's manuscript that will be submitted after a final internal review from the co-authors: T. Seemann, H. Claes, H. Stanjek. Insights into Sorbed Water in Mudrocks: Investigating Distribution Patterns, Controls & Mechanisms.

Chapter 4 addresses the origin and mechanisms of frequently encountered hysteresis of water vapour sorption isotherms of mudrocks along the complete partial pressure range. While elaborated models exist for N_2 and Ar, explanations for water vapour sorption hysteresis in mudrocks often do not advance much beyond literature reasoning, lacking evidence for the particular case studied. Starting with a summary of hysteresis phenomena, the study discusses the various underlying mechanisms of water vapour sorption hysteresis in mudrocks based on experimental data obtained for swelling and non-swelling (Cu-triethylenetetramine-exchanged) mudrocks and montmorillonite analogues. Hysteresis of water vapour sorption isotherms of mudrocks was linked to: (i) tightly bound water, (ii) swelling when expandable clays were present, (iii) to out-of-equilibrium ("kinetic") hysteresis associated with the choice of the equilibrium criterion, (iv) to capillary condensation joined with free evaporation and cavitation for Cu-triethylenetetramine-exchanged materials. Cavitation was proven to be active in Cu-triethylenetetramine-exchanged materials and could be tied to a pore size of ≈ 2.2 to 2.5 nm which, to the best of our knowledge, has not been shown before in such detail for mudrocks.

This chapter is the current author's manuscript that will be submitted after a final internal review from the co-authors: T. Seemann, H. Claes, H. Stanjek. Hysteresis in Water Sorption Isotherms of Mudrocks: Origins and Mechanisms.

Chapter 5 concludes the scientific contribution and provides "additional" findings, as well as a discussion of questions raised during the preparation of particular parts of this contribution. Finally, some concluding remarks are made involving an outlook and future research questions and topics.

Chapter 2

Argon Physisorption for Pore Analysis of Mudrocks, Clays and Engineered Analogues: Argon a better Choice than Nitrogen and Carbon dioxide?

The chapter is the published version of the present author's publication: Seemann T, Weber C, Bertier P, Claes H, Stanjek H. Argon physisorption for pore analysis of mudrocks, clays, and engineered analogues: is argon a better choice than nitrogen and carbon dioxide? *Clays and Clay Minerals*. 2025;73:e2. doi:10.1017/cmn.2024.3.

Abstract

Argon physisorption at 87 K is the new standard for texture analysis of microporous media recommended by the International Union of Pure and Applied Chemistry (IUPAC). However, geoscientists routinely use nitrogen (77 K) and carbon dioxide (273 K), both molecules with permanent polarization and the preference to interact with specific surface sites. In this work, N_2, CO_2 and Ar physisorption isotherms were measured and classical physisorption theories were applied to investigate the suitability of Ar physisorption for the porosity assessment of mudrocks, clays and (non)-porous analogues.

N_2 and Ar physisorption isotherms are qualitatively similar with the strongest discrepancies in the submonolayer range. Textural parameters reveal linear relations but parameter-ratios vary randomly, independent of the sorbent class. While N_2 and CO_2 (mostly) underestimate micropore volumes, nitrogen BET areas are consistently larger than argon BET areas. Those differences are most likely associated with differences in polarization. But its effect on molecular orientation, for example, is presumably masked by microporosity and a narrow spacing of specific surface sites.

Mesopore size distributions and Gurvich (total) pore volumes agree well for N_2 and Ar indicating nearly similar pore size- and -volume access. Combining both parameters proves effective in identifying saturation pressure offsets which pose the largest factor of uncertainty in this study. Ar-based micropore size distributions reveal three distinct classes of mudrocks differing in organic matter maturity, and its contribution to microporosity. Empirical α_s-plots corroborate this classification underlining the discrepancies in the micropore range of mudrocks. Comparative hysteresis loop analysis indicates cavitation as one dominant evaporation mechanism in mudrocks and clays effecting a sample-specific compartmentalization of their pore networks.

2.1 Introduction

Mudrocks play a central role in the oil- and gas industry, in environmental applications including carbon capture and storage (CCS) or long-term nuclear waste disposal. As a natural barrier system, they retard fluid flow and radionuclide migration by means of their complex and tightly interwoven pore network and beneficial mineralogy. The presence of clay minerals, for example, enhances sorption of radionuclides, lowers permeability and diffusivity. Further, mudrocks typically have broad pore size distributions (Clarkson et al., 2012, Clarkson & Solano, 2016), which requires different petrophysical methods for obtaining complementary information from pore-scale to fracture-scale level.

The most commonly employed methods to study the pore network of mudrocks in the nanometre range are gas- and vapour sorption, mercury intrusion porosimetry (MICP), imaging-based methods like computer tomography (µCT) and scanning electron microscopy (SEM) as well as scattering-based methods such as small angle X-ray and neutron scattering (SAXS, SANS). The latter methods cover length scales from sub-nano to millimetre scale, but they are not readily available (Anovitz & Cole, 2015, Busch et al., 2017). MICP has been used for decades to determine textural information of mudrocks but due to ink-bottle effects, the produced pore size distributions are biased towards smaller pore sizes. Furthermore, sample compression during pressure build-up in MICP is likely to change the textural properties of soft materials like mudrocks and, lastly, the sample is irretrievably lost. Such drawbacks are not encountered when gas (physi-) sorption is performed. At low gas pressures, information such as specific surface area (A_{BET}), micropore volume (V_0), (total) pore volume (TPV), pore size distribution (PSD) and accessibility are obtainable. In contrast, at high pressure the gas-storage capacity is measured. Such characteristic properties find their application in numerical models used to evaluate safety aspects of nuclear waste storage facilities or in production analysis of oil- and gas fields.

To characterise microporosity and pore size distributions in tight rocks, mostly nitrogen (N_2) physisorption and to a lesser extent carbon dioxide (CO_2) are used (Anovitz & Cole, 2015, Clarkson et al., 2012, Busch et al., 2016, Bertier et al., 2016, Fink et al., 2018, Qi et al., 2019, Shabani et al., 2020, Vranjes-Wessely et al., 2020, Lahn et al., 2020, Jacops et al., 2021, cf.). CO_2 physisorption, however, is limited to pore widths $\leq 1\,\mathrm{nm}$, because the saturation pressure (p^0) of CO_2 exceeds with 3.49 MPa at 273 K, the pressure range of commercial physisorption devices (Thommes et al., 2015). Further, because of its permanent polarity, there is the possibility that CO_2 similar to N_2 experiences specific interactions with surface groups.

Instead of N_2 or CO_2, the International Union of Pure and Applied Chemistry (IUPAC) recently recommended argon (Ar) physisorption at 87 K for textural characterisation of (micro-) porous media. The reason for that is the symmetry of the spherical Ar atom and the absence of a permanent polar momentum (e.g., quadrupole moment) (Ar: 0.0 Å^2, N_2: 1.52 Å^2, CO_2: 4.3 Å^2, data from Sircar (2006)). Moreover, its polarisability is significantly lower compared to N_2 and CO_2 (Ar: 1.64 Å^3, N_2: 1.76 Å^3, CO_2: 2.65 Å^3, data from Sircar (2006)). This results in higher filling pressures of micropores for Ar compared to N_2 and CO_2 (Thommes, 2007). The latter adsorptives are both affected by the close proximity of surfaces in micropores due to (i) overlapping force fields of opposing surfaces and (ii) specific attractive forces of surface functional groups (Lowell et al., 2006) prohibiting a direct

correlation of filling pressure and pore size (Thommes et al., 2015).

Despite the advantages of Ar physisorption and its frequent use for the characterisation of tailored materials (Cimino et al., 2013, Grosman & Ortega, 2008), applications in geoscience are still rare (Bertier et al., 2016). According to Medina-Rodriguez & Alvarado (2021), only 2% of physisorption isotherm measurements on mudrocks employed Ar while N_2 and CO_2 physisorption isotherms contributed 64% and 33% and krypton (Kr) 1%, respectively. Holmes et al. (2015, 2019) used Ar, N_2, and CO_2 physisorption to determine the pore network structure of artificial mudrocks in order to develop a predictive model based on mineralogy for CCS. Within the framework of shale gas production from unconventional reservoirs, Psarras et al. (2017) applied Ar physisorption in combination with CO_2 physisorption to determine PSDs based on quenched solid density functional theory (QSDFT). However, neither author presented a comparison of Ar and N_2 textural parameters. Dudek (2016) performed Ar and N_2 physisorption measurements at 77 K to compare PSDs from classical theory to state-of-the-art density functional theory (DFT) models and found clear differences for both adsorptives and approaches. Zhang et al. (2017) presented a more systematic study of N_2 and Ar physisorption on organic-rich mudrocks focusing on DFT approaches for mudrocks in combination with different probe molecules. Qi et al. (2019) used Ar physisorption to investigate the effect of solvent extraction on the nanostructure of continental and marine coals and mudrocks. Recently, Delle Piane et al. (2021) followed the recommendation of IUPAC and employed Ar physisorption (combined with NLDFT) to study the effect of organic matter type on the porosity evolution of the Wufeng-Longmaxi mudrock. Despite the growing interest in Ar physisorption, a systematic assessment and comparison of the isotherm data is regularly not available for geological materials and isotherms are often analysed, interpreted, and reported incautiously.

The present study systematically investigated the differences between argon, nitrogen and carbon dioxide physisorption with respect to their application to mudrocks, clays, engineered analogues (VYCOR controlled pore glass, SiAl-pellets) and oxides (hematite, silica). It aimed to decipher the complementary or alternative use of Ar physisorption with a special focus on traditional physisorption theory and textural parameters including micropore volume, specific surface area (BET-area), Gurvich (total) pore volumes and pore size distribution (micro- and mesopores).

2.2 Materials & Methods

2.2.1 Sample materials

To represent the diversity of sorbents, especially mudrocks, 29 samples of various chemical composition, textural properties and origin were selected. According to texture (here: porosity) the sample set is classified into porous (n = 21) and non-porous (n = 8) sorbents.

The latter class includes spherical silica (SiO_2) particles and non-spherical iron oxides (Fe_2O_3) as well as muscovite. Four classes of (mostly) amorphous silica spheres were obtained from *Denka*. The manufacturer's analysis of the respective batches provides mean diameters of 0.26 µm (SFP-20M), 0.56 µm (SFP-30M), 3.2 µm (FB-3SDC) and 15.6 µm (FB-105FD) (DENKA, 2023). The hematite particles and the muscovite (HLM3) were produced by *KMI*. The non-spherical iron

oxides have d_{98} values of $< 30\,\mu m$ (MIOX Micro 30), $< 5\,\mu m$ (MIOX Submicro 5) and $< 2.5\,\mu m$ (MIOX Submicro 2.5) (KMI-Industrial-Minerals, 2023).[1] These hematites contain minor amounts of quartz and amorphous matter. The muscovite is characterised by a d_{50} value of $3\,\mu m$ and a d_{98} value of $< 14\,\mu m$ (KMI-Industrial-Materials, 2022) and contains minor amounts of quartz, feldspars and amorphous materials.[2] All silicas and hematites were used in the "as received" state, whereas the muscovite was purified and made homoionically by repeated exchange with KCl and pressure filtration for excess salt removal.

The porous materials constitute various mudrocks (n = 12), purified and homoionically exchanged clay minerals (n = 5), and a natural clay mineral mixture (n = 2). The montmorillonite (Source Clay SWy2) was purified by Atterberg sedimentation combined with centrifugation and made homoionically with either sodium (SWy2-Na) or Cu-tetraethylenetetramine (SWy2-CuTrien). The clay fraction of the Ypresian Clay Elverdinge (YPC-E) was first enriched by gravitational settling in an Atterberg cylinder and then used either with its natural interlayer cation occupancy or in its Cu-Trien exchanged form. No other chemical treatment was performed. The kaolinite (DK25) has been studied by Küster et al. (2021) and consists of $0.97\,g\,g^{-1}$ kaolinite, $0.01\,g\,g^{-1}$ svanbergite and $0.02\,g\,g^{-1}$ anatase. The sample was purified and made homoionically by repeated exchange with KCl and pressure filtration for excess salt removal.

Furthermore, four amorphous materials of well-defined pore size were included as analogues comprising VYCOR controlled pore glasses (n = 3) and SiAl pellets (n = 1). The VYCOR controlled pore glasses (VYCOR cpg) with nominal pore sizes of 5 nm, 20 nm and 50 nm, respectively, were purchased from bora*ident* GmbH. The VYCOR cpgs are prepared by extraction from phase-separated borosilicate glasses (VYCOR) (HEGLA boraident GmbH, 2013). Further information (e.g. chemical composition) was not available. The SiAl pellets were provided by Micromeritics Instrument Corporation as a reference material for N_2 physisorption isotherm measurement verification at 77 K. They have the following properties: $A_{BET} = 215(6)\,m^2/g$, $V_{GV} = 0.6\,mL\,g^{-1}$ and average pore width $\approx 11.5\,nm$ (Micromeritics-Instrument-Corporation, 2012).

The mudrocks' geological age ranges from 443.8 Ma for the oldest mudrocks (lower Silurian Longmaxi mudrocks (LM(a) and LM(b)) to 27.8 Ma for the youngest mudrock (Rupelian Boom Clay (BCM)). Information on the mineralogical composition, total organic carbon content and cation exchange capacities of the mudrocks are shown in Table 2.1. They are named according to their formation and grouped with regards to their application as hostrocks for potential nuclear waste repositories (NWR), unconventional hydrocarbon reservoirs (UHCR) and caprocks (HCCR). Additional information about the mudrock set is presented in section A.1, Table A.1 in the appendix.

[1] d_{98} values define that 2% of the particles are larger than the given size
[2] d_{50} values define that 50% of the particles are bigger than the given size.

Table 2.1: Collection of general mineralogy obtained by XRD and Rietveld refinement. Qtz: quartz, Fsp: feldspar, Cb: carbonate minerals, Clays: illite + smectite + I/S + muscovite + kaolinite + chlorite, Traces: pyrite, gypsum, anhydrite, rutile, anatase, apatite, sphalerite; (...) = sum of illite and smectite with no differentiation of mixed-layer contribution. Total organic carbon (TOC) and cation exchange capacity (CEC) were measured for this study on all samples; * = literature data collected from Seemann et al. (2017), Lahn et al. (2020), Hu et al. (2021).

ID	**Qtz***	**Fsp***	**Cb***	**Clays***	**Traces***	**TOC**	**CEC**
				[g g^{-1}]			[mmol g^{-1}]
BCM*	0.32	0.12	0.01	0.53;(0.43)	0.02	0.011	0.306
BM(a)	0.18	0.12	0.16	0.45;(0.41)	0.03	0.019	0.123
BM(b)*	0.19	0.10	0.09	0.60;(0.55)	0.02	0.017	0.162
Cox*	0.21	0.07	0.32	0.40;(0.32)	0.01	0.021	0.198
HM*	0.25	0.09	0.11	0.52;(0.34)	0.03	0.035	0.127
LM(a)*	0.62	0.11	-	0.26;(0.26)	0.01	0.064	0.213
LM(b)*	0.61	0.03	0.22	0.14;(0.13)	0.01	0.029	0.109
OCM*	0.13	0.07	0.11	0.65;(0.26)	0.03	0.013	0.187
TM*	0.19	0.02	0.10	0.65;(0.45)	0.04	0.012	0.171
YPC(A)	0.20	0.07	0.02	0.70;(0.66)	0.02	0.003	0.490
YPC(E)	0.16	0.07	0.01	0.69;(0.67)	0.03	0.002	0.378
YPC(K)	0.52	0.12	0.01	0.33;(0.32)	0.01	0.002	0.271

2.2.2 Sample preparation for physisorption measurements

Mudrock samples were received either as millimetre-sized chips or powders of defined particle size (Bossier(a) (BM(a)): 63 to 200 µm) and equilibrated at ambient temperature and humidity. A representative amount of rock chips was gently crushed and dry-sieved to a particle-size fraction of 200 to 400 µm. All materials were stored above silica gel in a desiccator until the material was needed for experimentation. Unless stated otherwise, none of the materials were chemically modified or treated. In preparation for physisorption measurements, the samples were evacuated initially at room temperature ($\approx$ 1 to 2 h) and then heated to 378 K (the SiAl reference was dried according to protocol at 623 K) under vacuum for at least 24 h. For the preparation of N_2 and CO_2 physisorption measurements, a *VacPrep 061* (Micromeritics Instrument Corporation, Norcross, GA, USA) was used achieving pressures <5 Pa. Prior to argon physisorption measurements, the samples were evacuated in the instrument-internal drying stations equipped with a turbo molecular pump (P <13 mPa). The drying state of the material (only Ar) was assessed by a pressure-rise test before each measurement.

After the drying period, the samples were left to cool to room temperature, back-filled with either nitrogen (N_2 and CO_2 experiments) or argon (Ar experiments), and sealed with rubber stops. Following weighing and the installation in the sample station, the samples were immediately evacuated and the differential free space — reduced by a glass rod — was measured by helium expansion prior to the actual physisorption measurement. Subsequently, helium removal was performed at room temperature in the sample station.

2.2.3 Nitrogen and carbon dioxide physisorption

N_2 and CO_2 physisorption isotherms of dry materials were measured on 0.2 to 0.5 g of bulk sample

using the manometric instrument *Gemini VII 2390t* (Micromeritics Instrument Corporation, Norcross, GA, USA). N_2 physisorption measurements were performed in a liquid nitrogen bath (77 K) in a partial pressure (p/p^0) range between 0.001 and 0.995 at 100 discrete pressure points (adsorption: 64; desorption: 36). Isothermal CO_2 uptake at 273 K was obtained at 21 discrete pressure steps between $0.0001 \leq p/p^0 \leq 0.036$. The saturation pressure (p^0) was measured separately for each pressure point. Operational equilibrium was assumed when the pressure change was $< 0.01\%$ of the average pressure over a period of 0.5 min.

2.2.4 Argon physisorption

Ar physisorption isotherms were measured on approximately 0.2 to 1.0 g of dry bulk material using the manometric apparatus *Autosorb-I-MP* (Quantachrome Instruments, Boynton Beach, FL, USA). A CryoSync thermostat regulated the temperature at 87 K with a precision of ±0.1 K. The isothermal uptake was determined for at least 81 and 29 discrete pressure points in ad- and desorption mode between $10^{-7} \leq p/p^0 \leq 0.995$ for mudrocks and clays. Engineered materials were measured between $10^{-4} \leq p/p^0 \leq 0.995$. The saturation pressure was specified manually at 101 325 Pa (normal boiling point of argon at 87 K); i.e. p^0 (Ar) was assumed to be constant because of technical reasons. For p/p^0 of < 0.1 a tolerance of $p/p^0 = +0.0003$ and -0.0001 was allowed while above $p/p^0 = 0.1$ tolerances of $p/p^0 = +0.009$ and -0.003 were admitted. When the requested partial pressure was below the tolerance band, the data point was taken after the first dose of the instrument at the given p/p^0 (micropore range). Operational equilibrium was assumed when the pressure change was < 81 Pa for 5 min ($\approx 16\,\mathrm{Pa\,min^{-1}}$) for mudrocks and clays. For freely accessible pore networks (engineered materials) and non-porous solids an equilibration time of 1 min was employed.

Equilibration criterion and repeatability of argon physisorption

The effect of the equilibrium criterion on Ar uptake and the derived textural parameters was investigated on the Opalinus Clay (OCM), the Longmaxi(a) (LM(a)) mudrock and the Ypresian Clay-Kortemark (YPC-K). Equilibration times were tested from 1 to 13 min per pressure point for the OCM and from 1 to 10 min for the LM(a) along the entire pressure range. Equilibration time is defined as the time interval in which the pressure change was < 81 Pa and within the specified tolerance band of the pressure point. The YPC-K was used for boundary condition testing in the micropore range applying equilibration times of 5 min and 60 min, respectively. Other measurement conditions were held constant (see section 2.2.4). Equilibration time tests for N_2 physisorption measurements were performed in an earlier study by Bertier et al. (2016), but with a focus on low-pressure hysteresis.

Repeatability and precision were scrutinized on the SiAl pellets, the Boom Clay (BCM), the Opalinus Clay, and the Haynesville mudrock (HM). Ar physisorption isotherms were measured ten times (n = 10) with an equilibration time of 1 min for the SiAl pellets and at least five times (n = 5) for the mudrocks with 5 min equilibration time. Repeatability of N_2 physisorption measurements were not specifically conducted in this study, but coefficients of variation (CV; defined as relative standard deviation) were calculated from all isotherm measurements on dry mudrocks (identical

sample) and the reference material, ever performed with the used device in the study laboratory (data partly published in Lahn et al. (2020) for OCM).

Uncertainties for the complete sample set were estimated based on the interpolation of coefficients of variation ($CV = \sigma/X_{\mathrm{mean}} \times 100$) obtained for the aforementioned samples as function of parameter size (V_{GV}, A_{BET}, V_0). An arbitrary function was used for the interpolation. The mean parameter value (X_{mean}) and standard deviation (σ) were obtained from repetitive argon physisorption measurements. For scrutiny of the equilibrium criterion, 95% confidence intervals ($95\%CI = X_i \pm 1.96 \times \sigma_i$) were calculated from interpolated standard deviations (σ_i) for the parameter and sample of interest (X_i). The reader is advised that this procedure is considered as an approximation of the uncertainty of the textural parameters obtained from physisorption measurements. However, this does not necessarily imply a larger or lower uncertainty. The procedure probably results in an overestimation of uncertainty for small parameter values as usually the arbitrary function increased steeply towards zero. The materials employed for equilibrium tests and repeatability measurements are regarded as representative of the sample set.

2.3 Primary experimental results

The amount of liquid nitrogen in the dewar was usually too small to enable the measurement of the full Ar adsorption and desorption physisorption isotherm in a single run. Therefore, the isotherms were split into a low-pressure part from $p/p^0 = 10^{-7}$ to 0.1 and a high-pressure part between $0.001 \leq p/p^0 \leq 0.995$. Both runs were merged in the overlapping partial pressure range and duplicate data were omitted in the final analysis. Offsets between both isotherm parts were not visible except for microporous samples, which showed a step between $p/p^0 = 0.001$ and 0.002. The origin of this step was probably related to the instrument, which switched here from the 133 Pa transducer to the 133 kPa transducer (Figure 2.6). This observation is noted because the step can affect data fitting in the low-pressure range.

2.3.1 Argon, nitrogen and carbon dioxide physisorption isotherms

Figure 2.1 to Figure 2.4 show the complete collection of Ar, N_2 and CO_2 physisorption isotherms of the sample set. The corresponding textural parameters are summarised in section A.6 to section A.8 in the appendix (Table A.5, Table A.6, Table A.7).

Scrutiny of the isotherm set revealed subtle differences in isotherm shape at pressures $p/p^0 < 0.1$. Ar isotherms display smoother curvature than N_2 isotherms which indicates slightly greater uptake in the lowest pressure range (Figure 2.1 to Figure 2.4). Starting at the lowest partial pressure, the N_2 uptake increases faster than that for Ar, but levels to approximately the same slope displayed by the Ar isotherm. The initially higher volumetric uptake of N_2 shifts the whole isotherm above that of Ar. This difference reverses when plotted on a molar basis due to the difference in molar volume of both adsorptives at their respective experimental conditions (not shown). Isotherms converge towards greater partial pressure at which a steep upswing occurs. A complete convergence is not observed for the sample set as the upswings can occur at slightly lower p/p^0 for N_2 compared to Ar (cf. BCM, YPC-CF-CuTrien). At the limiting partial pressures, N_2 isotherms clearly exceed the

Ar isotherms, except for the SiAl pellets and the VYCOR cpg-50nm.

Ar (87 K) and N_2 (77 K) physisorption isotherms of natural porous materials are of type IV (Thommes et al., 2015), lacking a plateau at high partial pressures as observed for the controlled porous glasses (Figure 2.1, Figure 2.2, Figure 2.3). Generally, Ar and N_2 isotherms display qualitatively similar shapes including pronounced hysteresis of either type H3 or type H4 (Thommes et al., 2015). Micropore-dominated samples (Cu-Trien exchanged materials) are characterised by a type H4 hysteresis loop whereas meso- and macropore-dominated samples possess a type H3 hysteresis loop. Hysteresis loop closure points of mudrock and clay isotherms are identical for the respective absorptive with closing points at $p/p^0 = 0.45$ for nitrogen and $p/p^0 = 0.4$ for argon. Below the hysteresis critical pressure, adsorption is fully reversible for both adsorptives except for the HM, Bossier(b) (BM(b)) and both Longmaxi samples, which display slight low-pressure hysteresis.

Isotherms of the engineered materials and the kaolinite resemble a type IVa isotherm with individual hysteresis loops of either type H1 (VYCOR cpg-50nm, SiAl pellets, kaolinite) or type H2(a) (VYCOR cpg-20nm, VYCOR cpg-5nm). Accordingly, hysteresis loops close at pore-size specific partial pressures. The hysteresis loop of the kaolinite isotherm, for example, closes around $p/p^0 = 0.8$ and is narrow compared to those of the engineered materials (Figure 2.2h & Figure 2.3a to d). The upswing in adsorption occurs at a slightly lower partial pressure for N_2 than for Ar in the pore network of engineered materials. The desorption branches and hysteresis closure points are approximately equal for both adsorptives for all engineered materials as well as the kaolinite. All non-porous materials (muscovite, silicas and hematites) are characterised by a type II isotherm displaying little or no hysteresis. The small amount of hysteresis is attributed to inter-particle condensation and partially to instrumental reasons rather than to mesopores which are unlikely for these materials.

CO_2 physisorption isotherms were measured only for (micro-) porous samples (mudrocks, clays, and engineered materials) and are shown as inset in Figure 2.1, Figure 2.2a to g and Figure 2.3a to d. Independent of the solid the CO_2 uptake increased gradually lacking any peculiar feature. The uptake was mostly lower than those of Ar and N_2 at the same partial pressure. However, for some samples (BM(a), LM(a), VYCOR cpg(20 nm), SiAl pellets) the CO_2 uptake was similar to that of Ar on a liquid basis.

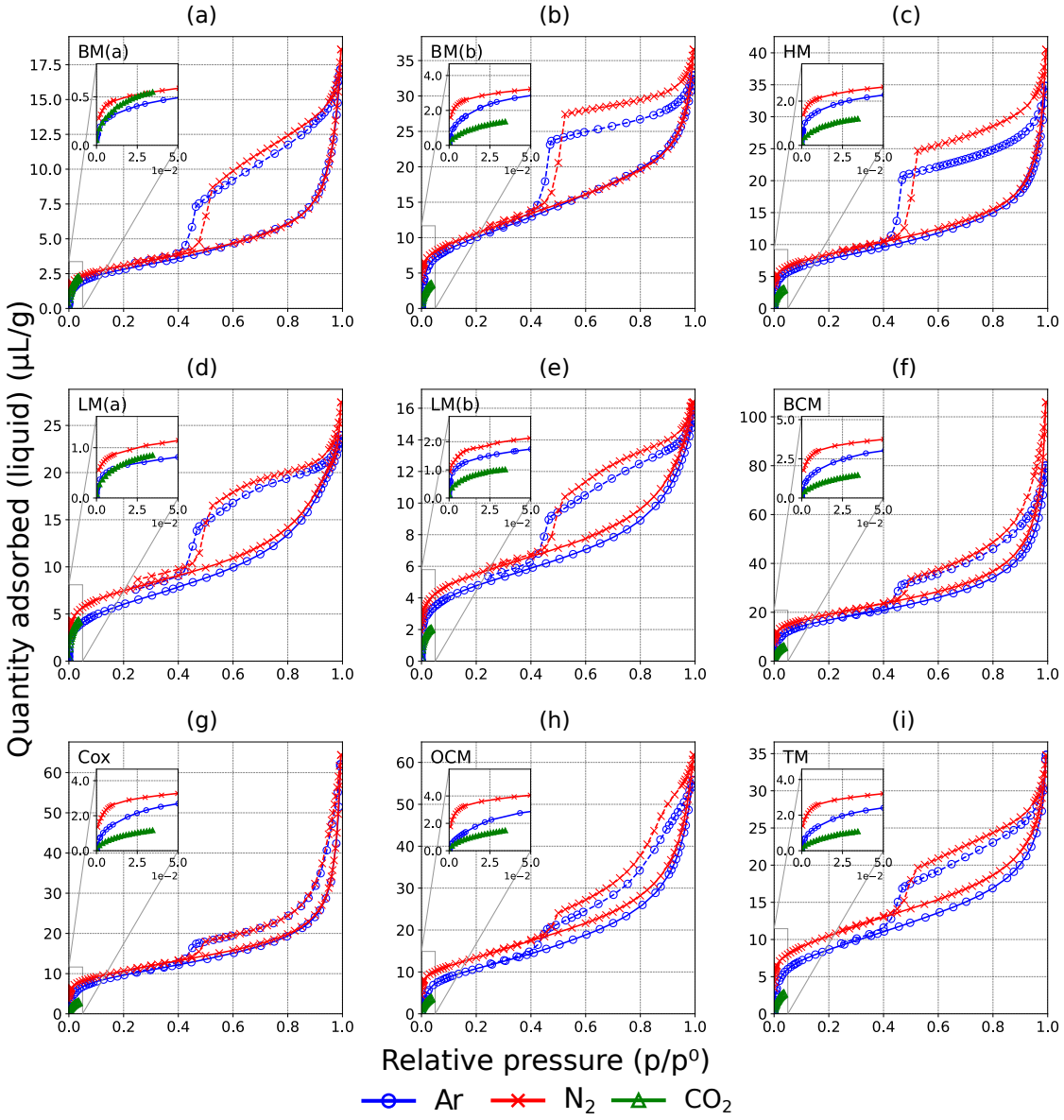

Figure 2.1: Ar, N_2 and CO_2 physisorption isotherms measured on the mudrock sample set at operational temperature of the adsorptive (a to i). The molar uptake is recalculated to liquid basis, assuming bulk liquid density of the respective fluid (cf. section A.2 Table A.2 in the appendix) for better comparison. The higher uptake of N_2 relative to Ar at $p/p^0 \ll 0.1$ shifts N_2 isotherms above those of Ar in the micropore range. CO_2 physisorption isotherms are either lower or equal to Ar physisorption isotherm on liquid basis.

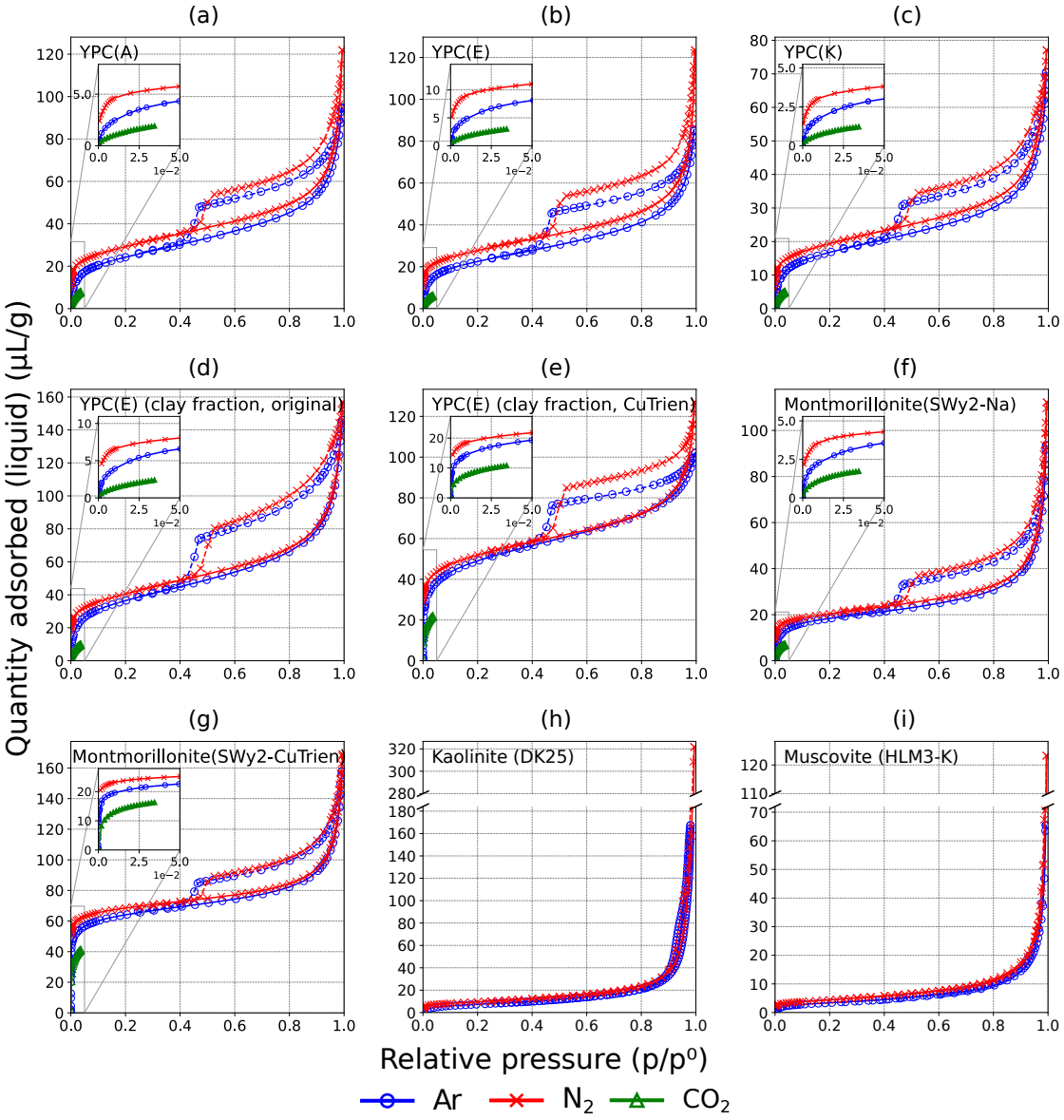

Figure 2.2: Ar, N_2 and CO_2 physisorption isotherms measured on mudrocks, clay minerals and clay mixtures at operational temperature of the adsorptive (a to i). Further explanation is found in Figure 2.1.

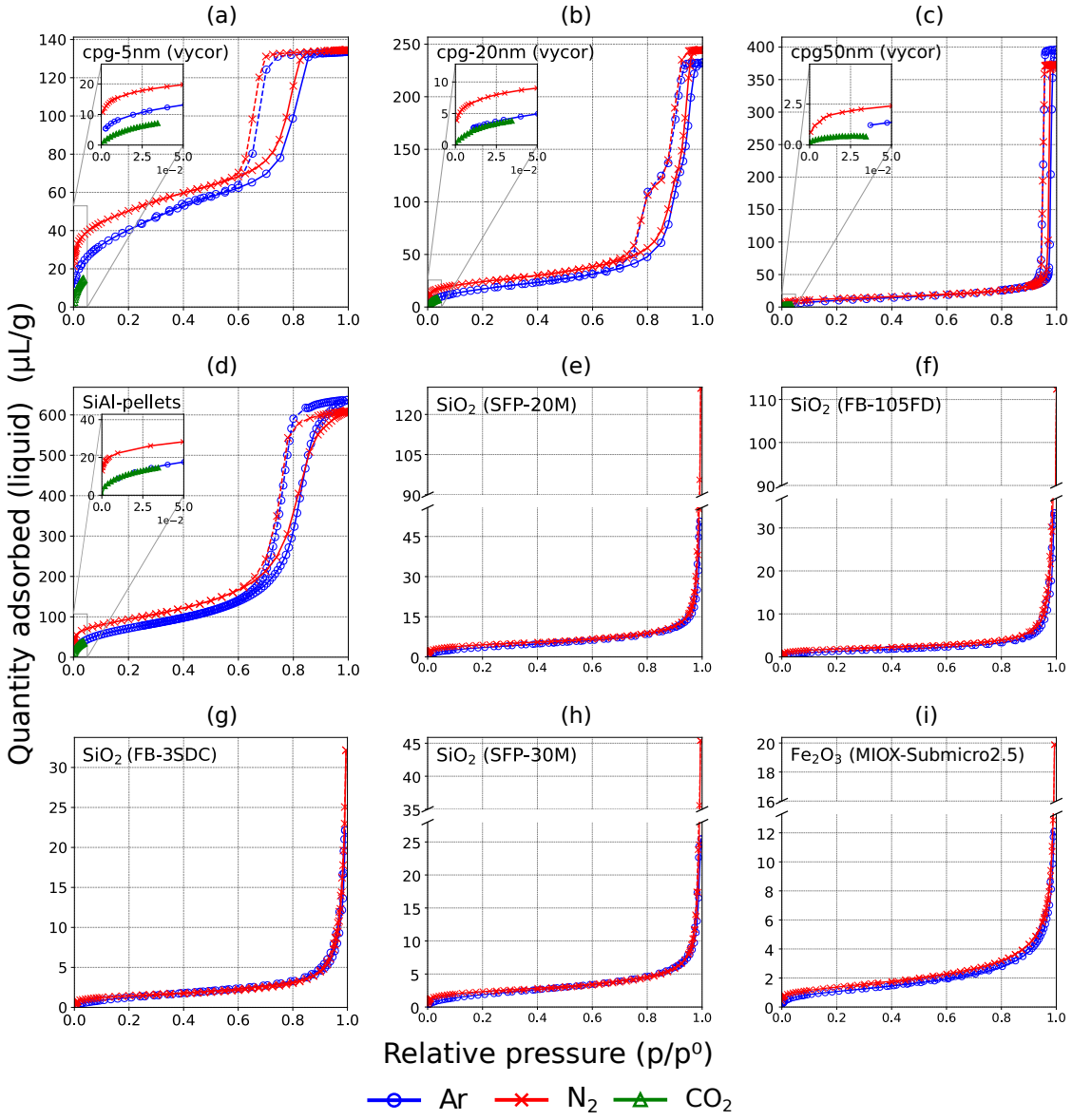

Figure 2.3: Ar, N_2 and CO_2 physisorption isotherms measured on engineered materials, silicas and Fe-oxides at operational temperature of the adsorptive (a to i). Further explanation is found in Figure 2.1

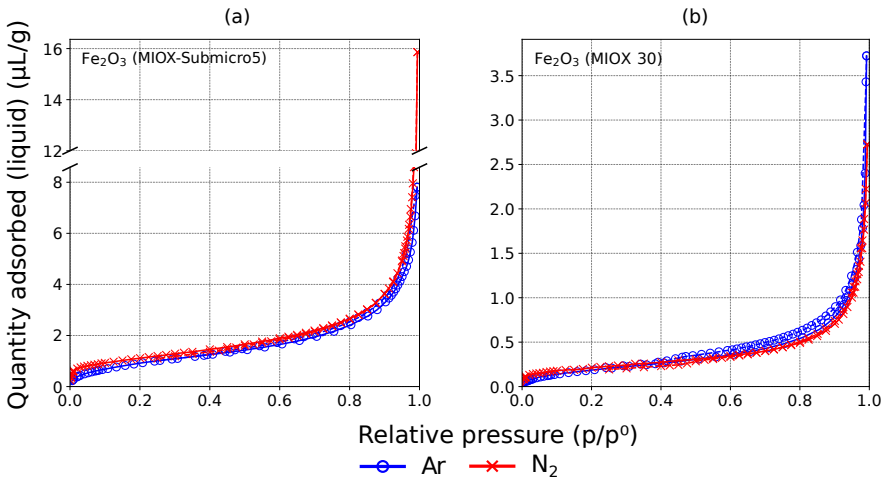

Figure 2.4: Ar and N_2 physisorption isotherms measured on the Fe-oxides at operational temperature of the adsorptive (a & b). Further explanation is found in Figure 2.1.

2.4 Quantitative evaluation of isotherms and discussion

In this section, various textural parameters will be derived from the primary experimental data by application of classical physisorption theories (Dubinin-Astakhov (DA) theory for micropore assessment (Dubinin & Astakhov, 1971), Brunauer-Emmett-Teller (BET) theory for specific surface area quantification (Brunauer et al., 1938), Barrett-Joyner-Hallenda (BJH) theory for mesopore size distribution (Barrett et al., 1951), Gurvich rule (V_{GV}) for (total) pore volume assessment (Gurvich, 1915), comparative α_s-plots (Sing & Williams, 2005)). Fluid specific parameters used in the isotherm analysis are summarised in section A.2 Table A.2 in the appendix.

State-of-the-art pore-texture assessment is performed by microscopic approaches like density functional theory or molecular simulation (GCMC). They describe the spatial density profile, fluid structure and its thermodynamic state close to the adsorbent surface accounting for the solid-fluid interaction potential, pore geometry (size and shape) and surface chemistry (Cychosz et al., 2017). The choice for classical physisorption models instead of density functional theory or molecular simulation models that are most commonly used in the literature on geomaterials, is intentional here (e.g., Li et al., 2015b, Zhang et al., 2017, Li et al., 2019b, Qi et al., 2019, Chen et al., 2022). According to Thommes & Cychosz (2014) and the IUPAC recommendation for physisorption (Thommes et al., 2015), the application of DFT models and molecular simulations can only provide reasonably accurate pore size distributions if a given nanoporous system is compatible with the chosen DFT/GCMC kernel. Unfortunately, suitable kernels are not available at present for materials with complex surface compositions and pore networks like those under consideration here. In case the chosen kernel does not apply to the experimental adsorptive/adsorbent system, the generated pore size distribution is generally significantly in error (Thommes et al., 2015, Schlumberger & Thommes, 2021). Classical physisorption models may also not yield accurate results for complex materials, yet they have been shown to be reproducible and are far less sensitive to mathematical model fitting quirks than the advanced models.

First, the effect of equilibration criterion will be addressed, followed by a reproducibility-,

repeatability- and reliability testing of argon physisorption measurements. This is supplemented by an uncertainty analysis. After a comparison of the physisorption isotherms of the different adsorptives and their general classification, micropore volumes, specific surface areas, Gurvich volumes and Gurvich porosities, micro- and mesopore size distributions will be discussed. Having discussed these parameters separately, an attempt will be made to correlate these quantities with characteristic parameters of the mudrocks. Finally, some general conclusions will be drawn regarding the experimental uncertainties and sorption mechanisms of the different adsorptives.

2.4.1 Equilibrium tests

Bertier et al. (2016) demonstrated the effect of equilibration time and diffusion control on N_2 physisorption in the pore network of mudrocks with special emphasis on low-pressure hysteresis. In line with Schlumberger & Thommes (2021), the authors highlighted a substantial underestimation of textural parameters for equilibration times which were too short.

Equilibration is particularly crucial in the micropore range when micropores control the access to larger pores (Schlumberger & Thommes, 2021) as it is often observed in mudrocks and clays through pore network effects. In contrast to N_2, Ar suffers less from diffusional constraints in tight pore networks because of the higher measurement temperature and the lack of specific interaction with surface groups preventing a shift in filling pressure to lower p/p^0, thus avoiding slower diffusion for Ar (Thommes, 2007, Cychosz et al., 2017).

The effect of equilibration time on Ar physisorption measurements was studied on the OCM and LM(a) mudrocks with equilibration times between 1 to 13 min and 1 to 10 min per pressure point, respectively (Figure 2.5). These were the maximum times that could be measured with a single dewar of liquid nitrogen.

Equilibration time tests on the OCM and LM(a) mudrock revealed sample-specific and non-monotonic effects in the increase of textural parameters (Figure 2.5). The OCM reached a plateau after 10 min equilibration time whereas the LM(a) plateaued from about 5 min equilibration time on. Raising the equilibration time from 1 to 13 min increased the limiting micropore volume and the specific surface area by a factor of ≈ 1.04, while the Gurvich pore volume increased by a factor of ≈ 1.09 for the OCM. This slight increase was achieved at the expense of an additional 1251 min of measurement time. In fact, an equilibration time of 5 min or 10 min produced a maximum relative difference of 1.2% for the LM(a) and 1.4% for the OCM in terms of textural parameters. Accounting for the estimated uncertainty of the Ar physisorption measurements showed that 95% confidence intervals overlap beyond 5 min of equilibration time for each characteristic parameter of both mudrocks (Figure 2.5b). This indicated that beyond equilibration times of 5 min textural parameters were not statistically different, suggesting a negligible control of the equilibration criterion on Ar physisorption for these particular mudrocks, if equilibration times were at least 5 min.

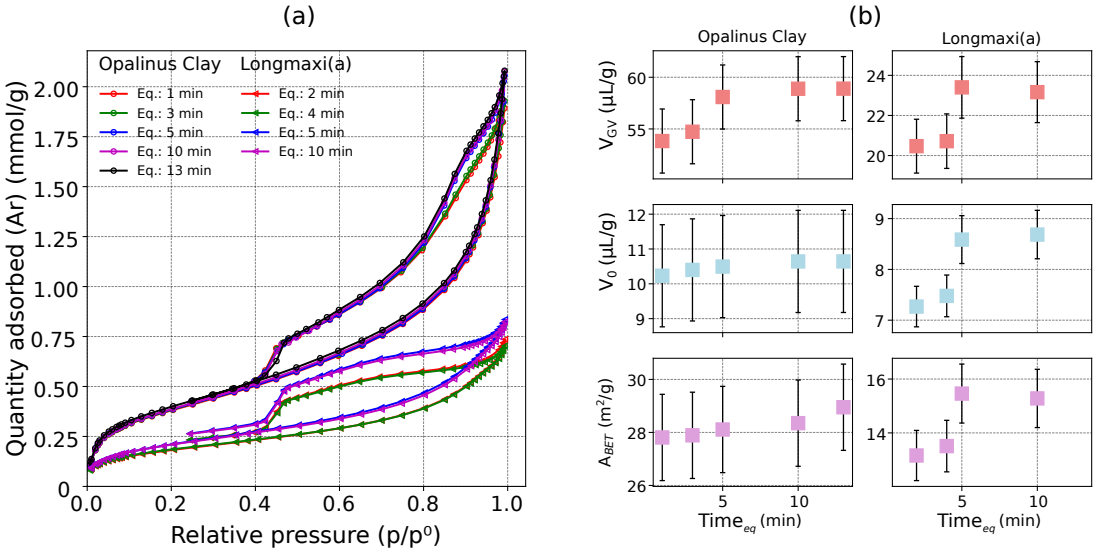

Figure 2.5: (a) Ar physisorption isotherm (87 K) of Opalinus Clay (OCM) and Longmaxi(a) (LM(a)) mudrock measured as a function of equilibration time (pressure drop of 81 Pa for 1 to 13 min and 2 to 10 min), respectively; (b) Plots of characteristic parameters (A_{BET}, V_0, V_{GV}) of OCM and LM(a) mudrocks as function of equilibration time. Error bars show 2 standard deviations obtained from repetitive measurements at 5 min equilibration time (OCM) or interpolation (LM(a)).

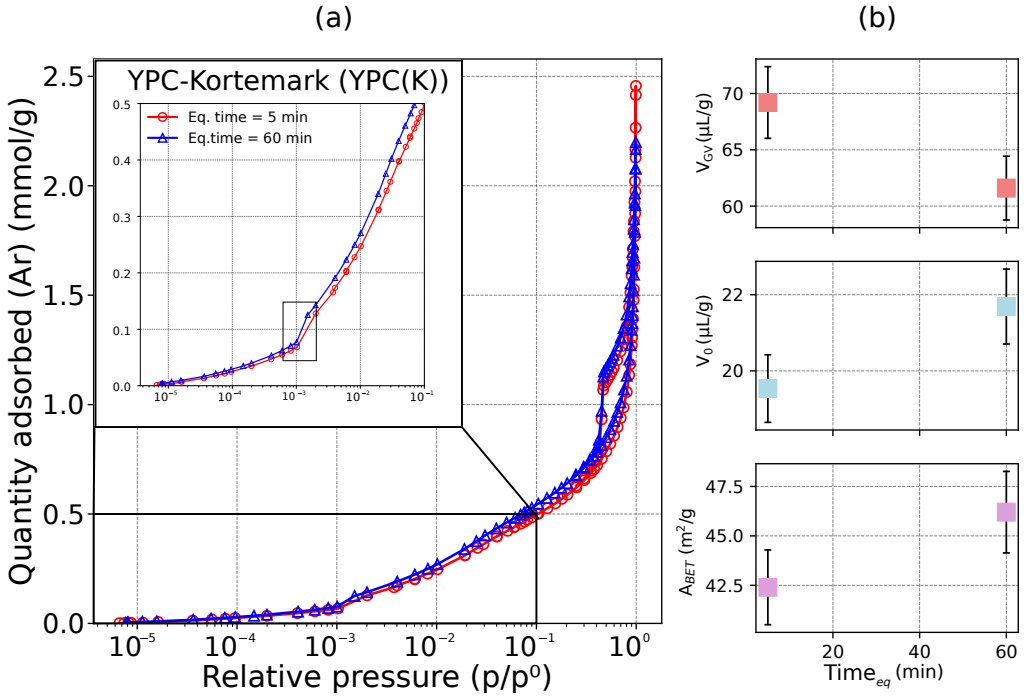

Figure 2.6: (a) Ar physisorption isotherms measured at 87 K at 5 min and 60 min equilibration time on the YPC-Kortemark mudrock. The inlay shows a zoom into the low-pressure region ($p/p^0 < 10^{-1}$); (b) Characteristic parameters (A_{BET}, V_0, V_{GV}) plotted as function of equilibration time including 2 standard deviations obtained from uncertainty interpolation. The Gurvich volume decrease of the 60 min sample is attributed to a saturation pressure offset (cf. section 2.4.3).

The YPC-K mudrock has been analysed with a focus on the micropore region when testing very long equilibration times (5 min *vs.* 60 min) (Figure 2.6). A slight shift of uptake towards greater partial pressure was recognised. This detectable difference quantified to approximately 10% in terms of micropore volume and BET area, which is consistent with the general isotherm offset. It remained unclear whether this difference was statistically insignificant because confidence intervals overlap with respect to BET area and no conclusion can be drawn (Figure 2.6b). Note, however, that the 95% confidence intervals overlapped only in the extreme tails by at most 4%. The difference in micropore volume remained significant as 95% confidence intervals did not overlap each other.

Though the shift of the isotherms (see inset of Figure 2.6a) was not substantial, it could still be indicative of an equilibration issue that causes underestimation of textural parameters. Therefore, ambiguity persisted whether a real effect at extreme conditions was detected or simply measurement uncertainty combined with sample heterogeneity. The latter cannot be ruled out as the test was not performed on the identical material (sample heterogeneity) and other unknown factors (p^0 offset; see the section 2.4.3) may have contributed to the observed difference.

The above demonstrates that an effect of equilibration time is detectable in the isotherm data though it should not be overvalued if no low-pressure hysteresis is observed. Systematic testing underlined that equilibration times were sample-specific and a general recommendation would be questionable, in particular for geological materials with complex pore structures. It is recommended instead that individual testing of equilibration criteria is performed in order to interpret data (and trends) reliably on an absolute and relative basis. However, from a practical point of view and conservatively accounting for uncertainty, an equilibration criterion of 16 Pa min^{-1} was acceptable in the present study as no significant low-pressure hysteresis was observed and other factors probably have a more substantial impact on isotherm measurements.

2.4.2 Reproducibility and precision of Ar physisorption measurements

The repeatability of Ar physisorption measurements was tested on the mesoporous SiAl pellets (n = 10) and three mudrocks covering a representative range of uptake (HM, BCM, OCM) (n = 5 to 10) (Figure 2.7). Coefficients of variation are defined as relative standard deviations and they are summarised together with the absolute standard deviations for the selection of representative samples in section A.3 Table A.3 in the appendix.

Considering the entire isotherm range, it was noted that the CVs varied with relative pressure. The CV for the SiAl pellets was $< 1\%$ at pressures below the level of capillary condensation and evaporation, respectively. Maximum coefficients of variation were obtained at the p/p^0 of sudden capillary condensation (2.1% at $p/p^0 = 0.825$) and evaporation (2.4% at $p/p^0 = 0.756$). For the Haynesville mudrock, the average CV was around 3.4% for the adsorption branch and 2.6% for the desorption branch. The highest CV values of 6.2% were observed in the ultra-low pressure range.

Statistical analysis of the main textural parameters (A_{BET}, V_0, V_{GV}) yielded CVs between 0.3 to 1.5% for the SiAl pellets and 0.3 to 3.5% for the Haynesville mudrock. The largest CV was observed for the micropore volume of the OCM amounting to 5.9%. For the other mudrocks smaller CVs were identified for all textural parameters. Generally, repeatability and precision were better for the SiAl pellets compared to the less sorbing mudrocks.

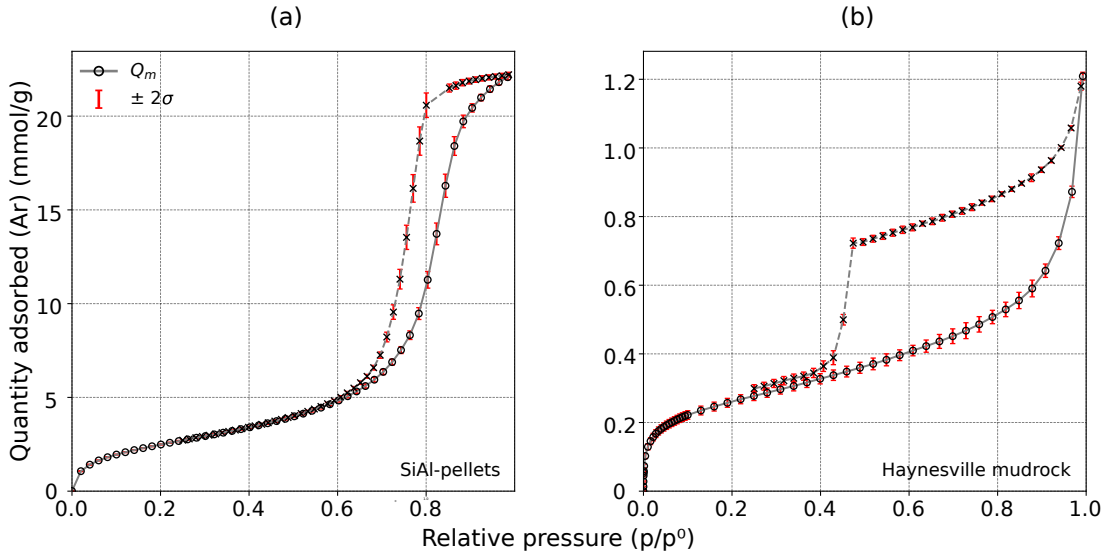

Figure 2.7: Ar physisorption isotherms (87 K) of repetitive measurements on (a) the SiAl pellets (n=10) and on (b) the Haynesville mudrock (n=5); The precision is represented by two standard deviations (2σ) shown for individual data points.

Explicit uncertainty data for Ar physisorption measurements in geoscience have not been found in the literature. For N_2 physisorption isotherms, Kuila & Prasad (2013) reported coefficients of variation of 2 to 6% for specific surface areas of mudrocks. Lahn et al. (2020) determined maximum coefficients of variation of 2.1% for Gurvich total pore volumes, 5.4% for BET areas and 5.3% for micropore volumes of moistened samples. For dry mudrocks, coefficients of variation ranged from 0.46% to at most 2.9% (calculated from physisorption data of Lahn et al. (2020)). This is in good agreement with the data presented. Furthermore, when considering a coefficient of variation of 5.9% (V_0 of OCM) on absolute scale, it yielded an absolute variation in micropore volume of 0.7 µL g^{-1} for the OCM. This is regarded as negligible when it comes to any application purposes involving micropore volumes as in pore network modelling. Thus, repeatability and precision were rated as good to excellent at constant experimental conditions. Therefore, the CV values presented here were regarded as small enough to allow interpretation of small differences between samples and the statistical analysis provided fair confidence in the Ar data presented.

2.4.3 Factors of uncertainty and the importance of saturation pressure

Isotherm analysis revealed four samples deviating outside of the confidence limits in textural parameters and isotherm shape (section 2.3). Ar physisorption isotherms of BCM, YPC-A, YPC-E and YPC-CF-CuTrien displayed isotherm-crossing at high p/p^0 (molar basis) resulting in a less steep approximation of the saturation pressure (Figure 2.8b). This crossing was not observed for the remaining sample set for which N_2 isotherms crossed Ar isotherms only in the low-pressure region (molar basis). The peculiarity was reflected in the Gurvich (total) pore volumes and BJH pore size distributions. The differences between Ar and N_2-based Gurvich pore volumes ranged

from 24 to 33% which is beyond the average deviation threshold reported in literature (McKee, 1959). In support, divergence in cumulative PSDs (ad- and desorption branch) increased as a function of pore size (Figure 2.8c). In fact, there are several parameters that can cause uncertainty during an isotherm measurement. Such factors include: (i) sample type (e.g., mineral fractionation, particle size etc.), (ii) sample treatment (drying (P_{vac}, T_{dry}), weighing etc.), (iii) gas purity, (iv) instrumental technicalities (volume calibration, pressure transducer etc.), (v) equilibration criterion, (vi) the operator's mood and care, to (vii) environmental conditions such as room temperature and atmospheric pressure fluctuations (not exhaustive). Schlumberger & Thommes (2021) additionally suggest (viii) helium entrapment in micropores (systematic dead-volume error) as well as (ix) thermal transpiration (here corrected) as factors of uncertainty. The systematic differences in this study were probably the result of saturation-pressure fluctuations induced by changes in the atmospheric pressure over the course of an isotherm measurement (i.e. $\approx$ 1 day).

Direct p^0 measurements provided evidence of the variation in saturation pressure during a physisorption measurement of up to 3 kPa (FB-105FD) (Figure 2.8a). These p^0 fluctuations are a direct result of atmospheric pressure changes that effect temperature oscillation in the liquid nitrogen bath; i.e. the boiling point of liquid nitrogen changes. Since the saturation pressure was not measured during the Ar physisorption measurements such fluctuations were not immediately accounted for when the isotherm was produced.

Atmospheric pressure fluctuations have substantial effects on the adsorbed amount since a temperature difference of 0.1 K varies the saturation pressure by approximately 1.07 kPa. Hence, an incorrect saturation pressure assumption yields either over- or underestimation of the amount adsorbed at a particular partial pressure because the thermodynamic state of the pore fluid (e.g., liquid density or cross-sectional area) is conjectured incorrectly and the p/p^0 is shifted depending on the offset direction. In detail, the p^0 offset provokes a shift in filling pressure of a particular pore size. In each case, the adsorbed amount (here for Ar) is assigned to a wrong pore size since the pore size is directly related to p/p^0 via the Kelvin equation (e.g., Seemann et al., 2017). The effect on liquid density is, however, negligible ($< 1\%$). Because the p^0 influence scales with pressure, the high pressure region and associated textural parameters (V_{GV}, PSD) are influenced more heavily than the low partial pressure region (V_0, A_{BET}) (Figure 2.8b,c). The assumption that beyond multilayer-formation, fluid-fluid interaction governs the sorption mechanism rather than solid-fluid interaction, suggests that N_2 and Ar adsorb in the same mesopore space (Kruk & Jaroniec, 2000, Thommes et al., 2012, Rouquerol et al., 2014). Therefore, similar PSDs should be obtained. Assuming that, N_2 isotherms are accurate[3] allowed to estimate the saturation pressure offset based on N_2 PSDs. In fact, the largest p^0 offset was estimated for the Boom Clay yielding a 13.3 hPa offset in saturation pressure (1026.03 hPa). Though, p^0 offsets were typically less than 5.3 hPa for the YPC-E, YPC-A and YPC-CF-E. Considering the Boom Clay, the saturation pressure offset caused a negligible difference in V_0 and A_{BET} of 1% and 0.37%, which was within the estimated 95% confidence interval for the BCM. On the most conservative assumption, a maximum relative difference of 46% has been obtained for the Gurvich pore volume whereas BET area and micropore volume change by $\approx$ 5% for the same sample (BCM). The maximum estimated differences in V_{GV} and A_{BET} were based

[3] p^0 of N_2 is measured continuously in the liquid nitrogen bath.

on all Ar physisorption isotherms ever measured in the study laboratory. Even though a rough and conservative approximation, the theoretical consideration conveys the view that the saturation pressure constituted the greatest uncertainty factor, especially for high partial pressures, for the presented Ar physisorption data as supported by the view of Schlumberger & Thommes (2021).

Direct p^0 measurements provided evidence for the above and emphasised the importance of continuous p^0 measurements instead of relying on a constant literature value for partial pressure transformation (Figure 2.8a). The p^0 offset was directly visible in the apparent pore size distribution and a cross-check with an independent physisorption measurement is highly recommended. Consequently, this observation underlined that pore size distributions and Gurvich total pore volumes have to be reviewed critically and cautiously in order to avoid misinterpretation caused by environmentally induced errors; yet they are good indicators for such a technical issue. Based on the above the BCM, YPC-A, YPC-E and YPC-CF-CuTrien qualify as significantly affected by saturation pressure offsets and their Gurvich (total) pore volumes and BJH PSDs were excluded from the following comparison.

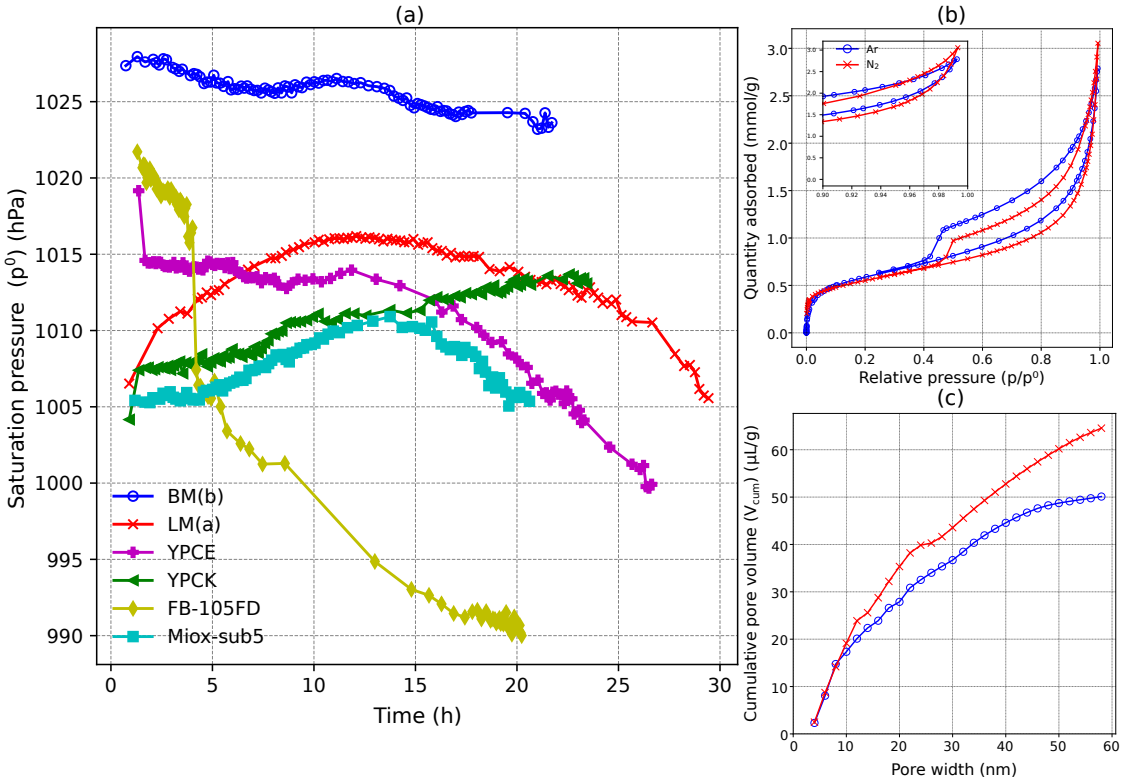

Figure 2.8: (a) Saturation pressure (p^0) fluctuations recorded during N_2 physisorption measurements performed on five (n = 5) porous and non-porous samples on a *Gemini VII 2340*; (b) Ar (p^0 offset) and N_2 physisorption isotherms of the Boom Clay sample plotted on a molar basis. The inset shows a zoom into the high partial pressure region; (c) Cumulative BJH-PSDs (adsorption branch) computed from Ar and N_2 physisorption isotherms measured on the Boom Clay sample.

2.4.4 Comparison and characterisation of N_2, Ar and CO_2 isotherms

Figure 2.1 to Figure 2.4 display Ar, N_2 and CO_2 physisorption isotherms of mudrocks, clays, engineered materials and non-porous oxides. Ar and N_2 isotherms are qualitatively similar in shape (e.g., Figure 2.1), yet some generally discriminating features were detected: (i) a differently shaped low-pressure region, (ii) deviating hysteresis loop closure points, and (iii) different upswing at high partial pressures.

(i) Differences in the low-pressure region N_2 physisorption isotherms exhibited a substantially steeper increase in uptake in the low-pressure region ($p/p^0 < 0.1$) compared to the well-rounded and smoother Ar isotherms. This feature was universal for the presented sample set and is commonly found in literature independent of the materials studied (Payne et al., 1973, Thommes et al., 2002a,b, Thommes, 2004, Thommes et al., 2013, Neimark et al., 1998, Schlumberger & Thommes, 2021, Sotomayor et al., 2018). The difference in low-pressure uptake was attributed to distinct and molecule-specific sorptive-sorbent interactions which are particularly prominent in the low partial pressure region; i.e. where volume filling of micropores and multilayering prevail (Dubinin, 1975, Rouquerol et al., 2014, Sotomayor et al., 2018). In contrast, the mesopore region showed only minor differences. This implies that the influence of surface forces on the sorption behaviour becomes less dominant beyond micropore filling and multi-layer formation (Rouquerol et al., 2014). However, surface forces likely transcend beyond the first few adsorbate layers and continue to influence adsorption but in a less significant manner compared to the low-pressure region. Thus, fluid-fluid interaction should be governing in the mesopore region, but latest at higher adsorbate loading.

Enhanced sorptive-sorbent interactions are linked to overlapping force fields and specific surface sites in combination with the adsorptive-specific polarisability and polar momentum. N_2 possesses a weak permanent quadrupole moment strengthening adsorption through specific interactions in addition to the action of van der Waals forces (Drain, 1953, Cychosz et al., 2017). In contrast, Ar lacks any permanent polar momentum reducing its interaction with a solid surface to pure van der Waals forces.

The existence of a quadrupole moment as for N_2 and CO_2 in combination with e.g., OH-groups or crystal defects can cause specific interaction forces that come on top of the ever-present van der Waals forces. Polarisation results in enhanced sorptive-sorbent interaction and evokes a reduction in the filling pressure of micropores for N_2 (Thommes et al., 2015). The listed features are present in mudrocks and clays, which often have a complex and heterogeneous surface chemistry (Zhang et al., 2017, Bai et al., 2020). In consequence, a substantial difference in uptake (isotherm shape) was expected and confirmed by the presented data in the region where these properties control fluid adsorption.

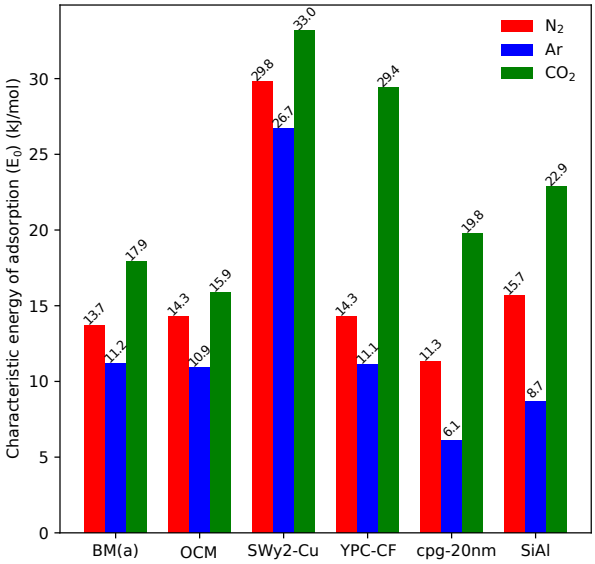

Figure 2.9: Characteristic energies of adsorption (E_0) calculated using DA-theory from N_2 (77 K), Ar (87 K) and CO_2 (273 K) physisorption isotherms of representative mudrocks (Bossier(a), Opalinus Clay), clays (SWy2-CuTrien, YPC-CF-E) and engineered materials (VYCOR cpg-20nm; SiAl pellets).

Enhanced sorptive-sorbent interactions of N_2 relative to Ar were substantiated by the characteristic energy parameter (E_0) calculated from DA-theory. $E_0(N_2)$ data were systematically higher providing qualitative evidence of the different energy levels involved in the adsorption process of both gases in micropores (Figure 2.9). This was further supported by the characteristic energy of CO_2 adsorption. $E_0(CO_2)$ was even greater than that of N_2 due to its stronger permanent polar momentum (section A.2 Table A.2 in the appendix). Clearly, the adsorption energy trend was substrate independent as illustrated by the heterogeneous selection of samples (Figure 2.9). However, ratios of characteristic energies were inconsistent. Thus, they are not exclusively governed by the adsorptive but by a combination of adsorptive and adsorbent.

The non-systematic variation could be attributed to the complexity of the pore network architecture, its constituents and eventually the share of an individual pore size to the total microporosity. Hence, a multi-factor control is expected to contribute to the adsorption distortion of N_2 and CO_2 while Ar is exclusively governed by pore geometry (size and shape).

Note that the characteristic energies are 'fingerprints' of the true physical energies and should be understood qualitatively. For a quantitative assessment of adsorption enthalpies, microcalorimetry is the analytical tool of choice. Fernandez-Colinas et al. (1989) employed microcalorimetry on activated carbons and could quantitatively corroborate that the stronger polarisation of N_2 yields appreciably larger differential enthalpies of adsorption compared to Ar (Rouquerol et al., 2014). This again supports the claim that N_2 sorption is enhanced relative to Ar in micropores.

(ii) Differences in hysteresis loops The hysteresis loops of N_2 and Ar isotherms displayed different closure points and varying width. Since hysteresis is a temperature-dependent phenomenon – as is the hysteresis critical pore size (Thommes, 2004)[4] – the width of the hysteresis loop is eventually governed by the thermodynamic state of the fluid. The thermodynamic fluid state diverges for N_2 and Ar, since Ar at 87 K is further away from the critical temperature than N_2 at 77 K ($T/T_c(Ar) = 0.58$ *vs.* $T/T_c(N_2) = 0.61$) (Thommes, 2004, Cychosz et al., 2017). Thus, the hysteresis critical pore size of N_2 and Ar differs slightly as do the hysteresis critical temperatures which eventually results in varying hysteresis width for both adsorptives. This distinction was, however, minor for the studied materials. Though, it should be noted that such a contrast in thermodynamic state means that an investigation of the volume trapped by the desorption controlling pore size is not straightforward and needs to be taken into account.

The closure point and its use in sorption mechanism analysis have been outlined by Thommes et al. (2006). The approach and its application to mudrocks and clays are discussed in section 2.4.11.

(iii) Differences in high-pressure region The high-pressure region of all geomaterials is defined by a gradual increase and asymptotic approximation of $p/p^0 = 1$ as well as the lack of a plateau in the isotherms. Both features are typical for mudrocks and clays indicating a broad pore size distribution as well as partial pore filling by both adsorptives. The broad pore size distribution leads to a lack of sharp pore condensation as is observed for engineered materials (Figure 2.1 *vs.* Figure 2.3). Furthermore, capillary condensation is delayed for both adsorptives because of the formation of metastable adsorbate layers complementary to a nucleation barrier for liquid bridges (Thommes & Cychosz, 2014, Cychosz et al., 2017). N_2 isotherms display a slightly earlier upswing compared to Ar isotherms. The observation is in line with literature on mudrocks and engineered materials (Zhang et al., 2017, Thommes et al., 2002a, 2006, 2013, Schlumberger & Thommes, 2021). This discrepancy is interpreted as the difference in strength of fluid-fluid and fluid-solid interaction of both adsorptives which is again a direct consequence of their distance to their critical points as well as the additional contribution of the quadrupole moment of N_2 to the fluid-fluid interaction.

2.4.5 Micropore volume

Micropore volumes of porous materials were obtained by means of DA theory and the α_s method (section 2.4.8 and section A.4 Table A.4 in the appendix). Micropores in mudrocks are commonly attributed to organic matter and clay minerals, both exerting control over sorption properties and storage capacity of fluids such as CH_4 or CO_2 (Chalmers & Bustin, 2008, Busch et al., 2016, Ziemiański et al., 2020). To assess the microporosity of mudrocks several researchers used DA-theory (Clarkson et al., 2012, 2013, Clarkson & Haghshenas, 2016, Furmann et al., 2016, Mastalerz et al., 2012, Chen & Xiao, 2014, Lahn et al., 2020, Shabani et al., 2020, Chen et al., 2021). It is considered suitable for geological materials because of its development for geometrically and chemically heterogeneous surfaces (Kruk et al., 1997, Dobruskin, 1998). Despite IUPAC's recommendation to use Ar or CO_2 for the assessment of microporosity, N_2 is regularly employed

[4] Fundamentally, temperature and pore size are complementary parameters with respect to hysteresis width; i.e. an increase in temperature has the same effect as a decrease in pore size (Thommes, 2004)

to quantify microporosity and it has been shown to weakly correlate with CO_2-based micropore volumes for a limited number of mudrocks and clays (Fink et al., 2017, Lahn et al., 2020, Ziemiański et al., 2020, Hu et al., 2021). Ar-based DA micropore volumes are shown as a function of N_2-based DA micropore volumes (Figure 2.10a). Note that the fitting ranges of the DA equation differed significantly for the two adsorptives. While N_2 isotherms could be fitted to $p/p^0 < 0.05$, the smoother and more rounded Ar isotherms allowed data fitting up to $p/p^0 \approx 0.2$. Exemplary fits of the DA-equation are shown in section 2.4.8 in Figure 2.13b. It has been noticed that Ar physisorption isotherms measured down to ultra-low pressures exhibit two linear regions (range 1: $\approx 10^{-7} < p/p^0 < 0.001$; range 2: $0.001 < p/p^0 < 0.1$) separated by a step that was not considered as a textural feature (section 2.3). The artificial step was not considered in the numerical fit, but fits converged with experimental data at lower partial pressure. However, the step affected especially the exponent of the DA-theory biasing fits when included in the fitting routine. DA micropore volumes varied between 3.9 µL g^{-1} and 94.7 µL g^{-1} for argon and from 2.5 to 96.3 µL g^{-1} for nitrogen (section A.6 Table A.5 and section A.7 Table A.6 in the appendix). Ar-based values were on average 5% larger than those of N_2 except for the SiAl pellets, for which a 2% larger N_2-based micropore volume was calculated (intercept statistically unequal to zero).[5] While a linear trend showed on absolute scale, ratios ($V_{0\mathrm{Ar}}/V_{0\mathrm{N_2}}$) scattered non-systematically. Deviation from unity was sample-specific but independent of the kind of sorbent. The largest differences were observed for the Bossier mudrocks (BM(a), BM(b)), the Callovo Oxfordian mudrock (COx) and

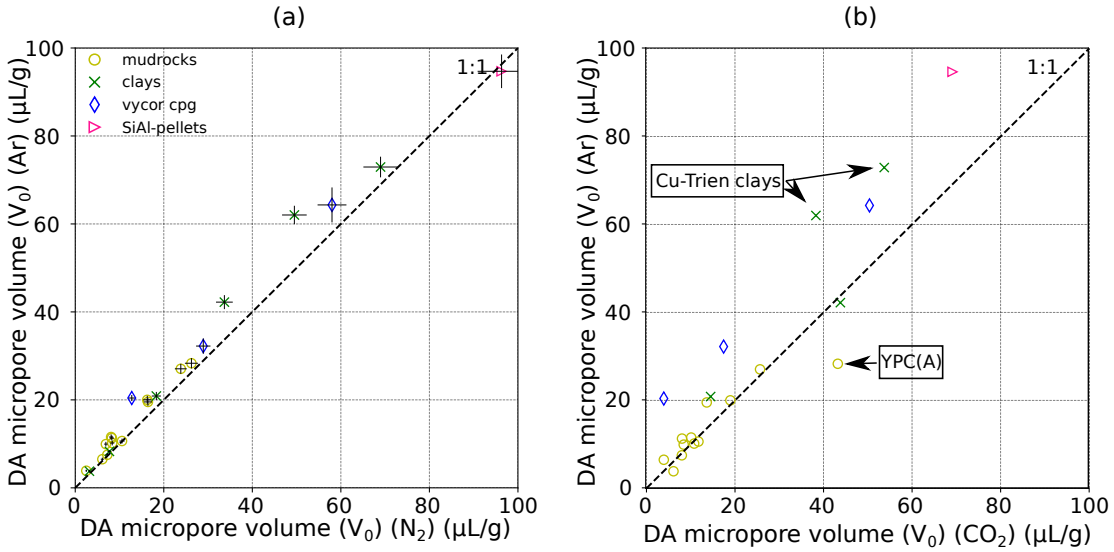

Figure 2.10: (a) Cross-plot of V_0 obtained from N_2 and Ar physisorption isotherms measured at normal boiling point temperature, respectively. Error bars represent two standard deviations and were obtained from interpolation of repeated measurements of representative mudrocks and the SiAl pellets; (b) Cross-plot of V_0 obtained from CO_2 and Ar physisorption isotherms measured at normal boiling point temperature (Ar) and 273 K (CO_2), respectively. No error bars are assigned because data for CO_2 isotherms are missing. The dashed line indicates unity.

DA micropore volumes of Ar were also compared to CO_2-based DA micropore volumes (Fig-

[5]Subsequently provided average values of deviations V_0, A_{BET} and V_{GV} correspond to the slopes of orthogonal distance regression of x_{i}(Ar) vs. $x_{\mathrm{i}}(N_2)$ or $x_{\mathrm{i}}(CO_2)$.

ure 2.10b). CO_2-based DA micropore volumes ranged between $3.9\,\mu L\,g^{-1}$ and $69.1\,\mu L\,g^{-1}$ (section A.8 Table A.7 in the appendix). The maximum fitting range for CO_2 isotherms was up to $p/p^0 \approx 0.036$. V_0 were mostly lower than those obtained from Ar isotherms, yet exceptions were identified for Bossier(a), Longmaxi(a), Opalinus Clay, Tournemire (TM), YPC-Aalbeke (YPC-A) and the clay fraction of the YPC-Elverdinge (YPC-CF-E). The micropore volumes of LM(a) and the YPC-A deviated by more than 35%. Notably, the micropore volumes of the Cu-Trien exchanged clays were considerably larger for argon than for carbon dioxide. The intercalation of Cu-Trien leads to a widening of the interlayer distance to 1.3 to 1.35 nm for smectites likely making the near-edge interlayer space accessible to nitrogen according to Kaufhold et al. (2010, 2011) and therefore to argon; i.e. edge pores created by the stacking disorder of crystallites (irregular stacking and overlap of crystallites) increase to values of approximately 1.5 nm according to DA micropore size distributions of Cu-Trien exchanged materials (cf. chapter 4). Assuming that the intercalation of Cu-Trien resulted in a major contribution of these 1.5 nm-edge-pores to total microporosity may explain the large imbalance between V_0(Ar) and $V_0(CO_2)$, since CO_2-access at 273 K is restricted to a maximum pore size of 1 nm in a conventional low-pressure instrument (Thommes et al., 2015). The third "outlier" (YPC-A) showed a significantly larger V_0 of CO_2. The YPC-A possesses the highest CEC of the mudrock set. According to Michot (2018), high-energy sites will disturb micropore analysis since they appear as apparent micropores, masking the "true" microporosity. Considering exchangeable cations as high-energy sites (relative) and the strong quadrupole moment of CO_2 may qualitatively explain this phenomenon. Generally, the data scattered stronger than those of Ar and N_2 and the average difference amounted to 30%. However, deviation from unity revealed no systematic trend and was again sample-specific and independent of the sorbent class. In fact, if surface chemistry was a key factor in micropore volume control of the presented samples, one would expect a clustering of the sorbents according to material type. Clustering was not observed suggesting that material-related surface chemical effects are either weak and undetectable or overprinted. The observed underestimation of N_2 and CO_2-based micropore volumes could further imply that N_2 and CO_2 either (i) do not penetrate similar pore space as Ar, or (iii) the access is kinetically constrained at operational temperature.

With regard to point (i), it is noted that the difference in accessibility of N_2, CO_2 and Ar may be associated with solid composition (section 2.4.10) or differences in sample preparation. While ultra-high vacuum (p <13 mPa) was used in the case of Ar, samples for N_2 and CO_2 measurements were outgassed at p <5 Pa. According to Cychosz et al. (2017) a pressure level of approximately 5 Pa is not sufficient to fully evacuate the entire micropore network. Especially, micropores have a high water-retention capacity and may only be outgassed at elevated temperatures, above 378 K, and at very low pressures (Ziemiański et al., 2020). In turn, compartments of the pore network may be blocked by remaining water and left undetectable by N_2 and CO_2 (Seemann et al., 2017). In consequence, micropore volumes would be underestimated by N_2 and CO_2 relative to Ar. Concerning (ii), note that N_2 (at 77 K) suffers stronger diffusional constraints than Ar in pores smaller than 0.7 nm (Cazorla-Amorós et al., 1998). This constrain relates to the required thermal energy, necessary to diffuse in narrow micropores which is mounted by Ar but not N_2 at their operational temperature. The phenomenon has exemplarily been shown by Reichenbach & Klank (2014) who

investigated N_2 uptake of a zeolite (pore width(W) = 0.4 nm) as function of temperature revealing pseudo-equilibria at 77 K and significant uptake when the diffusion barrier was broken. Supposing that a non-negligible amount of pore volume is either built or connected via such small constrictions may explain the observed difference for nitrogen.

CO_2 is not kinetically restraint but limited by the accessible pore size of 1 nm. However, considering the milder outgassing conditions for N_2 and CO_2 makes it more likely that the materials were not sufficiently outgassed and water resides in small micropores. In addition, the possibility of helium entrapment during the free space measurement can be an issue for samples containing significant amounts of pores inaccessible to nitrogen or argon (Thommes, 2007, Thommes et al., 2015). Helium-entrapment influences the isotherm shape in the ultra-low-pressure region, and thereby disturbs an unambiguous quantification of the microporosity (Silvestre-Albero et al., 2013). Besides, systematic errors in dead-volume cause cumulative dosing errors becoming important at high p/p^0 (Thommes et al., 2015).

2.4.6 Specific surface area

Specific surface areas of all samples were calculated from Ar and N_2 physisorption isotherms using BET theory. Fitting ranges were constrained by Rouquerol plots (upper p/p^0 limit) and goodness of fit (lower p/p^0 limit). Monolayer capacities were checked for consistency and molecular cross-sectional areas of nitrogen (0.162 nm^2) and argon (0.142 nm^2) were used according to ISO9277 (Deutsche Institut für Normung e.V., 2012) (section A.2 Table A.2 in the appendix). BET areas and monolayer capacities computed for micro/mesoporous materials were conceived in the framework of Rouquerol et al. (2007), thus representing apparent specific surface areas and strong retention capacities. As remarked by Rouquerol et al. (2007), the evaluation of the specific surface area is not straightforward and needs to be performed cautiously, if (i) micropores are present, or (ii) capillary condensation occurs in the BET-fitting range (Schlumberger & Thommes, 2021). The latter was neither the case for N_2 nor Ar in the studied sample set because of delayed capillary condensation (Figure 2.1). Micropores were present in all studied porous samples contributing to different degrees to total uptake (Rouquerol et al., 2007).

Figure 2.11a shows a cross-plot of N_2 vs $\cdot$ Ar BET areas including the unity line and error bars (2σ), respectively. BET areas ranged from 0.50 to 219 $m^2\,g^{-1}$ for nitrogen and 0.50 to 189 $m^2\,g^{-1}$ for argon (section A.6 Table A.5 and section A.7 Table A.6 in the appendix). N_2-based BET areas were systematically larger than or equal to Ar-based BET areas, yet (relative) differences were non-systematic and sample-dependent. The average difference amounted to $\approx$ 8% with an intercept statistically equal to zero. The largest relative difference of 24% was observed for the non-porous silica (FB105FD).

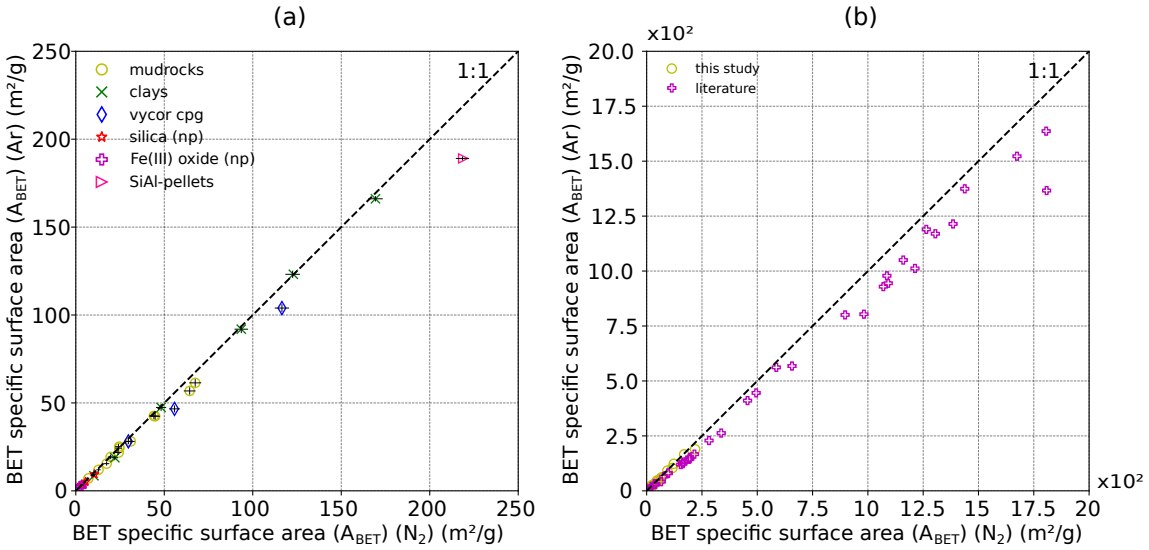

Figure 2.11: (a) Cross-plots of A_{BET} calculated from N_2 and Ar physisorption isotherms measured at normal boiling point temperatures, respectively. Error bars represent two standard deviations and were obtained from interpolation of repeated measurements of representative mudrocks and the SiAl pellets; (b) BET areas of this dataset combined with literature data ($n_{tot} = 70$) (Payne et al., 1973, Thommes et al., 2002a,b, Klank, 2021, Sotomayor et al., 2018). Dashed lines indicate unity.

The presented data set was augmented by literature values (sorbents: carbons, MCM-41, Al_2O_3, kaolinite, silicas, metal-organic frameworks, controlled pore glasses etc.; Figure 2.11b). Both data sets are in good agreement and while the divergence from unity increased on absolute scale, relative deviations from unity remained non-systematic, though average differences rose to $\approx 12\%$ (intercept statistically equivalent to zero). It is noted that only BET areas were compared and no further information of the literature data were scrutinised. Cluster analysis results were ambiguous and yielded neither a class- nor cross-class dependence for the calculated BET areas and their variance. Thus, divergences seem to be not substrate specific as it would be implied by a dominantly surface-chemistry-controlled process. According to Sotomayor et al. (2018), orientation effects promoted by specific surface sites cause the largest factor of uncertainty ($\approx 20\%$; Thommes et al. (2015)) on the cross-sectional area of N_2. Thus, an unambiguous stipulation of the cross-sectional area of nitrogen is not without ado. It is traditionally calculated from liquid configuration and amounts to $0.162\,\mathrm{nm}^2$. Employing the traditional cross-sectional area, Sotomayor et al. (2018) and Schlumberger & Thommes (2021) document deviations between Ar- and N_2-based A_{BET} of up to 25%. Similarly, Kruk & Jaroniec (2000) issued specific surface area differences of 29% for MCM-41. Klank (2021) published even larger deviations of up to 32% for a macroporous Al_2O_3 and 57% for a cellular concrete. The summarised range is in line with the presented data set. Maximum differences of 24% (non-porous) and 17% (porous) were observed utilising the traditional cross-sectional area of N_2.

Several researchers reported N_2 cross-sectional areas different from that of liquid configuration. Jelinek & Kovats (1994) obtained an effective cross-sectional area of $0.135\,\mathrm{nm}^2$ for nitrogen (for

fully-hydroxylated, spherical silica). Using 0.135 nm^2 as cross-sectional area, Sotomayor et al. (2018) compute a deviation for oxide specific surface areas of <4% and for fully hydroxylated materials of <1%. Adapting the molecular cross-sectional area of Jelinek & Kovats (1994) for this data set yielded nominally stronger deviations averaging 10% instead of the previous 8%. The approach of Sotomayor et al. (2018) may hold for oxides but it is unlikely to be suitable for mudrocks of locally varying and heterogeneous surface chemistry. It is more likely that orientation effects are not detectable in mudrocks and clays because of the narrow local distribution of specific sorption points such as surface groups or crystal defects. If these are spaced too close together, orientation effects will no longer be detectable since an effective change in molecular orientation is no longer possible in large numbers. Furthermore, the contribution of 'disoriented' molecules to the BET area could be either: (i) fairly low or (ii) simply masked by the overestimation of the monolayer capacity because of microporosity.

Eventually, the presented data point out that A_{BET}'s of Ar and N_2 can be regarded as equivalent at least for microporous mudrocks and clays and when rigorously used as an operational measure for texture. Especially, because absolute differences in A_{BET} can be fairly low (Figure 2.11). Still, it is acknowledged that for specific classes of sorbents (non-porous, clearly defined surface chemistry and distribution of surface sites) a cross-sectional area different from 0.162 nm^2 is probable and orientation effects are observable (Jelinek & Kovats, 1994). Hence, the importance of individual sample- and class-dependent comparison remains and is further emphasised by the observed "random" differences of this study.

2.4.7 Gurvich pore volume and porosity

Gurvich (total) pore volumes were computed for porous samples at a predefined BJH pore size of 250 nm (N_2: $p/p^0 = 0.9923$; Ar: $p/p^0 = 0.9916$) (section A.6 Table A.5 and section A.7 Table A.6 in the appendix). Pore volumes were obtained assuming that capillary condensation has taken place and the adsorbate approaches its liquid bulk density at operational temperature. Since the isotherms of the geological materials did not reach a plateau at maximum partial pressure, no recalculation to porosity was performed.

The maximum uptake of non-porous materials was intentionally not interpreted as Gurvich pore volume, because this uptake reflected more the kind of particle packing and less a textural property of the material itself due to condensation in the interparticle space. The resulting packing density is not sufficiently reproducible, and hence, quantitative estimates of the Gurvich volumes have little relevance.

Gurvich pore volumes of Ar are displayed as function of N_2-based Gurvich pore volumes supplemented by a unity line (Figure 2.12). The Gurvich pore volumes ranged between 16.8 $\mu L\,g^{-1}$ and 633.4 $\mu L\,g^{-1}$ for argon and 17.7 to 608.0 $\mu L\,g^{-1}$ for nitrogen. For the majority of samples N_2-based Gurvich volumes were slightly larger than those obtained from argon physisorption isotherms. The average difference of 5% (porous materials only) was significantly exceeded by individual samples; i.e. deviations by up to 20% and 33% were detected for the YPC-E and BCM samples, respectively. The Gurvich pore volumes of the non-porous materials were included in the plot but not in the calculation of the average difference between Ar and N_2 Gurvich volumes. No systematic

trend was evident when ratios were compared ($V_{GV}(N_2)/V_{GV}(Ar)$).

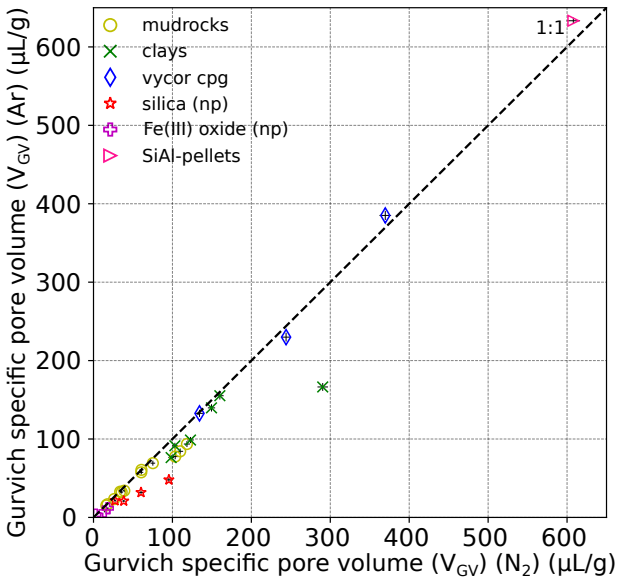

Figure 2.12: Cross plot of V_{GV} obtained for a pore size of 250 nm from N_2 and Ar physisorption isotherms measured at normal boiling point temperature, respectively. Error bars represent two standard deviations and were obtained from interpolation of repeated measurements of representative mudrocks and the SiAl pellets. The dashed line indicates unity. Gurvich pore volumes of the non-porous (np) silicas and Fe-oxides are only shown for completeness but not considered in the analysis for reasons outlined in section 2.4.7.

According to Rouquerol et al. (2014) the validity of Gurvich rule has been confirmed for a wide range of adsorptives on mesoporous sorbents. The level of agreement is ≈ 5% deviation from the mean value as calculated from the data reported by McKee (1959). Variations between pore volumes of N_2 and Ar have been documented by multiple researchers, albeit the discrepancies frequently exceed the level of 5% (Šolcová et al., 2011, Hartmann & Vinu, 2002, Kruk & Jaroniec, 2000).

The origin of these discrepancies can be manifold ranging from technical inaccuracies to physical effects. Theoretically, molecular sieving and -packing effects or a false (bulk) density assumption are possible in microporous materials. A correlation of Gurvich volume ratios and microporosity ratios could not be identified in this study suggesting that the origin of the difference in total pore volume did not originate from processes associated with the micropore space like, for example, molecular packing. A violation of the rigidity assumption of the sorbents, as alleged by Rouquerol et al. (2014) for some materials, seems unlikely given the nature of the investigated sorptive-sorbent system. It is rather probable that the assumption of a single bulk liquid density is too simplistic as it has been demonstrated to vary for supercritical fluids as function of pore size (Thommes & Findenegg, 1994, Schoen & Thommes, 1995, Schoen et al., 1997). Moreover, when the uncertainty of constant p^0, hence stable temperature, is taken into account, it appears likely that also in some instances the assumption of bulk liquid density of argon at its normal boiling point is questionable. Nonetheless, the agreement between Gurvich volumes of both adsorptives was good, making a discussion on the

origin of the offset dispensable and speculative; except for the aforementioned mudrocks and clays of strongest deviation. The strongest discrepancies in Gurvich volumes are accompanied by similar differences in BJH PSD and are attributed to the saturation pressure offset (section 2.4.3).

2.4.8 Micropore size distributions of porous materials

Micropore size distributions (µPSD) were calculated for Ar physisorption isotherms using DA theory in combination with Medek's approach for computing differential pore size distributions (Dubinin & Astakhov, 1971, Medek, 1977, Janssen & Van Oorschot, 1989) (Figure 2.13a). Medek (1977) derived the differential micropore volume distribution from the theory of volume filling according to Equation 2.1:

$$\frac{d\theta}{dr_e} = \frac{dV}{dV_0 dr_e} = 3n \left(\frac{k}{n}\right)^n r_e^{-(3n+1)} \exp\left(-\left(\frac{k}{E}\right)^n r_e^{-3n}\right) \tag{2.1}$$

Where θ is the fractional micropore volume filling obtained as ratio of V and V_0 being the micropore volume at a specific p/p^0 and the DA limiting micro pore volume, respectively. n and E are the DA exponent and the characteristic energy of adsorption obtained from least-square fitting of the DA equation, and k is the interaction constant of the adsorptive ($k_{\mathrm{Ar}} = 2.34\,\mathrm{kJ\,nm^3\,mol^{-1}}$). r_e is the equivalent pore radius obtained according to Equation 2.2:

$$r_e = \frac{\left(\frac{k}{E}\right)^{\frac{1}{3}}}{\Gamma\left(\frac{3n+1}{3n}\right)} \tag{2.2}$$

Here, Γ is the gamma function that can be approximated by a polynomial approximation. Janssen & Van Oorschot (1989) proved that Ar physisorption in combination with DA-theory yields physically realistic micropore size distributions for (mono modal) zeolites. Unfortunately, micropore size distributions of mudrocks are seldom reported in literature because of difficulties in their experimental assessment (e.g., Wang & Ju, 2015). Experimental issues associate to technical difficulties in performing accurate ultra-low-pressure measurements that are essential for micropore analysis but are limited by the device (Schlumberger & Thommes, 2021). Moreover, reliable models are not available for all materials of interest that accurately describe fluid-solid interaction under significant confinement.

A comparison of Ar, N_2 and CO_2-based µPSDs was omitted because of the polar momentum of N_2 and CO_2 and their incomplete low-pressure isotherms (no data $p/p^0 < 0.001$ for N_2 and no data below $p/p^0 \approx 0.000\,03$ for CO_2). In contrast to modern DFT models, DA-theory does not account for specific fluid-wall interactions, though it was developed for chemically heterogeneous surfaces (Kruk et al., 1997). Therefore, the pore size distribution is negatively affected in form of a shift in filling pressure for polar molecules impeding a direct correlation of filling pressure and pore size for N_2 and CO_2 (Thommes et al., 2015, Schlumberger & Thommes, 2021).

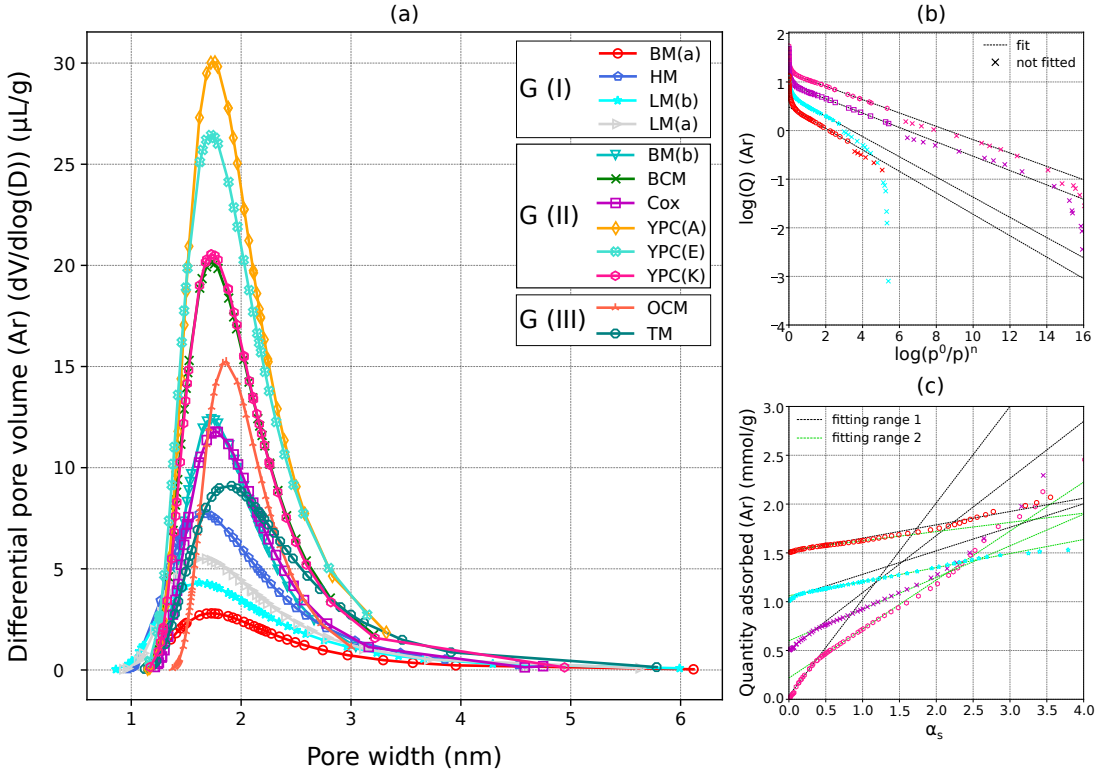

Figure 2.13: (a) Differential micropore size distributions (µPSD) of mudrocks computed using DA-theory from Ar physisorption isotherms. G(I) to G(III) represent the grouping of mudrocks according to their primary pore size; (b) Ar DA-plots of selected mudrocks. Data points represented by a cross (x) were not used for numerical fitting due to an instrumental step as explained earlier; (c) Ar α_s-plots of selected mudrocks using the reduced isotherm published by Kruk & Jaroniec (2000). α_s-plots displayed two linear ranges indicated by black and green regression lines.

The DA-equation described the micropore filling of Ar in mudrocks and clays well up to the limiting micropore filling pressure of $p/p^0 \approx 0.2$. Yet, it failed to asses particular pore-size populations. The reason is that instead of representing local adsorption, it describes average adsorption, i.e. the isotherm is generated by a broad micropore size population producing a continuous isotherm shape. Hence, the model extracts the average micropore size and the corresponding adsorption energy represented by the monomodal distribution (Dobruskin, 1998). Physically, the DA-based micropore size distribution is considered as an energy distribution by Dobruskin (1998). Further, the theory underestimates the true micropore size because of the assumption of bulk liquid density. In fact, a liquid configuration is not realised in micropores because of molecular packing restrictions (Cychosz et al., 2017). In turn, the presented µPSDs should only be considered for a relative comparison in order to discern textural trends instead of the true physical texture.

Based on the µPSDs, three groups of mudrocks were identified of which group I was characterised by broad micropore size distributions and slightly lower primary pore sizes ($W \approx 1.64(0.02)$ nm). In contrast, group II revealed a narrower distribution with nominally larger primary pore sizes of

$\approx 1.740(0.005)$ nm. Group III comprised only two mudrocks of major pore size of $\approx 1.88(0.02)$ nm. They were described by the largest primary pore size with a narrow distribution.

The width of the distributions is controlled by the exponent (n) in the DA-equation and it increases inversely to n. Following Dobruskin (1998), n is a measure of surface heterogeneity: the smaller n the greater the surface heterogeneity. Thus, a larger degree of heterogeneity of micropore hosting components may be attributed to the mudrocks of group I. This could be interpreted as a result of a mixed contribution of mineralogical and organic constituents to the micropore size distribution. Indeed, mudrocks of group I are defined as gas shales implying that they are thermally mature (Merkel et al., 2015, Seemann et al., 2017, Hu et al., 2021). Mastalerz et al. (2013), Chen & Xiao (2014) and Furmann et al. (2016) emphasised that thermal maturation of organic matter can cause overprinting of initial organic matter porosity and the creation of secondary porosity in the micropore range. Accordingly, a mixed contribution of clay- and organic matter-hosted microporosity to the pore size distribution is probable as clay minerals (esp. 2:1 clay minerals) are the main contributors to microporosity in mudrocks.

Pore size classes and microporosity Whilst DA-theory produces artificial monomodal µPSDs, a semi-quantitative description of the microporosity and its separation in specific pore size classes can be accomplished by the α_s-method. Fernandez-Colinas et al. (1989) applied the α_s-method to obtain evidence for the sequential filling of different groups of micropores on activated charcoal. The authors identified two linear regions in the comparative plots which they interpreted as separate pore size classes: (i) ultramicropores and (ii) supermicropores. Ultramicropores are occupied at very low partial pressure by means of primary micropore filling (primary linear region). Supermicropores are filled through cooperative micropore filling at higher partial pressures (secondary linear region). The secondary linear region extends into the multilayer region providing the total micropore volume according to theory (Rouquerol et al., 2014).

α_s-plots were obtained based on the reduced isotherm of a macroporous LiChrosphere-Si1000 silica for nitrogen and argon (Jaroniec et al., 1999, Kruk & Jaroniec, 2000). α_s-method micropore volumes are summarised in combination with DA-theory based micropore volumes (section A.4 Table A.4 in the appendix). α_s-values were consistently lower than those obtained from DA-theory for both adsorptives. Still, Ar-based total micropore volumes were typically larger than those obtained for N_2 from α_s-plots. Total micropore volumes ranged from 0.8 to 8.5 $\mu L\,g^{-1}$ for Ar and from 0.2 to 8.3 $\mu L\,g^{-1}$ for N_2. Ratios of Ar over N_2 varied by a factor of 1 to 4 for total micropore volumes supporting the view that N_2 underestimates micropore volumes because it lacks detecting ultramicropores. Ar α_s-plots displayed multiple linear regions for mudrocks whereas N_2 α_s-plots showed a single linear region extending in the mono-multilayer range (Figure 2.13c only Ar). The presence of two regions in Ar α_s-plots was not related to the noticed instrumental offset as they did not coincide. The shape of the α_s-plots differed slightly for both adsorptives in the lower α_s-range ($\alpha_s < 1$; $p/p^0 < 0.4$) and their linear regions did not coincide. Yet, the majority of α_s-plots merged towards $1\alpha_s$ and demonstrated capillary condensation at higher α_s-values indicated by deviation from linearity. This is in line with the view that beyond monolayer completion surface forces are negligible compared to adsorbate-adsorbate interaction (Jaroniec & Kaneko, 1997), though surface forces likely transcend multiple adsorbate layers. The slopes of linear regions of α_s-plots were

mudrock-specific. But, location and range of linearity were similar for most samples (Figure 2.13c). The difference in slope implies that each mudrock is characterised by variable shares of pore sizes contributing to ultra- and supermicropores, respectively.

The share of ultra- and supermicropore volume to total micropore volumes conforms with the previous grouping of mudrocks. For mudrocks of group I, ultramicropores constituted between 44% and 59% of the total micropore volume. This explains the smaller average pore size observed for group I as a significant contribution of ultramicropores results in a shift of the average pore size towards smaller values. In addition, a larger share of ultramicropores can also cause a broadening of the pore size distribution. That agrees with the previous, in which the contribution of clay- and organic matter hosted microporosity was elaborated for group I, explaining the broader µPSD based on apparent surface heterogeneity (n), hence the contribution of organic matter porosity. However, µPSD-broadening can also be purely pore size related because there is no exclusive host of a particular micropore size in mudrocks. Moreover, argon should not be sensitive to surface chemistry but exclusively sensitive to pore size. Thus, the creation of ultra-micropores in organic matter by thermal maturation will have the same effect than surface chemistry on the width of the pore size distribution and apparent surface heterogeneity is rather reflecting differences in surface potentials of micropores in the case of argon. The definite component hosting either ultra- and/or supermicropores could not be identified. For mudrocks of group II the relative share of ultramicropores to total micropore volume was less than 25%. It follows that a narrower distribution is expected as well as nominally larger pore sizes, as reported previously.

The presence of ultra- and supermicropores in mudrocks was exclusively supported by Ar α_s-plots. N_2 α_s-plots revealed only supermicropores which, theoretically, explains the underestimation of the total micropore volume by N_2 as presented earlier based on DA-theory. N_2-based α_s-plots reveal negative intercepts for the lower linear α_s-range implying the absence of ultramicropores. However, the approach needs to be regarded critically and the pore size class interpretation is not without doubt. The basic idea of comparison plots requires the reference solid to be similar in surface structure and chemistry to the solid of interest (and non-porous) (Jaroniec & Kaneko, 1997, Sing & Williams, 2005). Finding a suitable reference solid is especially difficult for materials composed of heterogeneous constituents. Hence, the application to mudrocks is debatable. Though, in view of argon's lack of specific interaction with surface groups, the choice of the reference solid should be less crucial from a surface chemical perspective than from a textural perspective. Nitrogen, on the other hand, is sensitive to surface chemistry and texture in the submonolayer region because of its permanent polarisation. Jaroniec & Kaneko (1997) demonstrated that deviation from linearity in α_s-plots in the lower α_s-range is not exclusively caused by texture but also by variation in adsorption energy distribution (specific surface sites). Because of that, the complementary use of adsorptives with different polarity in combination with α_s-plots could theoretically allow to scrutinise microporosity in more detail and may help to discriminate surface chemical- from texture-induced differences between samples. Premise for that is the rigorous use of the same reference solid, even though it may not be universally suited for all adsorptives and measurements down to ultra-low pressures with all adsorptives. In this study, a micropore analysis on the above basis was not possible since ultra-low pressure data were missing for N_2 isotherms which biases a comparison of

Ar and N_2-based α_s-data a priori.

2.4.9 Mesopore size distribution of porous materials

Meso and (partial) macropore size distributions (PSD) of porous materials were assessed by means of BJH theory. The statistical thickness of the adsorbate layer (t-curve) prior to capillary condensation was modelled by Harkins and Jura's general isotherm equation ($t = \sqrt{(13.99/(0.034 - log(p/p^0))))}$ obtained on a non-porous Al_2O_3) for nitrogen (Harkins & Jura, 1944b). For the PSD inversion of argon physisorption isotherms the t-curve was obtained from the isotherm of a macroporous LiChrosphere-Si1000 silica provided in form of numerical values between $1.29 \times 10^{-5} < p/p^0 < 0.993$ by Kruk & Jaroniec (2000).

PSDs were calculated from the ad- and desorption branch of the Ar and N_2 physisorption isotherms. A lower inversion limit of $p/p^0 = 0.3$ was applied for the adsorption branch. The hysteresis loop closure was excluded from PSD inversion of the desorption branch; i.e. PSDs were derived for $p/p^0 \geq 0.45$ and $p/p^0 \geq 0.40$ for N_2 and Ar, respectively. It is generally accepted that pore size distribution models represent simplifications with respect to geometry and that they relate an 'equivalent' pore width to sorptive uptake. In turn, PSDs are model-dependent, hence they are apparent rather than physically true (Sonwane & Bhatia, 2000). Kruk & Jaroniec (2000) as well as Thommes (2004) showed that uncalibrated BJH theory underestimates pore size up to 30% for pores <7.5 to 10 nm. Furthermore, BJH does not take into account the correct thermodynamic state of the pore fluid, its dependence on pore size, the occurrence of hysteresis and the delay in capillary condensation as a result of metastable adsorption films. Despite its apparent character, its shortcomings, and the lack of suitable DFT model, presented PSDs were computed by BJH theory and used on a comparative basis (section 2.4).

Cumulative and differential PSDs are presented for representative mudrocks (Bossier(a), Opalinus Clay), clay minerals (kaolinite, montmorillonite) and engineered materials (VYCOR cpg-20nm, SiAl pellets) (Figure 2.14 to Figure 2.16). These exemplary samples were chosen based on their prominent features in PSD curves and their representative character of the data set.

Cumulative and differential PSDs of mudrocks showed fair agreement with local deviations detectable for ad- and desorption branch-based PSDs (Figure 2.14). Cumulative PSD curves for Bossier(a) and Opalinus Clay complied qualitatively and local quantitative differences in uptake were at maximum 17% (BM(a)) and 10% (OCM); i.e. cumulative PSD curves of Ar and N_2 isotherms converged towards larger pore sizes. Differential PSDs were isotherm branch specific for both mudrocks. Adsorption branch-based PSDs were broad with minor detail for N_2-based PSDs; i.e. quantitative differences were present and peak positions of Ar-based PSDs were shifted towards smaller pore sizes. Differential PSDs calculated from the desorption branch agreed well with each other for BM(a) and OCM. BM(a) displayed no major peak, though differential PSD curves suggest that Ar and N_2-based PSDs converged towards smaller mesopores ($\approx$ 5 nm). The major pore size of the OCM revealed a shift from 12.7 nm(Ar) to 13.1 nm(N_2) corresponding to $\approx$ 3% of Ar-based PSDs towards smaller values (Figure 2.14d). Larger deviations were observed for the COx mudrock showing a deviation of 7.6 nm (=19.5%) from 39 nm(Ar) to 31.4 nm(N_2) for its primary pore size in adsorption mode (data not shown). Furthermore, cumulative PSDs (ad- and desorption branch)

of the BCM, YPC-A, YPC-E and the Cu-Trien exchanged clay fraction of the YPC-Elverdinge (YPC-CF-CuTrien) displayed continuous and sample-specific divergence for larger pore sizes. The above was exemplary shown for the Boom Clay (Figure 2.8c). PSDs of the remaining samples coincided well for both isotherm branches and no systematic deviations were detected.

Figure 2.15 displays the PSDs of kaolinite and montmorillonite (SWy2-Na). Cumulative and differential PSDs were qualitatively similar, yet they differed quantitatively and in resolution. The Ar physisorption isotherm of the kaolinite has been recorded with much higher point spacing ($\approx$ 2-fold). Ar-based cumulative PSDs of kaolinite were lower than N_2-based PSDs above 14 nm. Differential PSDs computed for the adsorption branch were broad and peak at $\approx$ 37 nm but showed a fair match up to 50 nm. Though Ar-based data scattered between 30 nm and 50 nm. Differential PSDs of the desorption branch aligned excellently yielding a difference of 1 nm ($\approx$ 3%) in major pore size (W(Ar) = 30.3 nm; $W(N_2)$ = 31.3 nm). Moreover, the differential PSD revealed significantly more detail (shoulder and sub-peaks) for argon compared to the "smeared" N_2-based PSD (Figure 2.15b). Cumulative PSDs of montmorillonite overlapped in the mesopore range, but diverged continuously towards larger pore sizes (W >50 nm) for the desorption branch (Figure 2.15 d). The difference in cumulative uptake maximised to 12 µL g^{-1} ($\approx$ 18% of Ar PSD) at the measured pore size threshold of approximately 230 nm. In contrast, adsorption branch-based cumulative PSDs converged again above 100 nm. Corresponding differential PSDs were unspecific and defined by a broad peak in the macropore range. Quantitative differences were obvious for pores above 15 nm. The differential PSD of the desorption branch resembled the broad peak of the adsorption branch.

Engineered materials indicated sample-specific differences in cumulative and differential PSDs (Figure 2.16). While the PSDs were qualitatively similar, quantitative disparities were noticed for both types of samples and PSDs. Ar-based cumulative PSDs of the VYCOR cpg-20nm were lower than corresponding N_2-based PSDs for adsorption ($W \geq$ 10 nm) and desorption ($W \geq$ 14 nm). The maximal divergence in uptake was 30% and corresponded to a pore size of $\approx$ 22 nm for both isotherm branches. Differential PSDs exhibited a larger deviation for adsorption- than for desorption-based PSDs (Figure 2.16a, b). The first population of pores (W(Ar) = 15.8 nm; $W(N_2)$ = 12.8 nm) shifted by 3 nm ($\approx$ 24% of Ar PSD) towards larger pore sizes for argon. For the second population a repositioning by 8.1 nm ($\approx$ 26% of Ar PSD) was detected for the adsorption branch (W(Ar) = 31.1 nm; $W(N_2)$ = 23.0 nm). In comparison, the deviations for the desorption-based differential PSDs were about 0.2 to 0.7 nm which corresponded to a consistent relative shift of less than 3% (population I: W(Ar) = 9.5 nm vs. $W(N_2)$ = 9.7 nm; population II: W(Ar) = 23.5 nm vs. $W(N_2)$ = 22.8 nm). Similarly, PSDs of SiAl pellets demonstrated better agreement for the desorption branch than for the adsorption branch. Generally, Ar-based cumulative PSDs exceeded N_2-based PSDs. This difference in uptake amounted to constant 5%. Differential PSDs obtained from the adsorption branch deviated by 4 nm ($\approx$ 32%) in peak position (W(Ar) = 8.5 nm; $W(N_2)$ = 12.5 nm). In contrast, an inverse difference of 1.2 nm ($\approx$ 13% of Ar PSD) relocation from 9.5 nm(Ar) to 8.3 nm(N_2) was identified for desorption branch-based PSDs.

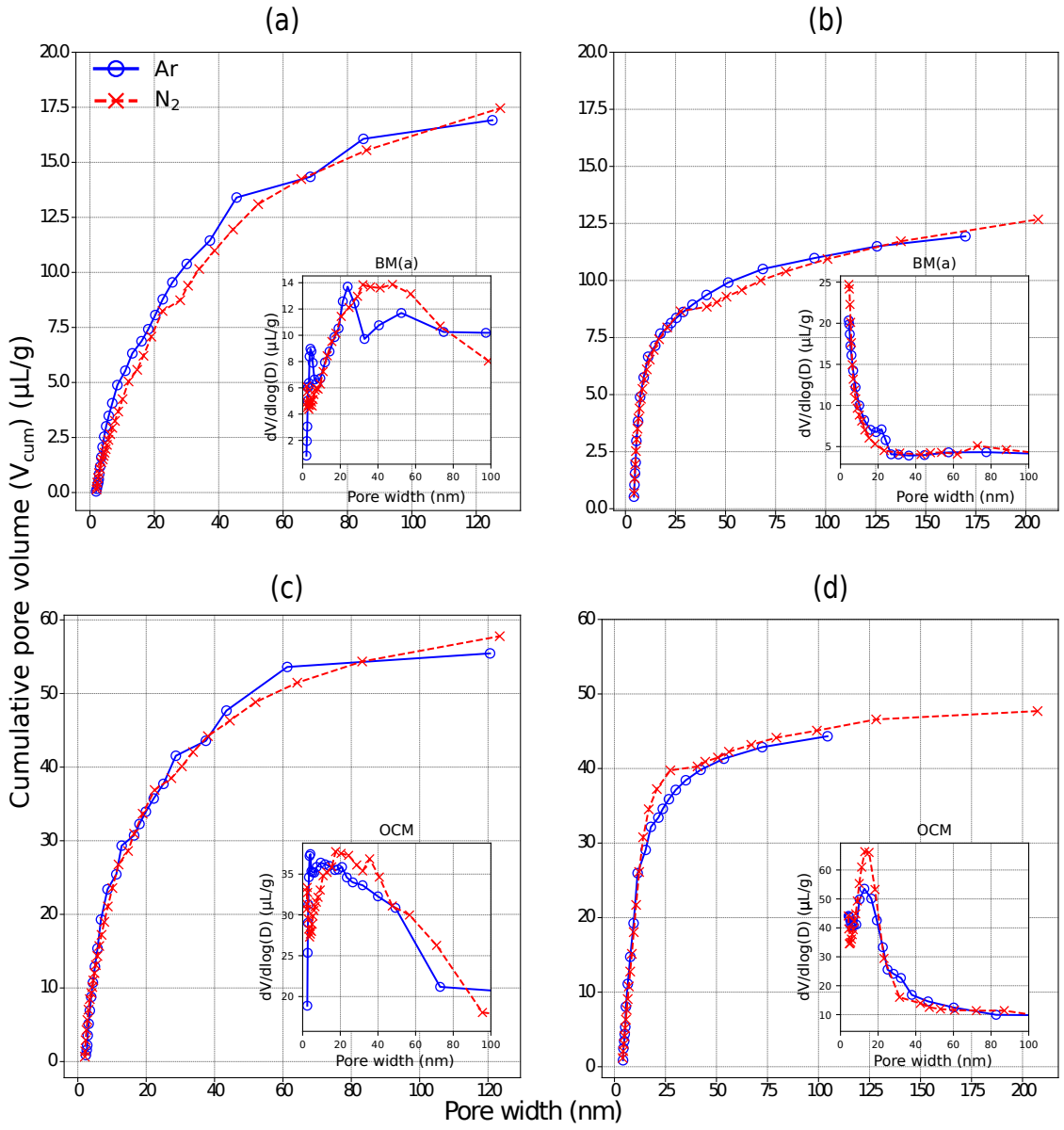

Figure 2.14: Meso- and macro pore size distributions calculated from the adsorption (a, c) and desorption (b, d) branch of Ar and N_2 isotherms using BJH-theory in combination with a thickness curve from Kruk & Jaroniec (2000) : a) PSD obtained for Bossier(a) mudrock from the adsorption branch, b) PSD obtained for Bossier(a) mudrock from the desorption branch c) PSD obtained for Opalinus Clay from the adsorption branch, d) PSD obtained for Opalinus Clay from the desorption branch. The differential pore size distributions are shown as inserts, respectively.

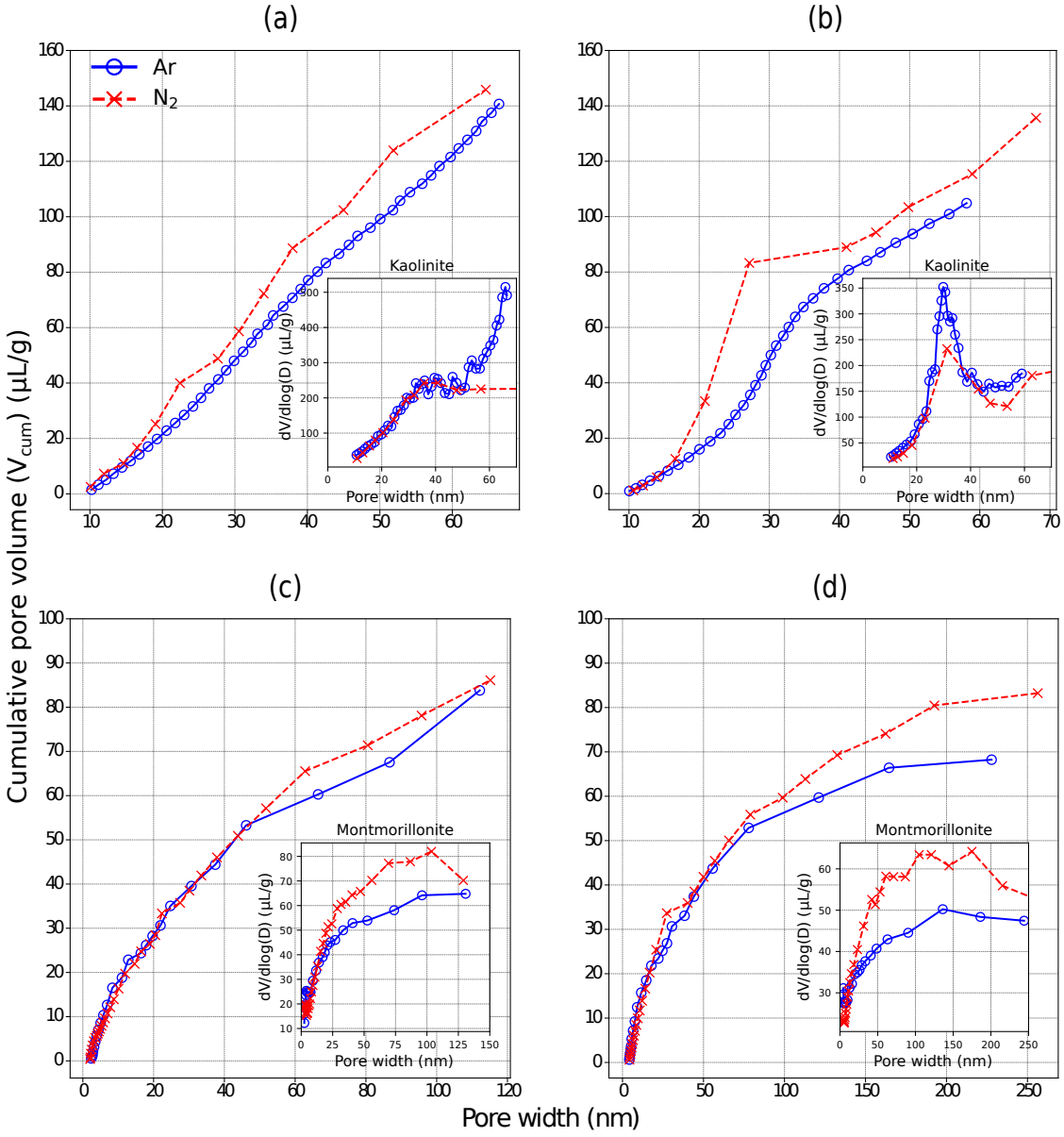

Figure 2.15: As Figure 2.14, but for a) PSD obtained for the Kaolinite from the adsorption branch, b) PSD obtained for the Kaolinite from the desorption branch c) PSD obtained for the Montmorillonite from the adsorption branch, d) PSD obtained for the Montmorillonite from the desorption branch.

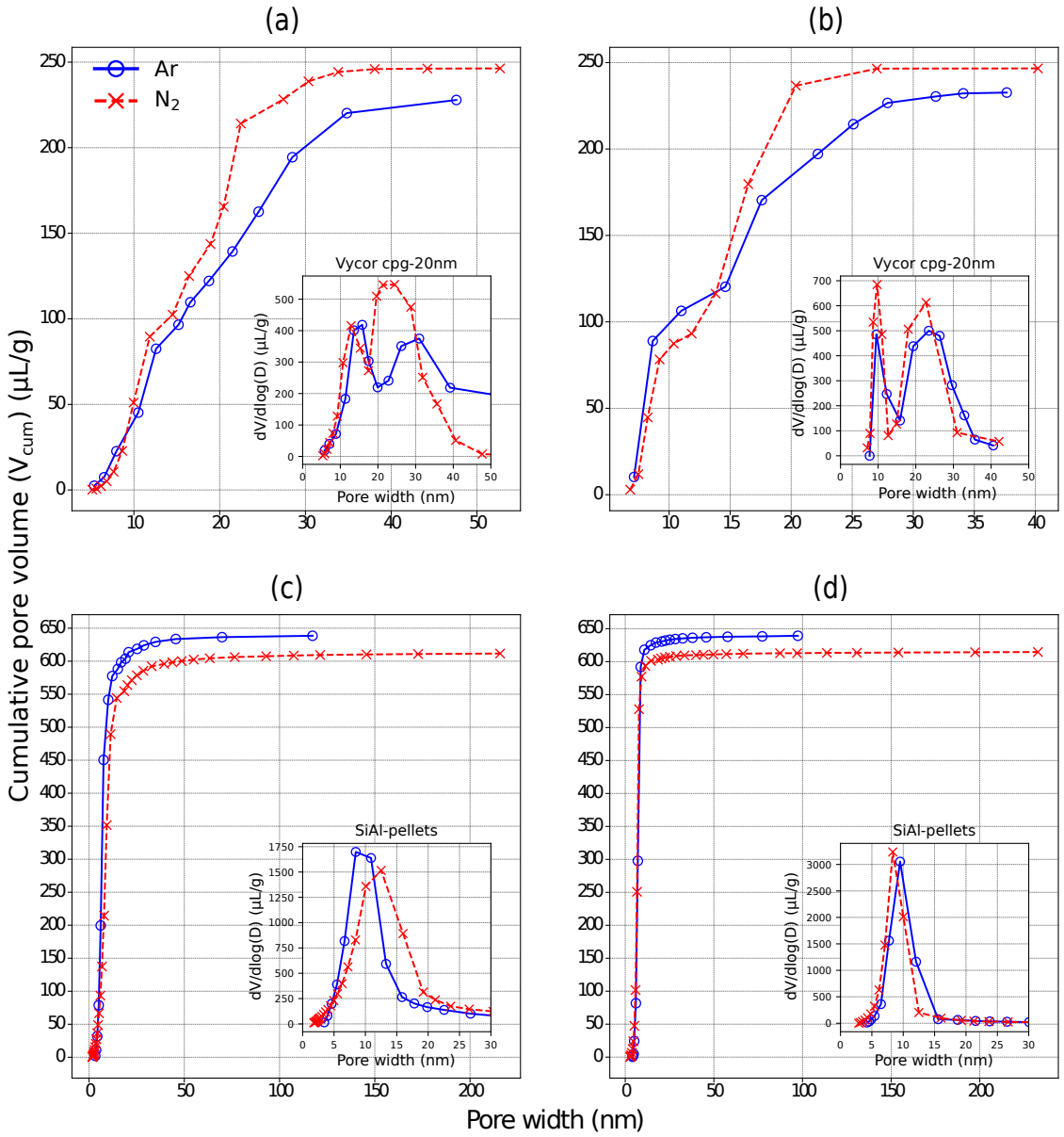

Figure 2.16: As Figure 2.14, but for a) PSD obtained for the VYCOR cpg-20nm from the adsorption branch, b) PSD obtained for VYCOR cpg-20nm from the desorption branch c) PSD obtained for SiAl pellets from the adsorption branch, d) PSD obtained for the SiAl pellets from the desorption branch.

Few data are available for mudrocks with respect to PSDs computed from Ar physisorption isotherms. The PSDs of Zhang et al. (2017), Chen et al. (2022) and Delle Piane et al. (2021) (no N_2 data presented) were obtained from non-local density functional theory only for Ar isotherms and reveal no prominent pore size. Still, the corresponding isotherm data follow the same trend as described in section 2.3.1. As pointed out, fair agreement existed for the majority of samples, but (i) shifts in BJH diameter (maxima of differential PSD curves) and (ii) differences in cumulative uptake were discovered.

The shift in the BJH diameter has been reported in the literature for engineered materials (Thommes et al., 2006, 2013, Rathouský & Thommes, 2007, Šolcová et al., 2011, Choma et al., 2008, Neimark et al., 1998). Similar to the presented data the magnitude of shift and direction expose no systematics. Similar to the data presented, the shifts found in literature are generally small and at maximum 0.7 nm (Thommes et al., 2006). The presented shifts (adsorption branch) are up to 7.6 nm (19.5%) for mudrocks and 4 nm (32%) for engineered materials and increase with pore size (Figure 2.14, Figure 2.16). Such systematics were not found in the reported literature. The lower shifts obtained from published work is attributed to the fact, that the physisorption measurements were likely performed in a liquid argon bath with separate p^0 recording making the measurements considerably more reliable (section 2.4.3). The shifts in (primary) peak position are significantly lower for the desorption branch-based PSD than for the adsorption branch-based PSD. This is highlighted by samples characterised by pore blocking and supported by the most frequent pore width of the OCM (Figure 2.14d, Figure 2.15, Figure 2.16). In fact, the agreement in peak position is at the level of 3% for Ar and N_2-based PSDs for the desorption branch. The difference in peak position is equivalent to a maximum of 1 nm but often lower and close to the limit of detection (LOD) when the molecular size of the adsorptive is considered as LOD. This provides good confidence in Ar and N_2 PSDs obtained from the desorption branch. The larger variation of adsorption branch PSDs could be a result of the inaccurate representation of the adsorption process by BJH theory and therefore related to the neglect of the fluid-specific delay in capillary condensation. Since these processes affect the inverted pore sizes (+ associated volumes), inaccurate accounting of them may cause such variations in PSDs. But, it is emphasised that large shifts, especially prominent in larger pore size, can be induced by technical issues associated with p^0 fluctuations (sections Factors of uncertainty and the importance of saturation pressure). Minor local differences are likely associated with incorrect assumptions of the thermodynamic state of the pore fluid (bulk parameters) and its neglect of pore size dependence (e.g., curvature effects and pore size dependence of surface tension e.g., Feng et al. (2020)). Further, the selection of the statistical thickness curve and uncontrolled experimental variations can cause such small variations. In this study, the statistical thickness curve of Kruk & Jaroniec (2000) was chosen for PSD inversion of Ar physisorption isotherms.

This yielded good results for this study, but systematic testing of thickness models (section A.5 Figure A.1 in the appendix) evinced that the model choice makes a difference at the lower percent level (8.54 ± 0.08 nm; CV $\approx 1\%$) when obtaining a pore size distribution. This is supported by testing different t-curves on a large mudrock data set, supposing that BJH theory is used in its valid partial pressure range (Bertier et al., 2016). However, it is more important that the thickness model resembles as closely as possible the solid-sorptive system of interest in terms of solid-fluid interaction. For the studied materials, oxides (Al_2O_3 and SiO_2) were regarded as the best available proxy at the moment of study. In Addition, Kuila & Prasad (2013) demonstrated that BJH partial pore volumes can vary between 10% and 20% which the authors associated with uncontrolled experimental conditions (not better defined). A systematic reproducibility study (25 laboratories) of Klobes et al. (2006) corroborates the above and the authors quantified a variation of 6.4% for pore volumes obtained from BJH theory.

Thus, the level of agreement complies with the reported results of this study implying that Ar and N_2 PSDs (mesopore range) can be regarded as equivalent under (ideal) experimental conditions. Putting the local differences of Ar and N_2 PSDs into perspective of experimental/technical uncertainties and the purpose of PSD analysis conveys that such differences should be recognised and critically evaluated. This is because of the PSDs' sensitivity towards external factors (technical issues) unrelated to the sorbent texture, which have a more severe impact on PSD inversion compared to theory-based issues (section 2.4.3). However, it is again emphasised that the agreement of desorption data is substantially better than for adsorption data.

2.4.10 Compositional control on differences in Ar, N_2 and CO_2based micropore volumes

A systematic trend of micropore volume towards compositional parameters was not identified (Figure 2.17). Bivariate plots of V_0 of Ar, N_2 and CO_2 versus TOC, total- and specific clay content (taken from Table 2.1) indicated no obvious relationship. The cation exchange capacity (CEC) displayed a weak linear trend (Figure 2.17b). The CEC trend was equivalent for all three adsorptives indicating no preferential attraction of the exchangeable cations, despite the polarity of N_2 and CO_2. However, Środoń & MaCarty (2008) and Kuligiewicz & Derkowski (2017) indicated that, at the given drying temperature, exchangeable cations – depending on their enthalpy of hydration – still carry a hydration shell, questioning a preferential interaction of any of the adsorptives with these cations. In addition, the CEC trend is likely a pseudo-trend originating from the smectites of the mudrocks. Smectite is a major donor of exchangeable cations, besides organic matter, but it is also a main contributor to microporosity (Woodruff & Revil, 2011, Środoń & MaCarty, 2008). Consequently, the CEC vs V_0 trend may reflect the influence of smectite on microporosity and not CEC.

The percentage difference of the contribution of the micropore volume to the Gurvich total pore volume ($(V_0(\mathrm{Ar})\text{-}V_0(\mathrm{N_2}))/V_{\mathrm{GV}}$) did not disclose any systematics or correlation either (Figure 2.17). This may imply that none of Ar, N_2 or CO_2 have a considerably better accessibility towards micropores hosted by any of these components. Otherwise, one would expect systematic differences in the micropore volumes and their contribution to the Gurvich total pore volume for a specific adsorptive for either TOC-rich mudrocks like the Longmaxi mudrocks (LM(a), LM(b)) or mudrocks rich in (expandable) clays like the Ypresian Clay samples (YPC-A, YPC-E, YPC-K) and especially pure swelling clays (SWy2). Differences in V_0 were, however, inconclusive because they varied between 4 to 6% for the TOC-rich Longmaxi while the clay-rich Ypresian Clay samples differed by 7 to 16% in microporosity (Ar, N_2).

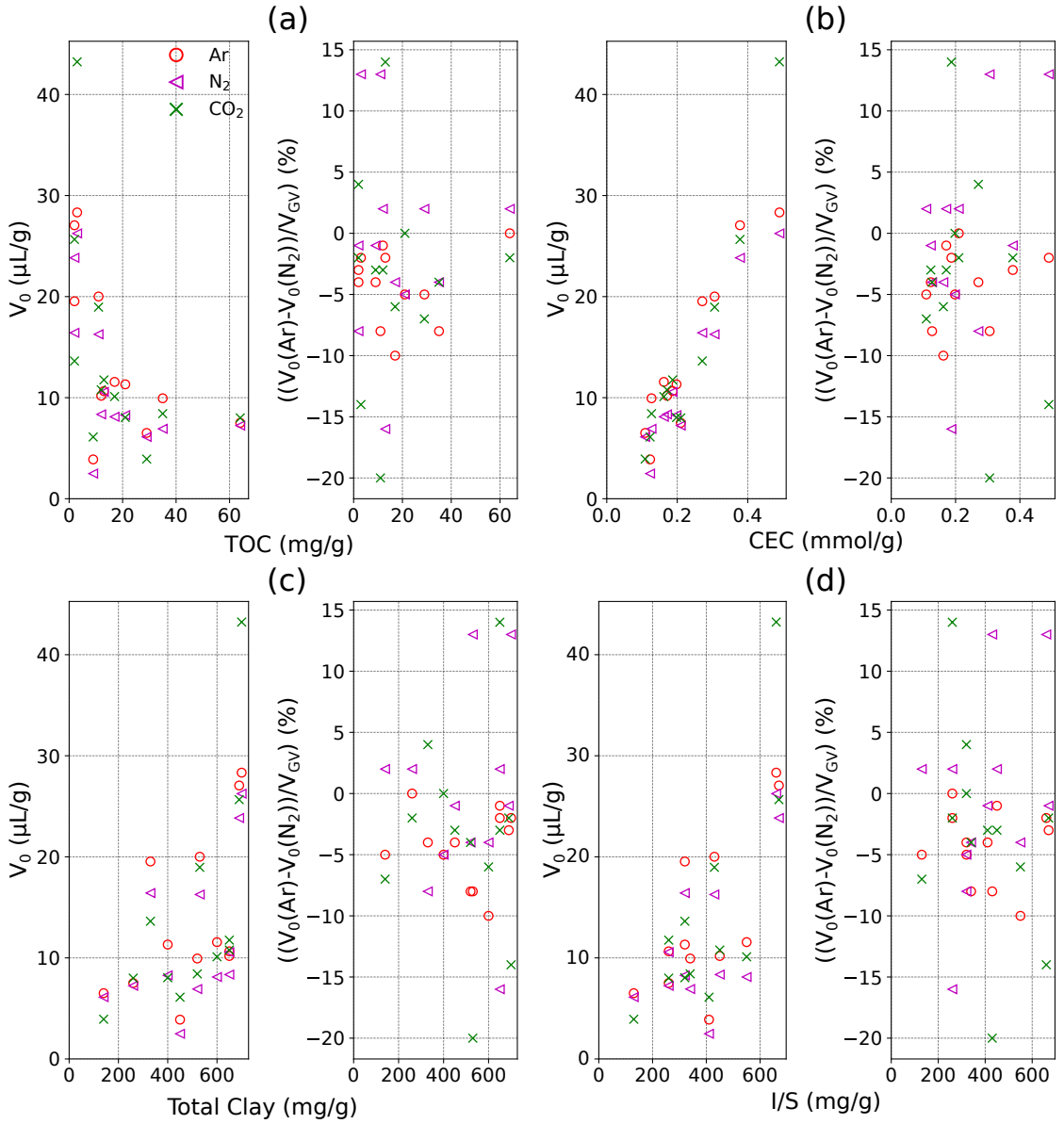

Figure 2.17: DA micropore volumes (V_0) calculated for Ar, N_2 and CO_2 physisorption isotherms and percentage difference of V_0(Ar and N_2) normalised to the Gurvich (total) pore volume (V_{GV}) plotted as function of (a) total organic carbon content (TOC), (b) cation exchange capacity (CEC), (c) total clay content, (d) mixed layer clay minerals including illite, smectite and muscovite (here: I/S).

The above presumes that one of these components dominantly hosts adsorptive accessible micropores and that micropores are not filled with tightly bound water. Furmann et al. (2016) described a dominant control of TOC and thermal maturity on micropore volume (CO_2). Thereby, the authors noted inconsistent trends (positive & negative) that indicate strong sample specificity. This is corroborated by a systematic study of Kuila et al. (2014) in which the correlation of TOC vs. V_0 depends on the individual sample. Similarly, Ross & Bustin (2009) observed no systematic

variation of micropore volume (CO_2) as function of TOC for Jurassic shales, though it was observed for the Devoninan-Mississipian shales (Muskwa & Besa River). Ross & Bustin (2009) point out that the main contributors to microporosity in mudrocks are organic matter as well as clay minerals. Neither total- nor specific clay content (illite/smectite) disclose any obvious control over micropore volumes determined from Ar, N_2 or CO_2 isotherms. This suggests that Ar does not have significantly easier access to clay-specific microporosity as to the interlayer space of dry, swelling clays which could provide additional micropore space unavailable to N_2 (kinetic restrictions) (Everett & Powl, 1976, Loganathan et al., 2018, Ziemiański et al., 2020). In turn a dominant control of clay minerals on Ar physisorption is excluded (Figure 2.17c-d).

Finally, the individual contribution of organic matter and clay minerals to microporosity varies with sample (e.g., formation) because of evolution- and component-dependent effects of, for example, type of organic matter, thermal maturity, particle- and crystallite size as well as internal- and assemblage architecture. Furthermore, as earlier addressed, the possibility of insufficient removal of water from the micropores prior to N_2 and CO_2 measurements remains and potentially disturbs an unbiased comparison.

2.4.11 Note on sorption mechanism

The complex pore network of mudrocks accommodates various interconnected pore classes indicated by a broad PSD and often no distinct step in adsorption. The desorption mechanism in the pore network of mudrocks has been a matter of debate since it has implications for the interpretation of pore size distributions (Bertier et al., 2016). Classical differentiation in pore body (adsorption) and pore throat (desorption) distribution is only possible when equilibrium adsorption and evaporation is encountered. Still, this is seldom the case in geological materials.

Thommes et al. (2006) demonstrated that the complementary use of (i) different adsorptives or (ii) isotherm measurements at different temperatures proves effective in sorption mechanism identification. Adapting Thommes et al. (2006)'s approach evidenced that all studied mudrocks and expandable clays (original + Cu-Trien exchanged) were characterised by a combination of pore network percolation and free evaporation at high partial pressure and cavitation. Cavitation was represented by a fixed closure point of the hysteresis loop that differed for N_2 and Ar (Figure 2.1). The forced closure would translate into deviating PSDs which are not shown because of their artificial character (Groen et al., 2003, Bertier et al., 2016). In the case of kaolinite, the VYCOR cpgs, and the SiAl pellets no cavitation was detected. Instead identical hysteresis closure points of both adsorptives and approximately similar PSDs were diagnostic of pore blocking.

With $\approx$ 4 nm the cavitation pore size of Ar is slightly smaller than for nitrogen ($W(N_2) \approx$ 5 to 7 nm) (Nguyen et al., 2011, Schlumberger & Thommes, 2021). It is noted that the pore size threshold for cavitation of N_2 varies slightly in literature, but specification of a definite pore size would be speculative for mudrocks and clays in any case. Still, the data proved that desorption in mudrocks and expandable clays was unambiguously controlled by a combination of network percolation and free evaporation at high partial pressure and cavitation at the hysteresis closure point.

The level of control of an individual mechanism was sample dependent. Thus, the pore volume

associated with the hysteresis loop closure varied with sample indicating the variable and individual level of control of pore necks in the pore network of mudrocks and clays. Such analysis conveys that a sample-specific- but non-negligible part of the pore network of mudrocks is only accessible via small meso- or micropores of non-specifiable size. This can have a tremendous effect on, for example, matrix transport or storage capacity since such constrictions represent the bottle neck for any fluid passing. Furthermore, the above supports the notion of the apparent character of BJH PSDs because the theory does not account for cavitation. This implies that certain pore populations and their pore volumes are not quantitatively accounted for in BJH PSDs. Hence, pore volumes will be underestimated when obtained from the desorption branch of physisorption isotherms measured on mudrocks and clays (Figure 2.14, Figure 2.15).

2.5 Conclusion

Six classes of sorbents of various surface chemistry and textural properties have been investigated by Ar (87 K), N_2 (77 K) and CO_2 (273 K) physisorption in order to systematically assess the complementary or alternative use of Ar for the textural characterisation of geological materials and their analogues.

- Ar, N_2 and CO_2 physisorption isotherms and their textural parameters revealed sorbent- and parameter-specific differences for the presented sample set. Discrepancies were most pronounced within the submonolayer range ($p/p^0 < 0.1$) and the transition to the mono-/multilayer range where fluid-sorbent interaction are strongest. Yet, textural parameters computed by classical physisorption theories demonstrated linear relations for individual parameter pairs, albeit sample-specific deviations from unity (slope + ratio) were common.

- N_2 underestimated micropore volumes while its µPSDs were distorted by its specific interaction with the solid caused by its quadrupole moment. Thus, any further use of N_2-based micropore volumes and µPSDs in, for example, kinetic or transport models, would result in a false estimation of the parameter of interest. In contrast, Ar offered the option to more reliably assess the microporosity of geological materials as it lacks permanent polar momentum.

- An unambiguous control for the differences in micropore volumes could not be determined. Neither a specific component (TOC, CEC, total or specific clay content) nor physical reasons for differences in accessibility could be conclusively identified negating adsorptive-specific preferences.

- Furthermore, the present study underlined that experimental boundary conditions must be critically reviewed and monitored. Hereby, the influence of saturation pressure offsets on textural parameters has been demonstrated and was linked to atmospheric pressure fluctuations. The Gurvich pore volume in combination with cumulative pore size distributions (BJH) proved effective in identifying such technical error. p^0 was regarded as the largest factor of uncertainty in this study and its effect was detrimental to data interpretation when not recognized.

- $A_{BET}(N_2)$ were overestimated when compared to BET areas obtained from argon physisorption isotherms which is in line with most literature. However, putting the difference of $A_{BET}(Ar)$ vs. $A_{BET}(N_2)$ into perspective suggested that the choice of the adsorptive for specific surface area quantification was less crucial than to acknowledge the limitation of the concept of BET areas. Even though, unequivocal evidence for orientation disorder of nitrogen was not acquired, the impact of microporosity on A_{BET} calculation is believed to be more substantial. Therefore, BET areas of Ar and N_2 are considered rather equivalent; at least for microporous mudrocks and clays and when used consistently as operational measure.

- The Gurvich (total) pore volumes and BJH PSDs of N_2 and Ar displayed fair agreement; the latter especially for the desorption branch. This implied that both adsorptives fill similar pore space except for the difference encountered in the micropore volume and the discussed

exceptions. Thus, reliable pore volumes and PSDs can be obtained from physisorption isotherms of both adsorptives.

- µPSDs could only be provided by Ar physisorption isotherms and were limited to mudrocks. The µPSDs indicated three groups of mudrocks which was supported by the empirical α_s-method. The difference in µPSDs was attributed to organic matter porosity and the formation of micropores upon thermal maturation.

- The complementary use of Ar and N_2 supplemented that cavitation was a dominant desorption mechanism together with pore network percolation and free evaporation, that controlled pore emptying to a substantial, yet sample-specific, level. This underlined the key role of smaller meso-/micropores in the accessibility of pore networks of mudrocks and clays.

It is generally recommended that textural properties of geological materials are analysed comparatively with argon and nitrogen and optionally carbon dioxide and that the textural properties are applied on a relative basis. Therefore, (i) a critical and open-minded analysis of physisorption isotherms, (ii) recognition of limits and insufficiencies of inversion models, (iii) good control and monitoring of experimental boundary conditions, and (iv) knowledge on pitfalls are indispensable for an objective characterisation of pore networks of porous materials.

Appendices

A.1 Background information on Materials

Table A.1: Geological background information of studied mudrocks including references to studies in which similar or identical samples are used; * = +Louisiana; (-) = no info.

ID	Formation	Basin	Setting	Age [Ma]	Geography
BCM	Boom Clay	Campine	(-) marine	Rupelian (33.9 to 27.8)	Flanders (BEL]
BM(a)	Bossier	East Texas	(deep) marine	Tithonian (152.1 to 145.0)	Texas* (USA)
BM(b)	Bossier	East Texas	(deep) marine	Tithonian (152.1 to 145.0)	Texas* (USA)
Cox	Callovo Oxfordian	Paris	(-) marine	Tithonian (152.1 to 145.0)	Bure (FRA)
HM	Haynesville	East Texas	(deep) marine	Kimmeridgian (157.3 to 152.1)	Texas* (USA)
LM(a)	Longmaxi	Sichuan	(-) marine	Lower Silurian (438 to 419)	Yangtze** (CHN)
LM(b)	Longmaxi	Sichuan	(-) marine	Lower Silurian (438 to 419)	Yangtze** (CHN)
OCM	Opalinus Clay	Molasse	(shallow) marine	Aalenian (174.1 to 170.3)	Jura (CHE)
TM	Toarcian	Causses	(-) marine	Toarcian (182.7 to 174.1)	Aveyron (FRA)
YPC(A)	Kortrijk	Campine	(-) marine	Ypresian (56 to 47.8)	Flanders (BEL)
YPC(E)	Kortrijk	Campine	(-) marine	Ypresian (56 to 47.8)	Flanders (BEL)
YPC(K)	Tielt	Campine	(-) marine	Ypresian (56 to 47.8)	Flanders (BEL)

ID	Use	Origin	Literature ID	References
BCM	NWR	core	K10	(Jacops et al., 2021)
BM(a)	UHCR	core	-	(-)
BM(b)	UHCR	core	Bossier	(Seemann et al., 2017)
Cox	NWR	core	EST48398	(Song et al., 2017, Seemann et al., 2017)
HM	UHCR	core	Haynesville	(Seemann et al., 2017)
LM(a)	UHCR	outcrop	S6 = Sinian	(Hu et al., 2021)
LM(b)	UHCR	core	Sichuan211	(Seemann et al., 2017)
OCM	NWR	core	CCP9	(Amann-Hildenbrand et al., 2015b, Busch et al., 2017)
TM	NWR	core	Tournemire	(Seemann et al., 2017)
YPC(A)	NWR	outcrop	-	(-)
YPC(E)	NWR	outcrop	YPC	(-)
YPC(K)	NWR	outcrop	-	(-)

A.2 Adsorptive Properties

Table A.2: Collection of physical properties of CO_2, N_2 and Ar collected from Sircar (2006).

Gas	Formular	Norm. boiling point [K]	Kin. diameter [Å]	Liquid molar vol. [mL mol^{-1}]
Carbon Dioxide	CO_2	195	3.3 to 3.9	37.4
Nitrogen	N_2	77	3.64 to 3.8	34.7
Argon	Ar	87	3.54	28.7

Gas	Formular	Polarisability [Å^3]	Quadrupole moment [Å^2]	Cross-sectional area [nm^2]
Carbon Dioxide	CO_2	2.65	4.3	0.164
Nitrogen	N_2	1.76	1.52	0.162
Argon	Ar	1.64	0	0.142

A.3 Statistical data of textural parameters of repetitive Ar physisorption measurements

Table A.3: Statistical data (X_{mean}, σ: standard deviation, CV: coefficient of variation) of textural parameters (V_{GV}= Gurvich specific pore volume, A_{BET} = BET specific surface area and V_0 = DA micropore volume) of SiAl-pellets and selected mudrocks (BCM, HM, OCM) calculated from repeated Ar physisorption isotherms (87 K); *The Gurvich specific pore volume of the BCM has been obtained from p^0-offset isotherms.

ID	V_{GV} [µL g^{-1}]	σ (V_{GV}) [µL g^{-1}]	CV (V_{GV}) [%]	A_{BET} [m^2 g^{-1}]	σ (A_{BET}) [m^2 g^{-1}]	CV (A_{BET}) [%]	V_0 [µL g^{-1}]	σ (V_0) [µL g^{-1}]	CV (V_0) [%]
SiAl-pellets	634.4	1.8	0.3	189.1	0.9	0.5	94.7	1.4	1.5
BoomClay	62.0*	1.4	2.2	42.5	0.8	1.8	20.4	0.4	1.8
Haynesville	34.5	0.3	0.7	18.5	0.7	3.5	9.9	0.3	2.7
OpalinusClay	56.7	1.5	2.7	28.9	0.8	2.8	12.5	0.7	5.9

A.4 Comparison of micropore volumes DA-theory and α_s method

Table A.4: Ar and N_2-based micropore volumes of mudrocks calculated from DA theory and α_s-plots using a macroporous LiChrosphere-Si1000 as reference solid. [x_i(Ar) | x_j(N_2)]; - = negative intercept; * = intercept statistically zero; V_0(DA) = micropore volume obtained from DA theory; V_{α_s}(t,mic) = total micropore volume obtained from α_s-plots; V_{α_s}(u, mic) = ultra-micropore volume obtained from α_s-plots; V_{α_s}(s, mic) = super-micropore volume obtained from α_s-plots.

ID **[Ar|N_2]**	V_0 (DA) [µL g^{-1}]	V_{α_s}(t, mic) [µL g^{-1}]	V_{α_s}(u, mic) [µL g^{-1}]	V_{α_s}(s, mic) [µL g^{-1}]
BCM	20.0|16.3	5.8|2.6	1.2|-	4.7|2.6
BM(a)	3.9|2.5	0.8|0.2	0.4|-	0.4|0.2
BM(b)	11.6|8.1	3.5|0.9	0.7|-	2.8|0.9
Cox	11.3|8.3	2.9|1.5	0.2|-	2.6|1.5
HM	9.9|6.9	3.3|1.4	1.6|*	1.7|1.4
LM(a)	7.5|7.2	1.6|1.0	0.7|-	0.9|1.0
LM(b)	6.5|6.1	1.7|1.4	1.0|*	0.7|1.4
OCM	10.6|10.6	2.6|2.1	0.0|-	2.6|2.1
TM	10.2|8.4	2.5|1.2	0.4|-	2.1|1.2
YPC(A)	28.3|26.2	8.5|6.2	1.3|-	7.2|6.2
YPC(E)	27.1|23.8	8.2|8.3	2.0|-	6.2|8.3
YPC(K)	19.5|16.4	6.2|4.4	1.1|-	5.1|4.4

A.5 Statistical thickness models

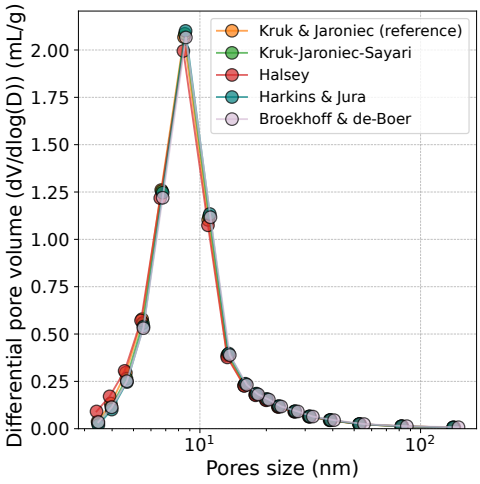

Figure A.1: Differential PSD of SiAl reference material calculated based on different statistical thickness curves. The mean pore size is 8.54 ± 0.08nm ($CV \approx 1\%$). The exact equations can be found in the manual of Micromeritics *Microactive*.

A.6 Textural parameter collection for argon physisorption isotherms

Table A.5: Textural properties of mudrocks obtain by physisorption analysis of Ar sorption isotherms measured at 87 K; V_{GV} = Gurvich (total) pore volume calculated at $p/p^0 = 0.9916$ (at $W_{BJH} = 250$ nm), A_{BET} = BET specific surface area, Q_{mono} = BET monolayer capacity, C = BET energy constant, V_0 = DA micropore volume, Q_0 = DA limiting micropore capacity, E_0 = DA characteristic energy of system, n = DA exponent.

ID	**Solid**	V_{GV} [µL g^{-1}]	A_{BET} [m^2 g^{-1}]	Q_{mono} [mmol g^{-1}]	C [-]	V_0 [µL g^{-1}]	Q_0 [mmol g^{-1}]	E_0 [kJ mol^{-1}]	n [-]
BoomClay	mudrock	77.6	42.6	0.50	83.6	20.0	0.70	12.3	1.61
Bossier(a)	mudrock	16.8	7.1	0.08	75.0	3.9	0.14	11.2	1.17
Bossier(b)	mudrock	32.3	25.1	0.29	82.2	11.6	0.41	12.4	1.68
Cox	mudrock	60.6	24.3	0.28	72.4	11.3	0.40	11.8	1.70
Haynesville	mudrock	34.1	19.3	0.22	106.0	9.9	0.35	13.1	1.20
Longmaxi(a)	mudrock	23.4	15.5	0.18	56.1	7.5	0.26	12.7	1.14
Longmaxi(b)	mudrock	15.3	12.0	0.14	93.1	6.5	0.23	13.	1.00
OpalinusClay	mudrock	57.5	28.1	0.33	62.5	10.6	0.37	10.9	2.59
Tournemire	mudrock	32.8	21.8	0.26	73.2	10.2	0.36	11.9	1.64
Ypresian-Aalbeke	mudrock	93.6	61.4	0.71	79.5	28.3	0.99	12.2	1.71
Ypresian-Elverdinge	mudrock	84.3	56.8	0.66	85.8	27.1	0.95	12.3	1.56
Ypresian-Kortenmark	mudrock	69.2	42.4	0.49	83.6	19.5	0.68	12.4	1.69
SWy2-Na	clay	91.4	47.4	0.55	112.9	20.9	0.73	12.4	1.71
SWy2-CuTrien	clay	155.2	166.1	1.93	597.1	72.9	2.56	26.7	1.03
Muscovite	clay	76.3	8.6	0.10	77.8	3.78	0.11	11.4	3.05
Kaolinite	clay	166.4	18.8	0.22	53.3	8.28	0.29	10.8	2.06
YPC-Cf-E	clay	139.7	91.9	1.07	87.1	42.2	1.48	11.1	1.69
YPC-Cf-CuTrien	clay	98.7	123.2	1.43	169.4	62.0	2.17	15.9	1.10
cpg-5nm	VYCOR cpg	132.7	103.7	1.21	48.4	64.3	2.25	8.0	1.00
cpg-20nm	VYCOR cpg	229.9	46.6	0.54	28.3	32.2	1.13	6.1	1.00
cpg-50nm	VYCOR cpg	385.1	28.1	0.33	24.5	20.4	0.72	5.5	1.00
SiAl-pellets	reference	633.4	189.1	2.20	36.6	94.7	3.32	8.7	1.47
FB-35DC	Si-Oxide	21.4	3.5	0.04	21.3	2.1	0.07	6.4	1.13
FB-105FD	Si-Oxide	31.9	3.4	0.04	29.0	2.0	0.07	7.2	1.20
SFP-20M	Si-Oxide	47.9	9.5	0.11	27.3	6.3	0.22	6.3	1.06
SFP-30M	Si-Oxide	20.9	5.2	0.06	23.6	3.1	0.11	6.7	1.15
MIOX-2.5 µm	Fe-Oxide	11.7	2.8	0.03	44.0	1.5	0.05	8.8	1.33
MIOX-5 µm	Fe-Oxide	7.4	2.5	0.03	26.3	1.7	0.06	7.1	1.00
MIOX-20 µm	Fe-Oxide	3.6	0.5	0.01	27.2	0.3	0.01	6.6	1.14

A.7 Textural parameter collection for nitrogen physisorption isotherms

Table A.6: Textural properties of mudrocks obtain by physisorption analysis of N_2 sorption isotherms measured at 77 K; V_{GV} = Gurvich (total) pore volume calculated at $p/p^0 = 0.9923$ (at $W_{BJH} = 250$ nm), A_{BET} = BET specific surface area, Q_{mono} = BET monolayer capacity, C = BET energy constant, V_0 = DA micropore volume, Q_0 = DA limiting micropore capacity, E_0 = DA characteristic energy of system, n = DA exponent.

ID	**Solid**	V_{GV} [µL g^{-1}]	A_{BET} [m^2 g^{-1}]	Q_{mono} [mmol g^{-1}]	C [-]	V_0 [µL g^{-1}]	Q_0 [mmol g^{-1}]	E_0 [kJ mol^{-1}]	n [-]
BoomClay	mudrock	103.5	44.1	0.45	196.5	16.3	0.47	14.0	2.69
Bossier(a)	mudrock	17.7	7.1	0.07	150.5	2.5	0.07	13.7	2.76
Bossier(b)	mudrock	35.7	24.5	0.25	134.0	8.1	0.23	15.1	2.94
Cox	mudrock	60.7	24.6	0.25	167.3	8.3	0.24	13.3	3.69
Haynesville	mudrock	39.0	19.7	0.20	168.6	6.9	0.20	15.2	2.52
Longmaxi(a)	mudrock	26.2	17.4	0.18	136.5	7.2	0.21	13.1	1.68
Longmaxi(b)	mudrock	16.2	12.8	0.13	166.0	6.1	0.18	12.9	1.29
OpalinusClay	mudrock	60.5	31.1	0.32	128.5	10.6	0.30	14.4	2.95
Tournemire	mudrock	33.8	24.2	0.25	150.6	8.4	0.24	14.2	3.00
Ypresian-Aalbeke	mudrock	118.4	67.5	0.69	209.7	26.2	0.76	13.9	2.36
Ypresian-Elverdinge	mudrock	109.8	64.4	0.66	220.2	23.8	0.69	14.4	2.68
Ypresian-Kortenmark	mudrock	75.2	44.8	0.46	193.4	16.4	0.47	13.9	2.76
SWy2-Na	clay	103.1	48.2	0.49	405.5	18.3	0.53	14.6	1.87
SWy2-CuTrien	clay	160.1	169.3	1.74	2307.7	69.0	1.99	29.8	1.45
Muscovite	clay	98.4	10.3	0.11	132.8	3.2	0.09	16.8	3.44
Kaolinite	clay	290.4	22.1	0.23	142.2	7.7	0.22	14.2	2.96
YPC-Cf-E	clay	149.5	93.5	0.96	236.7	33.7	0.97	14.3	2.98
YPC-Cf-CuTrien	clay	122.9	122.9	1.26	354.8	49.5	1.43	18.2	1.74
cpg-5nm	VYCOR cpg	134.3	116.5	1.19	197.3	58.0	1.67	13.5	1.15
cpg-20nm	VYCOR cpg	244.0	55.8	0.57	132.3	28.9	0.83	11.3	1.16
cpg-50nm	VYCOR cpg	369.7	29.7	0.31	122.6	12.8	0.37	11.3	1.93
SiAl-pellets	reference	607.9	218.9	2.23	123.2	96.3	2.55	15.7	1.43
FB-35DC	Si-Oxide	27.3	3.4	0.03	96.1	1.12	0.032	11.2	3.85
FB-105FD	Si-Oxide	60.2	4.3	0.04	107.3	1.55	0.045	11.9	2.62
SFP-20M	Si-Oxide	95.5	10.5	0.11	111.0	3.76	0.108	11.1	3.28
SFP-30M	Si-Oxide	38.3	5.5	0.06	109.3	1.82	0.052	11.2	4.20
MIOX-2.5 µm	Fe-Oxide	18.2	3.2	0.03	99.7	1.01	0.029	14.1	3.22
MIOX-5 µm	Fe-Oxide	14.0	2.6	0.03	80.8	0.85	0.025	11.9	3.82
MIOX-30 µm	Fe-Oxide	2.5	0.5	0.005	82.3	0.17	0.005	11.9	2.89

A.8 Textural parameter collection for carbon dioxide physisorption isotherms

Table A.7: Textural properties of studied materials obtain by physisorption analysis of CO_2 sorption isotherms measured at 273 K; Isotherm analysis is restricted to application of DA theory; V_0 = DA micropore volume, Q_0 = DA limiting micropore capacity, E_0 = DA characteristic energy of system, n = DA exponent.

ID	**Solid**	V_0 [µL g^{-1}]	Q_0 [mmol g^{-1}]	E_0 [kJ mol^{-1}]	n [-]
BoomClay	mudrock	19.0	0.46	15.72	1.24
Bossier(a)	mudrock	6.1	0.15	17.88	1.30
Bossier(b)	mudrock	10.1	0.25	16.81	1.39
Cox	mudrock	8.0	0.20	17.69	1.44
Haynesville	mudrock	8.4	0.21	17.73	1.34
Longmaxi(a)	mudrock	8.0	0.20	23.36	1.86
Longmaxi(b)	mudrock	3.9	0.10	23.66	1.68
OpalinusClay	mudrock	11.8	0.29	15.94	1.34
Tournemire	mudrock	10.8	0.26	13.46	1.15
Ypresian-Aalbeke	mudrock	43.2	1.05	10.24	1.00
Ypresian-Elverdinge	mudrock	25.7	0.63	12.55	1.07
Ypresian-Kortenmark	mudrock	13.6	0.33	17.53	1.46
SWy2-Na	clay	14.5	0.35	21.87	1.68
SWy2-CuTrien	clay	53.7	1.31	33.01	2.46
Ypresian-Elverdinge-Clayfrac-org	clay	43.8	1.07	1.06	1.09
Ypresian-Elverdinge-Clayfrac-CuTrien	clay	38.3	0.93	26.06	1.65
cpg-5nm	VYCOR cpg	50.4	1.23	15.03	1.40
cpg-20nm	VYCOR cpg	17.4	0.42	19.85	1.88
cpg-50nm	VYCOR cpg	3.9	0.10	27.82	1.83
SiAl-pellets	reference	69.1	1.69	22.90	1.80

Chapter 3

Insights into Sorbed Water in Mudrocks: Investigating Distribution Patterns, Controls & Mechanisms

This chapter is a longer version of the current author's manuscript that will be submitted to a peer reviewed journal after a final internal review from the co-authors: T. Seemann, H. Claes, H. Stanjek. Insights into Sorbed Water in Mudrocks: Investigating Distribution Patterns, Controls & Mechanisms.

Abstract

Water vapour sorption in mudrocks is controlled by a set of multiple parameters involving mineralogy, surface chemistry and pore structure dictating the distribution of sorbed water in the pore network. Hereby, expandable clay- and cation hydration are of utmost importance, but there is no general consensus about a unified interpretation with respect to controls and mechanisms of water sorption in mudrocks.

To gain insights into the water distribution, its controls and mechanisms in the pore network of mudrocks, a combination of water vapour- and nitrogen physisorption joint with compositional analysis was applied to a set of immature mudrock mostly considered in the framework of nuclear wastes storage. N_2 physisorption was performed on moisture-conditioned samples (11%RH, 32%RH, 56%RH, 75%RH, 97%RH) with ad- and desorption history revealing a reproducibility better than 5.3% difference from the mean at maximum relative humidity.

Smectite content and cation exchange capacity were identified as constitutive controls of water sorption in mudrocks explaining between 89% and 99.5% of the variance in water uptake as a function of relative humidity. The dominance of both parameters implied similar sorption mechanisms as for smectite including cation- and interlayer hydration via mixed-layer stages of water intercalation accompanied by volumetric expansion.

Swelling was associated with unpredictable pore network modifications, a factor contributing to the universally observed volume imbalance ($V(H_2O) > \Delta V_{GV})(N_2)$). A linear mixing-model of clay hydration combined with capillary condensation and swelling-induced pore network modification provided a fair approximation of the imbalance.

The differences in textural parameters and water distribution obtained via ad- and desorption conditioning were less than anticipated. The major effect of presorbed water concentrated in pores up to 20 nm while maximum filled pore sizes remained sample-specific. Supported by cavitation volume- and pore size distribution analysis, a maximum filled pore size of ≈ 8 nm at 97%RH was observed which was in contradiction to the modified Kelvin equation. Pore filling occurred only above 75%RH in adsorption while micropores were readily accessible after desorption conditioning $<$ 97%RH conveying delayed condensation and "far-reaching" evaporation.

3.1 Introduction

Mudrocks are fine-grained, argillaceous rocks of sedimentary origin and rich in clay minerals along with organic matter and carbonates (Potter, 2003). This most abundant sedimentary rock type plays a vital role in environmental and energy applications because of its favourable properties as a "barrier unit". Recognised for their tight networks, low permeabilities and diffusivities combined with high capillary entry- and breakthrough pressures, they serve as excellent caprocks for oil- and gas reservoirs as well as hydrogen- and carbon dioxide storage (Amann-Hildenbrand et al., 2015b). Moreover, the mudrocks' high clay content, large specific surface areas and ability to exchange cations are promising features to retain toxic elements and radionuclides, important for the confinement of toxic and nuclear waste. Therefore, mudrocks are of particular interest and importance for the current energy transition towards a carbon-friendly and sustainable industry.

Water constitutes the primary geofluid in the pore network of mudrocks and the understanding of water-rock interaction is instrumental for geological- and geochemical processes as well as for environmental and engineering applications. Comprehension of water-rock interaction has matured for several decades and is still actively researched (cf. Li et al., 2016a,b, 2017, 2019a, Lahn et al., 2020, Li et al., 2021, Zhang et al., 2022). Mostly discussed in the form of fluid saturation, water has been identified as a first-order control for effective rock properties including transport, storage and rock mechanics.

The water saturation levels in mudrocks, particularly in gas shales, exhibit considerable variability and are contingent upon the specific geological formations. According to Cheng et al. (2017) and Li et al. (2021) (& reference therein) water saturation varies between 10% and 60% for some American unconventional shales (Woodford, Marcellus, Fayetteville, Haynesville, Barnett). In contrast, southern Chinese gas shales revealed an even broader spectrum, with water saturations spanning from 10 to 90% (cf. Cheng et al., 2017, Yang et al., 2020a). This variability in water saturation underlines the complex matter of water-rock interaction in mudrocks, implying a multitude of geological, physical and chemical variables influencing the saturation characteristics of these formations.

The influence of water saturation is equally crucial for fluid and solute transport as it is for fluid storage considerations. Gasparik et al. (2014), Tan et al. (2014) and Merkel et al. (2015) demonstrated the impact of water saturation on gas storage disclosing competitive sorption for water and methane and a reduced pore network accessibility due to water blocking. A decrease by 40 to 60% was observed by Gasparik et al. (2014) for the Posidonia and the Alum mudrocks which the authors attribute to a displacement of approximately 0.2 to 0.3 molecules of CH_4 by H_2O. Hildenbrand et al. (2006) reported a reduction of CH_4 sorption capacity by 51 to 63% by the presence of 0.06 g/g of water in a sapropelic coal.

Regarding diffusive transport, Nunn et al. (2018) and earlier Savoye et al. (2010, 2012) indicated a reduction in solute/ion diffusivity with decreasing water saturation associated with a change of the systems' tortuosity. Contrastingly, gas diffusivity increases inversely to liquid saturation, but at present experimental data are scarce (Gowrishankar et al., 2023).

For advective fluid flow, Nolte (2021) showed a diminished effective gas permeability as a function of water content. The authors discerned a mechanistic change from advective single-phase flow

to capillary-pressure-controlled multi-phase flow. An earlier investigation of Ghanizadeh et al. (2013) corroborated the phenomenon and a continuing study by Ghanizadeh et al. (2014) revealed increasing stress sensitivity of matrix permeability as a function of saturation.

The stress sensitivity aligns with the effect of water saturation on rock mechanical properties (failure load, compressive strength, tensile strength, Young's modulus) (e.g. Lashkaripour, 2002, Guha Roy et al., 2017). Wong et al. (2016) presented data that quantified a loss in uniaxial compressive strength between 40% and 95% while Young's modulus ceased between 20% and 95% for moist samples relative to their dry state.

In recent years, the research focus drifted from saturation to water distribution in mudrocks. Several researchers like Li et al. (2016a,b), Cheng et al. (2017), Lahn et al. (2020), Li et al. (2021) or Chen et al. (2021) emphasised the importance of the water distribution in the pore network of mudrocks and the necessity to understand basic mechanisms and controls. Information on the location and the physical state of water, whether it forms a layer, an island or being condensed and filling a complete pore, is vital to comprehend and predict, for example, transport or mechanical properties of rocks because rocks behave fundamentally different under wet conditions. Moreover, small amounts of water may significantly inhibit transport when preferential pathways are blocked.

A fundamental understanding of water sorption has been developed by studying engineered and mono-mineralogical systems with a combination of analytical methods encompassing vapour sorption combined with scattering- and diffraction methods (SANS, SAXS, XRD), spectroscopy (FTIR, NMR) or thermoporometry (Iiyama et al., 1997, 2000, Cases et al., 1992, Sang et al., 2020b, Rinnert et al., 2005, Marreiros et al., 2021, Majda et al., 2018, Salles et al., 2008). The variety of water sorption data, mechanisms and potential controls published for mudrocks convey the complexity of the topic, especially when geological materials are investigated and boundary conditions can hardly be constrained (Sang et al., 2019). The moisture content in mudrocks is primarily attributed to hydrophilic clay minerals, yet a non-negligible contribution can be made by organic matter (Chalmers & Bustin, 2007). Despite that clay minerals and organic matter contribute to the total water uptake, it has not been possible to quantitatively discriminate their contributions from water vapour sorption isotherms of mudrocks (Feng et al., 2018, Sang et al., 2019, Bai et al., 2020, Yang et al., 2020b,a, Chen et al., 2021). Moreover, their individual share in terms of hosted pore size is controversial up to today because of their diverse nature and reaction towards burial.

Recently, a combination of water and nitrogen sorption provided new insights into the distribution of water in the pore network of mudrocks. Li et al. (2016a,b), Seemann et al. (2017), Lahn et al. (2020) as well as Li et al. (2021) adapted the approach of Alcañiz-Monge et al. (2001), Alcañiz-Monge & Lozano-Castelló (2002) and Prinz & Littke (2005) to measure nitrogen physisorption isotherms on samples of known moisture content in order to obtain information on the location and distribution of water within the pore network of mudrocks as a function of relative humidity. Published data and their interpretations are sometimes incoherent and leave room for different interpretations, especially since the physico-chemical properties of the solid need to be taken into account for the interpretation of H_2O isotherms. A quantitative control of either clay or organic matter content is often ambiguous and attributions of water content to a specific component remain

mostly qualitative. However, the role of clay is frequently addressed on a qualitative and descriptive level. The ambiguous and complex observation of water-rock interactions suggests competing effects of surface chemistry and pore structure, as shown by Thommes et al. (2012) and denies an easy generalisation of sorption mechanisms as a function of partial pressure like it has been established for nitrogen and argon.

The presented study is a continuation of the work of Seemann et al. (2017) and Lahn et al. (2020) on the distribution and sorption mechanism of water in the pore network of mudrocks assessed by a combination of water- and nitrogen sorption on moisture-conditioned mudrocks. The experimental approach has been extended towards the comparison of the water distribution achieved by ad- and desorption conditioning in organic-lean formations such as the Boom Clay, the Callovo Oxfordian argillite, the Opalinus Clay and the Tournemire argillite; formations considered in the framework on nuclear waste storage in Europe. The primary objective of this contribution is to identify the dominant compositional and textural parameters influencing water sorption in mudrocks. Hereby, the emphasis is to provide solid, quantitative data regarding their control. The experimental approach and interpretation scheme are critically evaluated while the fundamental sorption mechanisms are identified and discussed.

3.2 Theory and concepts of water sorption

Fundamental works on water vapour sorption mechanisms have been performed on natural and tailored materials for several decades (e.g. Hendricks et al., 1940, Mooney et al., 1952b, Quirk, 1955, Keren & Shainberg, 1975, Sposito & Prost, 1982, Cases et al., 1992, Cases, 1997, Ferrage, 2005, 2016). Water vapour isotherms are typically characterised by a broad variety of isotherms and hysteresis loops that vary in shape, depending on the solid's surface chemistry and pore structure (carbons, silicas, clays, mudrocks) (cf. e.g. Iiyama et al., 2000, Rother et al., 2020, Lindholm et al., 2019, Sang et al., 2019). The occurrence of hysteresis is observed for micro- as well as for mesopores and it is associated with different ad- and desorption mechanisms as well as structural changes during the hydration of expandable clays (Cases et al., 1992, Alcañiz-Monge et al., 2001, Alcañiz-Monge & Lozano-Castelló, 2002, Michot et al., 2005). Those sorption mechanisms and structural effects differ significantly from conventional adsorptives like nitrogen and argon which are neutral to the structure of the solid.

Tailored materials (ordered mesoporous carbons, active carbons, hierarchical MFI zeolites, silica and silica gels) served to systematically assess sorption mechanisms and their controls. The investigation of tailored systems demonstrated the complexity of physico-chemical water-solid interactions resulting in various sorption mechanisms accompanied by an intricate structural organisation of water molecules under confinement. Thereby, a multi-parameter control was identified involving (i) pore geometry, (ii) pore network connectivity, (iii) solid composition and (iv) surface chemistry (e.g. Iiyama et al., 1997, 2000, Kaneko et al., 1999, Alcañiz-Monge et al., 2001, 2010, Thommes et al., 2011, 2013, Baumgartner et al., 2019). Conversely, the interpretation of water vapour isotherms is not straightforward because several sorption processes occur concomitantly while pore geometry (shape & size) and surface chemistry compete for control over water vapour sorption (cf. Thommes

et al., 2012). Here, a short summary of the prevailing water vapour sorption concepts is provided for engineered and geological materials:

Water in tailored materials Various mechanisms were proclaimed to explain the water uptake of tailored micro- and mesoporous materials like carbons or silicas. These mechanisms include initial adsorption at primary hydrophilic sorption sites followed by hydrogen bonding and culminating in small-sized clusters formed by several molecules (Stoeckli, 1998, Horikawa et al., 2011b, 2013, 2017). The initially sorbed molecules serve as secondary sorption sites for further cluster growth as a function of relative humidity. At a critical cluster size, individual clusters coalesce to fill adjacent pore spaces, for example, by migrating into micropores when formed at their entrances (Do & Do, 2000, Thommes et al., 2013). According to Thommes et al. (2013), the critical cluster size is independent of temperature and merely controlled by relative pressure. The onset of water adsorption is governed by the number density of hydrophilic surface sites on the surface of the pore walls whereas the isotherm shape is dictated by surface chemistry and pore structure (Alcañiz-Monge et al., 2001). This conceptualisation has been proposed in multiple models like the Do-Do theory (Do & Do, 2000, Do et al., 2009), extended in the Horikawa-Do theory (Horikawa et al., 2011a) but most famously in the Dubinin-Serpinsky theory (Dubinin & Serpinsky, 1981). Besides cluster-mediated pore filling, micropore filling and layer sorption, similar to conventional fluids, as well as pore condensation have been used to explain water sorption in hydrophilic pore systems of silicas (Alcañiz-Monge et al., 2010, Saliba et al., 2016, Rother et al., 2020).[1] In contrast, cluster-mediated pore filling followed by capillary condensation is typically associated with hydrophobic surfaces. Interestingly, Alcañiz-Monge et al. (2001), Thommes et al. (2012) and Saliba et al. (2016) point out that micro- and mesopore filling by water is not always distinct, especially for broad and continuous pore size distributions. Therefore, the filling process may be regarded as gradual (simultaneous filling of multiple pore sizes) and not strictly progressive (pore size controlled) (Thommes et al., 2012). Still, Alcañiz-Monge et al. (2001) demonstrated a correlation of pore filling pressure with pore size, if surface chemistry does not differ significantly.

The desorption mechanism of water remains under debate and various mechanisms have been published. These mechanisms include desorption via (i) capillary evaporation by means of a receding meniscus (cf. Iiyama et al., 2000, Thommes et al., 2013, Chen et al., 2021) as well as (ii) pore emptying through cavitation (vapour bubble formation inside a water-filled pore due to spinodal evaporation) of a critically stretched water column occurring at a threshold partial pressure leaving behind individual water clusters (Maheshwari et al., 2017).

Water in clays In contrast to the mechanisms defined for tailored materials, water sorption on clayey matter takes a special position because of the potential for structural modifications during water uptake. The seminal works of Mooney et al. (1952b), Newman (1983), Cases et al. (1992), Cases (1997), Bérend (1995), Chiou (1997), Laird (1999), Ferrage (2005), Ferrage et al. (2007, 2010), Dazas et al. (2013), Lindholm et al. (2019) focused on clayey substrates and elucidated the superior role of expandable clay minerals (if present) in the water retention properties of geological

[1] Interestingly to note, capillary condensation resulted in the formation of a significant number of OH-groups on the surface of the mesoporous silica studied by Saliba et al. (2016) causing the removal of low-pressure hysteresis.

materials. These investigations highlight the key role of (i) clay mineral type, (ii) interlayer cation type (cf. hydration energy) and number (cf. cation exchange capacity), (iii) amount, location, and density of layer charge (octahedral vs. tetrahedral substitution), (iv) molecular organisation within the interlayer, (v) layer structure as well as (vi) processes and mechanisms involved in water-clay interaction.

In brief, the water vapour sorption isotherm of clayey materials is a composite isotherm reflecting water sorption on the external surface, in the interlayer space of clay minerals as well as capillary water uptake in the pore network formed by the assembly of the crystallites (stacks of tetra- and octahedral sheets along the c-axis). The initial uptake of water occurs on the external surface at surface groups and external cations at low partial pressures (Cases et al., 1992, Michot et al., 2005, Ng & Mintova, 2008). Simultaneously, the onset of sorption in the interlayer space is controlled by the exchangeable (interlayer) cations (size, valence, number) around which a hydration shell is formed (Cases et al., 1992, Cases, 1997, Bérend, 1995, Ng & Mintova, 2008). The order and magnitude of the above processes are, however, strongly dependent on the type of clay mineral, its exchangeable cation population and the cation's enthalpy of hydration as indicated by the variability of *d*-spacings measured as a function of relative humidity for various clay minerals (Cases et al., 1992, Cases, 1997, Chiou, 1997, Michot et al., 2005, Ferrage et al., 2010, Michot, 2018). Therefore, it is not easily feasible to establish a generalisation about the initial order of hydration of external surface and interlayer space in relation to relative humidity, especially for mudrocks without accompanying XRD measurements. For non-expandable clays like kaolinite or illite water sorption is limited to the external surface hydration (Grekov et al., 2019). Laird (1999) describes the hydration in the form of a cluster-mediated sorption mechanism regulated by exchangeable cations (capacity). This process can evolve into monolayer formation if the surface charge density is high enough (Quirk & Murray, 1999). Hydrogen bonding follows and the adsorption of water molecules in the interlayer space on the basal surface of expandable clay minerals. There, they form up to three randomly interstratified (mixed-) water layers, depending on the cation species, layer charge, charge distribution, layer structure and relative humidity (Ferrage et al., 2005, 2007, 2010, Ng & Mintova, 2008, Dazas et al., 2013).[2] The intercalation of water is accompanied by concomitant interlayer expansion (swelling clays only) by several angstroms compared to the dry state and the adsorption on the external surface of the crystallites. The final interlayer distance and the discrete expansion partial pressure depend on the type of expandable clay and the cation type (Ferrage, 2016). By applying microcalorimetry to measure the enthalpy of immersion as a function of preadsorbed water content, Cases et al. (1992) and Bérend (1995) observed that during initial water sorption, the crystallite size (thickness in the *c*-direction) can decrease, altering the external surface area, which is influenced by the assemblage architecture of the crystallites. At high partial pressure, water increasingly occupies the interparticle pore network by means of capillary condensation (Johnston et al., 1992, Newman, 1983, Rinnert et al., 2005, Ferrage et al., 2010, Lindholm et al., 2019). In parallel, secondary, osmotic swelling might occur at high partial pressure because of diffuse double layer formation when water liquifies in pores created by clay surfaces (Norrish, 1954, Salles et al., 2008).

[2]Preferential adsorption of water to basal OH-groups upon water layer formation is included in the water layer formation process.

Desorption proceeds via the dehydration of the interparticle space simultaneously with the interlayer space emptying. The hysteresis in *d*-spacings as a function of relative humidity indicates that water layers and interlayer spacing persist at lower partial pressures during desorption compared to their formation during adsorption (e.g. Michot et al., 2005). This yields substantial hysteresis and stepwise desorption isotherms (cation type dependent) representing interlayer contraction (Dazas et al., 2013). Similar to the adsorption processes intercalated water layers desorb gradually; i.e. simultaneously from 3 to 1 W layers at different degrees (cf. Ferrage et al., 2010).

3.3 Materials & Methods

3.3.1 Sample materials

The studied sample set consists of four clay-rich and immature mudrocks: (i) Boom Clay, (ii) Callovo Oxfordian argillite, (iii) Opalinus Clay and (iv) Tournemire argillite.

The Boom Clay (BCM) is a shallow marine mudrock of Rupelian age (29 to 32 Ma) deposited at a water depth between 50 to 100 m in the North Sea Basin (Vandenberghe et al., 2014). The used sample is part of the Boeretang member and originates from a depth between 167.92 to 168.02 m. Additional information can be found in Jacops et al. (2020) in which the sample is defined as K10.

The Callovo Oxfordian argillite (COx) is part of the Paris Basin and has been deposited under marine conditions (Pellenard & Deconinck, 2006). It is of Tithonian age (145 to 152 Ma) and forms an over-consolidated rock package of approximately 130 m thickness, located at a current depth of 420 to 550 m (Zhang et al., 2010). The subsample stems from an underground laboratory in Bure in the Meuse-Haute Marne site (borehole TPV1301) and it is referenced as EST48398 in Song et al. (2017).

The Opalinus Clay (OCM) is a shallow marine mudrock deposited between 174 Ma and 178 Ma ago (Aalenian age) (Marschall et al., 2005). The Opalinus formation is composed of shaly, sandy and carbonate-rich sandy facies (Bossart et al., 2017). The investigated sample is part of a 4 m long core taken in the Mont Terri underground laboratory situated approximately 300 m below surface. The core has been provided by NAGRA and SWISSTOPO and the employed sample is referenced as BHG-D1(9) in Amann-Hildenbrand et al. (2015b) and CCP9 in Busch et al. (2017).

The Tournemire argillite (TM) is a marine mudrock located in the Causses Basin on the southern border of the French Massif Central (Rejeb et al., 2007). The mudrock package is approximately 250 m thick and consists of mudrocks and marls which are of Toarcian age (174 to 183 Ma) (Peyaud et al., 2006, Rejeb et al., 2007). The sample originates from the underground laboratory in Aveyron and is referred to as Tournemire in Seemann et al. (2017).

The reader is made aware that the adsorption data (11 to 97%RH) of the Callovo Oxfordian argillite (Figure 3.3b) and the Opalinus Clay (Figure 3.3c) have already been published by Lahn et al. (2020) and that only a textural revision of the raw data has been carried out. The remaining data sets were newly collected for both conditioning histories.

3.3.2 Sample preparation

Mudrocks were received as millimetre-sized chips equilibrated at ambient temperature and humidity. A representative amount of material was gently crushed and dry-sieved to a particle size fraction of 200 to 400 µm. The mudrock particles were stored above silica gel in a desiccator before use.

The moisture conditioning was performed statically at 303 K using glass desiccators and the deliquescent points of saturated salt solutions of LiCl (11%RH), $MgCl_2$ (36%RH), NaBr (56%RH), NaCl (75%RH) and K_2SO_4 (97%RH) (Greenspan, 1977). Prior to moisturisation, the mudrocks were dried for 24 h at 378 K under vacuum ($P \leq 5$ Pa) to achieve equivalent starting conditions. Subsequently, the dry material was either immediately equilibrated at the desired relative humidity (adsorption) or initially conditioned at 100%RH above pure water and then desorbed to the desired relative humidity. For the initial equilibration at 100%RH, a time period of at least 50 days was chosen. At that moment the rate of mass change was at maximum 0.1 mg/d. An operational equilibrium criterion of $\leq$ 1 mg/d of mass change was assigned for moisture equilibration at a specific relative humidity. This criterion is above the balance uncertainty used to take the mass of the equilibrated samples. Operational mass-constancy was typically achieved within 7 to 14 d in both ad- and desorption conditioning at the desired relative humidity. For practical reasons, most samples were left to equilibrate longer.

3.3.3 X-ray diffraction

The mineralogical composition of the mudrocks was analysed by means of X-Ray powder diffraction (XRD). XRD-powder patterns were measured on a Bruker D8 diffractometer equipped with a graphite monochromator and using Cu Kα radiation (40 kV, 40 mA). Diffraction patterns were recorded between 2° and 92° 2θ at a step size of 0.02 and 5 s counting time. To ensure accuracy, a representative amount of bulk material (4 g of 200 to 400 µm) was spiked with 1 g α-Al_2O_3 (0.2 g/g). The dry mixture was milled for 15 min in a McCrone micronizing mill using ethanol as a lubricant and cooling agent to prevent heat- and strain damage and mineral dissolution. The suspension was dried at ambient conditions and subsequently homogenised in a mortar. Bulk powder beds were prepared by the topfill method including sieving and removal of the uppermost layer by an adhesive pink tape to reduce preferred orientation. Rietveld refinement was performed to quantify the mineralogical composition of the bulk material. For that purpose, the BGMN-based software Profex was employed and combined with customised (clay) mineral structures (Doebelin & Kleeberg, 2015, Ufer et al., 2008, Ufer & Kleeberg, 2015).

3.3.4 Cation exchange capacity

The cation exchange capacity (CEC) was measured on three subsamples of 0.2 to 1 g of bulk rock. The gently ground and dried material was exchanged with the Cu-triethylenetetramine complex (Cu-Trien) as described by Stanjek & Künkel (2016). The solid was dispersed in a 4 mM solution of Cu-Trien and equilibrated for 60 min while constantly shaken. After equilibration, the dispersion was centrifuged and filtered via a syringe-inline filter system. Its absorption was measured at 575 nm by means of visible photospectroscopy on a Specord210 Plus (Analytik Jena). The CEC

was corrected for the pH-dependence of the charge of the Cu-Trien complex (Stanjek & Künkel, 2016). The exchanged amount was recalculated from a previously determined standard calibration curve (4-point calibration).

3.3.5 Rock-Eval pyrolysis

Total organic carbon (TOC) and temperature of maximum hydrocarbon generation ($T_{\max}$) were determined by pyrolysis on ≈ 100 mg of powdered bulk material in a *Rock-Eval 7* (Vinci Technologies). A standard protocol (IFP Basic Method) was applied involving an isothermal heating stage of 180 s at 573 K followed by linear heating to 923 K at a heating rate of 25 K/min. Hydrocarbon release was quantified by a flame-ionisation-detector. A detailed description of the protocol can be found in Behar et al. (2001) or Grohmann et al. (2023).

3.3.6 Dynamic water vapour sorption

Water vapour sorption isotherms were determined gravimetrically by dynamic vapour sorption at 303 K in a *DVS ET* setup of Surface Measurement Systems Ltd (Alperton, London, UK). The dynamic flow system operates at a constant flow rate (here: $100\,\mathrm{cm^3\,min^{-1}}$, standard conditions) using vapour-loaded nitrogen as the carrier gas.

The vapour load was controlled by two independent mass flow controllers which were calibrated with saturated salt solutions. The relative humidity (RH)[3] was passively monitored by a dew point analyser. Isothermal uptake of water vapour was determined at 28 discrete pressure points in ad- and desorption mode between $0 < p/p^0 < 0.94$. An operational equilibrium criterion $\mathrm{d}m/\mathrm{d}t \leq m \times 0.5\,\frac{\mu g}{g\,min}$ over a period of 30 min was used. A maximum stage time per pressure step of 12 h was allowed. A detailed description and explanation of the system is given in Seemann et al. (2017).

3.3.7 Low-pressure nitrogen physisorption

Low-pressure nitrogen physisorption isotherms of dry and moisture equilibrated materials were measured on 0.2 to 0.5 g of bulk material using the manometric instrument *Micromeritics Gemini VII 2390t* (Micromeritics Instrument Corporation, Norcross, GA, USA). Sorption measurements were performed in a cryogenic nitrogen bath (77 K) between $10^{-3} < p/p^0 < 0.995$ at 100 discrete pressure points (adsorption: 64; desorption: 36) and the saturation pressure (p^0) was determined separately for each pressure point. Operational equilibrium was assumed when the pressure drop was below 0.01% of the target pressure over a time period of 20 to 30 s. The differential void volume between the reference cell and sample cell was measured by He expansion at 298 K for the dry material and at 273 K for the moisture equilibrated material, respectively. In order to avoid massive moisture loss for the equilibrated materials the initial evacuation phase was kept to the minimum of 1 min applying an evacuation rate of 133 kPa/min, realised due to the geometrical cross-sections of the tubing inside the apparatus combined with the rotary pump. Evacuation tests by Seemann et al. (2017) and Lahn et al. (2020) on the identical apparatus proved no significant loss

[3]Relative humidity is defined as the ratio of water's partial vapour pressure to the saturation vapour pressure of water at a given temperature provided as percentage. Here, RH is equivalent to partial pressure (p/p^0)

of pre-adsorbed water. This is confirmed by the good reproducibility of the isotherm measurements (section 3.4.5). The moisture content was verified by weighing after each isotherm measurement. Therefore, the samples were dried at 378 K under vacuum ($P \leq 5$ Pa for at least 24 h using a *VacPrep 061* (Micromeritics Instrument Corporation, Norcross, GA, USA). The moisture content and the molar uptake were normalised to the dry sample mass.

3.3.8 Low-pressure argon and carbon dioxide physisorption

Argon (Ar) and carbon dioxide (CO_2) physisorption isotherms were measured exclusively on 0.5 to 0.8 g of dry mudrocks. Bulk materials were dried at 378 K for about 24 h under ultra-low vacuum for the Ar isotherm measurements while drying for the CO_2 measurements was performed at a pressure ≤ 5 Pa for 24 h (*VacPrep 061*).

Ar isotherms were measured on the manometric apparatus *Autosorb-I-MP* (Quantachrome Instruments, Boynton Beach, FL, USA) at 87.3 K using a CryoSync thermostat that regulates the temperature at 87.3 K with a precision of ±0.1 K. The isothermal uptake was determined at 81 and 29 discrete pressure points in ad- and desorption mode between p/p^0 of 10^{-6} and 0.995. Operational equilibrium was assumed at a rate of pressure change $< 16\,\mathrm{Pa\,min^{-1}}$ in combination with a defined tolerance band per pressure point ($p/p^0 < 0.1 : +0.0003\,\& -0.0001$; $p/p^0 \geq 0.1 : +0.009\,\& -0.003$). The saturation pressure of argon was specified manually at 101.325 kPa (normal boiling point of argon at 87.3 K) because of technical reasons.

Isothermal CO_2 uptake was obtained at 21 discrete pressure steps between $10^{-4} < p/p^0 < 0.036$ at 273 K in an ice bath using the *Micromeritics Gemini VII 2390t*. The saturation pressure of CO_2 was measured separately for each pressure step and an operational equilibrium criterion of 0.01% of target pressure drop over a time period of 20 to 30 s was applied.

3.3.9 Textural analysis strategy

Textural properties of dry and moist mudrocks were obtained from Ar, CO_2 and N_2 isotherms via classical physisorption theories. The micropore properties (V_0, E_0) were computed by Dubinin-Astakhov theory (DA) of micropore volume filling (Dubinin & Astakhov, 1971). Medek's approach was used to compute apparent micropore size distributions from Ar physisorption isotherms only (Medek, 1977, Janssen & Van Oorschot, 1989, Prinz & Littke, 2005).

The specific surface area (A_{BET}) was obtained via Brunauer-Emmett-Teller theory (BET) applying Rouquerol plots to objectively constrain fitting intervals (Brunauer et al., 1938, Rouquerol et al., 2007). Specific surface areas are conceived as apparent areas representing the strong retention capacity of the adsorptive in a microporous sorbent (Rouquerol et al., 2007).

Pore size distributions were calculated for the meso- and partially macropore range by Barrett-Joyner-Halenda theory (BJH) (Barrett et al., 1951). Bulk liquid properties of the respective adsorptive were assumed and the Kelvin model was complemented by Harkins & Jura's t-curve accounting for (multi-) layer formation preceding capillary condensation (Harkins & Jura, 1944a). PSDs were acquired from the adsorption branch of Ar and N_2 isotherms between $0.3 < p/p^0 < 0.995$. For the conversion of argon physisorption isotherm to pore size distributions the BJH model was complemented by a statistical thickness model determined by Kruk & Jaroniec (2000) from an argon

isotherm measured on a macroporous LiChrosphere-Si1000 silica ($1.29 \times 10^{-5} < p/p^0 < 0.993$). Cumulative Ar-PSDs (DA + BJH) were merged at the transition of the micro- to mesopore range. In the process V_0 was assigned to the pore radius corresponding to the highest fitting point of the DA-theory. This corresponded to approximately 2 to 2.5 nm. The limiting micropore volume was progressively added to the meso/macropore PSD. A spline function was used to interpolate between experimental data points of N_2-based PSDs to obtain an even point spacing for comparison purposes.[4]

The (total) specific pore volume (V_{GV}) occupied by the adsorbate was determined via Gurvich's rule at $p/p^0 \approx 0.995$ using the bulk liquid density of the respective adsorptive ($\rho(\mathrm{Ar}) = 1.4\,\mathrm{g/mL}$, $\rho(N_2) = 0.808\,\mathrm{g/mL}$) (Gurvich, 1915). Gurvich volumes are reported with the maximum BJH pore size filled at the experimentally attained partial pressure. For better comparison, a common partial pressure was selected for V_{GV} calculation which was limited by the experimental data series of each mudrock.

3.4 Results

3.4.1 Composition of mudrocks

Quantitative X-ray diffraction analysis was combined with Rietveld refinement to obtain the mineralogical composition of the sample set (Figure 3.1; Table 3.1). According to the sedimentological classification scheme of Lazar et al. (2015) all samples are argillaceous mudrocks comprising clay minerals as primary components (0.407 to 0.639 g/g).

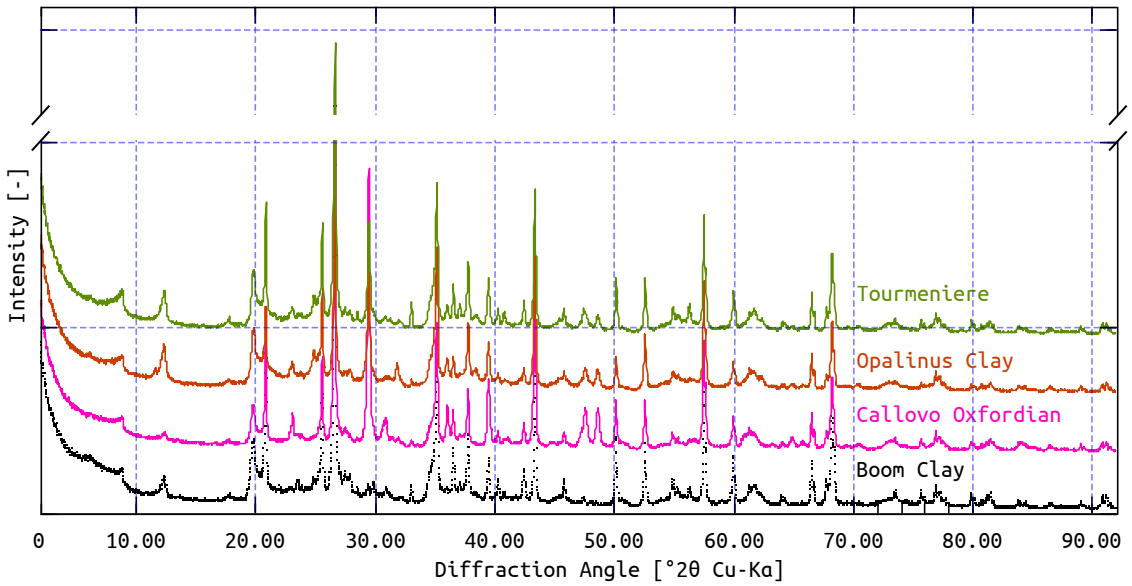

Figure 3.1: X-ray powder diffraction patterns of bulk mudrocks; Boom Clay (black), Callovo Oxfordian argillite (pink), Opalinus Clay (orange), and Tournemire argillite (green).

[4]Experimental and interpolated PSDs were scrutinised for validity.

All samples consisted of kaolinite (0.056 to 0.199 g/g), chlorite (0.013 to 0.054 g/g) and mixed-layer minerals (0.338 to 0.503 g/g). Smectite contents amounted to values between 0.147 g/g and 0.330 g/g while illite+muscovite contents ranged from 0.172 to 0.278 g/g. The sum of illite, muscovite and smectite were reported as mixed-layer minerals because the asymmetry of the 001 reflection (illite/muscovite) in the powder diffraction pattern pointed towards interstratified illite and smectite (Figure 3.1). Furthermore, the bulk analysis does not allow for accurate discrimination between illite and muscovite and the quantification of illite and smectite in mixed-layers is difficult. Quartz contributed between 0.130 to 0.233 g/g while carbonates (calcite, dolomite/ankerite and siderite) represented 0.040 g/g and 0.348 g/g. Minor amounts of pyrite (0.005 g/g and 0.024 g/g) and gypsum (0.008 g/g and 0.011 g/g) were quantified. Gypsum was likely a secondary product of pyrite oxidation during sample storage. K-feldspar dominated over plagioclase and varied from 0.038 to 0.070 g/g and 0 to 0.038 g/g, respectively.

The cation exchange capacity (CEC) represents the amount of exchangeable cations and ranged between 0.06 mmol(+)/g and 0.201 mmol(+)/g (Table 3.1). In accordance with the XRD analysis, the Boom Clay was characterised by the highest CEC while the Tournemire argillite had the lowest CEC. The CEC is typically controlled by the clay minerals and organic matter. However, the organic matter content of the sample set was low and differed between 0.0097 g/g and 0.0119 g/g (Table 3.1).

Table 3.1: Mineralogical composition, cation exchange capacity (CEC), total organic carbon content (TOC) and temperature of maximum hydrocarbon generation rate (T_{max}; maturity indicator). * = semi-quantitative phase quantities; MLM = sum of mixed-layer minerals (smectite + illite + muscovite (=Musc)).

Phase	**Unit**	**Boom Clay**	**Callovo Oxfordian**	**Opalinus Clay**	**Tournemire**
Quartz	[g/g]	0.233	0.191	0.130	0.191
K-feldspar	[g/g]	0.067	0.049	0.038	0.070
Plagioclase	[g/g]	0.038	n.d.	0.018	0.007
Calcite	[g/g]	0.016	0.285	0.111	0.089
Dolomite	[g/g]	0.025	0.058	0.007	0.011
Siderite	[g/g]	n.d.	0.005	0.019	n.d.
Pyrite	[g/g]	0.012	0.005	0.006	0.024
Gypsum	[g/g]	0.008	n.d.	0.011	n.d.
Anatase	[g/g]	n.d.	n.d.	0.021	n.d.
Kaolinite	[g/g]	0.085	0.056	0.199	0.176
Chlorite	[g/g]	0.014	0.013	0.054	0.037
Illite+Musc*	[g/g]	0.172	0.192	0.218	0.278
Smectite*	[g/g]	0.330	0.147	0.168	0.116
MLM	[g/g]	0.502	0.339	0.386	0.394
CEC	[mmol(+)/g]	0.201	0.107	0.118	0.06
TOC	[mg/g]	9.70	9.65	10.75	11.85
Tmax	[K]	688	702	697	707

3.4.2 Dynamic and static water vapour sorption isotherms of mudrocks

Figure 3.2 presents gravimetrically measured water vapour sorption isotherms obtained at 303 K under dynamic (a, DVS) and static (b, SVS) experimental conditions. The water vapour isotherms

were sample-specific in shape and uptake. The saturation pressure was approached asymptotically and the lack of a plateau indicated incomplete pore filling by water at p/p^0 of 0.94 (dynamic) and 0.97 (static). Static water sorption isotherms showed a higher uptake than DVS isotherms. Error bars indicated that the water contents at $p/p^0 = 0.97$ were statistically equivalent, though they were achieved by different conditioning pathways. A pronounced, sample-specific hysteresis characterised the isotherms along the complete partial pressure range narrowing down towards zero p/p^0.

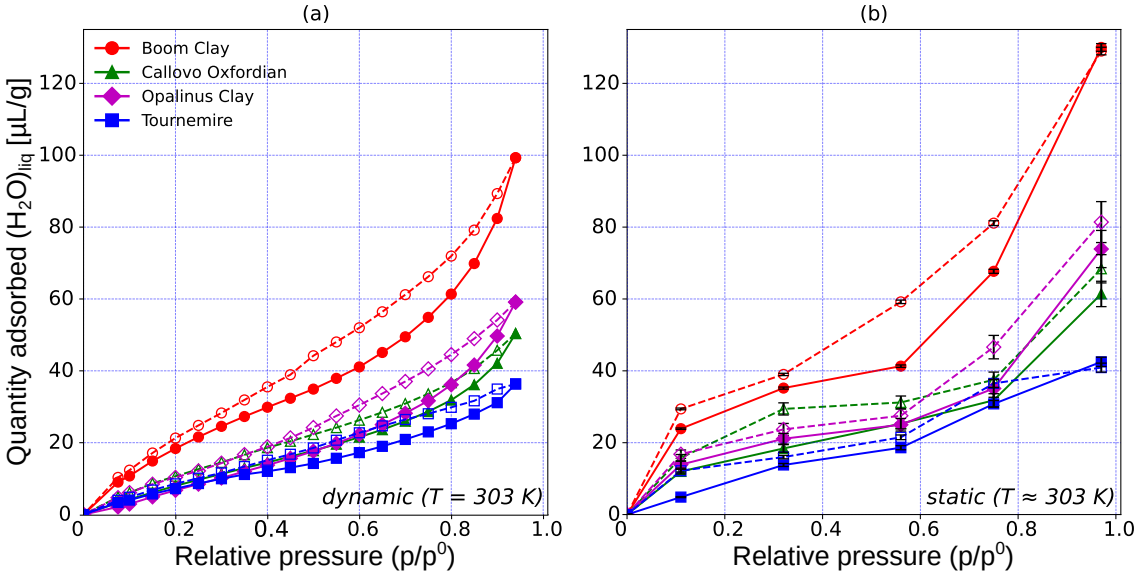

Figure 3.2: (a) Dynamic water vapour sorption isotherms measured at 303 K on dry mudrocks; (b) Static water sorption isotherms determined by weighing of individual subsamples of the respective mudrock. Error bars indicate standard deviations obtained from reproducibility measurements of mudrock subsamples conditioned at 97%RH in desorption mode.

Water vapour sorption isotherms revealed a sinusoidal shape upon adsorption while the desorption branches of Boom Clay, Opalinus Clay and Tournemire argillite exhibited a subtle step in desorption between p/p^0 0.45 and 0.55. A clear upswing was observed above a p/p^0 of 0.7 and 0.8 in DVS isotherms whereas for SVS isotherms the upswing occurred at $p/p^0 > 0.56$. The feature was least pronounced for the Tournemire argillite. The maximum uptake for DVS and SVS isotherms followed the order Boom Clay > Opalinus Clay > Callovo Oxfordian argillite > Tournemire argillite, respectively. Gurvich specific pore volumes were obtained at p/p^0_{max} assuming bulk liquid density of water ($\rho = 1\,\mathrm{g/mL}$). $V_{\mathrm{GV}}(\mathrm{H_2O})$ ranged between 36 µL/g and 99 µL/g (at $p/p^0 = 0.94$) for the DVS isotherms and 43 µL/g and 130 µL/g (at $p/p^0 = 0.97$) for the SVS isotherms.

3.4.3 Nitrogen physisorption isotherms of dry and moist mudrocks

According to the IUPAC classification (Thommes et al., 2015), N_2 isotherms of dry and moist mudrocks were of type IV[5] and characterised by partial pore filling indicated by the missing plateau

[5]The isotherm type was formerly defined as type IIb by Rouquerol et al. (1999) characterised by a type II adsorption branch complemented by a H3 hysteresis loop.

(Figure 3.3). The influence of the presorbed H_2O on the N_2 isotherms was detected along the complete p/p^0 range for both conditioning pathways, but the effect of presorbed water on nitrogen uptake appeared stronger upon desorption conditioning. This agreed with the moisture content of the mudrocks (Table B.2, Table B.3). All isotherms displayed H3 hysteresis loops that were affected by the presorbed water in the form of a continuous reduction in hysteresis width as a function of water content.

The effect of presorbed water was sample-specific; especially its strength of impact at different relative humidity. Generally, the strongest effect occurred at 11%RH independent of the conditioning history and was most obvious in the micropore range ($p/p^0 < 0.2$). At 11%RH the strength of impact follows the order: Tournemire argillite > Boom Clay > Callovo Oxfordian argillite > Opalinus Clay. With increasing relative humidity, the effect of water became continuous for the Boom Clay and Callovo Oxfordian argillite up to 97%RH in desorption conditioning. In adsorption conditioning, those samples revealed a secondary step at the transition from 75 to 97%RH. The Opalinus Clay showed a similar behaviour, albeit steps were present in ad- and desorption conditioning. N_2 isotherms of the Opalinus Clay demonstrated a more continuous decrease for desorption conditioning whereas the steps at 11% and 97%RH were striking in adsorption conditioning. The Tournemire argillite exhibited significant effects of presorbed water at 11% and 32%RH for both conditioning pathways, followed by a continuous decrease in nitrogen uptake up to maximum relative humidity. At 97%RH the reduction in N_2 uptake was lower relative to the other mudrocks.

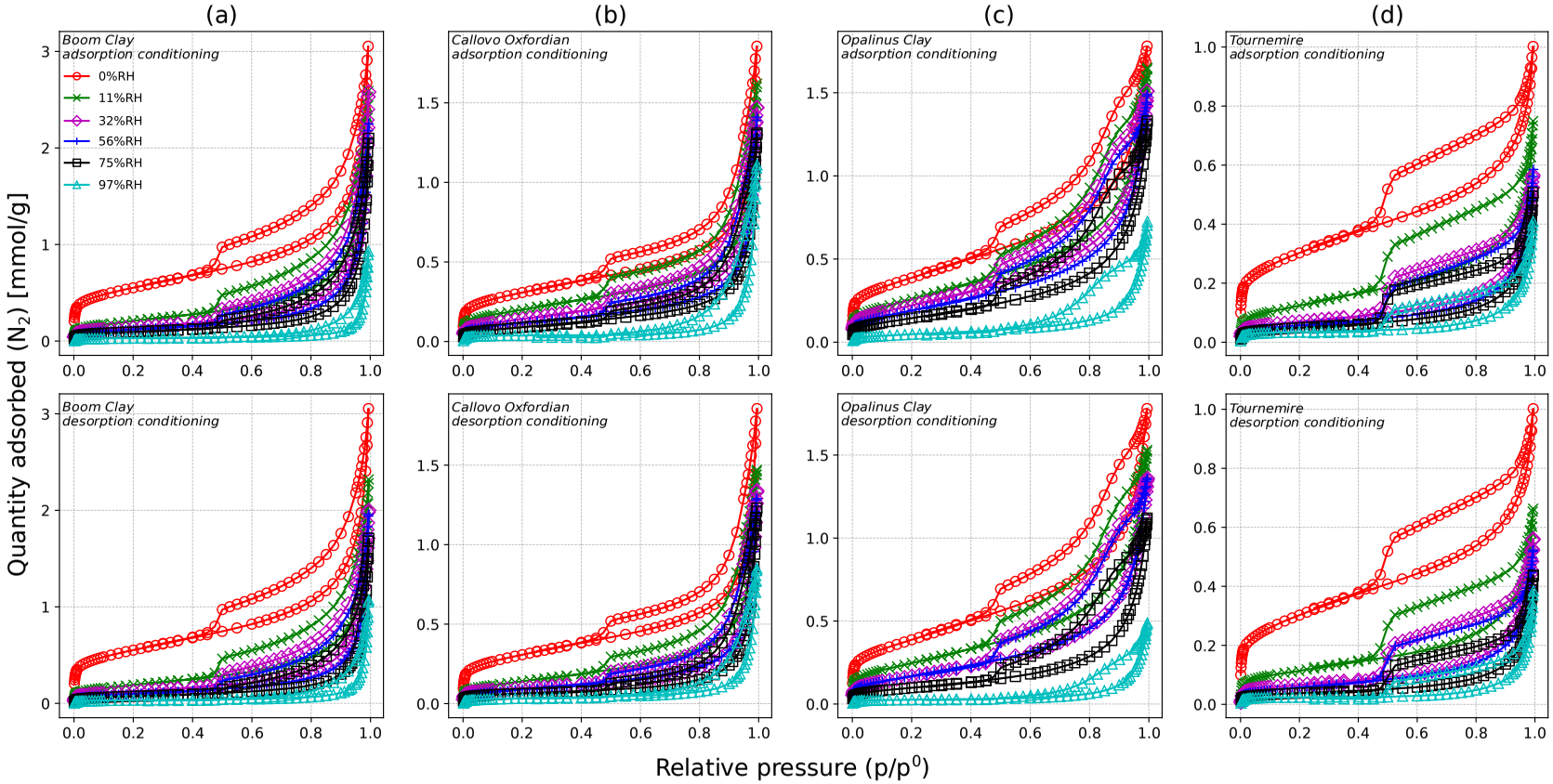

Figure 3.3: N_2 physisorption isotherms measured at 77 K on dry and moist mudrocks in ad- and desorption conditioning: (a) N_2 isotherm collection of Boom Clay; (b) N_2 isotherm collection of Callovo Oxfordian argillite, adsorption (11 to 97%RH) data of COx were taken from Lahn et al. (2020); (c) N_2 isotherm collection of Opalinus Clay, adsorption (11 to 97%RH) data of OCM were taken from Lahn et al. (2020); (d) N_2 isotherm collection of Tournemire argillite.

3.4.4 Secondary results and isotherm evaluation of moist mudrocks

Textural properties of dry and moist mudrocks were obtained from N_2 physisorption isotherms via classical physisorption theories. A detailed overview of the textural parameters and their change as a function of the amount of presorbed water is provided in Table B.2 and Table B.3 in section B.2 in the appendix. Ar and CO_2 physisorption isotherms served as references for textural parameters (V_0, A_{BET}, V_{GV}), and the results are reported in section B.1 Table B.1 in the appendix.

Microporosity of moist mudrocks

The N_2 accessible micropore volume of moisture equilibrated mudrocks reduced as a function of the sample-specific presorbed water content (Figure 3.4). $V_0(N_2)$ was generally lower in desorption than in adsorption moisture conditioning, and when plotted as a function of relative humidity a hysteresis was observed (not shown). The reduction of N_2 micropore volume as a function of increasing water content resembled a hyperbolic decay curve. Here, hysteresis was negligible but the effect of absolute water content — independent of the moisture conditioning history — was obvious. The strongest losses of 40 to 70% of $V_0(N_2)$ were observed at the first equilibration stage at 11%RH for all samples and for both conditioning pathways. The minimum N_2-accessible micropore volume was attained at 97%RH at which ≈ 86 to 95% of the initial micropore volume was inaccessible to nitrogen for adsorption conditioning and 90 to 95% for desorption conditioning. The characteristic energies decreased only slightly without apparent systematic differences (section B.2 Table B.2 and Table B.3 in the appendix).

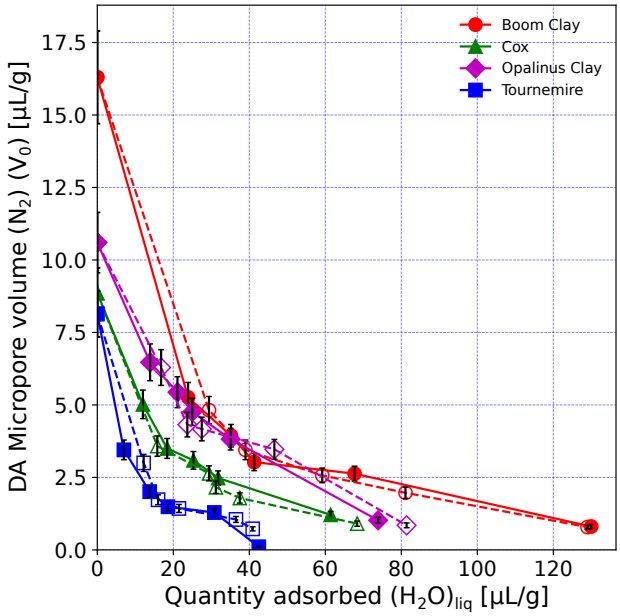

Figure 3.4: DA micropore pore volumes (V_0) calculated from N_2 physisorption isotherms measured on moisture conditioned mudrocks (ad-, desorption) plotted as a function of gravimetric water uptake. Closed symbols represent adsorption conditioning and open symbols refer to desorption conditioning. Connecting lines serve as guides to the eye. Error bars represent 95% confidence intervals calculated based on the relative standard deviations obtained from repetition measurements performed for the Opalinus Clay (97%RH desorption conditioning).

Specific surface area of moist mudrocks

BET specific surface areas decreased similarly to the DA micropore volumes as a function of water content revealing a hyperbolic drop with little to no hysteresis (Figure 3.5).[6] At 11%RH the reduction in A_{BET} was the strongest, followed by a monotonous decrease as a function of water content for the complete sample set. At 97%RH the BET specific surface areas fell below $\approx 10\%$ of their original (dry) values for both conditioning histories.

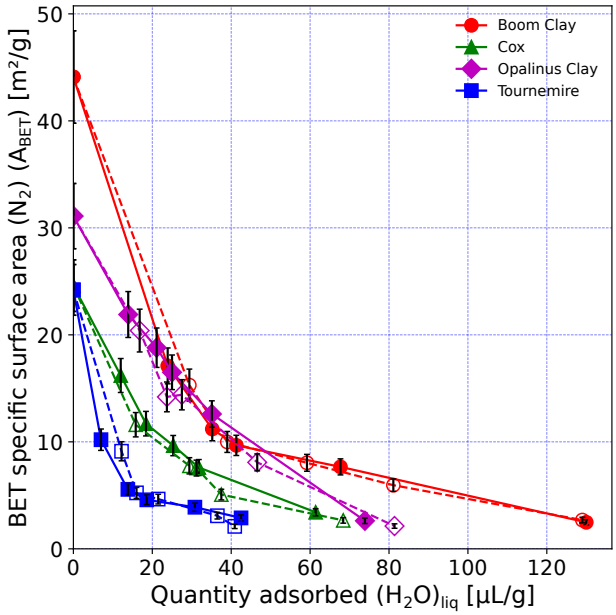

Figure 3.5: BET specific surface areas (A_{BET}) calculated from N_2 physisorption isotherms measured on moisture conditioned mudrocks (ad-, desorption) plotted as a function of gravimetric water uptake. Rouquerol plots were employed to constrain fitting intervals (Rouquerol et al., 2007). Closed symbols represent adsorption conditioning and open symbols refer to desorption conditioning. Connecting lines serve as guides to the eye. Error bars represent 95% confidence intervals calculated based on the relative standard deviations obtained from repetition measurements performed for the Opalinus Clay (97%RH desorption conditioning).

Total specific pore volume of moist mudrocks

The decrease in Gurvich specific pore volumes matched with the initial isotherm description. For both conditioning histories an approximately linear relationship between V_{GV} vs. $Q_{\mathrm{H_2O}}$ was observed for the Boom Clay, the Callovo Oxfordian argillite and the Opalinus Clay (Figure 3.6). A higher loss in V_{GV} was detected for the desorption-conditioned samples except for the Gurvich specific pore volumes of the Boom Clay at 97%RH. Boom Clay and Opalinus Clay revealed the highest drop between 75% and 97%RH resulting in 27 to 35% of the originally available pore space in desorption conditioning. The accessible pore space was slightly larger in adsorption conditioning for these samples varying between 30% and 34%. The Callovo Oxfordian argillite was characterised by a continuous loss in Gurvich specific pore volume along the relative humidity range for both

[6] The A_{BET}s, plotted as a function of relative humidity, exhibited the previously observed hysteresis between adsorption and desorption conditioning, which was sample-specific.

conditioning histories. Contrastingly, the Tournemire argillite lost most pore volume upon initial equilibration at 11%RH followed by a hyperbolic decrease up to the maximum water content reached at 97%RH.

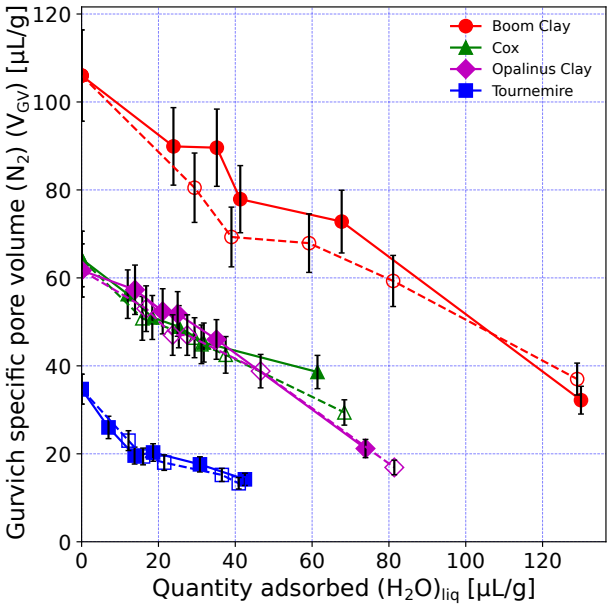

Figure 3.6: Gurvich (total) specific pore volumes (V_{GV}) calculated from N_2 physisorption isotherms measured on moisture conditioned mudrocks (ad-, desorption) plotted as a function of gravimetric water uptake. V_{GV} were obtained at maximum experimental partial pressure ($p/p^0 \approx 0.995$). Closed symbols represent adsorption conditioning and open symbols refer to desorption conditioning. Connecting lines serve as guides to the eye. Error bars represent 95% confidence intervals calculated based on the relative standard deviations obtained from repetition measurements performed for the Opalinus Clay (97%RH desorption conditioning).

Pore size distributions of moist mudrocks

Affected pore sizes and their pore volume losses were determined with respect to the reference curves of dry mudrocks (Figure 3.3). Generally, the strength of pore volume loss and its corresponding relative humidity was sample-specific and followed the earlier described isotherm trends concerning the featured steps at 11% and 97%RH. In accordance with the larger amounts of presorbed water, the loss in N_2-accessible pore volume was higher for desorption than for adsorption conditioning. Independent of the conditioning history, presorbed water caused pore volume losses primarily below 20 nm for the complete sample set and curve shapes were convex from 11%RH equilibration on in the given pore size range. The inflexion point shifted towards larger pores with increasing relative humidity. The samples conditioned via desorption indicated a stronger divergence in PSDs with respect to the reference curve from which an effect of presorbed water was detectable up to 100 nm, except for the Tournemire argillite that became parallel for all conditioning histories above 20 nm. The cumulative PSDs of the Callovo Oxfordian argillite and the Opalinus Clay were almost identical at 32% and 56%RH equilibration whereas the PSDs of the Boom Clay and the Tournemire argillite

distinguished themselves slightly at 32% and 56%RH.

To objectively constrain complete pore filling an occupation criterion was defined based on the limit of quantification (LOQ) of nitrogen uptake. The LOQ ($LOQ = 3.3 \times LOD$) was calculated based on the limit of detection (LOD), provided by Micromeritics Instrument Corporation as 4×10^{-3} µL/g. Complete pore filling was assumed when the nitrogen uptake reached at least ten times the LOQ ($Q(N_2) \geq 10 \times LOQ$). Notably, up to 75%RH, pore volume loss concentrated within smaller mesopores for both conditioning histories ($W \leq 5$ nm) and remained incomplete. At 75%RH and 5 nm pore size, the nitrogen accessibility reduced between 55 to 98%. The N_2 accessible pore volume for the given tuple (relative humidity and pore size pair) follows the order Boom Clay (4% and 2%)[7] < Tournemire (12% and 8%) < Callovo Oxfordian (20% and 4%) < Opalinus Clay (45% and 21%). On an absolute scale, the accessible pore volumes corresponded to a minimum of 0.3 µL/g and a maximum of 6 µL/g. The lower bound of 0.3 µL/g was still more than twice as high as the defined threshold for pore filling.

The strongest influence of presorbed water was observed at 97%RH, where the Boom Clay exhibited a maximum water-filled pore size (W_{max}) of 8 nm. In contrast, the Tournemire argillite revealed the smallest W_{max}, measuring 4.25 nm. The maximum occupied pore size of water was found to be primarily sample-specific. With respect to the conditioning history, W_{max} showed no consistent trend;[8] however, a maximum difference between W_{max}(ads) and W_{max}(des) of 1.75 nm was observed for the Tournemire argillite. For the remaining samples, the difference in W_{max} was comparable to the molecular size of nitrogen and was therefore considered negligible.

[7] The first percentage refers to adsorption conditioning and the second percentage to desorption conditioning.
[8] This refers to W_{max}(ads) vs. W_{max}(des)

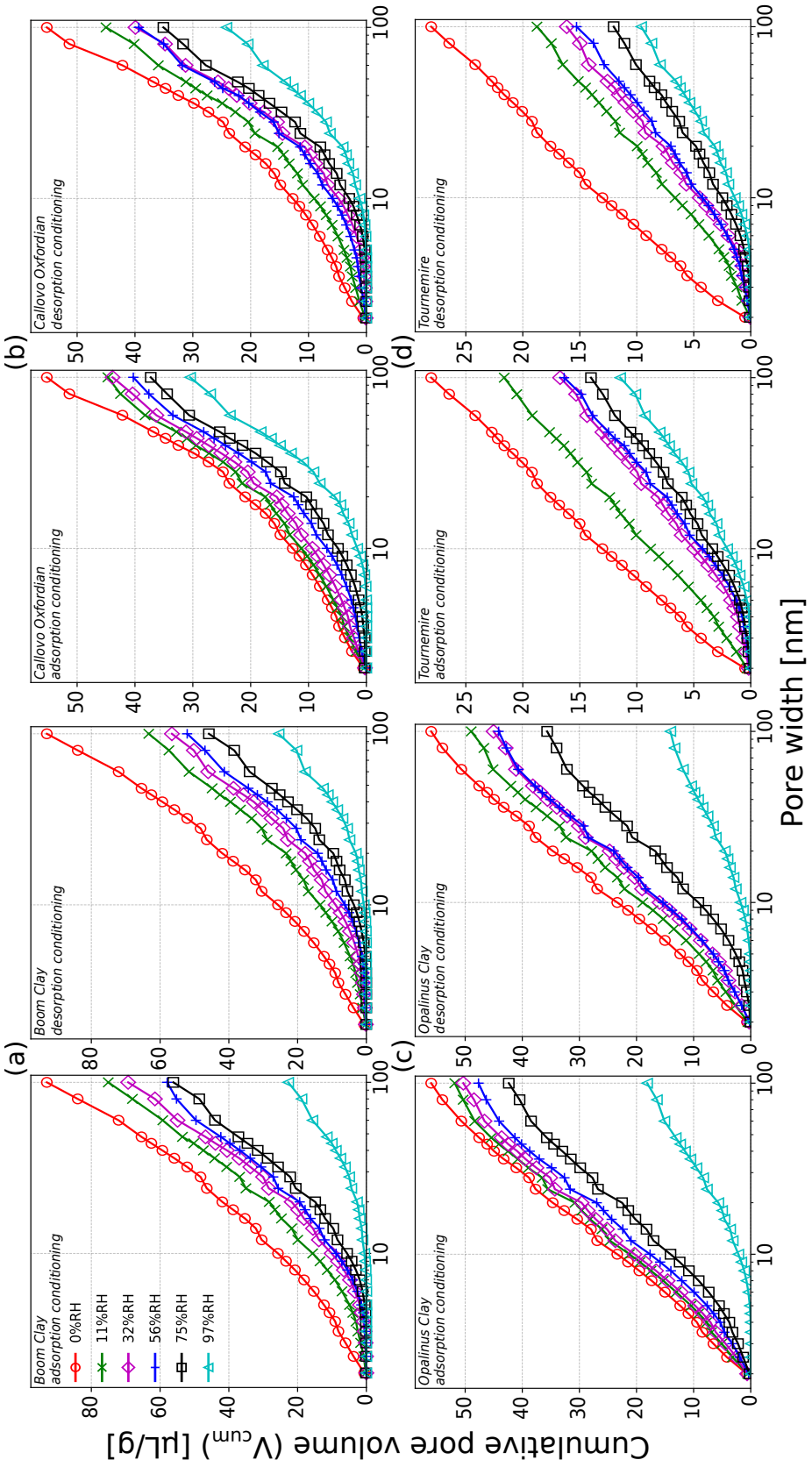

Figure 3.7: Cumulative pore size distributions (BJH) obtained from the adsorption branch of N_2 physisorption isotherms (77 K) measured on dry (reference curve) and moist mudrocks obtained from ad- and desorption conditioning; (a) PSDs of Boom Clay; (b) PSDs of Callovo Oxfordian argillite; (c) PSDs of Opalinus Clay; (d) PSDs of Tournemire argillite.

Cavitation volumes

Cavitation volumes ($V_c = Q_{N_2}(p/p^0 = 0.5) - Q_{N_2}(p/p^0 = 0.4)$) were obtained from the desorption branch of dry and moisture conditioned mudrocks (Figure 3.8). The cavitation volumes of the dry mudrocks ranged from 9.9 to 4.8 µL/g and served for normalisation of cavitation volumes. Even though, hysteresis loop shapes displayed only minor changes below 97%RH equilibration, the cavitation volumes reduced considerably as a function of relative humidity. The reduction in V_c was mudrock-specific, and up to 56%RH the difference between the conditioning histories was minor, except for the Callovo Oxfordian argillite (Figure 3.8b). The strongest loss in cavitation volume was detected between 75% and 97%RH for Boom Clay, Callovo Oxfordian argillite and Opalinus Clay. The final cavitation volumes at 97%RH were equivalent to 0.2 µL/g and 0.3 µL/g (ads, des) for Boom Clay, 0.7 µL/g and 0.4 µL/g (ads, des) for Callovo Oxfordian argillite, and 0.8 µL/g and 0.4 µL/g (ads, des) for Opalinus Clay. The alteration of the hysteresis loop shape and V_c was the lowest for the Tournemire argillite ending at 1.7 µL/g (adsorption) and 1.1 µL/g (desorption) at 97%RH.

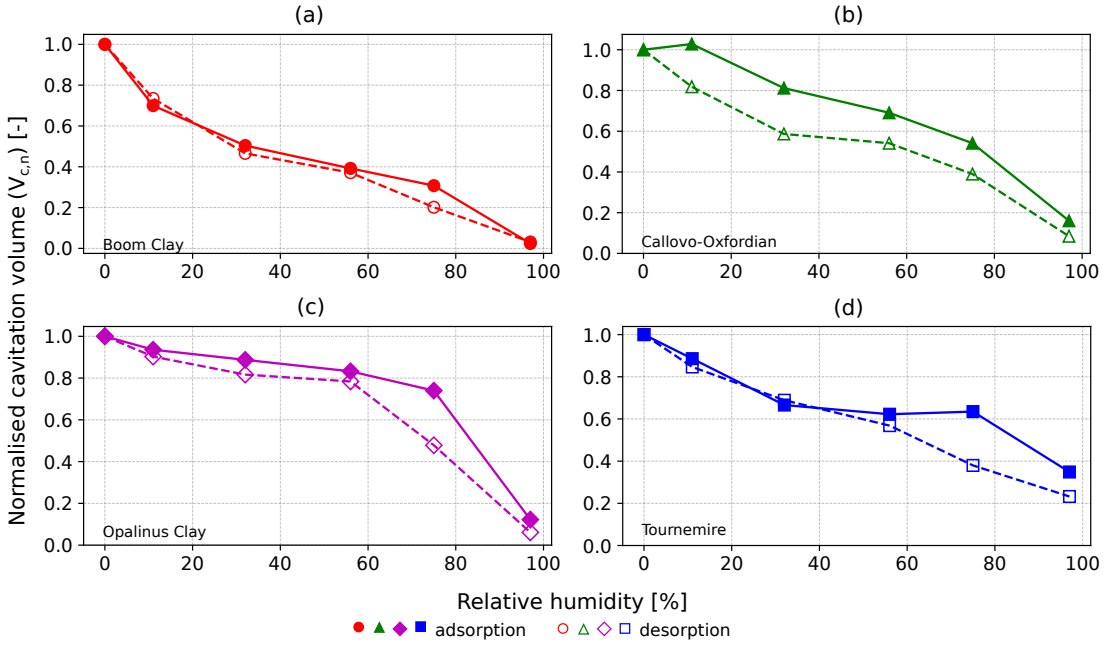

Figure 3.8: Normalised cavitation volume ($V_{c,n}$) at hysteresis loop closure of moisture conditioned mudrocks in ad- and desorption mode plotted as a function of relative humidity. The cavitation volume was converted to fluid volume by assuming the bulk liquid density of nitrogen ($\rho = 0.808$ g/mL) at 77 K and normalised to the cavitation volume of the dry mudrocks. Closed symbols represent adsorption conditioning and open symbols indicate desorption conditions. Connecting lines serve as guides to the eye.

3.4.5 Reproducibility

Reproducibility of N_2 physisorption measurements was tested by repetition on at least 5 individually prepared subsamples of the SiAl reference material of Micromeritics, the dry mudrocks, and the Opalinus Clay subsamples conditioned at 56%RH (adsorption) and 97%RH (desorption),

respectively. Data of the Opalinus Clay samples equilibrated at 56%RH (adsorption) and in dry conditions come from the reproducibility experiments of Lahn et al. (2020). The data set was newly analysed and extended for this study.

Figure 3.9 displays the mean N_2 physisorption isotherm and mean BJH PSD of the Opalinus Clay (97%RH desorption) including standard deviations as error bars ($\pm 1\sigma$). Coefficients of variation ($CV = \sigma_i / \bar{X}_i * 100$) revealed fair dispersion yielding maximum CVs of ±9.3% (micro-), ±16.8% (meso-) and ±4.7%(macropore), respectively.[9]

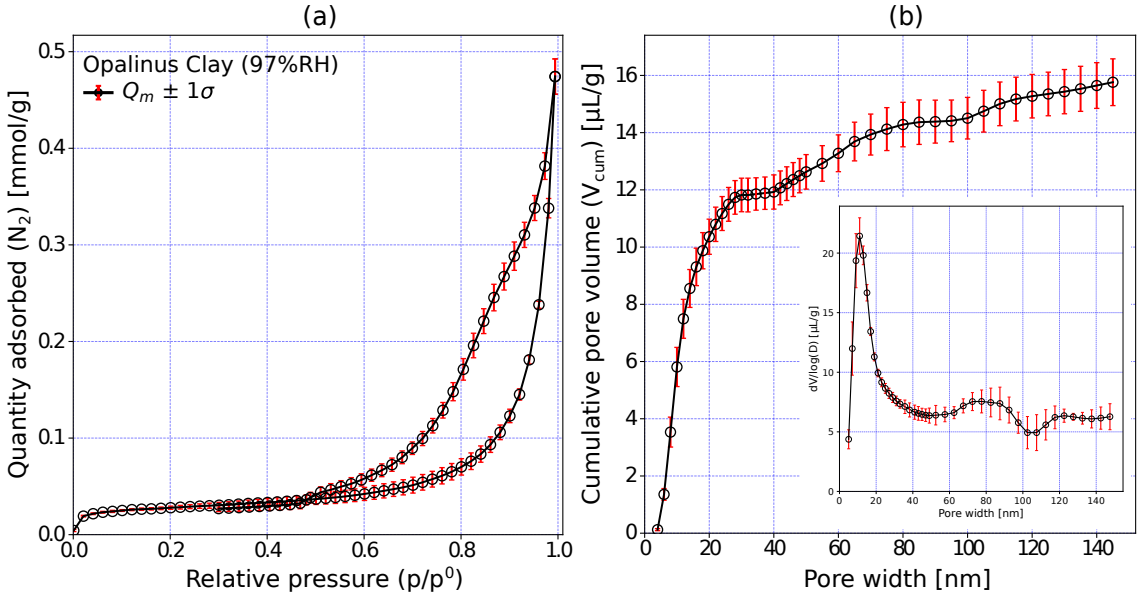

Figure 3.9: (a) N_2 physisorption isotherm determined from 5 repetitions measured on subsamples of the Opalinus Clay equilibrated at 97%RH along the desorption pathway; (b) Corresponding BJH PSD calculated from 5 repetitive N_2 physisorption isotherms. Error bars indicate one standard deviation in (a) and (b).

Figure 3.10a to c illustrates DA micropore volumes, BET specific surface areas and Gurvich (total) specific pore volumes of the given samples reported together with their coefficient of variation. Data indicated an increase of dispersion inversely to sorption capacity. The maximum uncertainty was attributed to the lowest sorption capacity and the highest water content. The SiAl-Standard had the lowest CV values for each category while its parameter values were at least ten-fold those of the mudrocks. The Opalinus Clay subsample conditioned at 97%RH (desorption) demonstrated the maximum encountered uncertainty in this study. It ranged between 5.1% and 5.3% (A_{BET} and V_{GV} at equal $W = 292\,\mathrm{nm}$) (Figure 3.10)[10]. The CV of the gravimetric water content calculated from the subsamples of the Opalinus Clay (97%RH, desorption) amounted to 5.8% (= 4.4 mg/g). CVs of dry mudrocks were sample specific and ranged from 0.5 to 2.9% (Figure 3.10d). The textural parameters of the Tournemire argillite revealed the lowest CVs slightly below 1%, while for the other mudrocks coefficients of variation were below 3%.

[9] $\bar{X}_i$ represents the mean value of the parameter of interest.

[10] The CVs of the Gurvich volumes were determined at an equal pore size which was not necessarily the maximum pore size of all measurements.

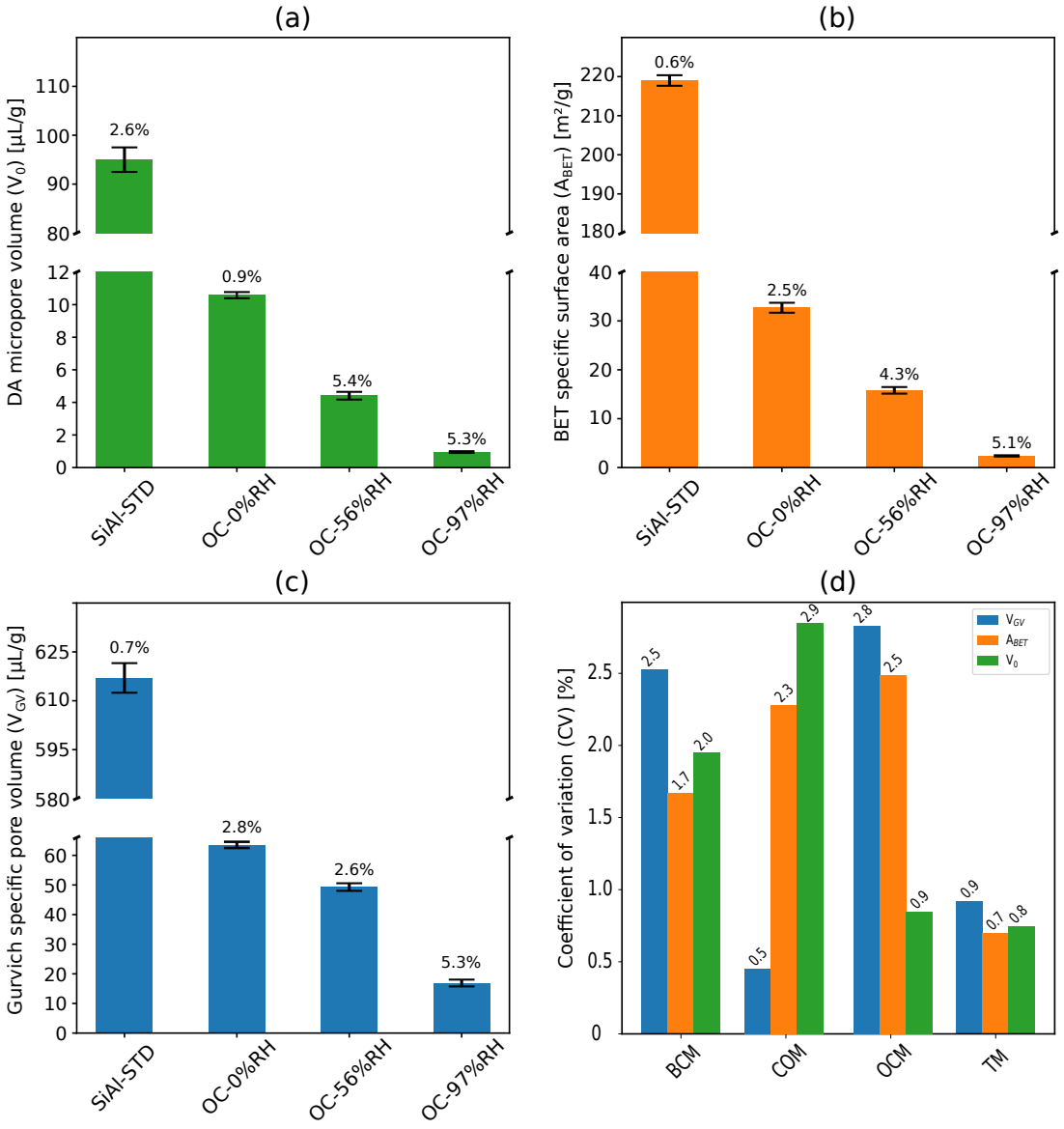

Figure 3.10: (a - c) V_0, A_{BET} and V_{GV} of SiAl reference material, Opalinus Clay in dry (0%RH) and moist conditions (56%RH adsorption; 97%RH desorption); Error bars indicate coefficients of variations computed from at least 5 reproducibility tests; (d) Coefficients of variation of Gurvich specific pore volume (V_{GV}), BET area (A_{BET}) and DA micropore volume (V_0) calculated from reproducibility measurements of N_2 physisorption isotherms of dry mudrocks.

3.5 Discussion

3.5.1 Reproducibility of physisorption measurements on moist mudrocks

Before discussing the mechanisms governing the water distribution as a function of moisture conditioning history, the uncertainty of the experimental approach was evaluated through reproducibility measurements on dry and moist mudrocks, which were complemented by measurements on a standard material (SiAl pellets). Uncertainty of physisorption measurements can be associated with the following factors (not exhaustive): (i) instrumentation uncertainty (limit of detection, limit of quantification, pressure transducer inaccuracy, gas purity), (ii) material-related uncertainty of the pore space (textural and compositional heterogeneity, surface chemistry, particle/aggregate size and mineral fractionation), (iii) human error (sampling, sample loading, weighing, balance error, error in data analysis) and (iv) any uncertainty related to moisture equilibration (temperature, saturation pressure, water loss during preparation, swelling of expandable clays, water expansion due to freezing, false dead volume by helium entrapment). For the presented approach uncertainty factor (iv) has most likely the severest effect on the physisorption measurements, but coefficients of variation were modest for dry as well as moisture-conditioned samples, even at high water contents.

In fact, CV values of dry mudrocks were consistently below 3%, indicating a low and consistent degree of pore network heterogeneity across the sample set (Figure 3.10d), supporting the assumption that the samples can be treated as equivalent with respect to sorption heterogeneity. The CVs of textural parameters obtained for the moist Opalinus Clay (97%RH desorption) were 5.1 to 5.3%, corresponding to absolute values below 0.05 µL/g (V_0), 1 µL/g (V_{GV}) and 0.12 m^2/g (A_{BET}). Spot testing of the remaining mudrocks confirmed the uncertainties previously identified for Opalinus Clay, as the CV values for individual mudrocks (97% RH desorption) were in good agreement. The maximum difference in CV was 4.1%, with CV_{GV}(BCM) = 1.2% and CV_{GV}(OCM) = 5.3%. But on an absolute scale, CVs of the samples were in the same order of magnitude and nearly identical. Based on these findings, it is reasonable to assume that the uncertainty-transfer approach used in this study is valid and may even be considered conservative, though some uncertainty remains.

Coefficients of variation of the specific water content (97%RH) were between 0.8% and 6.5% which related to absolute amounts of 1 to 4 µL/g. The acceptable CVs indicate a reproducible conditioning process and consistent isotherm measurements across the sample set. Consequently, substantial mineralogical fractionation, such as clay mineral enrichment, appeared unlikely, and the samples were considered representative. This was further supported by the fact that individual subsamples were always taken simultaneously from the bulk material and conditioned separately.

The employed experimental approach has been applied by several researchers (Prinz & Littke, 2005, Li et al., 2015a, Feng et al., 2018, Lahn et al., 2020), yet reproducibility data are seldom reported. Lahn et al. (2020) reported coefficients of variation ranging from 2.6% to 5.4% for moisturised Opalinus Clay (56%RH adsorption). Additionally, repeated wetting and drying tests of Lahn et al. (2020) followed by physisorption measurements confirmed that no permanent damage was enforced on the mudrocks' pore network which is regarded as premises for an unambiguous comparison of conditioned mudrocks. The data of the presented study and those of Lahn et al. (2020) agree well with each other as well as with the reproducibility descriptors of Jaroniec et al.

(1999). Jaroniec et al. (1999) reported coefficients of variation below ≈ 5% for $10^{-5} < p/p^0 < 0.1$ and up to 10% for partial pressures above 0.1 (dry materials). The literature data align closely with the reproducibility data for the Opalinus Clay conditioned at 97% RH, although they are less consistent than those for dry mudrocks. The reproducibility is further supported by the studies of Kuila & Prasad (2013) and Klobes et al. (2006). Kuila & Prasad (2013) reported average relative variations of 10.5% for BET specific surface areas and 7.2% for Gurvich specific pore volumes whereas Klobes et al. (2006) obtained coefficients of variation of 9.2% and 6.4% for A_{BET} and V_{GV} based on round-robin tests (25 laboratories).

Consequently, the N_2 physisorption measurements on dry and moist mudrocks are considered reproducible and therefore acceptable for a comparison of textural parameters of differently conditioned mudrocks.

3.5.2 Controls on water sorption

Previous studies pointed out the role of clay minerals, organic matter and texture in the process of water sorption in mudrocks (Sang et al., 2019, 2020a, Liu & Yu, 2022, Xie et al., 2023). Yet, observations are often ambiguous and inconsistent.

Figure 3.11 displays the cross-correlation matrix of compositional and textural parameters versus water uptake. The strongest linear correlations were identified for thermal maturity (T_{max}), smectite- and illite content, cation exchange capacity (CEC), micropore volume (V_0), BET specific surface area (A_{BET}) and Gurvich specific pore volume (V_{GV}) with respect to water uptake ($Q_{\mathrm{H_2O}}$).

T_{max} is a thermal maturity index and T_{max} vs. $Q_{\mathrm{H_2O}}$ showed a strongly negative linear correlation (r = −0.88 to −0.99). Such negative correlation was also observed for illite content vs. $Q_{\mathrm{H_2O}}$ (r = −0.65 to −0.95). To the contrary, smectite content and CEC revealed positive correlations (Sm: r = 0.89 to 1.0; CEC: r = 0.93 to 1.0) with water uptake, similar to textural parameters. The sub-matrix *composition + texture* indicated several cross-correlations, the strongest associated with T_{max}, smectite-, illite content and CEC. The T_{max} vs. illite content as well as smectite content vs. CEC correlated strongly positively. At the same time, smectite content and CEC covaried negatively with T_{max} and illite content, respectively. Extending the sub-matrix with textural parameters pointed towards further cross-correlations of V_0, A_{BET} and V_{GV} with T_{max} (strongly negative; r = −0.95 to −0.99) whereas smectite content and CEC showed positive linear correlations with these texture parameters (r = 0.97 to 1.0), respectively. Accordingly, all seven parameters revealed primary correlations with water uptake.

Mechanistically the covariation of T_{max}, smectite-, illite content, CEC and texture (V_0, A_{BET}, V_{GV}) may be explained by diagenetic processes initiated by burial; prerequisite: the necessary geochemical conditions need to be met. Smectite can be considered as a precursor for illite formation in sedimentary rocks. Upon burial and diagenesis, thermal maturation can effect clay mineral transformation like the continuous conversion of smectite to illite via intermediate mixed-layer stages (Środoń, 2003a,b). Such a mineral transformation is coupled with a reduction in the effective CEC of the rock since smectite is often a major donor of exchangeable cations and has a higher CEC relative to illite and other relevant clay minerals in mudrocks (Bergaya et al., 2006). The principal role of smectite in cation exchange for the studied mudrocks is confirmed by linear regression

analysis. Smectite content can explain ≈ 97% of the variation in CEC (Figure 3.13a). Besides, smectites, mixed-layer illite-smectite and illite are the principal hosts for micro- and mesoporosity (Michot, 2018) which control micropore volume, specific surface area and constitute major shares to the total specific pore volume of the investigated mudrocks. This is supported by the strong linear correlation of smectite content with V_0, and A_{BET}, respectively (section B.5 Figure B.3 in the appendix). Linear regression analysis establishes that above 98% of the variation in micropore volume and specific surface area is covered by smectite content.[11] Consequently, the correlation matrix and the control on water sorption can be reduced to a single constitutive factor in the form of smectite (content) because of its fundamental and mechanistic relation to T_{max}, CEC and texture of the studied mudrocks.

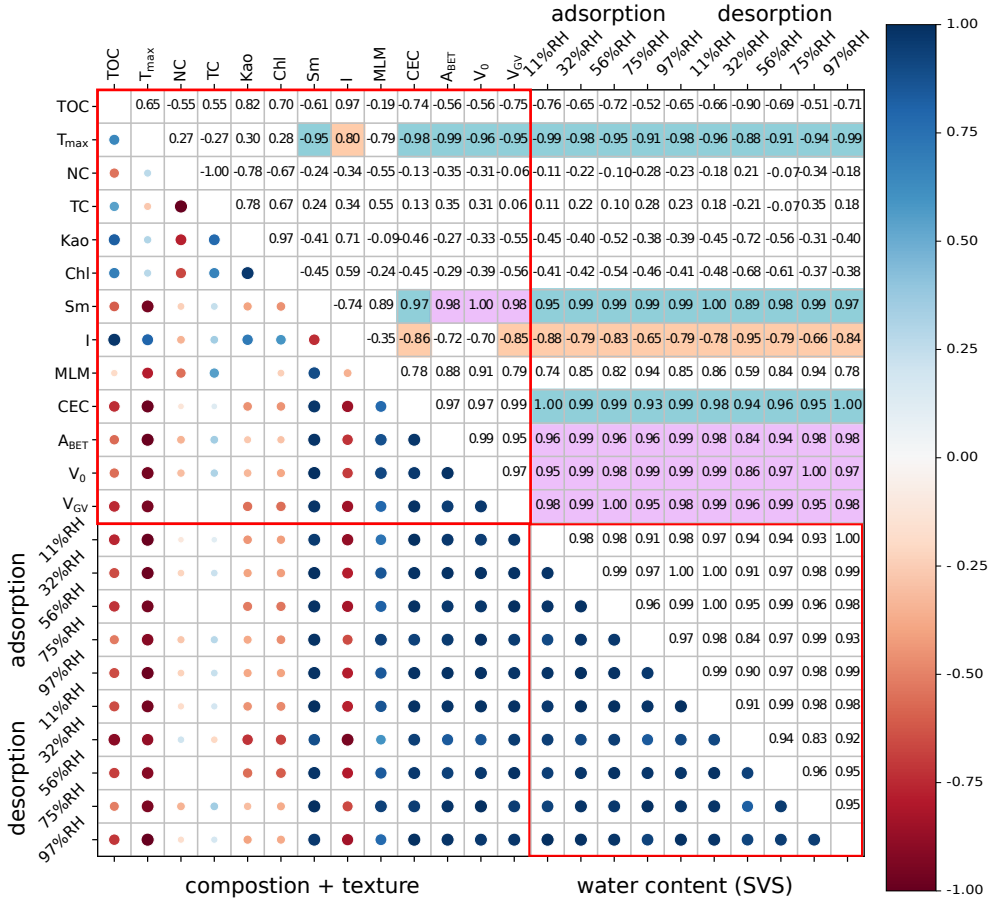

Figure 3.11: Correlation matrix of compositional and textural parameters vs. static water uptake as a function of relative humidity. Sub-matrices are highlighted for composition + texture and static water uptake (SVS) (red squares). The strongest correlations are indicated by blue and peach shades. Numerical values in the upper triangle indicate the correlation coefficients (r) of parameter pairs. Circles (lower triangle) visualise the strength of correlation by circle size and colour (colour bar on the right). Nc = sum of non-clay minerals, TC = sum of clay minerals, Kao = kaolinite quantity, Chl = chlorite quantity, Sm = smectite quantity, I = sum of illite and muscovite quantities, MLM = sum of illite, muscovite and smectite quantities, CEC = cation exchange capacity, A_{BET} = BET specific surface area, V_0 = DA micropore volume, V_{GV} = Gurvich (total) specific pore volume.

[11] A_{BET} and V_0 covary as microporosity is a principal contributor to specific surface area for microporous sorbents (Rouquerol et al., 2007, Ziemiański et al., 2020).

3.5.3 Compositional and textural influence on water sorption

In the following, the relationship between water vapour uptake and composition (organic matter content, clay content and type), and compositional properties (T_{max}, CEC) will be discussed of which an overview is provided in Figure 3.12. Furthermore, an attempt is made to discern controls for ad- and desorption conditioning, but the reader is advised that, due to the small sample number (n=4), generalisations are avoided and conclusions drawn only apply to the studied mudrocks. Moreover, multicomponent linear regressions are not dealt with since no substantial improvement of correlations was observed for any combination of parameters and water uptake.

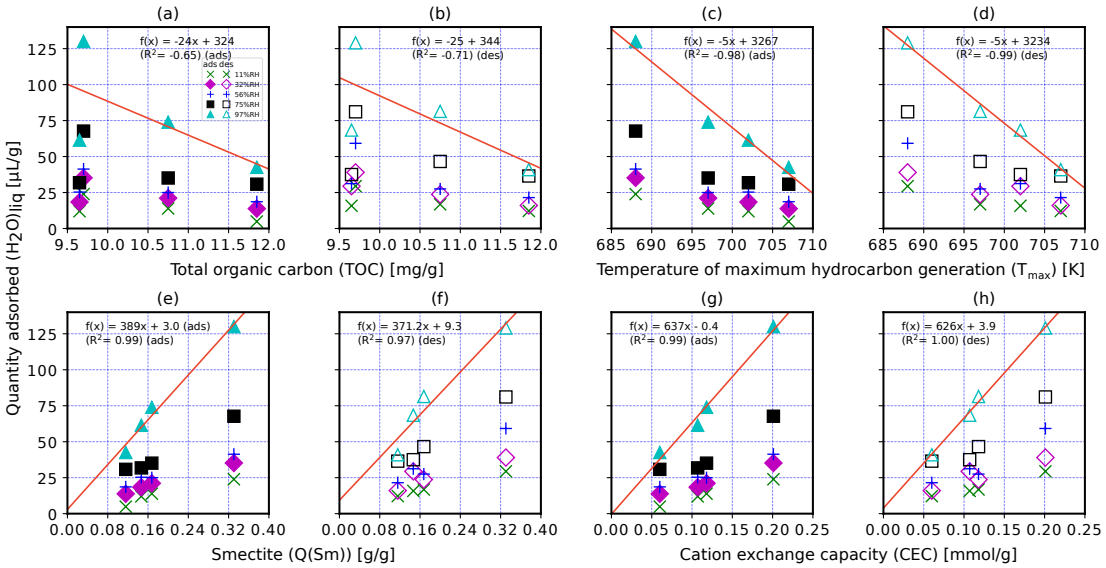

Figure 3.12: Overview of compositional parameters (TOC, T_{max}, smectite content, CEC) plotted against water uptake as a function of relative humidity (11 to 97%RH) in ad- and desorption conditioning. Red lines represent linear regression lines of numerical fits of water uptake at 97%RH. The remaining correlation lines are omitted for reasons of visual clearance.

Organic matter The role of organic matter (OM) is a subject of controversy regarding water vapour sorption in mudrocks. Attempted generalisations of the influence of OM on water sorption failed so far because of a lack of consistent data emphasising the complexity of the matter. Recently, Xie et al. (2023) addressed this controversy, highlighting both positive and negative correlations, as well as the lack of correlation, between water sorption and TOC. Xie et al. (2023) reported a weak positive relationship between total water uptake (95%RH) and TOC, similar to the correlation they observed between total clay content and total water uptake.

The studied mudrocks exhibited a weak negative trend between TOC and Q_{H_2O} for both conditioning histories, although the amounts of OM were limited to $< 0.012\,g/g$ (Figure 3.11, Figure 3.12a, b).[12] Similarly weak trends were published by Yang et al. (2020a), Ma et al. (2020) and Li et al. (2021), though these studies were performed on thermally overmatured mudrocks

[12]Notably, the effect of the small sample number was especially strong in the linear regression analysis because of the strong scatter.

(Longmaxii, Wufeng, lower Permian Shanxi-Taiyuan mudrocks). Initially, the negative trend suggests an increased level of hydrophobicity of the water-accessible pore space with rising TOC implying a ceasing number of surface functional groups acting as primary sorption sites of water in carbonaceous materials (Dubinin et al., 1955, Kaneko et al., 1999, Horikawa et al., 2017). However, the above does not a priori denote a causal relationship of TOC and water uptake because of the great variety of type- and surface chemistry of organic matter, both influencing water sorption (Chalmers & Bustin, 2008).

Thermal maturity The role of surface functional groups in the water sorption process has been proven and is underlined by the robust negative linear correlation of $T_{\max}$ vs. Q_{H_2O} (Thommes et al. (2012), Figure 3.11, Figure 3.12c,d). $T_{\max}$ is a thermal maturity index parameter according to which the investigated mudrocks were immature (BCM < OCM < COx < TM) (Table 3.1, Peters & Cassa (1994)). Increasing thermal maturity is associated with the loss of surface functional groups (e.g. dehydroxylation, decarboxylation) and potential (clay) mineral transformation as a direct result of the increased temperature and diagenesis during burial. As a result, an increase in hydrophobicity can be expected and was confirmed by the negative correlations of $T_{\max}$ and Q_{H_2O} (Figure 3.11, Figure 3.12c,d). This negative effect of $T_{\max}$ aligns with the observation of Li et al. (2021) or Chalmers & Bustin (2008) substantiating the role of thermal maturity in the context of water uptake, which is, however, independent of the presence of organic matter.

Clay minerals and cation exchange capacity Recently, Arthur et al. (2015), Woodruff & Revil (2011) and Ferrage (2016) revisited the role of clay minerals, CEC and fundamental processes of clay-water interaction. Clay's pivotal role in water sorption in mudrocks has been addressed by several researchers on a qualitative level (e.g., Sang et al., 2019, Chen et al., 2021). Yet, few authors (e.g., Newman, 1983, Woodruff & Revil, 2011, Dazas et al., 2013, Arthur et al., 2018, Lahn et al., 2020) attempted to quantify parameter-uptake relationships, the underlying principals and controlling factors. In contrast to the works of Seemann et al. (2017), Chen et al. (2021) or Xie et al. (2023), the total clay content (TC) in this study did not reveal a systematic relationship with water uptake (Figure 3.11). The lack of correlation (TC vs. Q_{H_2O}) coincides with the findings of Chalmers & Bustin (2008), Li et al. (2021) or Yang et al. (2020a) underlining the difficulty to generalise water uptake to bulk clay content without specifying clay types, cross-correlations, and their individual contributions. Sang et al. (2020a) stress the importance of acknowledging cation- and interlayer hydration of expandable clays while sorption studies on pure clays and their mixtures illustrate the great water sorption potential in association with smectite (Johansen & Dunning, 1957, Cases et al., 1992, Chiou, 1997, Laird, 1999, Ferrage et al., 2010, Woodruff & Revil, 2011).

Specific clay content vs. Q_{H_2O} displayed weak negative correlations for kaolinite and chlorite and a slightly stronger negative correlation with illite+muscovite (Figure 3.11). In contrast, smectite content and CEC demonstrated robust positive correlations with water uptake for both conditioning pathways (Figure 3.12e-h).

The quantitative role of smectite and exchangeable cations

Smectite content is the constitutive parameter in which the effect of T_{max}, CEC and texture culminate. The strong linear correlation of smectite content and CEC suggested smectite as the main cation exchanger exerting dominant control over water uptake independent of the conditioning history (Figure 3.13a). In fact, linear regression analysis shows that 89 to 99.5% of the variance in water uptake, depending on relative humidity, can be explained by smectite content and CEC. A strong linear correlation of CEC vs. Q_{H_2O} was also published by Newman (1983), Woodruff & Revil (2011) or Seemann et al. (2017), supporting the significant contribution of CEC to water uptake. Interestingly, both relations persisted over the complete relative humidity range up to 97%RH at which initially a deviation from linearity was expected due to capillary condensation. First, these observations oppose earlier interpretations of Newman (1983), Quirk & Murray (1999), Rinnert et al. (2005), Woodruff & Revil (2011), Seemann et al. (2017), Sang et al. (2019) or Chen et al. (2021), who argued for the importance of capillary condensation at high relative humidity. Such change in the sorption mechanism would imply less control of composition but the dominance of pore structure. However, the strong covariation of textural parameters and smectite content indicates that smectites and their mudrock-specific assemblage dominated the pore network structure. Therefore, a deviation from linearity even at high relative humidity may not be directly observed, because pore condensation is masked, though it occurs in the interparticle space created by the assembly of clay crystallites.

Following Woodruff & Revil (2011) and Kaufhold et al. (2011), normalisation of water uptake by smectite content (Figure 3.13b) or CEC (Figure 3.13c) yielded closely overlapping water vapour sorption isotherms of all mudrocks. The Tournemire argillite was an exception with respect to normalisation based on CEC (Figure 3.13b,c & Figure B.4 in section B.6 in the appendix).[13]

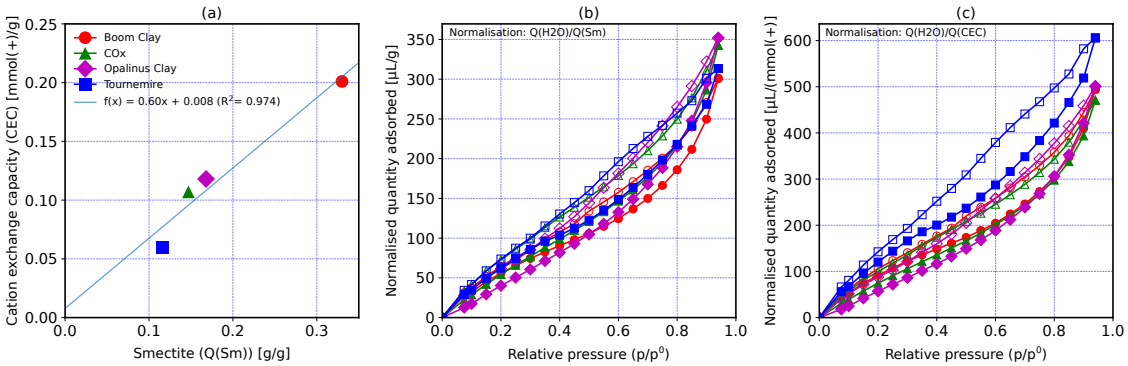

Figure 3.13: (a) Linear regression of smectite content vs. cation exchange capacity (CEC) of the investigated mudrocks; (b,c) Smectite content and CEC normalised water vapour sorption isotherms obtained from dynamic vapour sorption measurements of the investigated mudrocks.

The overlap of the normalised isotherms underlines that the largest difference in water sorption of the studied mudrocks is attributed to smectite content and CEC. The remaining variation in isotherm shape and uptake is likely shared between surface chemical heterogeneity and the

[13]The CEC of the Tournemire was likely underestimated when compared to earlier measurements on the same bulk material (Seemann et al., 2017).

architecture of the pore network. The pore networks of the sample set differed fairly according to the textural analysis of Ar, CO_2 and N_2 physisorption isotherms of dry mudrocks, especially in the micro- to intermediate mesopore range (section B.1 Table B.1 in the appendix). But as indicated above, smectite content likely controls texture/fabric at the relevant scale. However, Mooney et al. (1952b), Cases et al. (1992), Bérend (1995), Chiou (1997), Laird (1999), Michot et al. (2005) and Dazas et al. (2013) demonstrated also an influence of cation heterogeneity, layer charge (amount, distribution, location), type and level of structural hydrophobisation (by, e.g., fuorination of structural hydroxyl groups) of smectite on water sorption. These authors elaborate that the listed properties are reflected in the isotherm shape and can be responsible for a part of the remaining variation. Clearly, the delineation of the quantitative effect of pore network architecture, cation-, and smectite type is difficult, yet a simplified attempt is made in the following.

Cation exchange capacity Quantitative information on cation hydration was obtained from linear regression slopes providing average hydration numbers (H_2O/cation), yet neglecting any type of specificity like hydration energy or cation type heterogeneity. Determining the actual exchangeable cation population is, however, far from trivial and was not performed in this study. Even though, the presence of carbonates in all mudrocks increases the probability that calcium may be present as major interlayer cations. Average hydration numbers were approximately similar for ad- and desorption and range from 7 to 16 H_2O/cation (11 to 75%RH). These metrics are close to earlier calculated hydration numbers of Seemann et al. (2017) who obtained values between 2.5 H_2O/cation and 12.5 H_2O/cation (10 to 70%RH) for a broad collection of mudrocks. The reported values are in agreement with the collection of Woodruff & Revil (2011) who collected literature data varying between 4.6 H_2O/cation (Michot et al., 2005, only external Na), over 12 H_2O/cation (Henry & Bourlange, 2004) to 24 H_2O/cation (Laird, 1999) as a result of general hydration heterogeneity. At 97%RH hydration numbers became unrealistically high with 34 H_2O/cation. This unrealistic high hydration number conveys that an additional contribution needs to be made by another mechanism like interparticle pore condensation and sorption on the basal surfaces of expandable clays in between exchangeable cations.

Smectite hydration The smectite hydration proceeds via the earlier described heterogeneous intercalation of water, involving cation hydration, mixed-layer stages, and swelling. To resolve the contribution of smectite hydration to the water sorption of mudrocks, DVS water isotherms of analogue materials were tested against the water uptake of mudrocks. The analogues constituted two purified montmorillonites (Na and Ca SWy2) and a natural clay mineral mixture of which the isotherms were scaled by the estimated smectite content of the mudrocks (Figure 3.14). Hereby, smectite was assumed to be the main water sorbent, respectively. Additionally, desaturation of a sodium saponite was estimated based on the XRD profile modelling of Ferrage et al. (2010), similar to the approach of Lahn et al. (2020). These authors elucidated that $\approx$ 79% of water at 97%RH in Opalinus Clay could be attributed to smectite hydration.

The isotherms of the montmorillonites and the saponite differed considerably in isotherm shape and uptake compared to the mudrocks. Only above a p/p^0 of 0.8, the isotherms of the calcium SWy2 approached the mudrock isotherms to yield nearly similar maximum sorption capacities

(Figure 3.14). The sodium montmorillonite displayed the typical double-stepped isotherm shape already observed by Mooney et al. (1952a). The scaled isotherms were lower or equal to the mudrock isotherms and desorption branches approached each other at a mudrock-specific p/p^0 between 0.65 and 0.35. The sodium saponite showed a stepped desorption branch related to interlayer contraction and did neither resemble nor sorb a comparable amount of water as the mudrocks. Given the isotherm shape combined with the likelihood of the above clay mineral types to be present in such form in the studied mudrocks, they were excluded from further consideration. In fact, their application led to severe overestimation of water uptake similar to the water volumes estimated by Lahn et al. (2020).[14] In contrast, the natural clay fraction was considered the closest analogue to the natural mudrocks, as it likely preserved the original cation occupation, and its textural fabric might be more similar to that of the mudrocks than a highly purified montmorillonite. However, it was still unlikely to be identical.

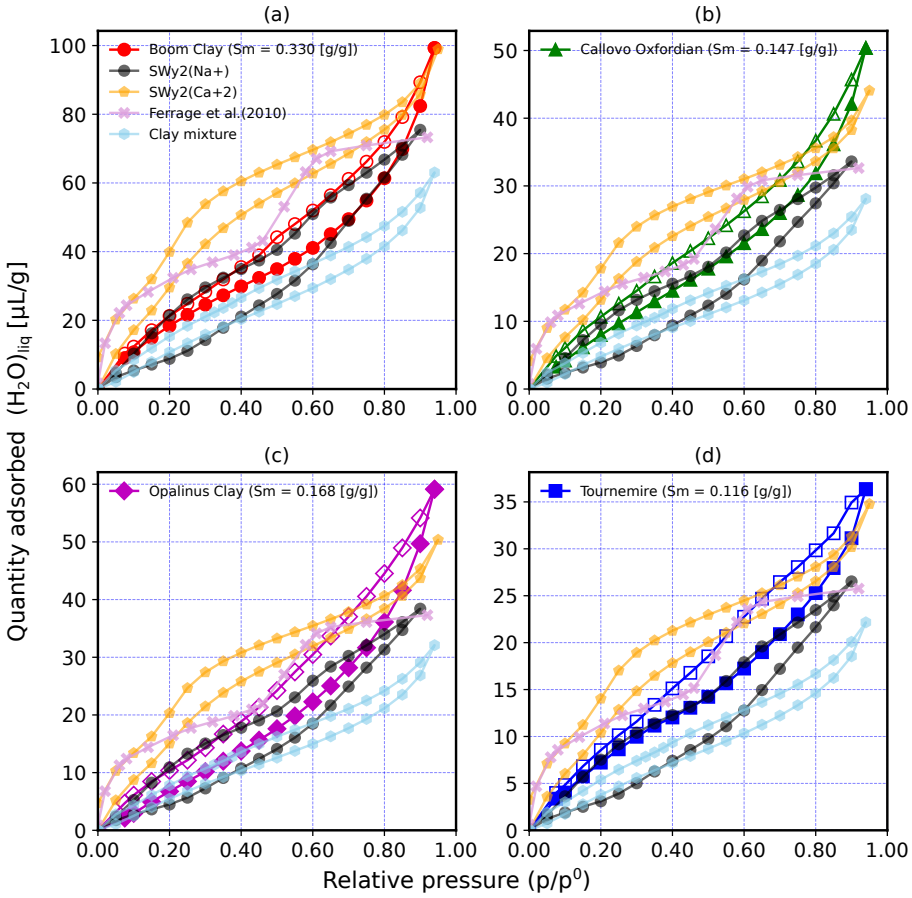

Figure 3.14: Overview of dynamic water vapour sorption isotherms of mudrocks and scaled sodium and calcium montmorillonite (SWy2) and a natural clay mixture. Original water vapour sorption isotherms of the montmorillonites and the clay mineral mixture were scaled based on the smectite content of mudrocks estimated by Rietveld refinement of XRD powder patterns. Plum coloured isotherms represent the desorption branch obtained from XRD profile modelling of water equilibrated sodium saponite (layer charge = 0.4) from Ferrage et al. (2010).

[14] Lahn et al. (2020) based their hydration estimation on desorption data of Dazas et al. (2013), but applied them to experimental adsorption data as a first approximation.

Quantitatively, the clay mineral mixture could account for about 43 to 86% at 11%RH and up to 63% at 97%RH of the water adsorption of the studied mudrocks. Considering static sorption, the relative share was slightly lower (up to 52% at 97%RH), though at low relative humidity at least 18% could be attributed to smectite hydration. The relative contribution of smectite hydration ceases with increasing humidity which was conceived as a growing contribution of interparticle space to the water uptake in the mudrocks. Thus, the discrepancy in uptake implies that besides cation- and smectite hydration fabric-controlled interparticle condensation should occur (cf. section 3.5.6). Such texture-associated uptake was already acknowledged by Cases et al. (1992) and Ferrage et al. (2010) who specifically noted that XRD profile modelling is restricted to inter-crystalline water but gravimetric measurements include capillary water. Clearly, condensation on the external surface or in the interparticle space was not accurately estimated with this simple approach, but a perfect match could not be expected when the negligence of the true cation population and differences in texture are taken into account.

Nevertheless, this simplified approach, combined with the evidence gained by water isotherm normalisation, advocates for a substantial control of smectite- and cation hydration on water uptake in mudrocks while interparticle condensation remains relevant to explain the presented observations, especially at higher p/p^0.

3.5.4 Water distribution and pore filling

In a recent study, Chen et al. (2021) measured water vapour uptake of mudrocks at different temperatures and concluded that desorption of water proceeds via capillary evaporation, hence a receding meniscus. Consequently, capillary condensation must have taken place during adsorption. Pore condensation is a progressive, pore-size-controlled process and has been proposed by various researchers as a primary water sorption mechanism in mudrocks (e.g. Zolfaghari & Dehghanpour, 2015, Sang et al., 2019, Zhang et al., 2022). Sang et al. (2019) and Li et al. (2021) emphasise that the contribution of capillary condensation to pore filling varies for each mudrock. Li et al. (2021) even suggest that the mechanism applies only to micropores in their sample set while Li et al. (2016a), Seemann et al. (2017), Lahn et al. (2020) and Ma et al. (2020) showed that pore condensation is a minor mechanism in water vapour adsorption below 97%RH. Besides, pore condensation concentrates in pores below $\approx 10\,\text{nm}$ (Li et al., 2016b, Lahn et al., 2020) (adsorption) where it associates with hydrophilic clay pores according to Li et al. (2016a).

The previous analysis demonstrated that smectite hydration alone cannot fully account for the observed water uptake, indicating that pore condensation within the interparticle pore space must also contribute. To investigate interparticle condensation, (relative) changes in the N_2 differential pore volume for specific pore size classes (5 nm, 20 nm, 50 nm) are examined as a function of relative humidity (Figure 3.15). The data were normalised to the N_2 differential pore volume of the dry mudrocks. This analysis allows to gain insight into how pore-filling behaviour varies with relative humidity — and consequently water content — both in general and for specific pore sizes. Since water uptake reduces N_2 accessibility, an inverse correlation with the differential N_2 pore volume is expected.

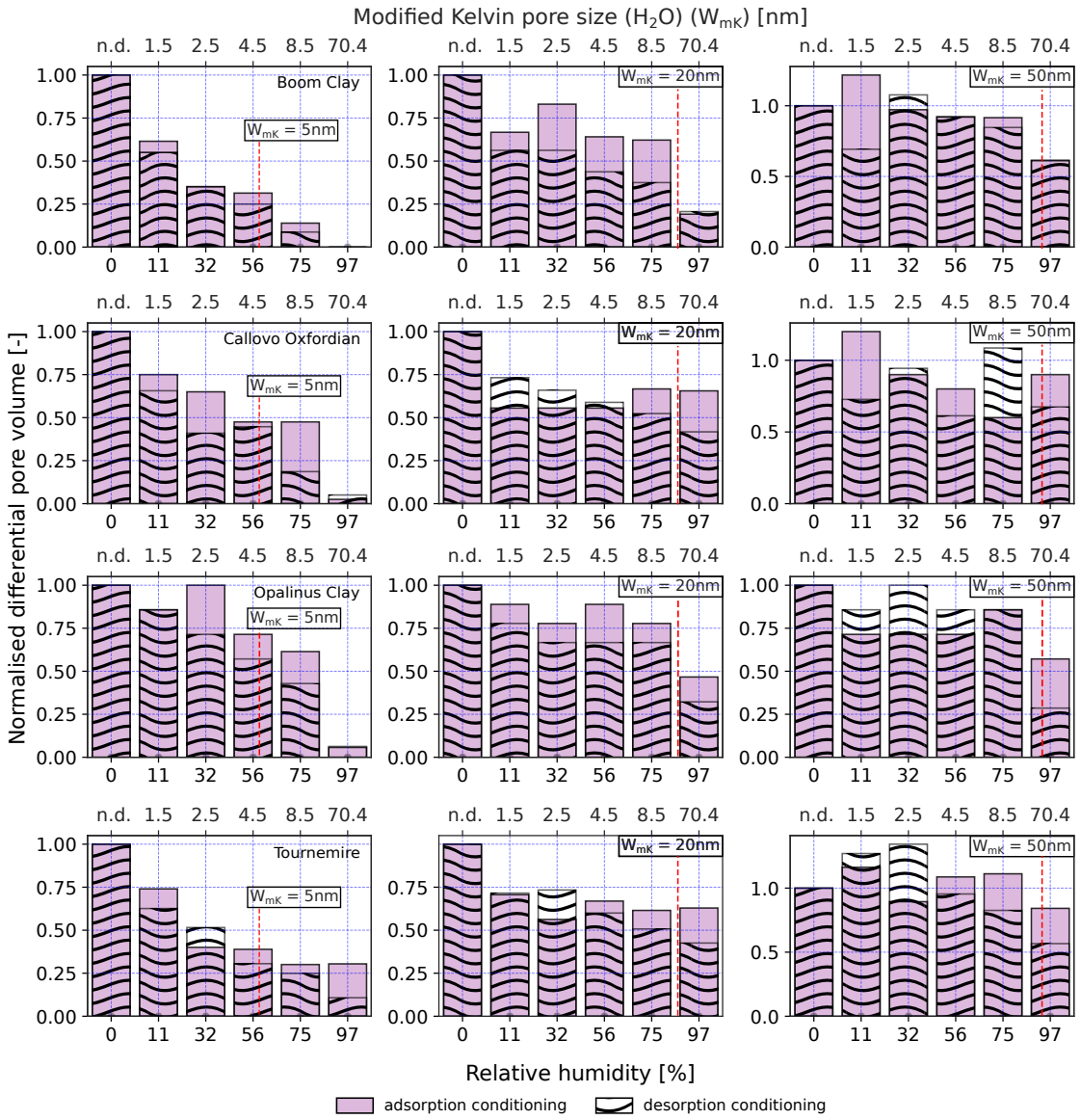

Figure 3.15: Fractional change of differential pore volume accessible to nitrogen after moisture conditioning. Relative changes were obtained by normalising the differential pore volume obtained from N_2 isotherms at a specific pore size (W = 5 nm, 20 nm and 50 nm) to their respective differential uptake of the dry sample. PSDs were computed by a combination of DA-theory and BJH-theory from the adsorption branch. The secondary x-axis (top) shows the corresponding pore width theoretically filled by water at the given relative humidity (primary x-axis) obtained from the Kelvin equation modified by the t-curve of Hagymassy et al. (1969). The vertical, red-dashed line indicates the relative humidity at which the targeted pore size (W_{mK}) is theoretically filled by water according to the modified Kelvin equation.

In the case of 50 nm pores, the differential pore volumes showed random variations. However, for 20 nm pores there was an immediate reduction in nitrogen accessibility at 11%RH. The effect persisted up to 75%RH, followed by a further drop for the Boom Clay and Opalinus Clay. The apparent randomness in the data for 50 nm pores was probably due to spline interpolation used

to obtain similar pore size binnings of the cumulative PSDs. The impact on 20 nm pores can be interpreted as either a differential pore volume reduction by pore volume filling or the reduced access by means of pore blocking by water of connecting pore throats as well as inward swelling of smectites. Differential pore volumes of 5 nm pores showed a mostly continuous decrease and almost complete inaccessibility was detected at 97%RH for Boom Clay, Callovo Oxfordian argillite and Opalinus Clay. Notably, only the Tournemire argillite showed significant uptake in 5 nm pores at 97%RH. The effect on 5 nm pores was consistent with the change in cavitation volume (Figure 3.8). Cavitation, a major desorption mechanism of nitrogen in pore networks (of mudrocks), occurs in pore bodies connected by pore throats of 5 to 6 nm (Ravikovitch & Neimark, 2002b, Morishige et al., 2006, Thommes et al., 2006, 2015).[15] Accordingly, cavitation volumes of Boom Clay, Callovo Oxfordian argillite and Opalinus Clay nearly ceased at 97%RH yielding about 15 to 10% of detectable cavitation volume in ad- and desorption (equivalent to $\leq 0.8\,\mu L/g$). For the Tournemire argillite, between 35% (adsorption) and 23% (desorption) of cavitation volume were accessible at 97%RH, proving partial pore filling of cavitation-controlling pore sizes in accordance with the PSDs. Despite that, the amount of water was theoretically sufficient to occupy the cumulative pore volume up to 6 nm.

To the contrary of expectations, data denoted incomplete pore filling for most of the pore network, despite the anticipation that water would occupy a considerably larger portion of the pore network upon desorption from nearly full saturation (100%RH). Consequently, the difference between adsorption and desorption conditioning was less than expected as indicated by the loss in micropore volumes, the cumulative PSDs, the normalised differential uptakes (Figure 3.3, Figure 3.4, Figure 3.7, Figure 3.15). The inflection points of the PSD curves during desorption conditioning occurred at slightly larger pore sizes, indicating a more significant effect of desorbing water. However, the final differences in pore volume occupation were minimal, despite the prominent hysteresis observed in the water sorption isotherms. The saturation differences in pore volume up to the earlier specified pore sizes ranged between 5% and 25% for ad- and desorption conditioning (Figure 3.7).

Significant pore filling occurred between 75% and 97% RH in nitrogen-accessible pores smaller than ≈ 10 nm for both conditioning histories. Complete pore filling was detected merely in pores up to 4 to 8 nm at 97%RH. This finding aligns with previous studies (Li et al., 2016a,b, Seemann et al., 2017, Feng et al., 2018, Lahn et al., 2020) and is supported by cavitation volume analysis (Figure 3.8). The variation in $W_{max}(H_2O)$ between adsorption and desorption conditioning was minor and sample-specific, suggesting a minimal impact of the conditioning history for samples equilibrated at 97%RH (section 3.5.5).[16] However, at lower relative humidity, a slightly stronger effect of the conditioning history was observed, evidenced by shifts in the PSDs inflection points.

Pore volumes stored in pores up to 20 nm demonstrated reduced N_2 accessibility after moisture equilibration, yet pore volume saturation was not fully achieved (Figure 3.7). At 97%RH, the amount of presorbed water was sufficient to theoretically fill the cumulative pore volume up to 50 nm, as calculated from the dry isotherms, except for the Tournemire argillite where the provided

[15] It is associated with forced hysteresis loop closure at $p/p^0 \approx 0.42$ (N_2 at 77 K) and the closure is frequently misinterpreted as a 4 nm peak in differential pore size distributions computed from the desorption branch (Groen et al., 2003, Landers et al., 2013, Bertier et al., 2016).

[16] For Tournemire argillite, the maximum difference in $W_{max}(H_2O)$ (ads vs. des) was 1.75 nm, while for other samples, the difference was at the molecular scale of nitrogen.

water content was too low (Figure 3.7, Table B.2, Table B.3). It is interesting to note, however, that full saturation of these pore volumes was not observed.

Partial pore filling has been recognised by several researchers independent of the moisture conditioning history (Li et al., 2016a, Seemann et al., 2017, Lahn et al., 2020, Li et al., 2021). Here, it was confirmed for the studied mudrocks. The mudrock-specificity of filled pore sizes contradicted a dominantly pore-size-controlled adsorption and desorption mechanism. This was also corroborated by the sample-specific filling pressure (H_2O) of micropore volumes (N_2) following the order BCM ($p/p^0 \approx 0.074$) < COx ($p/p^0 \approx 0.083$) = OCM ($p/p^0 \approx 0.083$) < TM ($p/p^0 \approx 0.185$). In a dominantly pore-size-controlled system, the variation in filling pressure was expected to be lower when the DA average micropore sizes are taken into account (section B.1 Table B.1 in the appendix). The prerequisite is, however, scale- and solid independent wettability which is unlikely for mudrocks and introduces a high level of uncertainty on any prediction involving wettability parameters (Alcañiz-Monge et al., 2001). The modified Kelvin equation (full wetting assumed) theoretically suggested filled pore sizes from 1.5 nm (11%RH) to 70.4 nm (97%RH), hence complete mesopore filling at 96%RH (Figure 3.15). However, the data evidenced incomplete pore filling of the predicted pore sizes. In fact, the modified Kelvin model substantially overestimated saturated pore sizes (Figure 3.15). Reasons could be the ignorance of (i) confinement effects on surface tension (γ = const.) of a fluid (Feng et al., 2020), (ii) idealised wetting conditions (θ= 0), despite that water is a partially wetting fluid and contact angles are individual for mudrocks (Thommes et al., 2012, Peng, 2019) as well as (iii) the influence of smectite swelling on pore network modification leading to an ambiguous picture of pore volume analysis.

The minor discrepancy in affected pore size between adsorption and desorption conditioning suggests that the impact of water on the pore network is essentially equivalent, regardless of the conditioning pathway or the governing mechanism. This effect was interpreted as a combination of smectite swelling and pore condensation because the presented observations do not comply with a single dominant mechanism such as capillary condensation. Furthermore, smectite was identified as the main water adsorber. At 97%RH, the role of further smectite swelling was considered negligible. This is because, upon adsorption, the smectite will have fully expanded, while, upon desorption, it might not yet have contracted. At lower relative humidity, the small differences were likely associated with a combination of pore occlusion by smectite swelling and pore condensation. Since both mechanisms inflict hysteresis, this combined effect might explain the small differences in saturation and affected pore sizes and other textural parameters between ad- and desorption conditioning. As a result, the conclusions of Chen et al. (2021) do not hold for the investigated mudrocks, and capillary condensation/evaporation of water appears to be less dominant compared to other processes. Nevertheless, the differential pore volume analysis acknowledges a sequential component in water uptake, which suggests a certain level of pore size control on water uptake.

3.5.5 The 97%RH conundrum and the issue of equilibrium

It has been shown that at 97%RH ad- and desorption data and their water contents cannot be reliably told apart and data are ambiguous. Moreover, equilibration times were excessively long and mass fluctuation was detected during preparation. Testing humidity equilibration on

centimetre-sized mudrock cores confirms the great difficulty of attaining humidity equilibrium and mass constancy at high partial pressure. There was frequent macroscopic condensation in the form of visible droplets building on the surface of the rock and desiccator walls. Despite temperature control, the temperature fluctuated by at least 1 K (Figure 3.16).

At 97%RH (K_2SO_4) the system is close to the saturation pressure of pure water and the relative humidity is immensely susceptible to temperature-induced changes in saturation pressure. Modelling the saturation pressure of water as a function of temperature by the Antoine equation (Bridgeman & Aldrich, 1964) implies that a 1 K drop in temperature is sufficient to effect humidity supersaturation (RH $>$ 100%RH) for a desiccator equipped with a saturated K_2SO_4 solution. That means slight cooling causes immediate condensation. While the system will restore equilibrium according to the Le Chatelier's principle, the reaction kinetics are likely too slow to prevent supersaturation with respect to moisture and macroscopic droplet formation on surfaces (Figure 3.16).

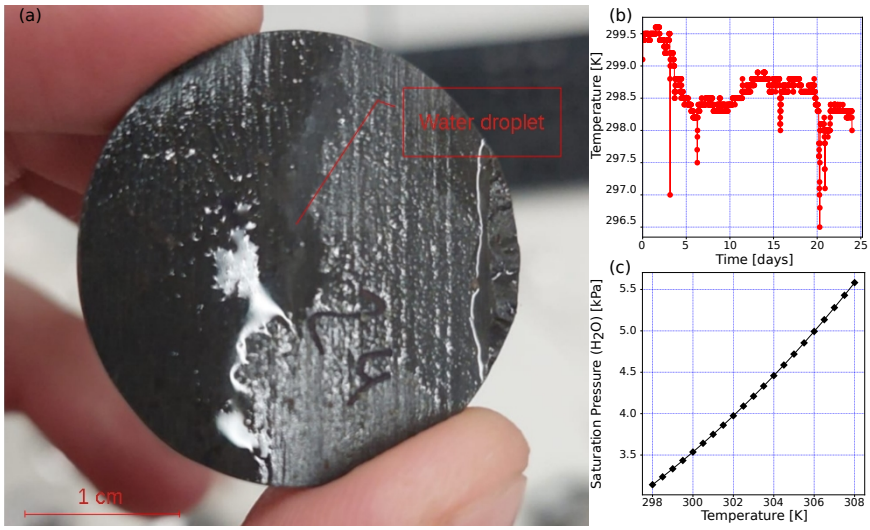

Figure 3.16: (a) Image of centimetre sized (d = 30 mm) mudrock core (top view) equilibrated at 97%RH using a saturated K_2SO_4 solution at room temperature ($T \approx 298$ K) exemplifying macroscopic condensation/ droplet formation on the outer surface of the cylinder, (b) Example of temperature fluctuations over the course of several days of a saturated K_2SO_4 solution; (c) Saturation pressure of water plotted as a function of temperature calculated via the Antoine equation obtained from NIST (2023).

The same process acts during the conditioning period ($\approx$ 7 weeks) of the 200 to 400 µm mudrock particles used in this study. Despite temperature control in a conventional oven set to 303 K, temperature fluctuations of up to 5 K were recognised (day- and night cycles, especially strong during summer and winter) arousing repeated ad- and desorption cycling during equilibration. Furthermore, spontaneous droplet formation can occur when removing the desiccator from the oven in winter. These temperature fluctuations correspond to saturation pressures between $\approx$ 4.25 kPa and 5.63 kPa for pure water. Such fluctuations avert an unambiguous discrimination of the conditioning path at high partial pressure. In a further consequence, the amount of presorbed water might be overestimated because of the macroscopic condensation in between particles. However, there were no droplets in between particles or obviously wet particles identified when the

materials were prepared for experimentation. Besides, total specific pore volumes of argon, nitrogen and water (SVS) are in fair agreement implying no significant overestimation.

Nevertheless, data interpretation for 97%RH conditioning is considered unreliable and substantially biased since it is not unambiguously known which conditioning path is investigated.

3.5.6 Mass-volume balance

The impact of presorbed water on the pore network accessibility of nitrogen was substantial, yet ambiguous. Figure 3.17 highlights a significant discrepancy in the mass-volume balance of presorbed water and loss in Gurvich pore volume ($\Delta V_{\mathrm{GV}}(\mathrm{N_2}) = V_{\mathrm{GV}}(\mathrm{N_2})(0\%RH) - V_{\mathrm{GV}}(\mathrm{N_2})(x\%RH)$). Typically, the gravimetric amount of presorbed water (measured post-analysis) exceeded the loss in Gurvich (total) pore volume by a factor of up to 2.4 at high relative humidity. Although the relationship between $Q_{\mathrm{H_2O}}$ and ΔV_{GV} was approximately linear, the deviation from a 1:1 ratio increased as a function of water content (Figure 3.17). Ratios ($\Delta V_{\mathrm{GV}}/Q_{\mathrm{H_2O}}(x\%RH)$) decreased for adsorption conditioning, whereas they remained relatively stable during desorption conditioning (not shown).

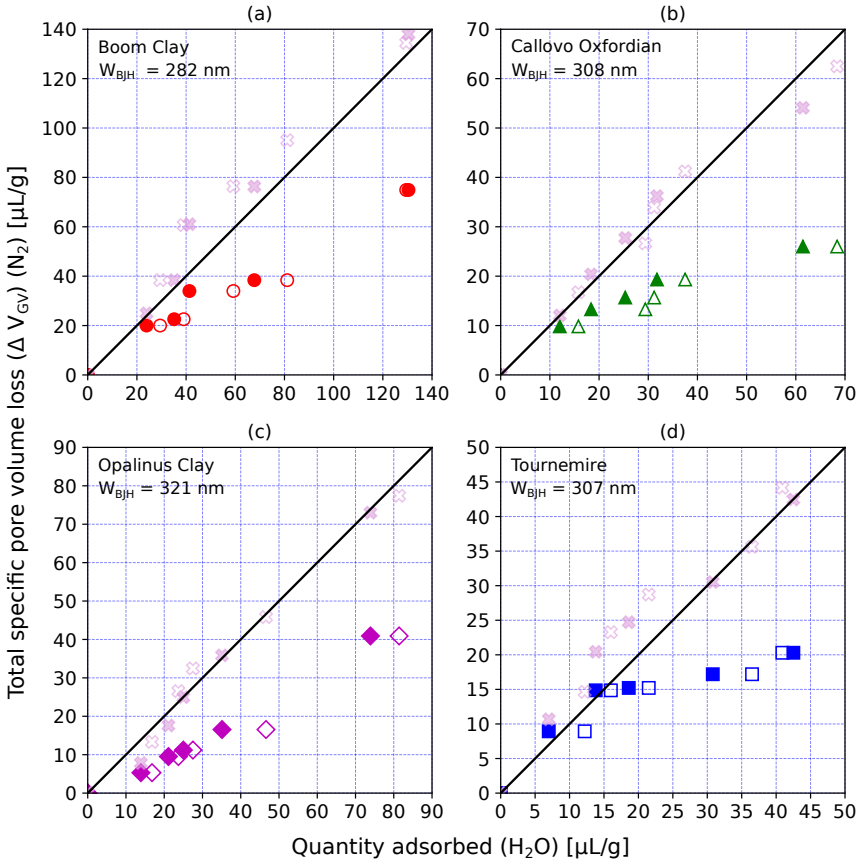

Figure 3.17: Comparison of presorbed water volumes and Gurvich pore volume loss at equivalent BJH pore width: (a) Boom Clay, (b) Callovo Oxfordian argillite, (c) Opalinus Clay, (c) Tournemire argillite. Unity is presented as a solid black line and adsorption conditioning is indicated by closed symbols whereas desorption conditioning is represented by open symbols. Plum coloured symbols represent the linear mixing model (Equation 3.1).

According to Cases et al. (1992) and Salles et al. (2008), the initial hydration ($p/p^0 \leq 0.2$) of clay minerals occurs on their external surfaces, hence in the interparticle pore space. However, the observed mismatch of ΔV_{GV} and $Q_{\mathrm{H_2O}}$ for all mudrocks — except the Tournemire argillite — indicates that external surface hydration at low p/p^0 is not the predominant process. In fact, the external surface hydration and its upper partial pressure threshold are strongly dependent on the type of clay mineral and the dominant interlayer cation in the case of expandable clays (Bérend, 1995), making the data interpretation more complex.

The presented imbalances were also reported in previous investigations using (i) the same experimental approach (Stoeckli & Huguenin, 1992, Alcañiz-Monge et al., 2001, Alcañiz-Monge & Lozano-Castelló, 2002, Li et al., 2016a, Seemann et al., 2017, Lahn et al., 2020) as well as (ii) for differing boundary conditions (P, T) and analytical techniques (Alcañiz-Monge et al., 2001, Peng, 2019). Stoeckli & Huguenin (1992), Alcañiz-Monge et al. (2001) and Alcañiz-Monge & Lozano-Castelló (2002) observed a larger pore volume loss than the presorbed water volume when studying the mechanistic behaviour of water in micro- and mesoporous activated carbon fibres. This difference was mechanistically interpreted as cluster-mediated pore blocking and physically as density depletion of water to 0.92 g/mL in micropores originating from an ice-like structural organisation. This higher-order structural organisation is thought to prevent water from freezing at nano-scale, thus invoking a reduced density. This hypothesis is supported by a scattering study of Iiyama et al. (1997) which did not detect a phase transition of water upon cooling from 303 to 143 K.

Recently, Rother et al. (2020) interpreted a reduced water density (0.84 to 0.99 g/mL) for microporous MCM-41S silicas of differing hydrophilicity. Hence, a density reduction is not restricted to microporous carbons but is generally attributed to the hydrophobic surface character (Thommes et al., 2013, Brovchenko & Geiger, 2002, Brovchenko et al., 2004, Brovchenko & Oleinikova, 2008).

A reduced density did not hold for the study presented. By assuming a reduced density of 0.92 g/mL, the discrepancies between $Q_{\mathrm{H_2O}}$ and ΔV_{GV} grew up to 26 to 18%. Therefore, it seemed rather unlikely that water would attain a lower density for the given mudrocks. In contrast, the presented data implied an apparent densification of water under confinement which was theoretically supported by the data of Peng (2019). In fact, to match the experimental ΔV_{GV} with $Q_{\mathrm{H_2O}}(\%\mathrm{RH})$ densification, like that of an adsorbed phase in supercritical sorption experiments would be necessary (cf. Melnichenko et al., 2009, Rother et al., 2012, for CO_2). Based on a simple theoretical calculation ($\rho(\mathrm{H_2O}) = m(\mathrm{H_2O})/\Delta V_{\mathrm{GV}}(\mathrm{N_2})$) this option was excluded because of the need of unrealistically high water densities of up to 2.36 g/mL.

Recently, Peng (2019) reported contrasting data for mudrocks of the Eagleford-, Barnett- and Wolfcamp formations. Based on gas-expansion experiments on partially saturated mudrocks, Peng (2019) observed a lower specific pore volume loss compared to imbibed water volume (by mass) latest at a saturation above 0.35, confirming the presented trends (Figure 3.17). The author interpreted the data as evidence for pore blocking by water (clusters) at the entrances of pore throats connecting specific domains of the pore network similar to an earlier interpretation of Seemann et al. (2017) for partially saturated mudrocks. This conclusion holds only for lower relative humidity. The ratios

($\Delta V_{GV}/V_{H_2O}$) were significantly lower than unity resembling this study.[17] However, Peng (2019) concluded a water mass overestimation due to fracture storage. In this study, such storage volume could generally be interpreted as an accessibility discrepancy; in particular: (i) micropores, (ii) macropores larger than 360 nm, or (iii) the interlayer space of expandable clays.

(i) The micropore volume of mudrocks has been quantified by Ar and CO_2 physisorption, contributing 8 to 21% and 9 to 24% of the total specific pore volume (helium pycnometry), respectively. Further, they are between 7% and 17%(CO_2) and 23% and 29%(Ar) larger than micropore volumes obtained from nitrogen measurements. Theoretically, the initial water uptake at 11%RH is sufficient to fully occupy the micropore volumes determined from Ar, CO_2, and N_2 physisorption isotherms. However, micropore volumes remain accessible even at high relative humidity in moisture-conditioned mudrocks (Figure 3.4), suggesting that the initially adsorbed water is only partially confined within micropores.

(ii) Helium accesses the total specific pore volume (TPV; open pores) of a solid down to its kinetic diameter ($\approx$ 2.6 Å) (Busch et al., 2017). At 97%RH approximately 56 to 100% of the TPVs(He) could be theoretically occupied by water (Table 3.2). Comparing specific water volumes with the TPV(He) indicates the theoretical possibility of storing excess water in the specific pore volume above 360 nm up to a conditioning level of 75%RH. At 97%RH there is not enough specific pore volume left available to account for the mass-volume imbalance. In the case of the Tournemire argillite, this possibility fails even at 75%RH. This, however, implies complete pore volume filling. Obviously, there is considerable sorption of nitrogen in meso- and macropores for the complete sample collection and both conditioning pathways. Furthermore, the match of the total specific pore volumes of water, argon and nitrogen indicated that considerable water sorption outside the pore network was also unlikely for the given sample set as earlier demonstrated by Seemann et al. (2017) and Lahn et al. (2020).

Table 3.2: Selection of petrophysical data collected from literature and personal communication or calculated based on measurements performed in this study. ρ_{gr} = grain density [g/mL], ϕ_{He} = helium porosity [-], ϕ_{N_2} = nitrogen porosity [-], ϕ_{H_2O}(SVS) = water porosity [-] from static vapour sorption measurements, ϕ_{H_2O}(DVS)= water porosity [-] from dynamic vapour sorption measurements. The grain density and helium porosity were obtained from literature and personal communication.

ID	ρ_{gr} [g/mL]	ϕ_{He} [m^3/m^3]	ϕ_{N_2} [m^3/m^3]	ϕ_{H_2O}(SVS) [m^3/m^3]	ϕ_{H_2O}(DVS) [m^3/m^3]
Boom Clay	2.74	0.39	0.22	0.26	0.21
Callovo Oxfordian	2.70	0.17	0.15	0.16	0.13
Opalinus Clay	2.71	0.21	0.14	0.18	0.14
Tournemire	2.69	0.10	0.09	0.10	0.09

(iii) Lahn et al. (2020) stated that the mass-volume imbalance can be a result of interlayer hydration of smectite in addition to pore filling of interparticle pores. Correlation analysis illustrated a strong correlation between smectite content and $\Delta V_{GV}(N_2)$ which was attributed to smectite's previously discussed strong control on water uptake and its co-variation with textural parameters.

[17] It is interesting to note that the described mass-volume imbalance seems to be independent of temperature at the experimental boundary conditions in the study of Peng (2019) and this study are different ($T_{Peng2019} = 298$ K vs. $T_{here} = 77$ K).

Additionally, the water uptake of the clay-mixture analogue could explain a significant portion, but not all, of the total water sorption. It was inferred that there was an additional contribution from the interparticle pore volume.

Combining interlayer hydration of expandable clays and interparticle condensation yields a simple mixing model:

$$Q_{\mathrm{H_2O}}(x\%RH) = Q_{\mathrm{clay}}(x\%RH) + \Delta V_{\mathrm{GV}}(\mathrm{N_2})(x\%RH) \tag{3.1}$$

Here the sorbed amount ($Q_{\mathrm{H_2O}}(x\%RH)$) is defined as the sum of clay hydration ($Q_{\mathrm{clay}}(x\%RH)$) and loss in (total) pore volume accessible to nitrogen ($\Delta V_{\mathrm{GV}}(\mathrm{N_2})(x\%RH)$) as a function of relative humidity. The quantitative clay hydration was estimated based on the experimental water vapour sorption isotherm of the natural clay mineral mixture. The water uptake of the natural clay mineral mixture was scaled by the amount of smectite quantified from XRD powder patterns for the individual mudrocks yielding combined external- and interlayer hydration of the analogue. The clay hydration was corrected for external surface hydration, which was assumed to be predominant up to 11%RH.

Figure 3.17 shows the mixing model complemented by the experimental raw data. Notably, the simplified mixing model reasonably resembles the unity line for the individual samples, implying coverage of the main processes and contributors to the mass-volume imbalance. In turn, the frequently observed imbalance of presorbed water and pore volume loss was understood as a primary product of interlayer sorption which is not captured by nitrogen physisorption. The loss in Gurvich specific pore volume, on the other hand, represents the general pore network modification probably due to combined capillary condensation and volumetric expansion of smectites into the interparticle pore space.

Obviously, such a mixing model is oversimplified, lightly constrained and not fully accurate. While the clay mineral mixture analogue may not precisely represent the actual composition of the examined mudrocks, fair correspondence of the model with unity implied little sensitivity of the model to the actual analogue, provided that clay mineral hydration is the predominant process and the water vapour isotherm of the analogue does not differ substantially from the target one (cf. section 3.5.3). The primary source of bias in the model is attributed to the uncertainty in the scaling factor derived from XRD analysis. Acceptable misfits and local overestimation of the mixing model may be explained by the fact that the clay-mixture isotherm remains an analogue and not an identical replication of the clay composition and fabric of the actual mudrocks. Moreover, the gravimetric isotherm combines dual interlayer hydration and interparticle sorption in the analogue which cannot be easily deconvoluted without additional analytical methods such as XRD. Thus, the mixing model offers, at best, a semi-quantitative resolution of the mass-volume imbalance and more sophisticated analogues and techniques are required to fully resolve the issue.

3.5.7 Experimental limitations and critical perspectives

The distribution of water in the pore network of mudrocks is complex and challenging and the applied method revealed some ambiguity towards pore volume loss and presorbed water volumes.

The experimental approach is a combination of vapour equilibration, sorbed water "binding" by cooling and nitrogen physisorption. A priori it does not evolve from first-order-principal methods and potential changes of the microstructure and physical properties of the sorbed water cannot unequivocally be excluded. Its findings should be regarded as a preliminary approximation of water distribution in mudrocks due to several limitations of the study, which are outlined below.

1. ***Moisture conditioning*** has been performed under static conditions in a desiccator above saturated salt solutions. Despite temperature control in a conventional oven, temperature fluctuations and therefore saturation pressure changes were observed over the course of equilibration (summer + winter term). While such fluctuations have minor influence at lower relative humidity, at 97%RH small fluctuations can quickly result in supersaturation and bulk condensation disturbing the actual process of interest (see section 3.5.5). Moreover, reoccurring fluctuations cause continuous cycling between the ad- and desorption branch leading to ambiguity which state is actually studied. In turn, when the described approach is used, a temperature incubator with heating and cooling function is recommended.

2. ***A short evacuation sequence*** of 1 min at an evacuation rate of 133 kPa/min was used during the initiation of the physisorption measurement. Though the moisture loss was tried to be kept to a minimum by immersion of the conditioned sample into an ice bath while the free space was measured, the possibility of moisture loss or reallocation remains. Weights, taken before and after the physisorption measurement, reveal slight mass losses depending on the presorbed amount of water. The average absolute mass changes amount from 0.3 mg (7%) at 11%RH to 4.7 mg (18%) at 97%RH. For individual samples, the relative mass loss could be significantly higher and up to 57%. Still, mass losses are close to the limit of quantification of the balance and the mass loss may have occurred between the end of the measurement and the weighing.[18] However, Lahn et al. (2020) showed that the moisture loss was minor and unsystematic for the instrument and the experimental method.[19] Dead volume tests on a clay-deficient and overmature mudrock (Longmaxii formation; ID = Sichuan211 in Seemann et al. (2017)) support the limited moisture loss during instrument preparation amounting to $\approx 3.0(0.6)$ µL obtained from dead volume measurements as well as weighing for two subsequent tests. It is noted, that dead volumes vary randomly between subsequent dead volume tests and only loosely bound, external surface water may be lost. Future tests should involve dead volume measurements after the actual measurements to reduce evacuation or potentially be completely avoided.

3. ***The cooling*** of the conditioned sample into an ice bath and a liquid nitrogen bath may lead to freezing of the confined water. This would cause a volumetric increase of 9% and a reduced density. Considering this physical change, the assumption of liquid bulk properties does not hold anymore and potential damage to the microstructure may be created. The latter appears negligible regarding the good reproducibility of dry isotherm measurements after recurrent wetting and repetition of physisorption measurements (Lahn et al., 2020). Besides, a reduced density has been shown to not fit the data.

[18] The time span was individual to the experiment and was up to several hours during which desorption took place.
[19] The exact same instrument (*Micromeritics Gemini VII 2390t*) has been used in the presented study.

4. ***The mixing model*** of clay hydration and interparticle condensation is only a rough approximation as it relies on an isotherm of a natural clay mineral mixture, scaled by the smectite quantity, obtained from Rietveld refinement of XRD profiles of the actual mudrocks. Both input parameters are not entirely accurate because (i) the clay mixture likely does not precisely represent the mudrocks, and (ii) mixed-layer mineral quantification by XRD is likely biased, as shown by the Reynolds Cup 2022. Additionally, DVS isotherms rely on an operational criterion and are usually lower than SVS isotherms implying an underestimation of water uptake. Besides gravimetric isotherms reflect a combination of interlayer- and external sorption that cannot be discerned unambiguously without simultaneous XRD measurements. Future attempts should at least include the separation of the natural clay fraction of the investigated mudrocks with detailed characterisations and its use as an analogue for the hydration model.

5. ***The pore network modification*** through swelling has been addressed on a qualitative level. It appears difficult to differentiate pore size modification induced by swelling from pore filling by water condensation. Accordingly, the solid-fluid system cannot be treated as a traditionally rigid system as is the case with nitrogen or argon. As a consequence, the PSDs of moisture-conditioned mudrocks cannot be used to determine the location of water in the pore network, but only the range of affected pore sizes relative to the PSD calculated from the dry reference isotherm. Quantitative discrimination of the pore network modification by swelling and pore condensation should be focused on in the next step.

3.5.8 Mechanistic implications for the interpretation of water vapour sorption isotherms

Smectite has been identified as the primary cause and control of water sorption in the studied mudrocks. Consequently, the dominant sorption mechanisms and processes observed in smectite hydration are expected to prevail in the studied mudrocks. Thus, clustering around exchangeable cations, just as interlayer hydration accompanied by volumetric expansion and external interparticle condensation are considered constitutive mechanisms of mudrock hydration.

Ziemiański et al. (2020) demonstrated that the pore size distribution in clayey materials is a representation of the clay mineral texture and their assemblage. In randomly organised clay assemblages, pore sizes are primarily controlled by the thickness of individual crystallites, which results from the stacking of fundamental particles (TOT units)[20], the degree of turbostratic disorder in smectites and associated mixed-layer phases, and the spatial juxtaposition of crystallites towards each other. These factors mainly lead to the formation of slit-shaped micropores at crystallite edges and interparticle mesopores, both of which influence the specific surface area of the bulk material (Quirk & Murray, 1999, Michot & Villiéras, 2006, Kaufhold et al., 2010, Michot, 2018). Due to the strong relationship between specific surface area and micro- to mesopores (Figure B.3, Rouquerol et al. (2007), Środoń & MaCarty (2008), Ziemiański et al. (2020)), significant modifications in pore structure within the micro- and mesopore range are anticipated when mudrocks are moisturised. This is supported by the presented pore size distributions and the decrease in DA micropore volume

[20]TOT refers to tetrahedral-octahedral-tetrahedral sheets.

and specific surface area as a function of water content (Figure 3.4, Figure 3.5). PSDs reveal a sample-specific, stepwise, yet sequential closure of pores up to 4 to 8 nm. Larger mesopores are already affected at low relative humidity, even though smaller pores remain partially open. Likewise, a hyperbolic reduction in micropore volumes – interchangeable with specific surface area – is recorded and complete closure occurs only at 97%RH (Figure 3.4, Figure 3.5). Theoretically, a modification of the larger pore structure (macropores) can be achieved by the spatial displacement of individual stacks of mixed-layer minerals through interlayer expansion of the smectitic components, since crystalline swelling pressure (disjoining pressure) can range up to several MPa (Whitley & Smith, 2004). This likely results in unpredictable changes to the clay mineral assemblage architecture when considering interlayer hydration through mixed-layer hydration stages (cf. Ferrage, 2005) and their random distribution within the clay mineral assemblages.[21] Despite the complexity of the pore network modification, the process is reversible, as indicated by repeated wetting and drying circles and subsequent N_2 physisorption measurements (Lahn et al., 2020). However, interpreting pore size distributions derived from water vapour isotherms is challenging because swelling and pore condensation cannot be unequivocally distinguished as functions of partial pressure. Additionally, the violation of the rigidity assumption prevents the application of the modified Kelvin equation.

The presented observations of water sorption and pore network modification align with the concept of heterogeneous smectite hydration; i.e. the coexistence of mixed-layer hydration stages present during ad- and desorption of water, which is associated with hysteresis. According to Ferrage (2005), Ferrage et al. (2005, 2007, 2010) and Ferrage (2016) smectite hydration and dehydration evolves via a mixed-layer mechanism resulting in a random distribution of mixed-layer hydration stages in smectites of similar type. Thus, at the same relative humidity crystallites coexist in the same agglomerate which intercalated 1, 2 or up to 3 layers of water depending on the actual type of expandable clay mineral and the relative humidity. This mixed-layer mechanism results in heterogeneous interlayer expansion and hardly to predict pore network modification, as the modification depends on the distribution of heterogeneously hydrated crystallites within the assemblage architecture and their contribution to a specific pore size. Regarding this concept, it is possible to modify larger pores before smaller pores are completely closed and without significant water condensation in such pores. Moreover, mixed-layer hydration stages will persist for both conditioning histories explaining the small differences in pore network modification depending on conditioning history. In the light of smectite swelling, a part of the detected hysteresis might be conceived as a type of strain hysteresis. In consequence, a direct relation between the observed N_2 pore volume loss and the amount of sorbed water should not be expected. The interlayer expansion will inevitably modify the pore network in an unpredictable manner and multiple processes will occur simultaneously in the same partial pressure range as elaborated by Thommes et al. (2012). Therefore, pore network modification is considered as a dual process caused by smectite hydration and swelling as well as concomitant interparticle condensation. However, quantitative discrimination of both mechanisms is not possible without the use of an independent technique like XRD profile modelling combined with gravimetric water sorption experiments (Ferrage, 2005).

In conclusion, while the observed water sorption and pore network modifications do not conform

[21] 'Architecture' refers to the spatial and geometric arrangement of crystallites, such as a card-house structure or a regularly stacked arrangement of cards.

with classical views of single processes, they seem to align with the concept of Ferrage (2005) of smectite hydration via randomly distributed, mixed-layer stages during interlayer hydration here combined with simultaneous condensation in the interparticle space.

3.6 Conclusion

The water distribution in the pore network of four immature mudrocks was assessed by means of a combination of water- and nitrogen physisorption. Hereby, the work focused on differences in water distribution achieved during ad- and desorption conditioning and to discern governing controls and mechanisms.

- Smectite and cation exchange capacity were identified as the main controls of water vapour sorption in the studied mudrocks. Both parameters explained about 89 to 99.5% of the variance in water uptake as function of relative humidity. Moreover, the smectite content was the major cation donor and it covaried with the microstructure of the investigated mudrocks indicating its significant control over microstructure.

- The major influence of smectite implied that fundamental sorption mechanisms of smectite apply to the studied mudrocks. This included interlayer- and cation hydration, as well as volumetric interlayer expansion and simultaneous interparticle condensation. In turn, N_2 accessible pore volume was interpreted to be modified by concomitant smectite swelling and interparticle condensation implying that the modified Kelvin equation was not applicable to water sorption. It remained impossible to quantitatively discriminate the effect of both processes on nitrogen accessibility.

- Presorbed water and pore network modification occurred mainly in N_2 accessible pore space below 20 nm but complete pore filling was limited to a maximum of 8 nm and found to be specific for each sample. Generally, differences between adsorption and desorption conditioning were identifiable, but relatively minor, with a maximum variation in $W_{\max}$ of 1.75 nm at 97%RH. However, humidity conditioning at 97%RH was ambiguous due to cyclic changes between adsorption and desorption caused by temperature fluctuations. The textural parameters (V_0, A_{BET}, V_{GV}) exhibit immediate and significant losses at the lowest relative humidity, yet their current trends suggest that the absolute amount of sorbed water plays a more critical role than the conditioning history.

- The mass-volume imbalance between presorbed water and N_2 Gurvich specific pore volume loss could be estimated when clay hydration and Gurvich specific pore volume loss were combined as a linear mixing model using a natural clay mineral mixture as an analogue for the clay hydration. This approach was conceived as an approximation and the remaining imbalance was attributed to unaccounted swelling and simplifications regarding smectite hydration (cation type etc.) and the employed clay analogue.

- Water vapour sorption by mudrocks and the pore network modification by swelling and capillary water could be explained by the model of heterogeneous interlayer hydration which includes mixed-layer stages of water intercalation and therefore heterogeneous swelling and pore network modification, randomly distributed throughout an agglomerate of clay mineral crystallites.

Appendices

B.1 Carbon dioxide and argon physisorption isotherms of dry mudrocks

Ar physisorption isotherms are classified as (pseudo) type IV isotherms according to the IUPAC classification (Figure B.1) (Thommes et al., 2015). The hysteresis loops are of type H3 indicating partial filling of the pore network.

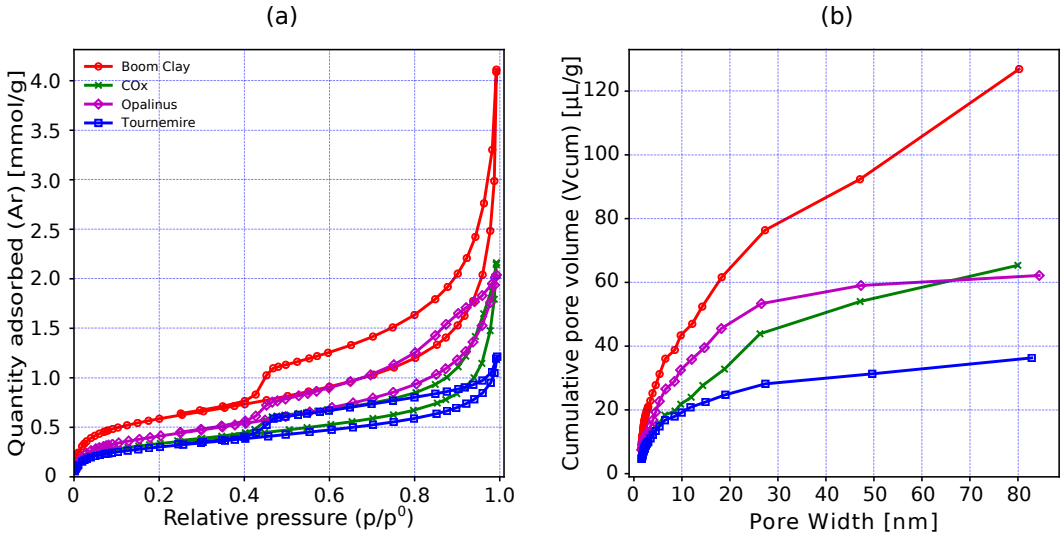

Figure B.1: (a) Argon physisorption isotherms measured at 87 K on dry mudrocks; (b) Cumulative pore size distributions were obtained from the adsorption branch of the isotherms of the dry mudrocks. PSDs were computed by a combination of DA-theory and BJH-theory.

The total Ar accessible specific pore volume ranged from 35 to 117 µL/g ($p/p^0 \approx 0.995$), with the lowest V_{GV} observed for the Tournemire argillite and the highest V_{GV} for the Boom Clay (Table B.1).

The BET specific surface areas of the mudrocks varied from 21.6 to 42.3 m^2/g. The strong retention capacity (Q_{mono}) and the adsorption energy parameter (C) are listed in Table A.5 together with the micropore characteristics (V_0,E_0,n) of Ar and CO_2 physisorption isotherms. Micropore volumes of Ar and CO_2 related linearly to each other (average difference $\approx$ 12%; intercept equivalent to zero). CO_2 micropore volumes ranged between 9 µL/g and 19 µL/g for pores up to maximum 1 nm (Thommes et al., 2015). V_0(Ar) were slightly larger and ranged from 10 to 21 µL/g.

Merged cumulative DA and BJH pore size distributions were derived from the adsorption branch of the Ar physisorption isotherms (Figure B.1b). The major pore volume of the Tournemire argillite was in pores < 20 nm ($\approx$ 65%). Contrastingly, pores between 10 nm and 25 nm contributed $\approx$ 34% to the total pore volume of the Callovo Oxfordian argillite. The PSDs of the Boom Clay and Opalinus Clay revealed significant storage volumes in pores up to $\approx$ 28 nm, ranging from 61 to 88%, respectively. Hereby, major contributions of 50%(OCM) and 26%(BCM) to the total specific pore volume were made by intermediate mesopores (10 to 25 nm). Above 30 nm the PSD curve of the Boom Clay increased almost linearly whereas the PSD curve of the Opalinus Clay nearly plateaued.

Table B.1: Textural properties of dry mudrocks by physisorption analysis of Ar and CO_2 physisorption isotherms measured at 87 K and 273 K, respectively; x_i(Ar) ; $x_j(CO_2)$; V_{GV} = Gurvich (total) specific pore volume calculated at maximum pore size (W_{BJH}) assessed [µL g^{-1}], A_{BET} = BET specific surface area [m^2 g^{-1}], Q_{mono} = BET monolayer capacity [mmol g^{-1}], C = BET energy constant [-], V_0 = DA micropore volume [µL g^{-1}], E_0 = DA characteristic energy of system [kJ mol^{-1}], n = DA exponent [-], D = mean micropore size [nm].

ID	V_{GV} [µL g^{-1}]	$W_{BJH}(V_{GV})$ [nm]	A_{BET} [m^2 g^{-1}]	Q_{mono} [mmol g^{-1}]	C [-]	V_0 [µL g^{-1}]	E_0 [kJ mol^{-1}]	n [-]	D [nm]
Boom Clay	117	267	42.3	0.509	78	21;19	12.0;15.7	1.5;1.2	1.81
Callovo Oxfordian	62	265	24.1	0.290	73	11;10	11.9;17.1	1.7;1.2	1.83
Opalinus Clay	58	268	29.9	0.359	61	12;12	12.2;15.9	2.2;1.3	1.85
Tournemire	35	351	21.6	0.260	72	10;9	11.8;15.8	1.2;1.3	1.82

B.2 Compilation of textural parameters of nitrogen physisorption isotherms of dry and moist mudrocks

Summary of textural parameters obtained by nitrogen physisorption measurements on moisture equilibrated mudrocks. Classical physisorption theories were used for the textural characterisation including DA theory of micropore filling, BET theory for specific surface area quantification, BJH theory for pore size distribution calculation and Gurvich rule for specific pore volume determination at maximum attained partial pressure. The adsorption data (11 to 97%RH) of the Callovo Oxfordian argillite (Figure 3.3b) and the Opalinus Clay (Figure 3.3c) have already been published by Lahn et al. (2020) and only a textural revision of the raw data has been carried out.

Table B.2: Textural properties of Boom Clay, Callovo Oxfordian argillite, Opalinus Clay, and Tournemire argillite equilibrated at different relative humidity in adsorption mode obtain from N_2 physisorption isotherms measured at 77 K; RH = relative humidity [%], Q_{H2O} = gravimetric water content [µL g^{-1}], V_{GV} = Gurvich (total) specific pore volume calculated at given pore width (W_{BJH}) [µL g^{-1}], A_{BET} = BET specific surface area [m^2 g^{-1}], Q_{mono} = BET monolayer capacity [mmol g^{-1}], C = BET energy constant [-], V_0 = DA micropore volume [µL g^{-1}], E_0 = DA characteristic energy of system [kJ mol^{-1}], n = DA exponent [-].

ID	RH [%]	Q_{H2O} [µL g^{-1}]	V_{GV} [µL g^{-1}]	$W_{BJH}(V_{GV})$ [nm]	A_{BET} [m^2 g^{-1}]	Q_{mono} [mmol g^{-1}]	C [-]	V_0 [µL g^{-1}]	E_0 [kJ mol^{-1}]	n [-]
Boom Clay (BCM)	0	0.0	105.9	281.6	44.10	0.452	196	16.30	14.0	2.69
Boom Clay (BCM)	11	23.9	85.9	281.6	17.10	0.176	72	5.26	12.6	3.55
Boom Clay (BCM)	32	35.2	83.3	281.6	11.20	0.115	121	3.94	12.1	3.13
Boom Clay (BCM)	56	41.3	71.9	281.6	9.67	0.099	97	3.03	12.5	3.63
Boom Clay (BCM)	75	67.7	67.5	281.6	7.66	0.079	107	2.63	12.1	3.08
Boom Clay (BCM)	97	130.0	31.0	281.6	2.48	0.025	127	0.81	10.8	4.96
Callovo-Oxfordian (COx)	0	0.0	63.1	307.6	24.60	0.252	167	8.86	13.5	2.88
Callovo-Oxfordian (COx)	11	12.0	53.3	307.6	16.20	0.166	98	5.02	13.4	3.40
Callovo-Oxfordian (COx)	32	18.4	49.8	307.6	11.70	0.120	62	3.50	13.5	3.01
Callovo-Oxfordian (COx)	56	25.3	47.4	307.6	9.65	0.099	72	3.09	13.7	2.68
Callovo-Oxfordian (COx)	75	31.8	43.8	307.6	7.60	0.078	49	2.48	13.0	2.21
Callovo-Oxfordian (COx)	97	61.4	37.1	307.6	3.42	0.035	242	1.21	11.4	4.92
Opalinus Clay (OCM)	0	0.0	61.7	321.05	31.10	0.319	129	10.60	14.4	2.95
Opalinus Clay (OCM)	11	13.9	56.4	321.05	21.90	0.225	48	6.83	13.8	2.56
Opalinus Clay (OCM)	32	21.1	52.2	321.05	18.80	0.193	48	5.44	14.1	2.87
Opalinus Clay (OCM)	56	25.0	50.5	321.05	16.50	0.169	39	4.76	14.1	2.52
Opalinus Clay (OCM)	75	35.1	45.2	321.05	12.60	0.129	36	3.82	13.2	2.29
Opalinus Clay (OCM)	97	73.9	20.8	321.05	2.62	0.027	201	1.02	11.2	3.14
Tournemire (TM)	0	0.0	34.5	306.6	24.16	0.248	160	8.14	14.0	3.35
Tournemire (TM)	11	7.0	25.6	306.6	10.20	0.104	80	3.45	13.0	2.55
Tournemire (TM)	32	13.8	19.6	306.6	5.56	0.057	139	2.01	13.0	2.72
Tournemire (TM)	56	18.6	18.5	306.6	5.19	0.053	178	1.82	12.8	3.50
Tournemire (TM)	75	30.8	17.3	306.6	3.89	0.040	180	1.29	11.1	5.51
Tournemire (TM)	97	42.5	14.2	306.6	2.89	0.030	307	1.10	12.3	3.57

Table B.3: Textural properties of Boom Clay, Callovo Oxfordian argillite, Opalinus Clay and Tournemire argillite equilibrated at different relative humidity in desorption mode obtain from N_2 physisorption isotherms measured at 77 K; For parameter description cf. Table B.2

ID	RH [%]	Q_{H2O} [µL g^{-1}]	V_{GV} [µL g^{-1}]	$W_{BJH}(V_{GV})$ [nm]	A_{BET} [m^2 g^{-1}]	Q_{mono} [mmol g^{-1}]	C [-]	V_0 [µL g^{-1}]	E_0 [kJ mol^{-1}]	n [-]
Boom Clay (BCM)	11	29.4	76.0	281.6	15.30	0.157	114	4.82	12.7	3.70
Boom Clay (BCM)	32	39.0	67.5	281.6	9.99	0.102	90	3.45	12.6	2.72
Boom Clay (BCM)	56	59.2	63.7	281.6	8.04	0.082	80	2.57	12.3	3.22
Boom Clay (BCM)	75	81.1	55.0	281.6	5.95	0.061	85	1.97	12.0	3.10
Boom Clay (BCM)	97	129.0	34.4	281.6	2.69	0.028	172	0.79	11.6	5.75
Callovo-Oxfordian (COx)	11	15.8	50.2	307.6	11.60	0.119	69	3.58	12.9	3.47
Callovo-Oxfordian (COx)	32	29.4	46.4	307.6	7.76	0.080	170	2.64	13.2	3.54
Callovo-Oxfordian (COx)	56	31.2	44.5	307.6	7.55	0.077	51	2.16	11.8	4.34
Callovo-Oxfordian (COx)	75	37.5	41.6	307.6	5.07	0.052	244	1.79	12.4	3.66
Callovo-Oxfordian (COx)	97	68.4	28.7	307.6	2.66	0.027	147	0.91	10.8	4.45
Opalinus Clay (OCM)	11	16.8	52.7	321.05	20.30	0.208	70	6.16	14.2	3.20
Opalinus Clay (OCM)	32	23.7	46.5	321.05	14.20	0.145	48	4.32	13.7	2.44
Opalinus Clay (OCM)	56	27.5	46.7	321.05	14.40	0.147	45	4.17	13.7	2.72
Opalinus Clay (OCM)	75	46.6	38.4	321.05	8.08	0.082	71	3.47	11.7	1.49
Opalinus Clay (OCM)	97	81.4	16.4	321.05	2.13	0.022	236	0.85	11.5	3.03
Tournemire (TM)	11	12.2	22.8	306.6	9.12	0.093	153	3.00	13.0	3.87
Tournemire (TM)	32	16.0	19.1	306.6	5.23	0.054	212	1.73	10.8	6.41
Tournemire (TM)	56	21.5	17.8	306.6	4.65	0.048	97	1.43	13.4	3.51
Tournemire (TM)	75	36.5	14.4	306.6	3.09	0.032	163	1.05	12.5	3.77
Tournemire (TM)	97	40.9	12.5	306.6	2.10	0.022	332	0.73	11.5	5.48

B.3 Validation of statistical treatment

To quantitatively discern statistically significant differences of textural parameters of mudrocks conditioned along the ad- or desorption pathways a simplified statistical treatment of the experimental data was devised. The outlined approach is considered as an oversimplification with respect to statistical descriptors and the statistical treatment of experimental results. Yet, such simplification does not automatically imply the same, a lower or higher level of uncertainty for the dataset because of unknown factors. For the approach's validation, a short derivation of the applied procedure is considered necessary:

To encourage the statistical significance of the observed textural differences 95% confidence intervals ($CI = 1.96 \times \sigma/\sqrt{n}$) were coupled with quantitative overlap analysis of uncertainty intervals. Hereby, the maximally found uncertainty (CV of OCM 97%RH desorption) of a particular textural parameter was transferred to the complete dataset and the approach was cross-checked by spot testing the coefficients of variation (2 to 3 repetitions) of the other mudrocks conditioned at 97%RH (desorption).

The calculated and transferred uncertainty quantities are regarded as theoretical and conservative estimates because the approach accounts for the shares listed in section 3.5.1 but is not limited to them.

(i) The technical uncertainty is covered by reference material measurements which reveal low dispersion and evidence technical reliability of the instrumentation (Figure 3.10). The textural parameter bias is below 3% for the mean value of the investigated parameters and within the given uncertainty interval of the reference material (Micromeritics-Instrument-Corporation, 2012).

(ii) Physisorption isotherms of dry mudrocks indicate minor textural heterogeneity for the N_2 accessible pore space of the mudrocks. The data comprise the physisorption specific heterogeneity of the sample set as well as human error. Further, it includes the technical uncertainty because of the significantly lower uptake of nitrogen of the mudrock sample set $Q_{N_2}(\mathrm{mr})$ with respect to the SiAl-Standard ($Q_{N_2}(\mathrm{SiAl})$ ($Q_{N_2}(\mathrm{mr}) \approx \frac{1}{10} \times Q_{N_2}(\mathrm{SiAl})$). The uncertainty is still substantially below that of the moist samples, but obviously larger on absolute scale.

(iii) The maximum uncertainty is identified for the highest moisture content and lowest nitrogen uptake. This uncertainty includes all the above factors and is complimented by the uncertainty related to moisture conditioning. The acceptable CVs of the water content and the textural parameters of the equilibrated samples (section 3.5.1) revealed a reproducible conditioning and measurement process. Hence, substantial mineralogical fractionation and uncontrollable water loss during sample preparation appear unlikely rendering samples as representative and the process reliable, despite its earlier outlined limitation (section 3.5.7). The reproducibility data of the moisturised samples also cover the uncertainty related to sample heterogeneity and technical difficulties arising from the low sorption capacity. It should be noted that the sorption capacity is still above the provided limit of detection and limit of quantification of the instrument.

Finally, transferring the found maximum experimental uncertainty to the complete dataset was considered as the most conservative uncertainty estimate possible in the study presented. Therefore, the devised procedure was regarded as inherently sound for statistical testing of the acquired dataset.

B.4 Validation of textural differences

The prominent hysteresis loop of water vapour sorption isotherms indicates that individual moisture contents differ when achieved via different conditioning processes (Figure 3.2). This, however, does not directly imply a statistically significant change in textural parameters.

The comparative approach is exemplarily shown for the mudrock collection conditioned at 97%RH (Figure B.2). On absolute scale, all textural parameter pairs of the sample set differ as expected by the measured water content ($X_{des}(RH_s) < X_{ads}(RH_s)$)[22]. An exception are the Gurvich specific pore volume and the BET specific surface area of the Boom Clay conditioned at 97%RH. Scrutiny of these parameter pairs indicates a higher water content for adsorption than for desorption conditioning of the Boom Clay. This unexpected deviation of the presorbed water content is also detected for the Tournemire argillite at 97%RH. Clearly, larger amounts of water are observed for adsorption conditioning (Figure 3.2). Though unexpected, textural parameters obtained for desorption conditioning are smaller for the Tournemire argillite compared to the corresponding adsorption data (Figure B.2).

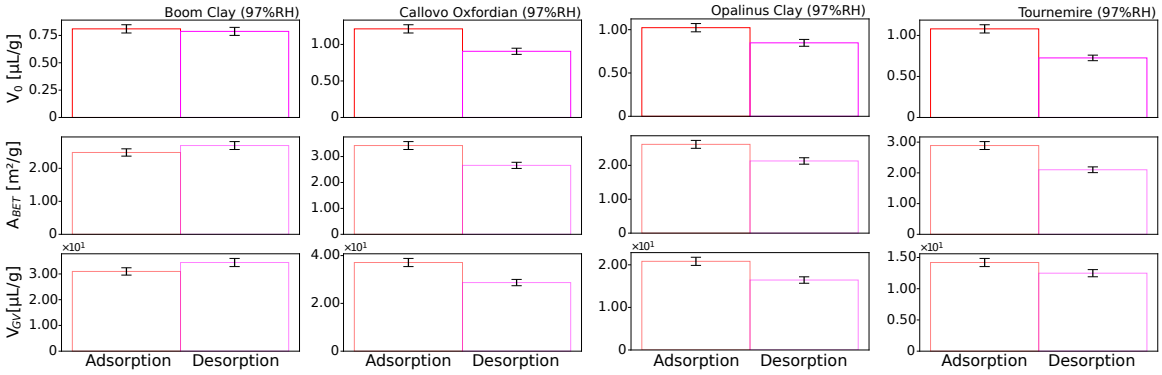

Figure B.2: Comparison of V_0, A_{BET} and V_{GV} determined for ad- and desorption conditioning at 97%RH for Boom Clay, Callovo Oxfordian argillite, Opalinus Clay and Tournemire argillite. Error bars represent 95% CIs calculated from standard deviations of 5 repetitive isotherm measurements on Opalinus Clay (equilibration at 97%RH).

Accounting for the estimated uncertainty, all textural parameters of the mudrocks equilibrated at 97%RH are identified as statistically significantly different, except for the earlier noted case of the Boom Clay. The textural parameters cannot be distinguished as statistically significantly different at 97%RH, yet they differ for the lower relative humidity conditioning. Similar to the Boom Clay, a small number of parameter pairs (13 out of 45 pairs) are classified as not statistically different, though they differ on absolute scale by $\approx 10\%$. The parameter pairs include the Gurvich specific pore volumes (11 to 75%RH) of the Callovo Oxfordian argillite. The Gurvich specific pore volume and the BET specific surface area of the Opalinus Clay conditioned at 11% and 32%RH and the V_{GV} of the Tournemire argillite conditioned at 32% and 56%RH as well as the A_{BET} at 32%RH. For the given parameter pairs confidence intervals overlap and therefore no conclusion on the difference can be drawn. Still, the water contents are clearly different and were reached via

[22] $X_i(RH_s)$ refers to a textural parameter and i to the equilibration process and s to the specific relative humidity.

different processes. A general exception are the samples conditioned at 97%RH. While the textural parameters may be significantly different, water contents are indistinguishable when 95 %CIs are considered (Figure 3.2b).

B.5 Compositional control on microstructure

Bivariate plot of smectite content vs. specific surface area and micropore volume obtained via BET theory and DA theory. The linear correlation of the given parameters supports the claim of, for example, Środoń & MaCarty (2008) that smectite exerts a substantial control on the microporosity and specific surface area of (here: the studied) mudrocks.

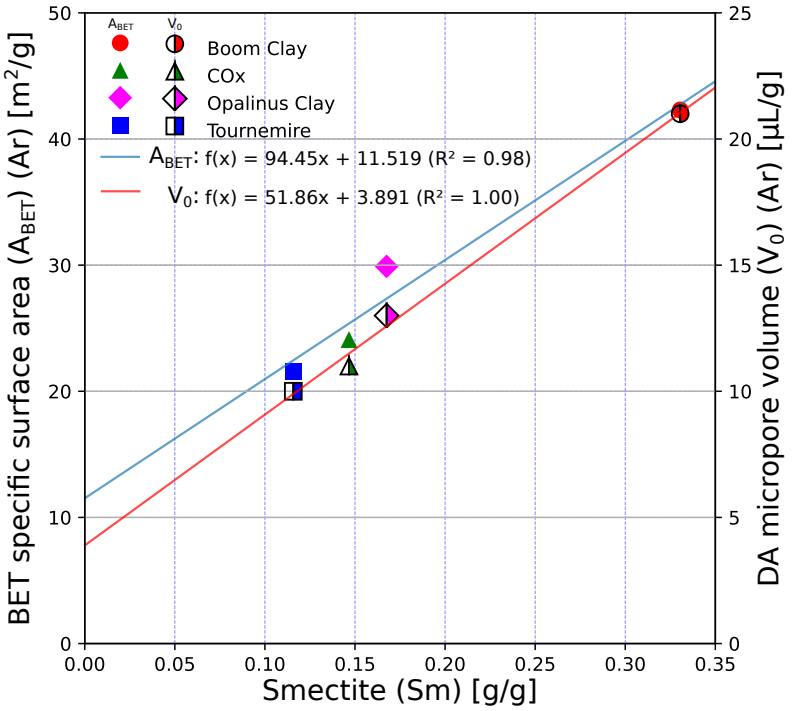

Figure B.3: Cross plot of smectite content (x-axis), BET specific surface area (left y-axis) and DA micropore volume (right y-axis). Linear regression curves are shown for each parameter pair including regression equations and the coefficient of determination (R^2).

B.6 Normalised static water vapour sorption isotherms of mudrocks

CEC and smectite content normalised static water sorption isotherms support the fair agreement of the normalised DVS isotherms discussed in the main text (section 3.5.3). Hereby, they corroborate the claim of the main influence of the given parameters on water uptake in mudrocks. The remaining difference has been attributed to variation in texture created by the fabric of the mudrocks.

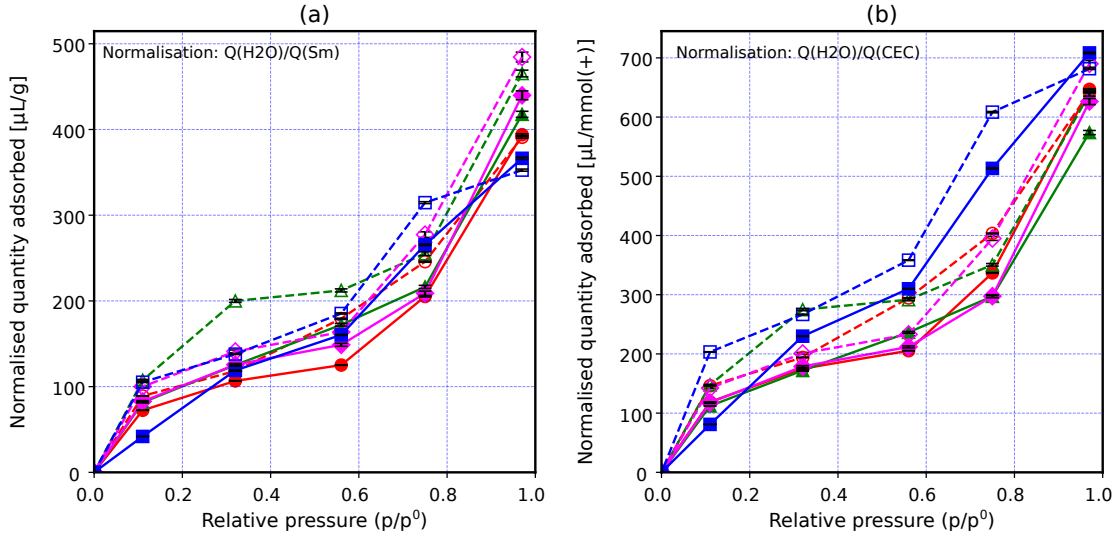

Figure B.4: Static water vapour sorption isotherms (gravimetric) normalised to (a) smectite content determined by XRD and (b) cation exchange capacity (CEC) measured by the Cu-Trien method (Stanjek & Künkel, 2016).

Chapter 4

Hysteresis in Water Sorption Isotherms of Mudrocks: Origins and Mechanisms

This chapter is a longer version of the current author's manuscript that will be submitted to a peer reviewed journal after a final internal review from the co-authors: T. Seemann, H. Claes, H. Stanjek. Hysteresis in Water Sorption Isotherms of Mudrocks: Origins and Mechanisms.

Abstract

The water sorption isotherms of mudrocks exhibit significant high- and low-pressure hysteresis, a phenomenon often abstractly discussed. This study systematically analysed the hysteresis properties of an untreated and Cu-triethylenetetramine exchanged Ypresian Clay mudrock, its clay fraction, and a purified montmorillonite. Focusing on the mechanistic understanding and parameters in control of hysteresis, the mineralogical composition and microstructure were scrutinised and linked to hysteresis phenomena. General hysteresis phenomena involve tightly bound water at zero partial pressure, sensitive to cumulative errors in uptake created by out-of-equilibrium sorption associated with kinetic hysteresis. Incomplete equilibration appeared more severe in adsorption than in desorption. For untreated and smectite-bearing samples, hysteresis is attributed to predominant smectite hydration and volumetric interlayer expansion besides interparticle condensation of water.

For swelling-suppressed, Cu-triethylenetetramine exchanged materials distinct sorption mechanisms active during ad- and desorption were mainly responsible for hysteresis. Scanning isotherms reveal capillary condensation above $p/p^0 = 0.4$ and free evaporation followed by cavitation-controlled desorption at $p/p^0 = 0.3$ to 0.45 for Cu-triethylenetetramine exchanged materials as hysteresis governing mechanisms. Cavitation is associated with a critical neck width of approximately 2.2 to 2.5 nm and aligns with capillary condensation during adsorption.

4.1 Introduction

The general definition of adsorption hysteresis reads: hysteresis emerges when ad- and desorption branches do not coincide during partial pressure (p/p^0) increase and decrease (Thommes et al., 2015). The feature has been observed for various nanoporous materials of tailored (activated carbons, metal-organic framework silicas, silicas, zeolites etc.) and geological (clays, mudrocks) origin and an empirical classification is given by the International Union of Pure and Applied Chemistry (IUPAC) (Thommes et al., 2015). Hysteresis is commonly attributed to distinct sorption mechanisms in ad- and desorption. For standard adsorptives (N_2 and Ar) hysteresis is discussed in the framework of metastable states (nucleation barrier) during adsorption causing delayed (spinodal)[1] condensation, consistent with the classical van der Waals theory, and capillary evaporation via receding menisci during desorption (Neimark et al., 2000, Neimark & Ravikovitch, 2001, Schlumberger & Thommes, 2021). Pore emptying is either unrestricted (free evaporation from independent pores) or delayed by the pore network architecture (disordered systems) in the form of pore network effects (pore blocking) and/or cavitation.

Distinctive features of a hysteresis loop are its width and its closure point defined by the p/p^0 of the merging ad- and desorption branch. The width of the hysteresis loop is determined by the thermodynamic state of the adsorptive which depends on operational temperature and pore size. The operational temperature indicates the proximity to the (pore) critical point and the pore size controls the shift of the critical point in the phase diagram under confinement (Thommes, 2004, Schlumberger & Thommes, 2021). Both parameters are complementary in that an increase in temperature effects a similar reduction in hysteresis loop width than a reduction in pore size (at constant temperature). In consequence, a fluid-specific hysteresis critical pore width (W_{hc}) and a hysteresis critical temperature (T_{hc}) can be defined which denote either the appearance ($W_{\mathrm{i}} > W_{\mathrm{hc}}$ or $T_{\mathrm{i}} < T_{\mathrm{hc}}$) or absence ($W_{\mathrm{i}} < W_{\mathrm{hc}}$ or $T_{\mathrm{i}} > T_{\mathrm{hc}}$) of hysteresis for a particular pore size (here W_{i}) at the experimental temperature (T_{i}). In the absence of hysteresis, pore filling occurs either reversible — i.e., pore condensation and evaporation take place at equilibrium — or continuous, meaning that no distinct pore condensation occurs in pores below the condensation critical pore width (W_{c}) at T_{i} or at temperatures above the (pore) critical temperature (T_{c}), where fluid behaviour is influenced by proximity to the bulk or pore critical point (Neimark et al., 2000, Thommes, 2004). The reader is referred to Thommes (2004), Horikawa et al. (2011a) and Schlumberger & Thommes (2021) for an in-depth discussion of pore- and hysteresis criticality.

The closure point of the hysteresis loop depends either on the neck width or a combination of pore geometry (neck size & shape) and adsorptive properties. Exclusively neck-width-controlled hysteresis closure is independent of the adsorptive and the closure point relates directly to a specific neck width linking pore- and bulk fluid (Thommes et al., 2006). Such type of closure is associated with pore network effects and blocking of pore bodies by smaller necks. A combined influence of the adsorptive and neck size on hysteresis loop closure is attributed to cavitation. Traditionally, cavitation has been understood as an adsorptive-dependent "*forced*" closure of the hysteresis loop

[1] Spinodal condensation is defined as the spontaneous separation of a previously homogeneous phase into two separate phases in order to minimise the free energy of the system; i.e., the spinodal coexistence curve of vapour and liquid is passed.

due to the destabilisation of the receding meniscus (Groen et al., 2003). Forced closure occurs at a partial pressure of approximately 0.42 for nitrogen and ≈ 0.35 for argon. It has sometimes been misinterpreted as indicating a specific pore size (see Bertier et al. (2016) for a discussion). Cavitation occurs only when the neck width falls below a critical threshold of 5 to 7 nm for nitrogen and argon (Ravikovitch & Neimark, 2002a,b, Thommes et al., 2006). Mechanistically, cavitation is linked to spinodal evaporation, whereby a critically stretched, metastable liquid within a pore body undergoes spontaneous bubble nucleation (cavitation). The liquid becomes stretched when its pressure falls below the saturated vapour pressure (at constant temperature), driving it into a metastable state where evaporation is thermodynamically favourable. This metastability persists until the confined liquid reaches its fluid-specific spinodal limit, beyond which the intermolecular forces are too weak to counteract the instability, resulting in cavitation. In porous materials such as mudrocks and clays, cavitation is predominantly heterogeneous, as the heterogeneous surface chemistry and morphology of the pore walls provide nucleation sites for bubble formation. Following cavitation, the pore body empties while the pore throat remains filled with liquid adsorbate. Mass transfer from the pore body to the bulk vapour phase occurs via molecular diffusion, where vapour molecules dissolve into the liquid-filled pore throat and diffuse towards the exterior bulk vapour phase.

In recent years, low-pressure hysteresis (LPH; $p/p^0 < 0.42$ for N_2) has been observed for various materials. Silvestre-Albero et al. (2012) and Bertier et al. (2016) demonstrated that LPH is attributed to a lack of achieving equilibrium in adsorption when other responsible factors such as chemisorption and sorbent deformation by swelling (e.g., hydrocarbon absorption into the structure of carbons) do not apply (Silvestre-Albero et al., 2012, Rouquerol et al., 2014). Obviously, a lack of equilibrium renders adsorption data unusable because textural features will be underestimated to an unknown extent. The proportion of apparent low-pressure hysteresis is influenced by the sorbent's porosity, its pore size distribution, the maximum analysis pressure, the experimental temperature, and the molecular size of the adsorptive (Silvestre-Albero et al., 2012). Moreover, Fink (2017) identified a strong linear correlation of the absolute amount of LPH with TOC content for the Newark "shale" which the author interpreted as a significant contribution of organic matter to the slow diffusion kinetics of nitrogen.

Water vapour sorption measurements, especially of clay-bearing materials, yield a wide variety of isotherm and hysteresis loop shapes that do not categorise within the IUPAC classification (Martin, 1957, Van Olphen, 1965, Sposito & Babcock, 1966, Likos & Lu, 2006, Arthur et al., 2015, 2020, Seemann et al., 2017). Water molecules are sensitive to surface chemical groups (e.g., OH^-, exchangeable cations) and textural properties of the sorbent resulting in a composite isotherm produced by a complex interplay of surface chemistry and pore network architecture. Hereby, a multitude of mechanisms are concomitantly active along the p/p^0 range (Thommes et al., 2012); i.e., an unequivocal deconvolution of one specific mechanism attributed to a specific p/p^0 range is not easily possible. Furthermore, in contrast to nitrogen and argon, water sorption hysteresis occurs both in meso- and micropores implying substantially different hysteresis critical pore sizes and temperatures for water compared to nitrogen and argon (Thommes et al., 2012, 2013, Rother et al., 2020).

Water vapour sorption isotherms of clay-bearing, fine-grained sedimentary rocks (mudrocks) are typically characterised by extensive hysteresis along the complete partial pressure range. Especially, swelling clays like smectites show stepped water vapour isotherms with notable hysteresis that is attributed to (i) interlayer expansion and contraction (stepwise change in basal d_{001}-spacing measurable by XRD) via heterogeneously distributed, mixed-layer hydration stages of interlayer water governed by the type of interlayer cation and the layer charge (Cases et al., 1992, Bérend, 1995, Laird et al., 1995, Laird, 1999, Chiou, 1997, Michot et al., 2005, Ferrage, 2005, Ferrage et al., 2007, 2010) and (ii) interparticle condensation at high partial pressure (Johnston et al., 1992, Rinnert et al., 2005, Lindholm et al., 2019). Additionally, the enthalpy of hydration ($Mg^{2+} > Ca^{2+} > Na^{+} > Cs^{+}$) stipulates the magnitude of tightly bound water associated with the hydration shell of the interlayer cation (Kuligiewicz & Derkowski, 2017).

While water vapour sorption is less common compared to Ar and N_2, by now an ample number of water vapour sorption isotherms of mudrocks have been published for various formations, compositions and burial histories revealing various, individual isotherm shapes (Tang et al., 2017, Seemann et al., 2017, Sang et al., 2019, Ma et al., 2020, Chen et al., 2021, Hou et al., 2021). Extensive hysteresis is also observed for smectite-lean mudrocks like the thermally overmature Longmaxi and Wufeng formation (Seemann et al., 2017, Ma et al., 2020, Chen et al., 2021, Yang et al., 2020a, 2021). The absence of swelling clays as well as the complex isotherm shape insinuate that factors other than volumetric expansion actively influence the hysteresis of water vapour sorption in mudrocks. Attempts to force the closure of hysteresis loops in water sorption isotherms have occasionally been reported in the literature but are rarely discussed in detail.[2] Yang et al. (2020a) studied organic-rich samples of the Longmaxi and Wufeng formation, for which steps in the desorption branch are observed between $0.45 < p/p^0 < 0.55$. Contrastingly, Yang et al. (2021) and Seemann et al. (2017) published water vapour sorption isotherms of Ordovician and Silurian mudrocks presenting forced closure attempts between $0.4 < p/p^0 < 0.5$ and between $0.525 < p/p^0 < 0.625$, respectively. Sang et al. (2019) presented water vapour sorption isotherms of mudrocks collected from a coal mine in the Illinois basin revealing no step upon desorption while in their most recent study, the authors show closure attempts between approximately $0.58 < p/p^0 < 0.75$ for the Yibin mudrock (Sang et al., 2020a).

In fact, the currently available data sets of water vapour sorption isotherms of mudrocks form an inconsistent picture with respect to the qualitative and quantitative assessment of hysteresis. Especially, the manifestation of low-pressure hysteresis in mudrocks is neither fully understood nor is there a thorough mechanistic description of the attempted hysteresis closure for water vapour sorption on mudrocks provided in the literature.

The present study aims to provide insight into the mechanism of (low-pressure) hysteresis and the hysteresis closure of water vapour sorption isotherms observed for mudrocks and clay minerals (+ mixtures). To assess the source of hysteresis and its mechanism, natural mudrocks of the Ypresian Clay formation were selected. These mudrocks were part of earlier studies in light of their radioactive waste hosting potential and consequently, a large data set with background characterisation was available for this study. Besides the Ypresian Clay and its separated clay fraction, a purified

[2]'Attempted' forced closure of hysteresis loops refers to the incomplete overlap of the adsorption and desorption branches at relative pressures below the step in the desorption branch.

source clay (SWy2 montmorillonite) was included as an analogue. The sample set was texturally characterised by multiple adsorptives (H_2O, N_2, Ar) in its natural and chemically treated state. The chemical treatment was Cu-triethylenetetramine exchange in order to fix the basal distance of the interlayer and prevent swelling. The textural description was accompanied by a mineralogical and geochemical characterisation to correlate textural and compositional modifications and relate them to the occurrence of hysteresis and its mechanisms.

4.2 Materials and Methods

The sample set comprises a Wyoming montmorillonite (SWy2) and a Ypresian Clay mudrock (YPC) from the location Elverdinge (Belgium). Prior to experimentation, sample materials were split into representative batches and processed to obtain an original and a Cu-triethylenetetramine (Cu-Trien) exchanged subsample. The samples were stored in a desiccator above silica gel until experimentation.

4.2.1 SWy2 montmorillonite (source clay)

The Wyoming montmorillonite was purchased as a source clay from The Clay Minerals Society. The raw material was purified by repeated Atterberg treatment at room temperature ($\approx 298(2)$ K). The enriched SWy2 was homoionically exchanged (n = 4) by adding 50 mL of a 1 M NaCl solution to about 1 g of clay. After centrifugation, the supernatant was discarded and replenished by the 1 M NaCl solution. This was repeated four times. Excess salt was removed by several washing steps with deionised water followed by dialysis until the electrical conductivity equalled that of deionised water ($\kappa \leq 0.02\,\mu S$). Subsequently, the material was dried, mortared and sieved (63 µm mesh).

4.2.2 Ypresian Clay mudrocks

The Ypresian Clay mudrock was received as air dried hand specimen. A representative amount of sample was gently crushed to an aggregate size $\leq 400\,\mu m$ and split into three subsamples (a_1: XRD, a_2: clay separation, a_3: sorption experiments). Subsample a_1 was used for mineral quantification and treated according to section 4.2.6. The second subsample a_2 served for clay fraction separation which was performed by means of sedimentation in an Atterberg cylinder (≤ 5 g of bulk sample per 1 L of deionized water). The initial dispersion was prepared by 5 min of ultrasound bathing. The dispersion was left to settle for 24 h at room temperature (298(2) K). The clay fraction enrichment was terminated after a clear supernatant free of particles was reached (app. 7 d). Afterwards, the clay dispersion was pressure-filtered ($< 0.45\,\mu m$), air dried, homogenised in a mortar and sieved (63 µm mesh). The clay fraction was split evenly into two subsamples (YPC-CF, YPC-CF-CuTrien) for further analysis. Subsample a_3 was milled in a McCrone micronizing mill (15 min in ethanol) and subsequently dried, mortared and sieved (63 µm mesh). Any chemical treatment was avoided to prevent chemical alteration of the parent material.[3]

[3]TOC and TIC analysis supported by quantitative XRD analysis revealed minor amounts of organic matter and carbonates.

4.2.3 Cu-triethylenetetramine exchange

To test the effect of clay swelling on water (low-pressure) hysteresis the subsamples of the bulk material (YPC), the clay fraction (YPC-CF) and the purified montmorillonite (SWy2-Na) were homoionically exchanged with the index cation Cu-triethylenetetramine (Cu-Trien). To assure a quantitative exchange with Cu-Trien the samples were shaken in a 4 mM Cu-Trien solution for 24 h (mass-fluid ratio $\approx$ 0.3 to 0.5 g/50 mL). After the exchange, the material was dispersed in deionised water and pressure-filtered (< 0.45 µm) until the washing solution reached the electrical conductivity level of deionised water. It was assumed that any excess Cu-Trien was removed by this procedure. The exchanged material was air-dried, gently mortared and sieved (63 µm mesh).

4.2.4 Water vapour sorption

Gravimetric water vapour sorption isotherms were measured at 303 K between $0 \leq p/p^0 \leq 0.94$ (flow rate 100 $\mathrm{cm^3\,min^{-1}}$)[4] using a *DVS ET* instrument (Surface Measurement Systems Ltd.).[5] Approximately 16 to 35 mg of material was installed in an aluminium sample holder and dried at 378 K for 24 h under a constant nitrogen stream (99.999% purity) flowing at 200 $\mathrm{cm^3\,min^{-1}}$. An operational equilibrium criterion of $\mathrm{d}m/\mathrm{d}t \leq m \times 0.5\ \frac{\mu g}{g\,min}$ over a period 0.5 h was assigned including a maximum stage time of 12 h. The instrument was multi-point calibrated using saturated salt solutions that cover a partial pressure range from 0 to 0.93 (cf. Seemann et al., 2017). Standard isotherm measurements were supplemented by adsorption and desorption scanning between $0 \leq p/p^0 \leq 0.94$ according to the protocol of Grosman & Ortega (2005, 2008) and Cimino et al. (2013). First, the enveloping isotherm is measured followed by cyclic isotherms of which the maximum (descending) or minimum (ascending) partial pressure becomes successively smaller. Hereby, the hysteresis loop was consecutively scanned. A time-based equilibrium criterion of 5 h per partial pressure was imposed. Scanning isotherm tests were limited to Cu-Trien-exchanged materials. The schematics of the hysteresis scanning are displayed in Figure 4.8 in section 4.4.

4.2.5 Physisorption measurements (N_2, Ar)

The textural characterisation of the materials was performed by nitrogen (N_2, 77 K) and argon (Ar, 87 K) physisorption on dry and evacuated materials ($T_{\mathrm{dry}} = 378$ K for 12 h, $P_{\mathrm{vac}}(N_2) \leq 5$ Pa, $p_{\mathrm{vac}}(\mathrm{Ar}) \leq 13$ mPa). A pressure-rise test was conducted prior to argon physisorption measurements accepting maximum pressure-rise rates of 2.7 Pa/min at room temperature. A detailed measurement protocol is given in *chapter 2*.

N_2 physisorption isotherms were measured in the manometric instrument *Gemini VII 2390t* (Micromeritics Instrument Corporation, Norcross, GA, USA) assuming operational equilibrium when the pressure drop was less than 0.01% of the target pressure over 30 s. N_2 physisorption measurements were performed in a p/p^0 range between 0.001 and 0.995 at 100 discrete pressure points (adsorption: 64; desorption: 36). The saturation pressure (p^0) was measured separately for

[4] $\mathrm{cm^3\,min^{-1}}$ refers to the total gas flow rate at standard conditions by Surface Measurement Systems Ltd..

[5] Relative humidity is defined as the ratio of waters partial vapour pressure to the saturation vapour pressure of water at a given temperature provided as percentage. Here, relative humidity is equivalent to the partial pressure of water given as p/p^0.

each pressure point.

Argon physisorption isotherms were measured in the manometric apparatus *Autosorb-I-MP* (Quantachrome Instruments, Boynton Beach, FL, USA). Operational equilibrium was assumed when the rate of pressure change was below 16 Pa/min and within the defined tolerance band per pressure point ($p/p^0 < 0.1$: +0.0003 & -0.0001; $p/p^0 > 0.1$: +0.009 & -0.003). The isothermal uptake was determined at 81 and 29 discrete pressure points in ad- and desorption mode between $5 \times 10^{-7} < p/p^0 < 0.995$. The saturation pressure was specified manually and assumed to be constant because of technical reasons (101.325 kPa at the normal boiling point of Ar at 87 K).

Quantitative analysis of the physisorption isotherms was performed by means of the classical physisorption theories encompassing Gurvich rule, Brunauer-Emmett-Teller theory (BET), Dubinin-Astakhov theory (DA), and Barrett-Joyner-Halenda theory (BJH) (Gurvich, 1915, Brunauer et al., 1938, Rouquerol et al., 2007, Dubinin & Astakhov, 1971, Barrett et al., 1951). For a succinct and applied summary of the above theories, the reader it referred to Seemann et al. (2017).

4.2.6 X-ray diffraction

The mineralogical composition of the bulk materials and the separated clay fraction of the YPC was investigated by X-ray diffraction (XRD). For phase quantification the particle size fraction ≤ 400 µm of the bulk mudrock was spiked with 0.2 g/g internal standard (α-Al_2O_3) and milled in a McCrone micronizing mill for 15 min. To avoid excessive strain and heat damage, ethanol was used as cooling agent. The spiked dispersion was air-dried and manually homogenised. Powder beds were prepared by sieving (63 µm mesh) using the top-fill method. To secure random orientation and avoid excessive texturing, the uppermost layer was removed using adhesive tape.

Detailed clay mineral identification was performed on oriented samples prepared by sedimentation from dispersion in deionized, micro-pure water. The dispersion was pipetted on either a glass or ceramic substrate and air-dried. Following the protocol of Środoń (2006) glycerol saturation was performed as well as heating the oriented samples to 673 K and 823 K for 90 min for mineral identification. After the heating period, the samples were cooled in a desiccator for at least 12 h.

The randomly oriented powder beds and the oriented samples were measured on a Bruker D8 diffractometer equipped with a secondary graphite monochromator and a scintillation counter using Cu Kα radiation (40 kV, 40 mA). Diffraction patterns of random powder beds were recorded under ambient conditions (P, T, RH) between 2 to 82° 2θ while oriented samples were measured from 2° and 32° 2θ, both at a step size of 0.02° 2θ and 5 s counting time. The mineral quantification was performed by Rietveld refinement using the BGMN-based software Profex (Doebelin & Kleeberg, 2015). Customised clay structure models of Ufer et al. (2008) and Ufer & Kleeberg (2015) were employed for mineral quantification.

4.2.7 Cation exchange capacity

The effective cation exchange capacity (CEC) was measured by means of the Cu-Trien method (Stanjek & Künkel, 2016). Approximately ≤ 0.5 g of dry, micronized material was added to 4 mM Cu-Trien solution (2 mL of 0.1 M Cu-Trien solution + 48 mL deionized, micro-pure water) and equilibrated for 1 h while shaking. The supernatant was filtered via an in-line syringe filter

(<0.45 µm) and its Cu-Trien concentration was quantified photometrically via UV-VIS spectroscopy on a Specord210 Plus (Analytik Jena). The Cu-Trien concentration was recalculated based on a four-point standard calibration and a pH-dependent charge correction of the Cu-Trien complex was applied.

4.2.8 Total (in-) organic carbon content

The organic matter content was quantified based on total organic- (TOC) and inorganic (TIC) carbon analysis using a liquiTOC II analyser. The analysis protocol of Grohmann et al. (2018) was employed. Briefly, 0.1 g of micronized bulk material was heated to 823 K and the temperature was held for 10 min. Subsequently, the material was cooled to 673 K and heated again to 1273 K for 400 s. The carbon dioxide release was continuously monitored by an infrared cell detector (detection limit = 10 µg/g, TOC error = 0.006 g/g, TIC error = 0.016 g/g).

4.3 Results

4.3.1 Mineralogical composition

The quantitative and qualitative composition of the sample set is provided in Table 4.1. Diffraction patterns of the original and Cu-Trien-exchanged Ypresian Clay are presented with and without internal standard (Figure 4.1). The YPC comprised mainly clay minerals (total clays = 0.68 g/g) distributing into illite (0.17 g/g), dioctahedral smectite (0.48 g/g) and minor kaolinite (0.03 g/g). This finding was qualitatively supported by XRD measurements on oriented samples and the dioctahedral nature of the smectite by scrutiny of the d_{060} at 1.5 Å (section 4.3.1, Figure 4.2, Figure 4.3). The broad low-angle peak attributed to smectite nearly merged with the 001 peak of the illite suggesting interstratification of illite and smectite, corroborated by the unusually broad higher order peaks of illite (Figure 4.1, Figure 4.3). The higher d-spacing of the original material was associated with undefined hydration states during the XRD measurement (ambient humidity conditions) and the unknown original cation occupancy of the Ypresian Clay. Quartz constituted 0.17 g/g and feldspars 0.1 g/g and 0.02 g/g of alkali feldspar and plagioclase while carbonates (here dolomite/ankerite), pyrite, gypsum and rutile were identified as accessories (< 0.01 g/g). Gypsum was likely an alteration product of oxidised pyrite. The Cu-Trien-exchanged subsample exhibited the same mineralogical composition within the expected error, with differences in quartz and smectite contents of less than 0.02 g/g. Gypsum was not detected in the Cu-Trien-exchanged samples and has probably been dissolved during the Cu-Trien exchange.

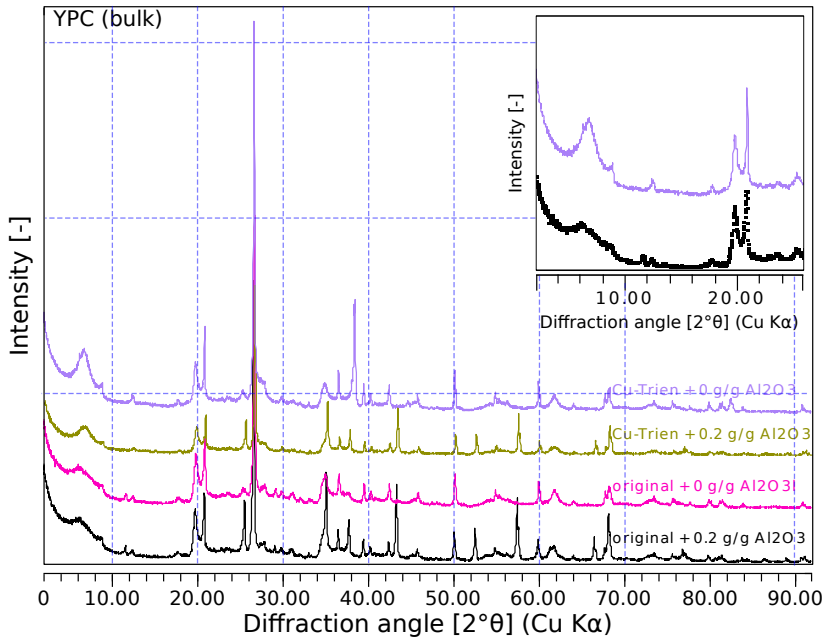

Figure 4.1: X-ray diffraction powder patterns of the original and Cu-Trien-exchanged Ypresian Clay mudrock. The samples were measured with (0.2 g/g α-Al_2O_3) and without (0 g/g α-Al_2O_3) internal standard. The black line (original) and the green line (Cu-Trien) represent XRD powder patterns of samples infused with internal standard and the pink (original) and lilac (Cu-Trien) patterns represent samples measured without internal standard. The inset shows a zoom-in of the lower 2°θ range of the original and Cu-Trien-exchanged materials indicating the shift in the 001 reflection of the smectite.

Table 4.1: Mineralogical composition obtained by XRD and Rietveld refinement using bulk powder preparation (YPC) and oriented samples of the separated clay fraction (YPC-CF, Atterberg treatment) and the purified montmorillonite (SWy2); d. = detected not quantified; n.d. = not detected; n.m. = not measured.

ID	**Unit**	**YPC**	**YPC-CuTrien**	**YPC-CF**	**SWy2-Na**
Quartz	[g/g]	0.17	0.19	d.	d.
Alkalifeldspar	[g/g]	0.10	0.11	d.	n.d.
Plagioclase	[g/g]	0.02	0.03	n.d.	n.d.
Ankerite/Dolomite	[g/g]	0.01	0.01	n.d.	n.d.
Pyrite	[g/g]	0.01	0.01	n.d.	n.d.
Gypsum	[g/g]	0.01	n.d.	n.d.	n.d.
Rutile	[g/g]	n.d.	0.01	n.d.	n.d.
Kaolinite	[g/g]	0.03	0.03	d.	n.d.
Smectite	[g/g]	0.48	0.46	d.	d.
Illite+Muscovite	[g/g]	0.17	0.17	d.	n.d.
TOC	[mg/g]	3.6	n.m.	4.8	2.6
TIC	[mg/g]	0.35	n.m.	0.9	0.9
CEC	[mmol(+)/g]	0.32	n.m.	0.58	0.81

Clay mineralogical composition

Oriented samples were used for clay mineral identification (Figure 4.2a) and to record the effect of the Cu-Trien exchange on the *00l* reflections of the expandable clays (Figure 4.2b; exemplary shown for SWy2). Three different types of phyllosilicates have been identified based on their *00l* reflections and their behaviour upon glycerol and heat treatment.

Intercalation of glycerol shifted the broad and asymmetric 12.4 Å reflection towards higher *d*-spacing of about 17.7 Å. Upon heating to 673 K and 823 K this peak collapsed to 10 Å. This was indicative of smectite. It was not unequivocally clear whether all illite and smectite were interstratified or also separate phases were present. Analysis of the 060 (d_{060}) reflection in the powder diffraction pattern of the clay fraction of the Ypresian Clay evidenced the dioctahedral nature of the smectite due to the d_{060} value of 1.50 Å (Figure 4.3, Środoń & MaCarty (2008)).

The asymmetric 10 Å peak merged with the broad peak of the 001 reflection of the smectite. It experienced no alteration by glycerol, yet its intensity increased upon heating to 673 K. The above supported the presence of illite.

The 7 Å peak was asymmetric and displayed a duplex peak. It was insensitive towards glycerol intercalation and heating to 673 K. Yet, it collapsed when the sample was heated to 823 K which pointed to potentially two kaolinites. Chlorite could not be identified in the clay fraction. Additionally, minor quartz and feldspar contaminations were detected in the clay fraction as well as corundum artefacts at 25.5, 35.1 and 37.8 $2°\theta$ originating from the ceramic holder which were used for pattern alignment.

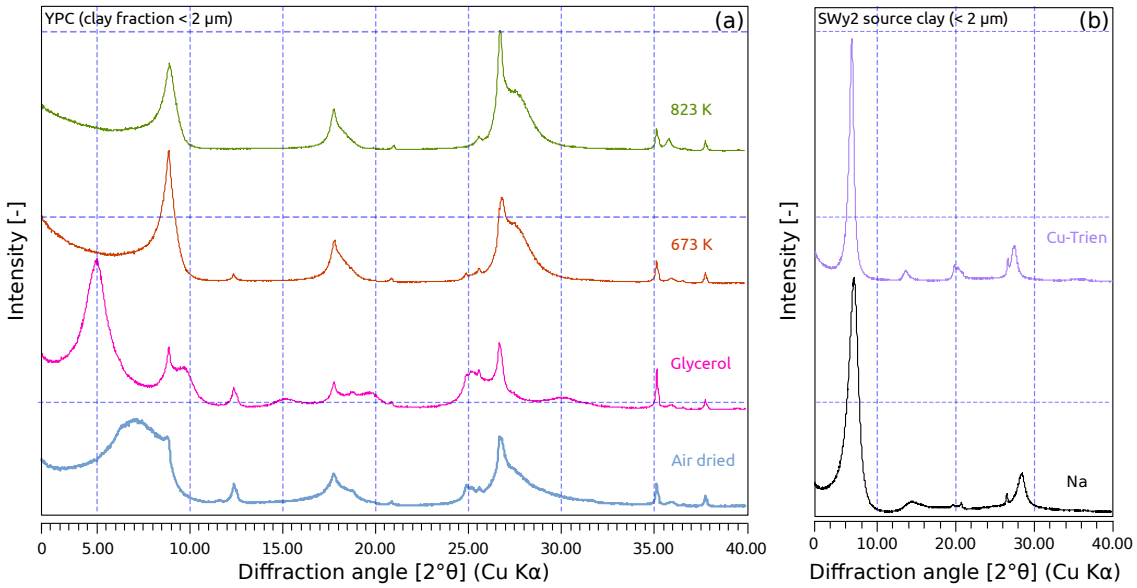

Figure 4.2: (a) Diffraction patterns of the oriented samples of the clay fraction (<2 µm) of the Ypresian Clay mudrock including the original material, the glycerol expanded material (glass carrier) and the heated materials (673 K and 823 K; ceramic carrier); (b) Diffraction patterns of the oriented SWy2 montmorillonite showing the Na- and Cu-Trien-exchanged material.

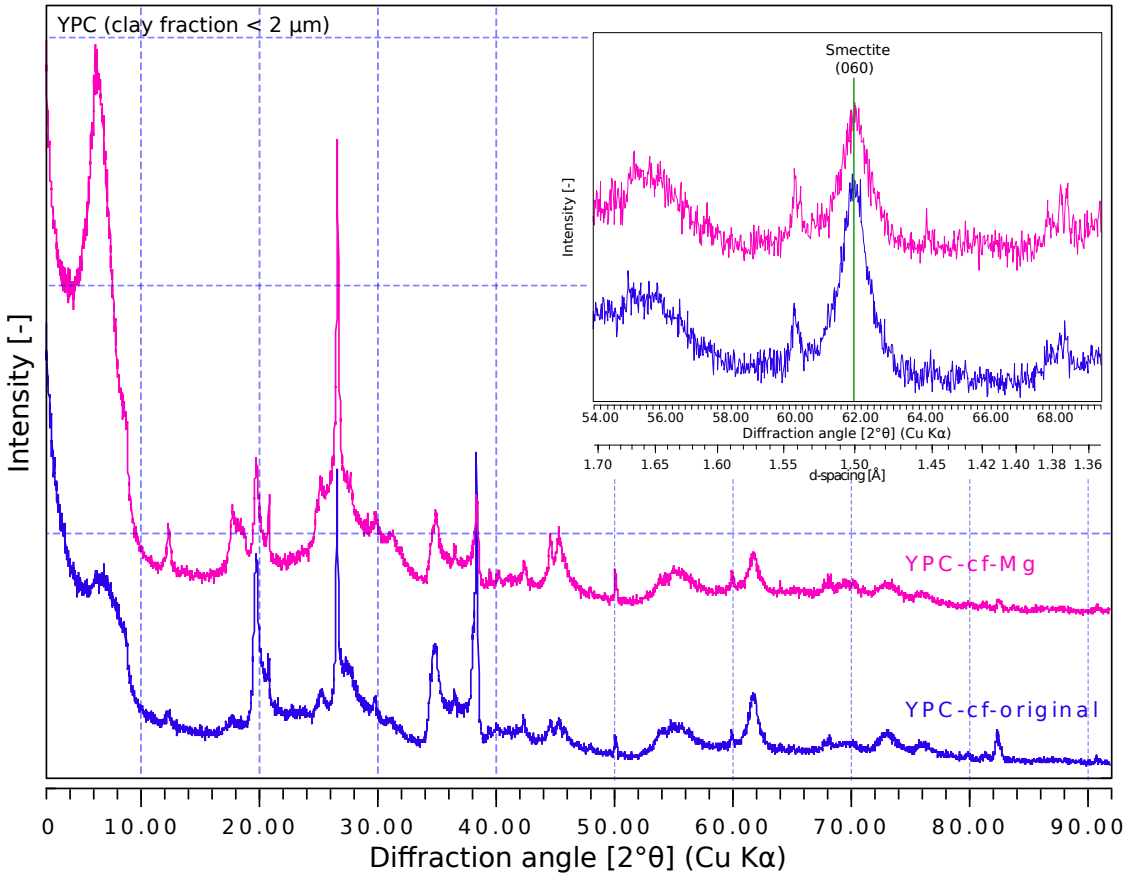

Figure 4.3: X-ray diffraction powder patterns of the separated clay fraction (Atterberg treatment) of the Ypresian Clay mudrock. The original material is presented by a blue line and the Mg-exchanged material is represented in pink. The inlet shows a zoom-in of the higher $2°\theta$ range (lower d-spacing) to discriminate di- and trioctahedral smectites based on the position of the 060 reflection.

The purified montmorillonite was analysed qualitatively as oriented samples to verify its purity and the effect of Cu-Trien exchange on the basal spacing (Figure 4.2b). The SWy2 was composed of montmorillonite and minor amounts of quartz were recognised which was used for pattern alignment. The Cu-Trien intercalation in the interlayer shifted the 001 reflection of the smectite from 12.3 to 13.1 Å.

TOC, TIC and CEC

In addition to mineralogy, CEC, TOC and TIC were measured (Table 4.1). The CECs of the YPC, YPC-CF and SWy2-Na were 0.32 mmol(+)/g, 0.58 mmol(+)/g and 0.81 mmol(+)/g, respectively. TOC ranged between 3.6 mg/g and 4.8 mg/g for the bulk material and the clay fraction, respectively. TIC values were below 1 mg/g for all samples. TOC and TIC were low and fell within the analyser's error band (cf. section 4.2.8), rendering the data prone to error and, therefore, unreliable. However, the effect of such low organic matter content was considered negligible for the scope of the study, though there is a general lack of consistency in the published literature regarding the effect of organic matter on water uptake in clay-bearing materials (Xie et al., 2023). The negligible inorganic carbon

content fitted the minor amounts identified by XRD.

4.3.2 Pore structure characterisation

Ar and N_2 physisorption isotherms are consistent in isotherm type (IV; no plateau) and hysteresis loop type (H3, H4) according to the IUPAC classification (Thommes et al., 2015) (Figure 4.4 and Figure 4.5).

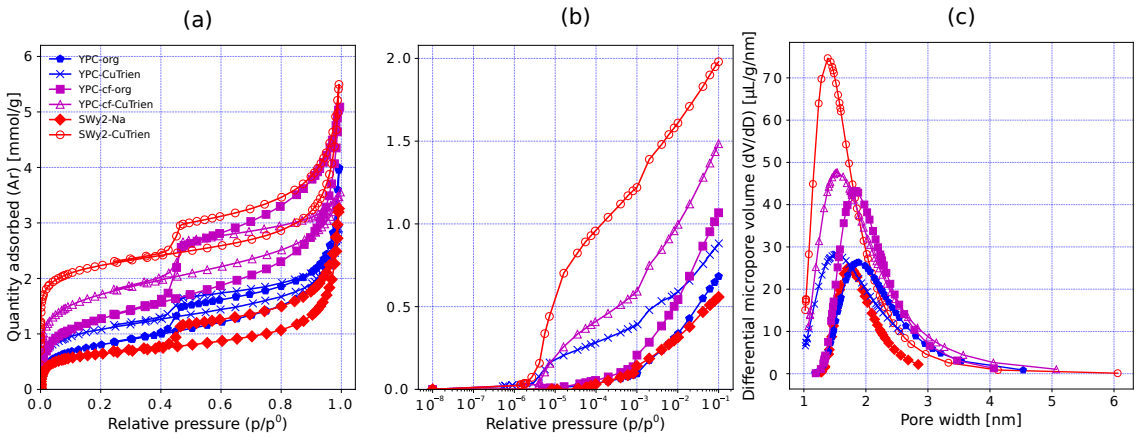

Figure 4.4: (a) Overlay of molar Ar physisorption isotherms measured at 87 K of untreated and Cu-Trien-exchanged SWy2, YPC, and YPC-CF; (b) Semi-logarithmic plot of Ar physisorption isotherms in the ultra-low pressure region ($p/p^0 \leq 0.1$) of untreated and Cu-Trien-exchanged SWy2, YPC and YPC-CF; (c) Micropore size distributions calculated according to Medek (1977) based on DA theory; Isotherms of SWy2-Na, SWy2-CuTrien, YPC-CF and YPC-CF-CuTrien were collected from *Chapter 2* since the identical sample material was used for the presented study.

Argon isotherms revealed changes in the low p/p^0 region upon Cu-Trien treatment; i.e. the exchanged materials showed substantial uptake in the micropore region. Figure 4.4b emphasised this difference in semi-logarithmic display of the ultra-low-pressure region. Ar-isotherms of the Cu-Trien-exchanged samples showed uptake in a consistent and narrow pressure range between $2\times10^{-6} < p/p^0 < 4\times10^{-6}$. Contrastingly, Ar adsorption started only at $2\times10^{-5} < p/p^0 < 3\times10^{-5}$ for the original materials and the uptake was considerably lower (Figure 4.4b). This difference was also reflected in the micropore size distributions indicating a shift towards lower average pore size (1.50(0.02) nm) for the Cu-Trien-exchanged materials.

The above trends were quantitatively assessed by the classical textural parameters including Gurvich specific pore volume (V_{GV}), BET specific surface area and monolayer capacity (A_{BET}, Q_{mono}), and micropore volume and micropore capacity (V_0, Q_0). V_0 and A_{BET} of Cu-Trien-exchanged materials increased relative to the original material and ranged from 20.9 to 72.9 µL/g (Ar) and 47.4 to 166.1 m^2/g (Ar), respectively. The largest increase was identified for the SWy2 samples which was 3.5-fold (Ar) and 3.8-fold (N_2) for the micropore capacity and the specific surface area. Generally, N_2-based textural parameters denoted similar trends to Ar, yet slightly different quantities were calculated (section C.1 Table C.1 and Table C.2 in the appendix).

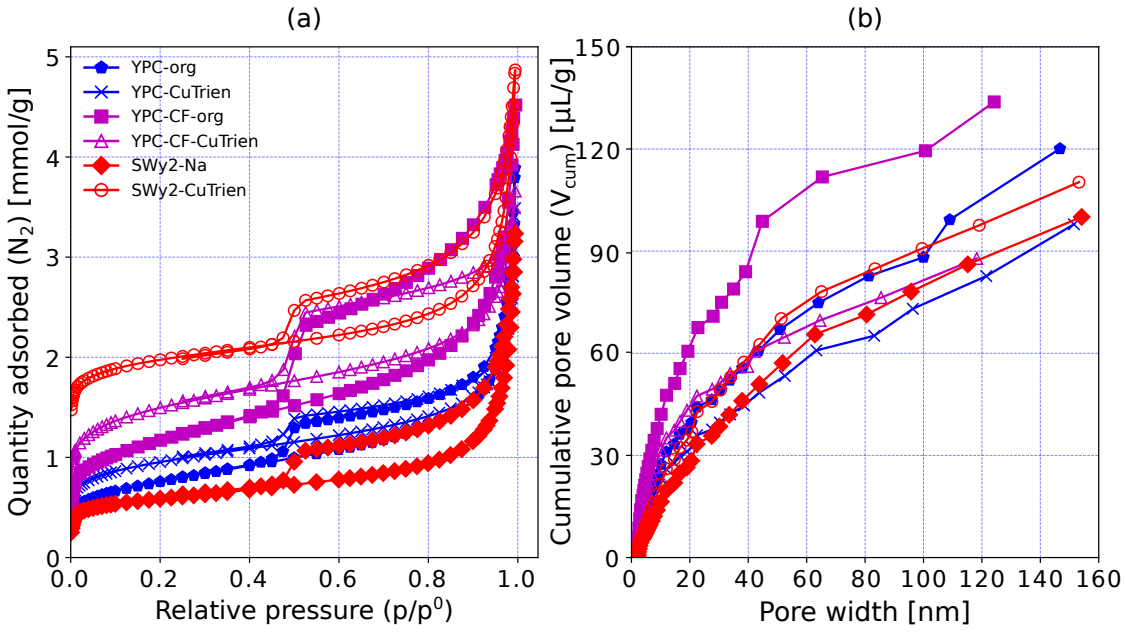

Figure 4.5: (a) Overlay plot of molar N_2 physisorption isotherms measured at 77 K of untreated and Cu-Trien exchanged SWy2, YPC and YPC-CF; (b) Cumulative pore size distributions calculated by BJH theory in the meso/ macropore range obtained from the adsorption branch of the nitrogen isotherms; Isotherms of SWy2-Na, SWy2-CuTrien, YPC-CF and YPC-CF-CuTrien were collected from *Chapter 2* since the identical sample material was used for the presented study.

Gurvich specific pore volumes ($W_{\mathrm{BJH}} = 250\,\mathrm{nm}$, $p/p^0 = 0.9923$) increased only for the SWy2 upon Cu-Trien treatment. The V_{GV} of YPC and YPC-CF displayed a slight decrease. The V_{GV} reduction was confirmed by cumulative pore size distributions obtained from nitrogen physisorption isotherms in the meso- and macropore size range calculated via BJH theory (Figure 4.5b). Cumulative pore size distributions emphasised that pore network alteration was not restricted to the micropore range upon Cu-Trien-exchange but was also detectable in the meso- and macropore regions of the materials. The cumulative PSD of the SWy2 material diverged below 20 nm and ran parallel above this threshold. In contrast, both YPC samples showed continuously diverging PSD curves which were stronger for the YPC-CF than for the YPC mudrock. No specific pore size was detected in the mesopore range for the studied samples.

4.3.3 Water vapour sorption isotherms

Water vapour isotherms of the YPC and YPC-CF resembled a type IV isotherm whereas the isotherm of the SWy2-Na did not fit IUPACs' classification (Figure 4.6). All isotherms approached p^0 asymptotically and displayed (low-pressure) hysteresis. Low-pressure hysteresis was more pronounced in the original materials; in the Cu-Trien-exchanged samples, it was largely reduced, although a slight hysteresis with a variable width along the lower p/p^0 range persisted. The retained amount of water after desorption to $p/p^0 = 0$ is provided in Table 4.2. The water vapour isotherms of Cu-Trien-exchanged materials possessed a similar step between p/p^0 0.45 and 0.3 which was

hardly detectable for the original materials. In contrast, the water vapour isotherm of the SWy2-Na revealed two distinct steps that disappeared after Cu-Trien treatment at the discrete partial pressures (Figure 4.6a). The isotherm of the SWy2-Na was consistent with published water vapour isotherms of sodium montmorillonite (Cases et al., 1992, Bérend, 1995, Lindholm et al., 2019). Gurvich specific pore volumes ($p/p^0 = 0.94$, $\rho_{H2O} = 1\,g/mL$) ranged between $275\,\mu L\,g^{-1}$ and $98\,\mu L\,g^{-1}$ (Table 4.2). Generally, the maximum water uptake ranked for untreated and Cu-Trien-exchanged materials in the order SWy2 > YPC-CF > YPC.

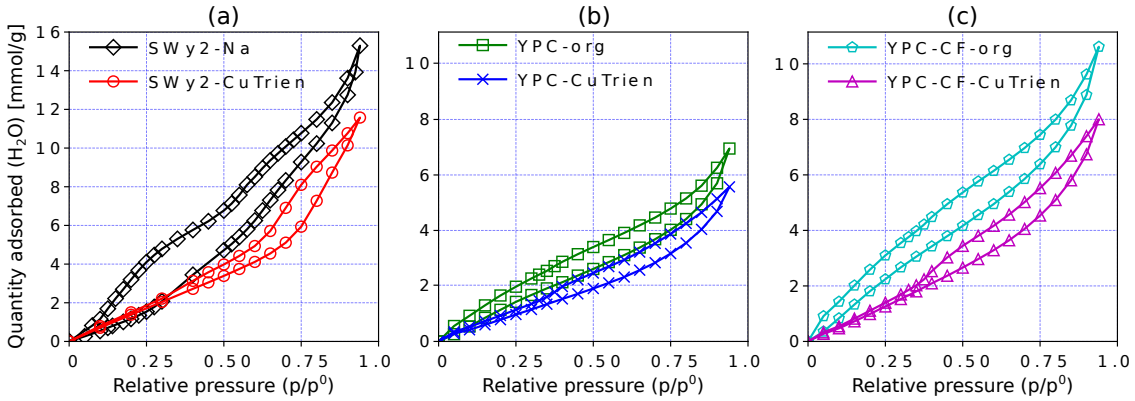

Figure 4.6: Water vapour sorption isotherms (303 K) measured on untreated and Cu-Trien-exchanged samples of the SWy2 montmorillonite, the YPC mudrock and the clay fraction (YPC-CF) of the Ypresian Clay mudrock. Isotherms were measured gravimetrically using the dynamic vapour sorption method.

Table 4.2: Collection of descriptive isotherm parameters obtained from the H_2O vapour sorption isotherm of the YPC mudrock, its clay fraction (YPC-CF) and the purified Wyoming montmorillonite (SWy2); Gurvich volumes (V_{GV} [µL/g]) were calculated at $p/p^0 = 0.94$ assuming bulk liquid density of water ($\rho = 1\,g/mL$); The strong retention capacity of water (Q_{SRC} [mmol/g]) was obtained from the residual moisture after desorption to zero p/p^0; the hysteresis loop closure range (attempted H-loop closure) was established by the step range in the desorption branch.

ID	V_{GV} [µL/g]	Q_{SRC} [mmol/g]	H-loop closure [p/p^0]
SWy2-Na	275	0.30	0
SWy2-CuTrien	208	0.27	0.3 to 0.4
YPC-org	123	0.46	0
YPC-CuTrien	98	0.05	0.3 to 0.45
YPC-CF-org	191	0.74	0
YPC-CF-CuTrien	144	0.10	0.3 to 0.4

4.3.4 Scanning isotherms of Cu-Trien-exchanged materials

Cyclic ascending and descending water vapour scanning isotherms were measured by the DVS method at 303 K of the Cu-Trien-exchanged SWy2 and YPC-CF (Figure 4.7). The scanning isotherms revealed clear differences between the enveloping isotherm cycle and the sub-cycles. The adsorption branches of the enveloping isotherms were consistently lower or equal to the recorded sub-cycles while the desorption branches of sub-cycles displayed good agreement with the enveloping

isotherm after merging at approximately $p/p^0 \leq 0.45$. Sub-cycles were in good agreement with respect to their individual ad- and desorption branches.

Ascending scanning isotherms were measured to a minimum partial pressure of 0.48 and 0.38 for the SWy2-CuTrien and the YPC-CF-CuTrien covering the complete upper hysteresis loop, respectively (Figure 4.7b, d). All sub-cycles exhibited hysteresis, with the hysteresis loop broadening as the minimum partial pressure during scanning decreased. The adsorption branches of the sub-cycles approached the saturation pressure asymptotically and merged at their maximum p/p^0 (> 0.9) with the enveloping curve. The desorption branches of the enveloping isotherm and the sub-cycles matched each other well.

Descending hysteresis scanning was performed between p/p^0_{max} 0.3 and 0.80 and revealed two notable features: (i) boundary curve merging of enveloping isotherm and sub-cycles at the attempted closure step between $0.3 < p/p^0 < 0.45$ and (ii) absence of low-pressure hysteresis below $p/p^0_{max} = 0.4$ of sub-cycles (Figure 4.7a, c; Figure 4.11). Adsorption branches of descending sub-cycles of the SWy2-CuTrien and YPC-CF-CuTrien were above or approximately equal ($p/p^0 \leq 0.3$) to the enveloping isotherms, yet they overlapped each other well.

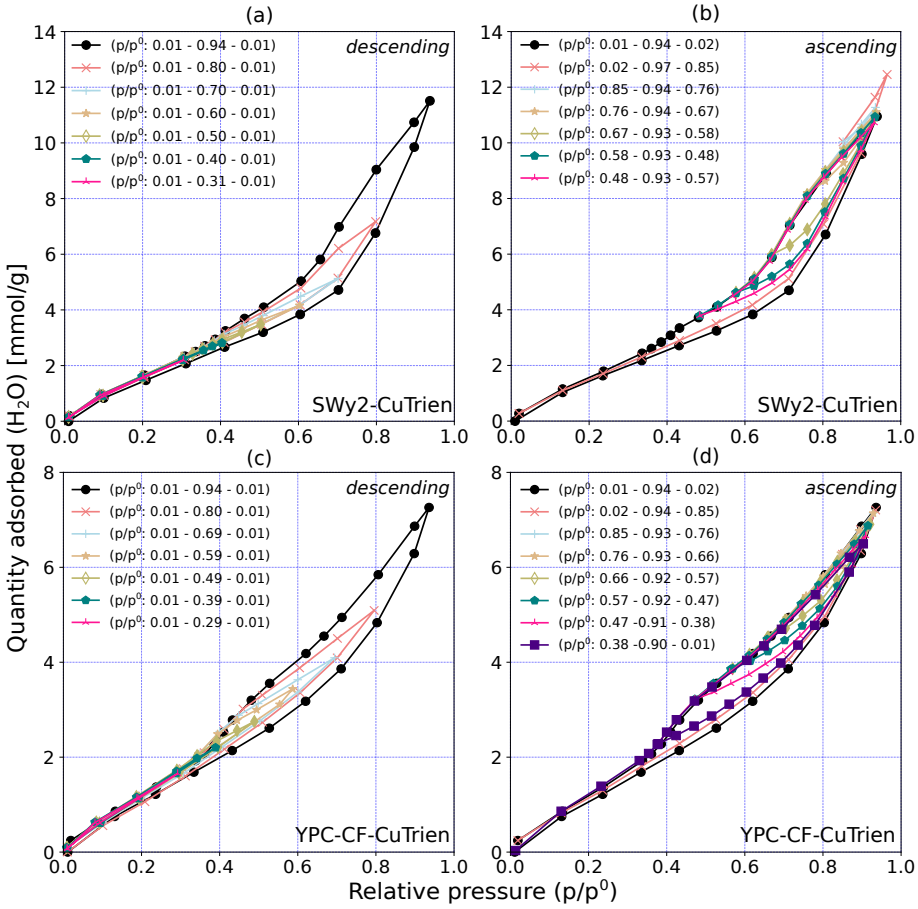

Figure 4.7: (a, c) Descending and (b, d) ascending water scanning isotherms of Cu-Trien-exchanged SWy2 (a, b) YPC-CF (c, d) measured by the DVS method with a time-based equilibrium criterion ($\mathrm{d}m/\mathrm{d}t = 5\,\mathrm{h}$). During the first sub-cycle measured on the SWy2-CuTrien the apparatus over-generated the target humidity and a maximum p/p^0 of 0.97 was reached instead of the target p/p^0 of 0.94. Therefore, the first cycle exceeds the enveloping water vapour isotherm.

4.4 Discussion

The following will discuss various sources of hysteresis in water-clay-bearing systems. For an overview of the following discussion, Figure 4.8 schematically illustrates the hysteresis loop of a mudrock water vapour isotherm, with key features highlighted — including examples of ascending (blue) and descending (light red) scanning isotherms. Moreover, some specific mechanisms are shown, that are of concern specifically for non-swelling, Cu-Trien-exchanged materials. Generally appearing and more specific sources of (low-pressure) hysteresis will be discriminated, including (i) tightly bound water in the form of a strong retention capacity, (ii) kinetic/out-of-equilibrium hysteresis, (iii) sorbent swelling and (iv) distinct sorption mechanisms. Finally, an attempt is made to discern primary controls and mechanisms of hysteresis in mudrocks, with a special focus on desorption mechanisms of Cu-Trien-exchanged materials, taken as potential analogues for non-swelling mudrocks.

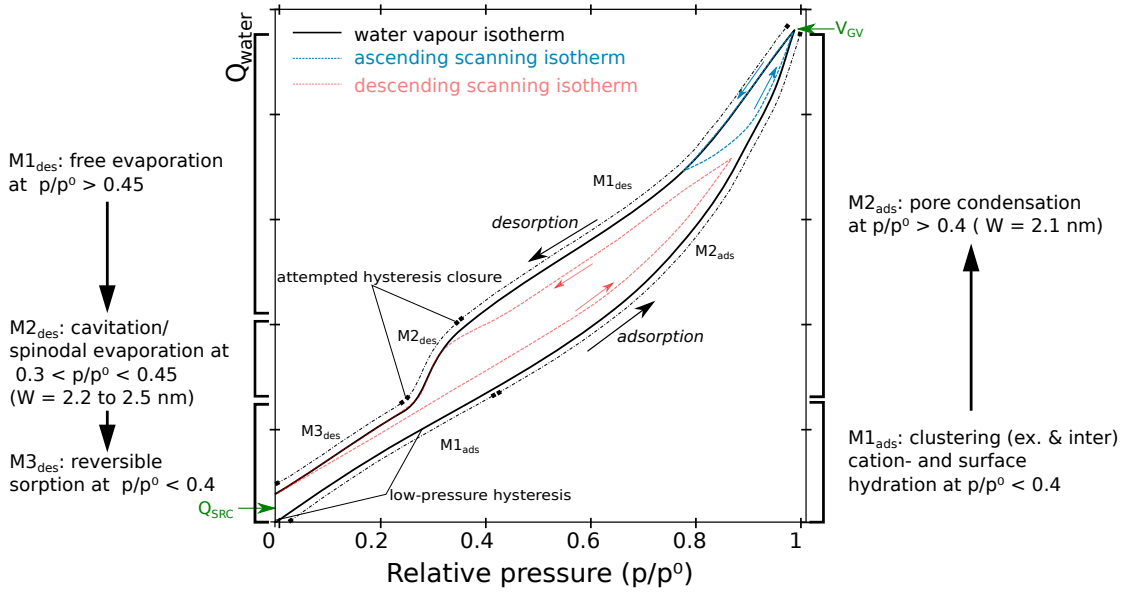

Figure 4.8: Sketch of a theoretical water vapour sorption isotherm (black solid line) of a mudrock; special hysteresis features (low-pressure hysteresis and attempted hysteresis closure) and specific sorption mechanisms separated for ad- ($M1_{\mathrm{ads}}$ to $M2_{\mathrm{ads}}$) and desorption ($M1_{\mathrm{des}}$ to $M3_{\mathrm{des}}$) are indicated. The relative pressure range of the particular sorption mechanisms is indicated by the black dashed envelop lines. Strong retention capacity (Q_{SRC}) and Gurvich specific pore volume (V_{GV}) are shown at zero p/p^0 and maximum p/p^0, respectively. The directions of ascending (pale blue, dashed line) and descending (pale red dashed line) scanning isotherms are shown and discussed in detail in the main text. The mechanisms are based on the data analysis presented in the main text. The specific role of crystalline swelling (p/p^0 dependent on actual cation type) and osmotic swelling (p/p^0 > threshold p/p^0 of capillary condensation) has not been indicated.

4.4.1 Tightly bound water and low-pressure hysteresis

A common feature of water vapour sorption isotherms of mudrocks and clays is low-pressure hysteresis and the often absent isotherm closure at $p/p^0 = 0$. Seemann et al. (2017) observed a lack

of closure for a broad selection of mudrocks, confirmed by various authors for various formations (Tang et al., 2017, Yang et al., 2020a,b, 2021, Chen et al., 2021). A similar observation was made by Bérend (1995) and Cases (1997) for different homoionically exchanged montmorillonites, while Martin (1957) and Sposito & Babcock (1966) identified low-pressure hysteresis for kaolinite-water systems. No systematics have been discerned so far for mudrocks regarding the quantity of strongly retained water at zero p/p^0 and low-pressure hysteresis whereas for pure clays explanations like cation hydration and swelling were outlined (Martin, 1957, Sposito & Babcock, 1966, Michot et al., 2005). The lack of consistency and systematics of the published mudrock data is likely related to an insufficiently detailed isotherm- and experimental uncertainty analysis combined with a comprehensive characterisation of the exchangeable cation population, their surface chemistry and the micropore size distribution of mudrocks. Generally, the residual amount of water at $p/p^0 = 0$ (here termed strong retention capacity) was low for the studied samples ranging from 0.05 to 0.75 mmol/g corresponding to 2 to 7% of the total uptake (Table 4.2). Distributed over the specific surface area of the materials, the residual water corresponded to 0.6 to 8.1 µmol/m^2. On absolute scale, the strong retention capacity and the low-pressure hysteresis (width) were above (i) the erratic weighing error of the instrument ($\Delta m_{\max} \approx 14$ µg over five days) and (ii) larger than the average hysteresis width during a blank isotherm measurement ($\Delta m_{\mathrm{hw}} \approx 1.2$ µg); both metrics were measured on a non-porous 100 mg reference weight. Analysis of time-mass data indicated a non-negligible influence of the equilibrium criterion on the strong retention capacity, as the operational equilibrium was not achieved during the final desorption stage (Figure 4.9). Rates of mass change calculated over the last 100 min of the final desorption stage ($p/p^0 = 0$) were about 1.5× the defined equilibrium criterion for the Cu-Trien-exchanged materials and they were approximately four times higher for the untreated materials. This observation is interpreted as *kinetic* contribution to the strong retention capacity and low-pressure hysteresis (cf. section 4.4.2).

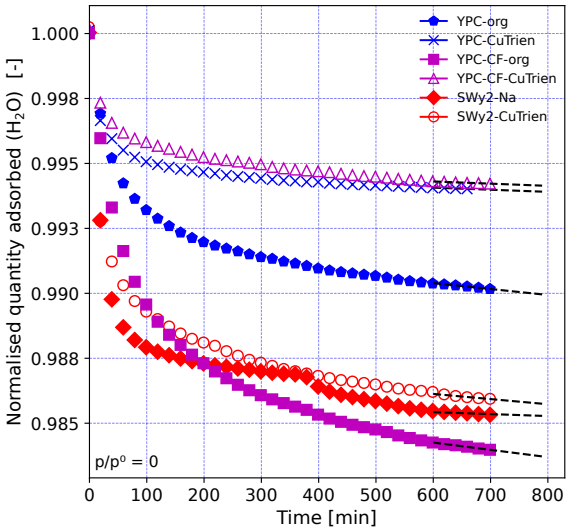

Figure 4.9: Normalised time-mass plots of untreated and Cu-Trien-exchanged samples obtained at the final desorption stage ($p/p^0 = 0$); dashed lines indicate linear regression fits of the final 100 min of the stage time illustrating the sample-specific slope of time-mass data. The qualitative trend remains valid when the calculation is performed over shorter times like 30 min. The mass at the beginning of the p/p^0 stage ($t = 0$) was used for normalisation.

Interestingly, ascending and descending sub-cycles of scanning isotherm measurements on Cu-Trien-exchanged samples revealed a nearly complete absence of low-pressure hysteresis upon the second sorption cycle (Figure 4.7). Considering that sub-cycles of scanning isotherms were started without drying at elevated temperatures in between cycles emphasised the role of the strong retention capacity in low-pressure hysteresis. The behaviour was interpreted as the saturation of sorption sites responsible for the strong retention capacity of water during the initial sorption cycle. As a result of this saturation, there was no longer a noticeable low-pressure hysteresis detected. In consequence, the strong retention capacity was not understood as a mere artefact of incomplete equilibration, but a true physical factor contributing to low-pressure hysteresis in water vapour sorption isotherms — at least for the Cu-Trien-exchanged materials, since the original materials were not subjected to hysteresis loop scanning. However, Michot et al. (2005) noted that the "quasi-equilibrium" status of the gravimetric water sorption technique also contributes to low-pressure hysteresis as indicated above. Furthermore, crystalline swelling or, as expressed in broad terms by Dang et al. (2021), interlayer water ($p/p^0 < 0.2$) will additionally affect LPH for smectite-bearing materials as exemplified by the sodium montmorillonite in this study (cf. section 4.4.3 or Michot et al. (2005)).

The control over the strong retention capacity remained abstract up to now but water sorption hysteresis is often attributed to cation hydration, swelling, the strong interaction potential in micropores down to the molecular size as well as specific interactions with surface functional groups or abstractly to strong water-mudrock interactions (Martin, 1957, Sposito & Babcock, 1966, Tang et al., 2017, Sang et al., 2019).

Chiou (1997) demonstrated that the water sorption behaviour is substantially influenced by the type of exchangeable cation, controlling water uptake in swelling clays. Effectively, the hydration enthalpy of cations ($Mg^{2+} > Ca^{2+} > Na^{+} > K^{+} > Cs^{+}$ taken from Smith (1977)) stipulates the quantity of strongly bound water associated with the hydration shell of the exchangeable cations (Chiou, 1997, Derkowski & Kuligiewicz, 2022). While for the homoionic source clay the major cation was sodium, the exchangeable cation mix and its quantitative distribution were unknown for the Ypresian Clay samples. Based on thermogravimetric data summarised by Derkowski & Kuligiewicz (2022), it was assumed that the hydration shell of sodium was likely removed during sample drying, whereas for YPC samples a *"quasi dry"* state had to be assumed. Quantitative analysis of exchangeable cations yielded effective CECs of 0.81 mmol/g (SWy2-Na) > 0.58 mmol/g (YPC-CF) > 0.31 mmol/g (YPC) (Table 4.1). Translated into hydration numbers ($X_i = Q_{\mathrm{SRC,i}}/CEC_{\mathrm{i}}$), the strong retention capacity amounted to 0.4 H_2O/cation (SWy2-Na), 1.3 H_2O/cation (YPC-CF) and 1.5 H_2O/cation (YPC), respectively. These hydration numbers were significantly lower than those reported by Michot et al. (2005) and Woodruff & Revil (2011), which may be attributed to cation exchange processes that are not exclusively governed by smectites, as was the case in their studies. However, despite also being derived from montmorillonites, the hydration numbers reported by Bérend (1995) and Cases (1997) fall within the same data range as observed in the presented study. This apparent discrepancy questions whether the strong retention capacity is solely determined by the hydration of exchangeable cations, given the unexpectedly low hydration values. Instead, the estimated strong retention capacity may be regarded as an addition to an existing hydration shell,

particularly in smectite-bearing materials, due to the previously described incomplete drying at 378 K.

Moreover, the Cu-Trien-exchanged materials showed a strong retention capacity and low-pressure hysteresis as well, despite that Cu-Trien supposedly does neither form a hydration shell nor does it expand (Kaufhold et al., 2011). While the strong retention capacity could be an artefact of a lack of equilibration, Kaufhold et al. (2023) recently demonstrated that the cation exchange with Cu-Trien as index cation may be incomplete leaving behind remnants of the original cation population as non-exchangeable but likely hydratable cations. The non-exchangeable cations (mostly Na^{+}, Ca^{2+} or Mg^{2+}) may still have or form a hydration shell during the isotherm measurement that remains stable at zero relative humidity unless heating is applied to the samples (Kaufhold et al., 2011, 2023, Derkowski & Kuligiewicz, 2017). In turn, the retention of a small amount of hydratable, but non-exchangeable cations may at least partially explain the minor LPH of the Cu-Trien-exchanged samples. A removal of LPH by surface rehydroxylation, as suggested by Saliba et al. (2016) for silicas, is considered irrelevant because the materials were heated to merely 378 K; a temperature insufficient for the dehydroxylation of clay minerals (Emmerich, 1999, Derkowski & Kuligiewicz, 2022).

Alternatively to the hydration of exchangeable cation, the strong retention capacity of water and low-pressure hysteresis could also be associated with surface adsorption in micropores. Micropores possess overlapping surface force fields strong enough to retain sorbed water, if no additional energy (temperature) is applied. The presence of surface functional groups, such as hydroxyl groups, within the micropore region might have enhanced this retention process, by engaging in specific interactions driven by the dipole moment of water. Consequently, lowering the partial pressure is insufficient to remove tightly bound surface water in micropores. According to Cychosz et al. (2017) and Schlumberger & Thommes (2021), an ultra-low vacuum at high temperature is even required to withdraw water from smaller micropores. A correlation to any of the micropore descriptors could, however, not be established based on the available data.

The collective findings of this study suggest that the strong retention capacity contributes to low-pressure hysteresis, although its magnitude is likely overestimated due to incomplete equilibration. In Cu-Trien materials, the absence of LPH in secondary sorption cycles indicates that the so-called strong retention sites became saturated during the initial cycle. For smectite-bearing materials, interlayer expansion was the dominant control on low-pressure hysteresis, while interlayer hydration likely contributed to their overall strong retention capacity.

4.4.2 Kinetic hysteresis

Kierlik et al. (2001) and Woo et al. (2002) stated the idea that hysteresis in disordered materials, such as Vycor controlled pore glasses, can arise from out-of-equilibrium fluid states during physisorption experiments. This behaviour is linked to metastable fluid states, a process described by Thommes (2004) as *long time dynamics*. Long time dynamics fall within the category of kinetic hysteresis and are governed by adsorptive diffusivity and sorption kinetics combined with the complexity of the pore network, making them specific to the sorptive-sorbent system. The deviation of the sorption process from thermodynamic equilibrium can be quantified by the Deborah number

(De), where $De \approx 0$ indicates a state close to equilibrium, while higher values correspond to increasing kinetic limitations, and therefore a greater distance to equilibrium (Keller & Staudt, 2005).

Kinetic limitations can present a significant challenge in isotherm measurements, particularly at low temperatures. In general, long time dynamic processes suggest that thermodynamic equilibrium is not attained during the measurement; however, these processes evolve so slowly that hysteresis remains highly reproducible. Consequently, long time dynamics are difficult to distinguish experimentally, as they extend beyond the timescales accessible in standard adsorption measurements (Thommes, 2004).[6]

In an earlier DVS study on 13 mudrocks, the effect of equilibrium criterion was tested on an overmature Longmaxi mudrock (smectite lean) in the range of $\mathrm{d}m/\mathrm{d}t = m \times 10\,\frac{\mu g}{g\,min}$ to $m \times 0.3\,\frac{\mu g}{g\,min}$ over 10 min (Seemann et al., 2017). The data indicated that thermodynamic equilibrium was not reached, but the effect was only relevant at $p/p^0 > 0.925$. Comparison of DVS isotherms with static isotherms measured on smectite-bearing mudrocks taken from *chapter 3* revealed a diminished hysteresis loop width for the Opalinus Clay in the static measurements, but not for the other mudrocks. However, static isotherms showed higher absolute water uptake for all samples implying a consistent lack of equilibration of the DVS measurements.

DVS isotherms of geological materials are commonly measured with the producer-recommended equilibrium criterion of $m \times 10\,\frac{\mu g}{g\,min}$ to $m \times 20\,\frac{\mu g}{g\,min}$ over a period of 10 min (Sang et al., 2019, Lindholm et al., 2019, Hou et al., 2021). Sometimes the equilibrium criterion is not reported, despite its importance for the judgement of the data quality (e.g., Yang et al., 2020a,b). The applied equilibrium criterion in this study ($\mathrm{d}m/\mathrm{d}t \leq m \times 0.5\,\frac{\mu g}{g\,min}$ over 0.5 h) was far stricter than recommended by *Surface Measurement Systems Ltd.* or used by other researchers. Still, it may have been insufficient for "true" equilibrium measurements, especially for swelling-clay-bearing materials as suggested earlier (Figure 4.9).

Comparing DVS isotherms measured with a time criterion (p/p^0 constant for 5 h and 1 h) and a mass change criterion ($\mathrm{d}m/\mathrm{d}t \leq m \times 0.5\,\frac{\mu g}{g\,min}$ over 0.5 h) provided indication of the effect of the equilibrium criterion on the overall water sorption hysteresis. Figure 4.10 displays the areal hysteresis index (AHI) computed after Tang et al. (2017) where A_i denotes the integral area under the respective isotherm branch:

$$AHI = (A_\mathrm{des} - A_\mathrm{ads})/A_\mathrm{ads} \times 100 \tag{4.1}$$

The AHI was consistently higher for the time-based criteria increasing the values between 17% and 33% for the Cu-Trien-exchanged materials. Especially, for the "margin" case of the untreated and smectite-rich YPC (1 h vs. $m \times 0.5\,\frac{\mu g}{g\,min}$ over 0.5 h) the AHI rose by 45% for the time-based criterion, revealing the substantial effect that the equilibrium criterion has on the isotherm and the hysteresis width of the untreated sample. Moreover, the "margin" case emphasised that the earlier discussed strong retention capacity will be overestimated by the systematic lack of equilibrium because of its cumulative character. For the given case, the strong retention capacity grew by 0.32 mmol/g (i.e. $\approx 70\%$).

[6] This interpretation assumes comparable adsorption and desorption rates, which does not hold in general and still hysteresis is reproducible (cf. discussion in Bertier et al., 2016).

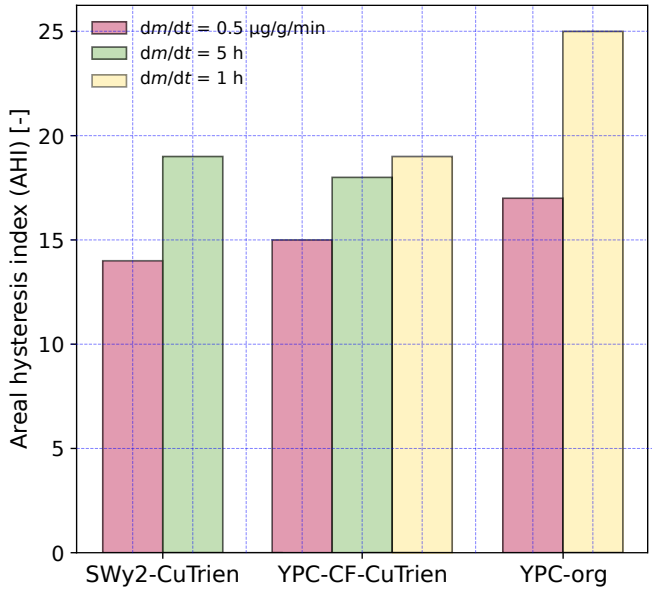

Figure 4.10: Areal hysteresis index (AHI) of Cu-Trien-exchanged materials and the Ypresian Clay bulk rock measured by the DVS method with different equilibration criteria (mass-based vs. time-based). The AHI was calculated after Tang et al. (2017).

Comparison of the time-based and dm/dt-based isotherms for the Cu-Trien-exchanged materials reveals further differences in sorption behaviour. Adsorption branches of time-based isotherms consistently showed lower uptake compared to those measured with a dm/dt criterion. Deviations become more pronounced at high p/p^0 values suggesting that kinetic effects in adsorption increase as a function of partial pressure. This, ultimately, results in a significantly higher maximum uptake when isotherms are measured with a dm/dt criterion. This discrepancy aligns with a systematic lack of equilibrium in the adsorption process, as evidenced by the time dependency of uptake.

In contrast, desorption branches exhibited characteristics consistent with equilibrium conditions. Once the desorption branches of time-based and dm/dt-based isotherms converge, their differences between are minimal (relative difference of 3 to 5%). It should be noted that the p/p^0 of convergence is specific to the individual equilibrium criterion because the convergence is affected by the governing mechanism of desorption as well as the maximum uptake governed by the incomplete equilibration during adsorption (see section 4.4.5).

The equilibrium status of the desorption branch was further corroborated by sub-cycles of ascending and descending scanning isotherms. These generally showed excellent overlap, both with each other and with the boundary curve (Figure 4.7). These observations support the conclusion that the desorption branch is in equilibrium, while the adsorption branch is not. If both isotherm branches were systematically out of equilibrium, scanning isotherms would have resulted in a stepwise increase in uptake due to the cumulative retention of adsorbate at the lowest target p/p^0. Instead, overlapping desorption branches are observed, consistent with equilibrium conditions in the desorption process.

Consequently, a portion of the hysteresis observed in both swelling and non-swelling clay-bearing

materials may be attributed to the selected equilibrium criterion, leading to kinetic hysteresis. A loosely defined equilibrium criterion can greatly contribute to hysteresis at both high and low p/p^0 owing to its cumulative effects. Moreover, it adversely impacts the strong retention capacity and promotes low-pressure hysteresis (section 4.4.1). It should be emphasised that this observation does not imply control of long time dynamics, but rather highlights the general influence of the equilibrium criterion on hysteresis. This is consistent with the findings of Michot et al. (2005), who characterised water vapour sorption as a 'quasi-equilibrium' technique prone to incomplete equilibration, thereby producing low-pressure hysteresis. Finally, it should be noted that the extent of these effects strongly depends on the combination of equilibrium criterion and sample.

4.4.3 Sorbent swelling and geometrical deformation

Silvestre-Albero et al. (2012) specified sorbent swelling as a source of permanent hysteresis because of the integration of, e.g., paraffin into the molecular structure of organic matter. Expendable clay-bearing materials are characterised by extensive water vapour hysteresis; primary, a ramification of cation hydration and the intercalation of water via mixed-layer stages in the interlayer space of expandable clay minerals which is significantly affected by cation type and layer charge (Mooney et al., 1952b, Barrer, 1978, Cases et al., 1992, Cases, 1997, Bérend, 1995, Chiou, 1997, Laird, 1999, Ferrage, 2005). The sodium SWy2 contained only montmorillonite and quartz as accessory mineral (Table 4.1). Its water sorption isotherm resembled the typical isotherm shape of a sodium montmorillonite with two discrete steps in desorption and an ill-defined double-step upon adsorption presented by various authors (Barrer & Reay, 1957, Cases et al., 1992, Laird et al., 1995, Lindholm et al., 2019, Arthur et al., 2020).

Cases et al. (1992) and more recently Lindholm et al. (2019) discussed the sorption processes of sodium montmorillonite in broad detail and correlated the stepped isotherm shape with changes in d-spacings along the c-axis of the clay mineral measured by XRD. The authors inferred that the interlayer expansion and concurrent geometric deformation played a substantial role in both the water sorption isotherm and the hysteresis shape of sodium montmorillonite. These observations also applied to analogous swelling-clay-water systems for which a similar interpretation holds (e.g., Mooney et al., 1952b, Van Olphen, 1965, Cases et al., 1992, Cases, 1997, Bérend, 1995, Ferrage, 2005, Lindholm et al., 2019).[7] Michot et al. (2005) specifically noted a perfect reproduction of low-pressure hysteresis in the evolution of d-spacings leading to the conclusion that LPH in swelling-clay-bearing mudrocks is likely associated with swelling. Though, Cases et al. (1992) as well as Lindholm et al. (2019) remarked that interlayer expansion was not the only source of hysteresis. In XRD measurements, performed as a function of relative humidity, an increase in d-spacing accompanied by hysteresis was observed for sodium montmorillonite only above a threshold of $\approx 20\%$RH, whereas scanning isotherms exhibited hysteresis even at lower $p/p^0_{\max}$. The threshold is, however, dependent on the interlayer cation and cannot be regarded as universally valid (cf. data in Michot & Villiéras, 2006).

Water vapour sorption isotherms of the Ypresian Clay and its clay fraction were characterised by substantial hysteresis along the complete p/p^0 range but the isotherms were otherwise featureless

[7] Van Olphen (1965) presented the double step for a sodium vermiculite-H_2O system.

except for a very subtle step upon desorption (Figure 4.6b,c). Mineralogical analysis yielded clay minerals (0.68 g/g) as major components of the Ypresian Clay mudrock bearing dioctahedral smectite (0.48 g/g) and illite (0.17 g/g) as major constituents (Figure 4.1, Table 4.1).

Integrating compositional information with isotherm shapes of the untreated Ypresian Clay samples suggested that smectite hydration (cation hydration + intercalation of mixed-water-layers) and associated swelling were major contributors to hysteresis for these samples. In fact, water uptake typically scales with the amount of expandable clay minerals (Woodruff & Revil, 2011). In support, a strong correlation of smectite content and water uptake was presented in *chapter 3* where nearly 90% of the variation in water uptake could be explained by smectite content. For that reason, smectite was regarded as the main water sorbent for the YPC samples, predominantly controlling water sorption processes. It should be noted, however, that the type of interlayer cation is crucial in the water-clay interaction as the cation dictates the swelling behaviour of expandable clay and therefore the onset of interlayer sorption as well as the discrete partial pressure of d-spacing increase (Bérend, 1995, Cases, 1997, Chiou, 1997). Thus, an exact resemblance of a mudrock isotherm and a clay isotherm is not to be expected.

In consequence, similar sorption processes as in smectites should apply to the materials in which smectite dominates water uptake, hence for the Ypresian Clay mudrock and its clay fraction. Thus, the hysteresis of the untreated YPC samples was interpreted as a primary product of smectite hydration and its volumetric swelling; that includes low-pressure hysteresis as well as the strong retention capacity. In turn, the interpretation of a swelling-induced geometrical deformation of the sorbent insinuates that the hysteresis could be regarded as a kind of strain hysteresis induced by water intercalation which is, however, dependent on the interlayer cation. However, interparticle adsorption ("external" surface) and condensation in micro- and mesopores (interparticle space) likely represented an additional source of hysteresis as these processes were also identified for swelling clays (Cases et al., 1992, Johnston et al., 1992, Prost et al., 1998, Rinnert et al., 2005).

4.4.4 Hysteresis in Cu-Trien-exchanged materials

To study hysteresis unrelated to swelling, the Ypresian Clay mudrock, its clay fraction and the montmorillonite were homoionically exchanged with Cu-triethylenetetramine. The Cu-Trien complex intercalates into the interlayer space of swelling clays fixing the interlayer distance to a constant value between 13 Å and 13.5 Å (Kaufhold et al., 2011, Stanjek & Künkel, 2016). In this study, d-spacings of the Cu-Trien-exchanged materials yielded similar values, specifically d_{001} values were $\approx$ 13.1 Å. Moreover, the Cu-Trien complex neither decomposes at the drying temperature of 378 K typically used for mudrocks nor does it allow massive interlayer adsorption of water in between the flat-oriented Cu-Trien molecule (Kaufhold et al., 2011). Supported by d-spacing measurements of Cu-Trien-exchanged smectites by means of XRD, Kaufhold et al. (2011) demonstrated the stability of the interlayer distance between 10% and 90% relative humidity. Accordingly, the occurrence of swelling as a result of extensive cation hydration was excluded as a potential source of hysteresis for the Cu-Trien-exchanged materials.

The Cu-Trien exchange produced notably different isotherm- and hysteresis loop shapes compared to the natural materials; most pronounced, a distinct reduction in hysteresis width in the

low-pressure range and a diminished total water uptake by 20 to 25% was recognised (Figure 4.6, Table 4.2). Figure 4.11 shows the DVS isotherms in combination with the interpolated hysteresis width as a function of partial pressure of the Cu-Trien-exchanged materials. The hysteresis width ($\Delta Q(p/p_i^0)$) is computed as the difference in uptake of the ad- ($Q_{ads}(p/p_i^0)$ and desorption ($Q_{des}(p/p_i^0)$) branch.

$$\Delta Q(p/p_i^0) = Q_{des}(p/p_i^0) - Q_{ads}(p/p_i^0) \tag{4.2}$$

The SWy2-CuTrien as well as the Cu-Trien-exchanged Ypresian Clay samples (YPC-CuTrien, YPC-CF-CuTrien) still exhibited hysteresis along the complete partial pressure range, but low-pressure hysteresis ($p/p^0 < 0.3$) was substantially reduced compared to the parent materials. Moreover, LPH was quantitatively similar for all samples (Figure 4.11b). A common feature of the water vapour sorption isotherms for Cu-Trien-exchanged materials was an attempted hysteresis loop closure within the p/p^0 range of 0.3 to 0.45, as indicated by the steep reduction in loop width (Figure 4.11b).

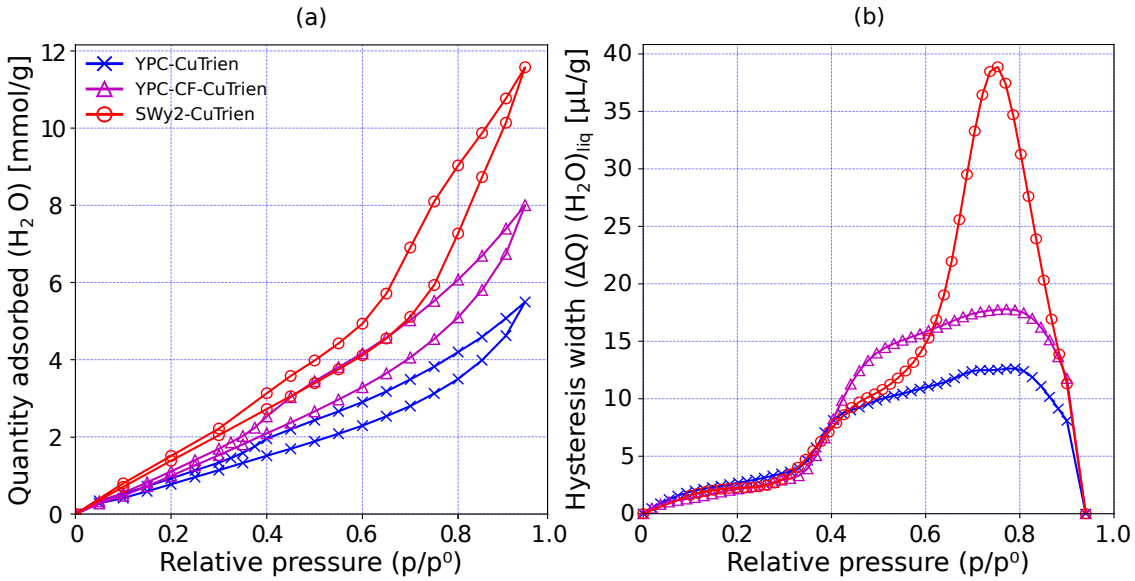

Figure 4.11: (a) Overlay of gravimetric water vapour sorption isotherms (303 K) of the Cu-Trien-exchanged Ypresian Clay mudrock, its clay fraction, and the montmorillonite; (b) Hysteresis width ($\Delta Q(p/p_i^0)$) of Cu-Trien-exchanged SWy2, YPC mudrock, and YPC-CF calculated according to Equation 4.2.

Earlier studies have observed a distinct step in desorption in the water vapour sorption isotherms of some mudrocks, yet the attempted closure of the hysteresis loop did not occur at a constant partial pressure — even though all experiments were conducted at 303 K (Seemann et al., 2017, Sang et al., 2020a, Yang et al., 2021). Since the temperature was held constant, the pore fluid's thermodynamic state — and thus its distance from the bulk critical point (here: $T/T_c(H_2O) = 0.46$; e.g., $T/T_c(N_2) = 0.61$) — remained identical across all experiments. Such a step is common for nitrogen and argon physisorption isotherms obtained for mudrocks and clays (Figure 4.4, Figure 4.5) and it is associated with pore emptying by means of cavitation (Bertier et al., 2016). Yet, the

attempted closure observed in the presented studies may also reflect pore blocking, as conveyed by the variation in closure points. However, no specific pore size accounting for this phenomenon was identified by either Seemann et al. (2017), Sang et al. (2020a) or Yang et al. (2021).

Mineralogical analysis of the Cu-Trien-exchanged materials revealed minor changes in composition (Table 4.1). Besides the alteration of the natural cation population and the fixation of the interlayer space to a constant interlayer spacing, the dissolution of gypsum was recognised. The original YPC mudrock contained about 0.01 g/g of gypsum that was not detected after Cu-Trien treatment. Volumetrically, the amount corresponded to 4.3 µL/g implying additional void volume formation or pore network deconstruction in parts where gypsum was present. Other mineralogical changes were minor and regarded within the uncertainty of the quantification which is mainly affected by the clay mineral quantification. To obtain further information on the origin of the attempted closure and the general isotherm alteration beyond suppressed swelling, the microstructure of the exchanged materials was analysed by argon and nitrogen physisorption and compared to the parent materials.

Generic analysis of the low-pressure region of Ar physisorption isotherms indicated a narrow p/p^0 range ($2 \times 10^{-6} < p/p^0 < 4 \times 10^{-6}$) in which uptake occurred that was absent in the original samples (Figure 4.4). Generally, the micropore volume increased substantially by a factor up to 3.5 providing between 47% and 63% of the total accessible pore volume of the Cu-Trien-exchanged samples (Ar, section C.1 Table C.1 in the appendix). DA micropore size distributions of Cu-Trien-exchanged materials displayed a consistent shift compared to the parent materials and yielded comparable primary pore sizes of 1.5(0.2) nm (Figure 4.4). The shift towards smaller pore sizes was attributed to changes in fabric architecture in micropores rather than interlayer adsorption. The actual interlayer distance after Cu-Trien intercalation is lower than the diameter of Cu-Trien (5.6 Å in Kaufhold et al. (2011)). Geometrical analysis of a structural, molecular model of Cu-Trien confined in between two TOT stacks in *VESTA* (Momma & Izumi, 2008) suggested an actual distance slightly larger than ≈ 2.85 Å, since the Cu-Trien complex lies flat in the interlayer space.[8] Hence, the interlayer distance was considerably lower than the estimated DA micropore size. From that, it was deduced that the primary pore size obtained via DA theory was related to the fabric architecture and not the interlayer space itself. Following the explanations of Kaufhold et al. (2010) and Michot (2018) the created micropores might have originated from slit-shaped "edge" pores at the margin of crystallites created by turbostratic stacking disorder of the smectitic crystallites. This, however, cannot be validated at this point.

Interestingly, the narrow p/p^0 range of first-time Ar uptake, the obtained primary pore size and the systematic step in water sorption isotherm were consistent and in a fairly narrow range for all Cu-Trien-exchanged samples. This implies that these observations were directly related to the Cu-Trien treatment and might be linked to each other. But besides microporosity modification, PSD analysis revealed changes in the mesopore region that could theoretically also contribute to the observed changes in hysteresis of the Cu-Trien-exchanged samples (Figure 4.5).

Clearly, the microstructure as well as the composition have been altered by the Cu-Trien exchange while swelling has been effectively suppressed. Yet, hysteresis still occurred which could

[8] The Cu-Trien model was provided via personal communication with C. Weber by C. Ufer.

not be attributed to swelling but rather to other sources such as differing sorption mechanisms dominating ad- and desorption like cluster-mediated water adsorption followed by pore condensation at a critical cluster size and evaporation via a receding meniscus as interpreted by, for example, Chen et al. (2021). Considering the microstructure modification in relation to the literature and the uniting pore size of $\approx$ 1.5 nm initially conveys the possibility of delayed pore evaporation induced by pore blocking. Up to now, this suggestion is, however, speculative and of a qualitative nature, because no unequivocal evidence could be acquired besides the consistent phenomenological link. Still, as remarked in section 4.4.1 a contribution of the strong retention capacity and kinetic hysteresis continues to effect hysteresis in the Cu-Trien-exchanged samples, but obviously hysteresis does not exclusively relate to swelling. Taking the Cu-Trien-exchanged materials as analogues for non-swelling mudrocks implied that water sorption hysteresis in those materials occurs, but it seems unrelated to the volumetric expansion of swelling clays.

4.4.5 Mechanisms of water sorption in non-swelling geomaterials

A mechanistic understanding of the prevailing desorption mechanism can be achieved via (i) a comparison of PSDs obtained from the ad- and desorption branch, (ii) PSD analysis with different adsorptives at their normal boiling points (N_2 (77 K) vs. Ar (87 K)), (iii) sorption measurements at different temperatures with the same adsorptive, or (iv) hysteresis loop scanning.

To assess the pore network architecture in more detail and to discern sorption mechanisms of water, ascending and descending scanning isotherms of the Cu-Trien-exchanged SWy2 and YPC-CF were measured by the DVS method at 303 K (Figure 4.7). Descending scanning isotherms revealed two notable features: (i) boundary curve merging at the attempted hysteresis closure step initiated at $p/p^0 \approx 0.45$ and 0.4 which is close to the cavitation partial pressure (p/p^0_{cav}) of bulk water and the p/p^0_{cav} observed for hardened cement paste (Maruyama et al., 2018). (ii) Fully reversible water sorption was identified below $p/p^0_{\max} = 0.4$ of descending sub-cycles (Figure 4.7b,d). Complete reversibility has not been observed in an earlier attempt of scanning isotherm measurements on a smectite-lean Longmaxi mudrock which displayed hysteresis independent of the maximum partial pressure (Seemann et al., 2017).

Isotherm merging of descending- and enveloping isotherms at the attempted closure step are typical for complex, disordered pore networks in which often a combination of either free- or cooperative evaporation and cavitation are in control of desorption. Above the returning points to the enveloping isotherm, the pore fluid desorbs nearly unconstrained from the pore network revealing a great share of freely accessible pore space in the Cu-Trien-exchanged samples. The systematic merging of the descending scanning isotherms and the enveloping isotherm at the attempted closure step indicated constraint pore evaporation from certain parts of the pore network. The constraint evaporation was interpreted as cavitation-controlled desorption, hence spinodal evaporation (definition in Lowell et al., 2006), which typically produces the observed types of descending scanning isotherms (Cimino et al., 2013, Garcia-Martinez et al., 2014). Unlike pore blocking, cavitation is independent of the filling state of neighbouring pores (partial pore filling independence) in a pore network since spontaneous gas bubble nucleation occurs inside a pore while the constriction remains filled. In contrast to cavitation-controlled evaporation, free evaporation

in independent pores would produce a descending scanning curve crossing nearly parallel to the x-axis until it merges with the boundary curve. Furthermore, descending scanning isotherms of pore-blocking controlled systems would display converging sub-cycles that return to the enveloping isotherm only at the beginning of reversible sorption and not at the attempted closure step because of its dependence on the filling state of neighbouring pores (Tompsett et al., 2005, Cimino et al., 2013, Cychosz et al., 2017). Qualitatively, the above is supported by the fact that both Cu-Trien-exchanged samples showed an attempted closure in the same narrow p/p^0 range (0.45 to 0.3), even though pore networks were unlikely to be akin, especially after the performed treatments.

Reversible water adsorption observed at $p/p^0_{max} \leq 0.4$ indicates that pores affected by cavitation remained unfilled below this threshold (p/p^0_{cav}), implying that cavitation was not applicable in this pore size regime. At $p/p^0 > p/p^0_{\mathrm{cav}}$, cavitation became relevant and occurred independently of the overall saturation state of the pore network, as evidenced by its insensitivity to p/p^0_{max}. It should be noted that cavitation does not take place in the pore throats (W_{t}) — constrictions linking adsorbate and bulk vapour phase — of the pore network but rather in adjacent pore bodies (W_{pb}). If these constrictions are narrower than or equal to the cavitation critical pore width ($W_{\mathrm{t}} \leq W_{\mathrm{cav}}$), connected pore bodies ($W_{\mathrm{pb}} > W_{\mathrm{cav}}$) empty via cavitation in (disordered) pore networks. Accordingly, the cavitation threshold (p/p^0_{cav}) defines the largest pore throat width (W_{cav}) at which cavitation dominates over pore-blocking-induced delayed evaporation ($W_{\mathrm{t}} > W_{\mathrm{cav}}$). Extending these theoretical considerations to the hysteresis critical temperature ($T_{\mathrm{i}} > T_{\mathrm{hc}} \rightarrow$ no hysteresis) suggested that at $p/p^0 \leq 0.4$ pores were filled for which the hysteresis critical temperature was below the experimental temperature of 303 K. It is, however, remarked that $T_{\mathrm{i}} > T_{\mathrm{hc}}$ does not necessarily imply a supercritical state of the pore fluid in the concerned pores (Thommes, 2004).

Moreover, cavitation requires a continuous liquid phase within the pore network. Thus, based on the descending scanning isotherms, a phase transition can be inferred suggesting the occurrence of capillary condensation above a p/p^0 of 0.4 in specific parts of the pore network during adsorption for the investigated mudrocks. These specific parts of the pore network need to consist of pore bodies larger than the later approximated cavitation threshold pore size. Furthermore, this implies that hysteresis at higher partial pressure is a product of capillary condensation. The cavitation volume (Q_{cav}) was, however, modest compared to the amount desorbed via slightly- or unconstrained evaporation above p/p^0_{cav} for the Cu-Trien-exchanged samples.[9] Quantitatively, the freely accessible pore volume (60 to 70%) dominated over the constraint pore volume (8 to 12%) in the Cu-Trien-exchanged materials. The remaining sorption occurs reversibly below $p/p^0 \leq 0.3$.

To substantiate the theoretical considerations, the strategy of Maruyama et al. (2018) was adapted who demonstrated cavitation of water in pores connected by constrictions smaller than $\approx$ 2 to 2.5 nm in hardened cement paste. Cavitation of water has been presented for various nanoporous materials (zeolites, MCM-41, cement) for which experimental conditions were close to the ones of this investigation. Furthermore, the attempted closure regimes fall within the presented p/p^0 range (Rathouský & Thommes, 2007, Thommes et al., 2012, Maruyama et al., 2018). Scrutiny of in the literature reported pore sizes yielded an interval between 2.5 nm and 3.2 nm connected by smaller pore necks for which cavitation has been identified to be the controlling desorption

[9] The cavitation volume was computed as the difference between the amount desorbed at $0.4 > p/p^0 > 0.3$: $Q_{\mathrm{cav}} = Q_{\mathrm{des}}(p/p^0 = 0.4) - Q_{\mathrm{des}}(p/p^0 = 0.3)$.

mechanism of water.

To obtain an estimate of the cavitation critical pore size, the Kelvin equation has been applied assuming complete wettability of the system ($\cos\theta = 1$):[10]

$$r_{\mathrm{K}} = (2\gamma \times V_{\mathrm{m}} \times \cos\theta)/(R \times T \times \log(p/p^0)) \tag{4.3}$$

Computing the pore width at the cavitation pressure returned a maximum equivalent constriction width (= pore-throat size) of $\approx$ 2.2 to 2.5 nm at 303 K. Above this threshold pore width, cavitation is supposed to be not dominant anymore. Instead pore volumes empty via a different mechanism like free evaporation implying that a large part of the pore network is controlled by constrictions larger than the estimated 2.2 to 2.5 nm. Obviously, considering an increased level of hydrophobicity, which is likely for the Cu-Trien-exchanged materials according to Kaufhold et al. (2011), would reduce the cavitation critical pore-throat size accordingly. In contrast, a statistical thickness model like that of Hagymassy et al. (1969) would increase the estimated cavitation critical constriction width to about 3 to 3.4 nm. Thus, the reported pore size should be regarded as an estimate of the cavitation critical pore-throat size rather than an absolute value due to uncertainties in parameters such as the contact angle.

The cavitation critical pore width was supported by the independent relation given by Coasne (2016). Coasne (2016) provided a simple relationship between experimental temperature (T), bulk critical temperature (T_{c}) and the adsorptive molecular diameter (d_{m}) to estimate the critical pore radius (r_{c}) above which capillary condensation can be observed in association with hysteresis:

$$r_{\mathrm{c}}(T) = 2d_{\mathrm{m}} \times T_{\mathrm{c}}/(T_{\mathrm{c}} - T) \tag{4.4}$$

The relationship is purely physical, meaning that the chemical properties of the adsorptive are less important making the relation applicable to any adsorptive (Coasne, 2016). The (hysteresis) critical pore width for capillary condensation amounted to 2.1 nm which is close to the cavitation critical pore size obtained via the Kelvin equation. Moreover, it indicates that smaller pores empty reversibly which is in good agreement with the threshold p/p^0 of 0.4 — observed during hysteresis loop scanning — and the corresponding pore size of 2.2 nm. The approximated pore sizes were both in fair agreement with the caviation critical pore width presented by Maruyama et al. (2018) based on different approaches ($W_{\mathrm{cav}} \approx$ 2 to 2.5 nm). In fact, the difference between both values was on the scale of the molecular size of water. Therefore, the computations, comparisons, and interpretation provided by the adsorption and desorption branches were considered consistent.

Inferred from the microstructure analysis, cavitation was likely controlled by micropores forming a connected network with interparticle pores created by the arrangement of clay crystallites. With respect to the earlier determined primary micropore size, it is theoretically possible that these pores were, at least partly, responsible for cavitation in larger interparticle pores. However, more work needs to be done to unequivocally identify which kind of pore population effects cavitation and to exactly discern the responsible structures. To support the cavitation mechanism, future water vapour sorption isotherms could be measured at different temperatures in order to observe a

[10] r_{K} [nm] is the cylindrical pore radius, γ [N/m] is the interfacial tension of the liquid-vapour interface at the operational temperature (T [K]). V_{m} [m^3/mol] is the liquid molar volume of the gas while θ is the contact angle of the fluid. R [J/K/mol] is the molar gas constant.

transition from pore blocking towards cavitation as it has been done, for example, by Chen et al. (2021). Moreover, tests on non-swelling Cu-Trien-exchanged muscovite or kaolinite could provide insight into the possibility that the step in desorption and the initiation of first-time argon uptake were truly related to the provided pore sizes and not an artefact of a functional group associated with the Cu-Trien molecule.

4.5 Conclusion

The hysteresis of water vapour sorption isotherms of mudrocks and clays has been addressed by means of a combination of mineralogical and microstructural analysis of natural and Cu-triethylenetetramine- exchanged materials. Dynamic vapour sorption isotherms were generically analysed for general (1 & 2) and specific (3 & 4) sources of hysteresis.

1. Isotherms consistently exhibited tightly bound water, referred to as strong retention capacity, which could not be desorbed at zero partial pressure. The strong retention capacity was sample-specific and remained abstract in the sense that neither exchangeable cations nor micropores or specific surface functional groups were unequivocally identified as responsible controls. Rehydroxilation of clay minerals was excluded. The amount of strong retention capacity was, however, likely overestimated by kinetic hysteresis effects.

2. Kinetic hysteresis was related to the choice of the equilibrium criterion and induced a cumulative error in uptake that propagated along the complete isotherm, culminating in the overestimation of the strong retention capacity. Adsorption branches were stronger affected by the lack of equilibrium whereas desorption branches appeared to be at equilibrium. Clearly, kinetic hysteresis was independent of the composition of the material but quantitative differences are likely to depend on the material composition as well. For future DVS isotherm measurements, it should be considered to systematically test for the lowest hysteresis width in order to set an objective operational equilibrium criterion.

3. Water vapour hysteresis of smectite-rich materials was attributed to volumetric interlayer expansion via cation hydration and water layer intercalation. The geometrical sorbent deformation was interpreted as a type of strain hysteresis that was likely supplemented by a contribution of interparticle space condensation to hysteresis. The underlying sorption mechanisms of smectite-rich mudrocks were interpreted to be equivalent to the processes occurring in pure expandable clays when exposed to water vapour.

4. The Cu-Trien-exchanged, non-swelling materials revealed distinct isotherm- and hysteresis loop shapes featured by distinct attempts of hysteresis loop closure ($p/p^0 \approx 0.45$ to 0.3). The prevention of interlayer expansion indicated hysteresis independent of crystalline swelling but likely related to distinct sorption mechanisms upon ad- and desorption. The changes in isotherm shape were associated with the microstructure modification and a modified governance of hysteresis controlling processes.

5. Scanning isotherms of Cu-Trien-exchanged materials provided evidence that water sorption was reversible at $p/p^0 \leq 0.4$. For scanning isotherms measured to a $p/p^0 > 0.4$, cavitation became a prominent desorption mechanism from which capillary condensation was deduced as governing sorption mechanism above $p/p^0_{cav} \geq 0.4$. The cavitation critical constriction width was estimated to about 2.2 to 2.5 nm for the Cu-Trien-exchanged materials aligning with a hysteresis critical pore size of 2.1 nm. Above the cavitation critical constriction width other processes were in control of evaporation. Cavitation is likely masked for mudrocks and clays in which smectite hydration was the governing mechanism for water uptake and hysteresis.

Appendices

C.1 Textural parameters of mudrocks and clays

The textural parameters of the investigated materials are provided in Table C.1 and Table C.2. The data were collected from *chapter 2*, as exactly the same materials were used in this study with the exception of the original and Cu-Trien-exchanged Ypresian Clay mudrock.

Table C.1: Textural properties of mudrocks obtain by physisorption analysis of Ar sorption isotherms measured at 87 K; V_{GV} = Gurvich (total) pore volume calculated at $p/p^0 = 0.9916$ (W_{BJH} = 250 nm) [µL g^{-1}], A_{BET} = BET specific surface area [m^2 g^{-1}], Q_{mono} = BET monolayer capacity [mmol g^{-1}], C = BET energy constant [-], V_0 = DA micropore volume [µL g^{-1}], Q_0 = DA limiting micropore capacity [mmol g^{-1}], E_0 = DA characteristic energy of system [kJ mol^{-1}], n = DA exponent [-]. Textural data of SWy2-Na, SWy2-CuTrien, YPC-CF, and YPC-CF-CuTrien were taken from *Chapter 2*.

ID	V_{GV} [µL g^{-1}]	A_{BET} [m^2 g^{-1}]	Q_{mono} [mmol g^{-1}]	C [-]	V_0 [µL g^{-1}]	Q_0 [mmol g^{-1}]	E_0 [kJ mol^{-1}]	n [-]
SWy2-Na	91	47.4	0.55	113	20.9	0.73	12.4	1.71
SWy2-CuTrien	155	166.1	1.93	597	72.9	2.56	26.7	1.03
YPC-CF-org	140	91.9	1.07	87	42.2	1.48	11.1	1.69
YPC-CF-CuTrien	99	123.0	1.43	169	62.0	2.17	15.9	1.10
YPC-org	111	58.2	0.68	80	27.0	0.95	10.9	1.66
YPC-CuTrien	82	78.0	0.91	150	41.0	1.44	15.2	1.00

Table C.2: Textural properties of mudrocks obtain by physisorption analysis of N_2 sorption isotherms measured at 77 K; V_{GV} = Gurvich (total) pore volume calculated at $p/p^0 = 0.9923$ (W_{BJH} = 250 nm) [µL g^{-1}], A_{BET} = BET specific surface area [m^2 g^{-1}], Q_{mono} = BET monolayer capacity [mmol g^{-1}], C = BET energy constant [-], V_0 = DA micropore volume [µL g^{-1}], Q_0 = DA limiting micropore capacity [mmol g^{-1}], E_0 = DA characteristic energy of system [kJ mol^{-1}], n = DA exponent [-]. Textural data of SWy2-Na, SWy2-CuTrien, YPC-CF, and YPC-CF-CuTrien were taken from *Chapter 2*.

ID	V_{GV} [µL g^{-1}]	A_{BET} [m^2 g^{-1}]	Q_{mono} [mmol g^{-1}]	C [-]	V_0 [µL g^{-1}]	Q_0 [mmol g^{-1}]	E_0 [kJ/mol]	n [-]
SWy2-Na	103	48.2	0.49	405	18.3	0.53	14.6	1.87
SWy2-CuTrien	160	169.3	1.74	2310	69.0	1.99	29.8	1.45
YPC-CF-org	150	93.5	0.96	237	33.7	0.97	14.3	2.98
YPC-CF-CuTrien	123	122.9	1.26	355	49.5	1.43	18.2	1.74
YPC-org	125	60.7	0.62	208	21.9	0.63	14.2	2.88
YPC-CuTrien	112	77.5	0.80	362	29.9	0.86	18.2	1.97

Chapter 5

Outlook and concluding remarks

In this scientific contribution, an extensive data set of gas and water vapour sorption data has been compiled for mudrocks, clay minerals and engineered analogues of various compositions and textures. The data has been critically discussed in relation to their individual controls and mechanisms with respect to the particular adsorptive properties. Hereby, limitations and implications were outlined in *chapters 2, 3* and *4*. Concluding remarks and future research options are briefly discussed below.

5.1 Traditional and advanced physisorption protocols

High-quality isotherm data are the foundation for a proper characterisation of a porous material. To obtain high-quality data, operators need to be aware of systematic errors, technical difficulties and pitfalls in data interpretation. Moreover, there is a need for often neglected transparency with regard to sample preparation protocols, because sample treatment can have a profound effect on the obtained results (Michot, 2018).

For the presented argon physisorption data the saturation pressure has been identified as the greatest factor of uncertainty, as it could not be measured separately with the used instrument. During the review of *chapter 2* two questions were raised with regard to the accessibility of micropores: (i) is a vacuum of $P \leq 5\,\mathrm{Pa}$ sufficient for micropore evacuation and (ii) does the helium free-space measurement lead to micropore clogging by "*helium entrapment*"?

In the following, preliminary tests and recommendations are summarised for the above questions focusing on frequently used textural measures like micropore volume and BET specific surface area.

Saturation pressure accuracy is crucial for interpreting physisorption isotherms, especially in the sensitive high-pressure region. According to Lowell et al. (2006), a 0.7% deviation in saturation pressure can lead to a 10% error in pore size distribution at $p/p^0 = 0.95$. The argon saturation pressure correction suggested by the operator's manual of the *CryoSync* consists of a single-point calibration of the temperature probe. Such a single-point calibration relies on a single offset value and implies completely stable atmospheric conditions over the course of the following isotherm measurements. However, stable atmospheric conditions are rarely the case, if no constant

temperature and pressure laboratory is available. In *chapter 2*, a single point calibration has been shown to be insufficient, even when performed daily, because atmospheric pressure changes induce saturation pressure fluctuations of the adsorptive that negatively affect isotherms and textural parameters in the high-pressure range.

From a practical point of view, the issue can be resolved by measuring a physisorption isotherm in the traditional instrumental setup for which liquid argon is used as a coolant with separate p^0 measurements. However, liquid argon is considerably more expensive and special argon dewars are necessary for long-term storage.

An empirical approach to account for saturation pressure fluctuations is to adapt the principle of a more reliable multi-point calibration curve. The multi-point calibration involves the identification of the offset value of the temperature probe by means of a single-point calibration followed by recording the saturation pressure as a function of atmospheric pressure over a prolonged time from which a calibration curve can be established. The calibration curve relates the saturation pressure offset directly to atmospheric pressure but it relies on the constancy of the initially determined single-point offset. By measuring the atmospheric pressure simultaneously along the physisorption isotherm measurement it should be possible to correct for the gross of p^0 fluctuations using the calibration curve.

Alternatively, a theoretical approach could involve the application of the Clausius Clapeyron equation to obtain the actual coolant (liquid nitrogen) temperature in dependence on the atmospheric pressure conditions. Based on the computed temperature of the coolant and under the assumption of a constant offset value, the saturation pressure can be recalculated using experimental $T - p^0$ data obtained from, for example, the National Institute of Standards and Technology.

Outgassing conditions and protocols of geological samples are highly variable, despite that high-resolution preparation protocols exist, like the IUPAC guide (Thommes et al., 2015). Singh et al. (2021) provided an overview of the diversity of preparation protocols in geoscience literature which Gu et al. (2021) blamed on the fact that no generally accepted protocol, particularly for "shales", exists. In fact, many authors do not provide details on sample preparation beyond sample crushing and outgassing temperature (cf. e.g., Chen & Xiao, 2014, Cao et al., 2015, Xue et al., 2016, Sun et al., 2017).

Holmes et al. (2017), Singh et al. (2021) and Gu et al. (2021) dealt specifically with the subject of outgassing temperature of mudrocks and indicated that outgassing temperatures below 373 K are insufficient to remove water stored in micropores. The authors recommend temperatures above 423 K (Gu et al., 2021) or even 523 K (Holmes et al., 2017) to completely dry mudrocks. Such harsh treatment can lead to irreversible damage of the microstructure and may invoke compositional changes; especially when immature organic matter is present. Milder outgassing temperature ($T \approx 378$ K) is usually preferred combined with ultra-low vacuum reached via a turbomolecular pump. According to Schlumberger & Thommes (2021), ultra-low vacuum is a requirement to desorb water from ultramicropores which are close to the molecular scale of most adsorptives. However, the (economic) relevance may be questionable, especially from the perspective of industrial applications in geoscience.

The influence of vacuum on the isotherm measurements and derived textural parameters of

the low-pressure region (V_0, A_{BET}) was tested on representative subsamples of a random lower Jurassic mudrock of low organic matter content (TOC[1] $\approx 0.0094\,\mathrm{g/g}$) and a Cu-Trien exchanged montmorillonite outgassed at 378 K (24 h) at $P \leq 5\,\mathrm{Pa}$ and at $P < 13\,\mathrm{mPa}$ followed by argon physisorption measurements at 87 K in liquid argon under similar conditions as given in *chapter 2*.

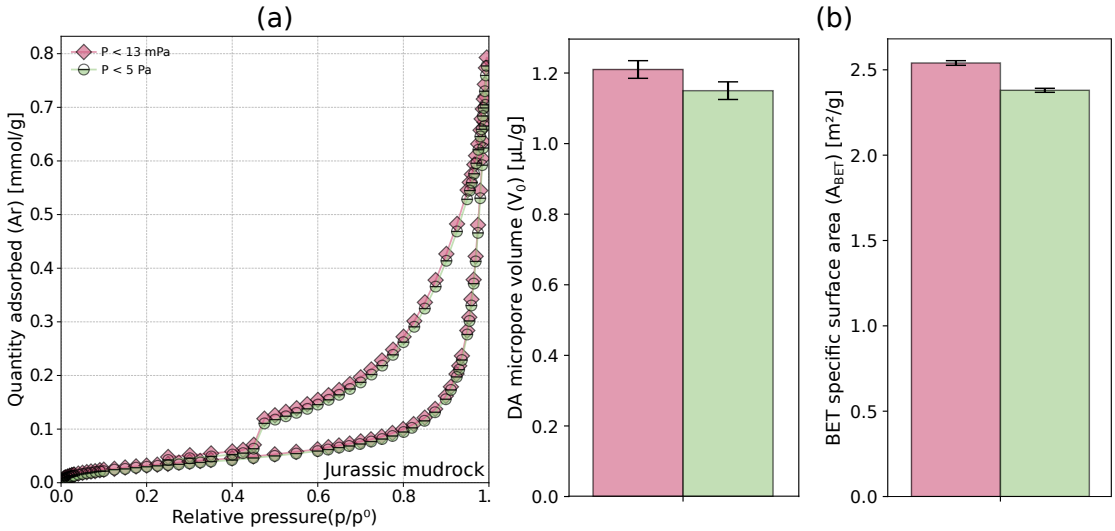

Figure 5.1: (a) Argon physisorption isotherms of a random lower Jurassic mudrock outgassed at $P < 5\,\mathrm{Pa}$ and $P < 13\,\mathrm{mPa}$ at $T = 378\,\mathrm{K}$ for 24 h; (b) Bar plots of micropore volume and specific surface area; error bars represent uncertainties of the fit.

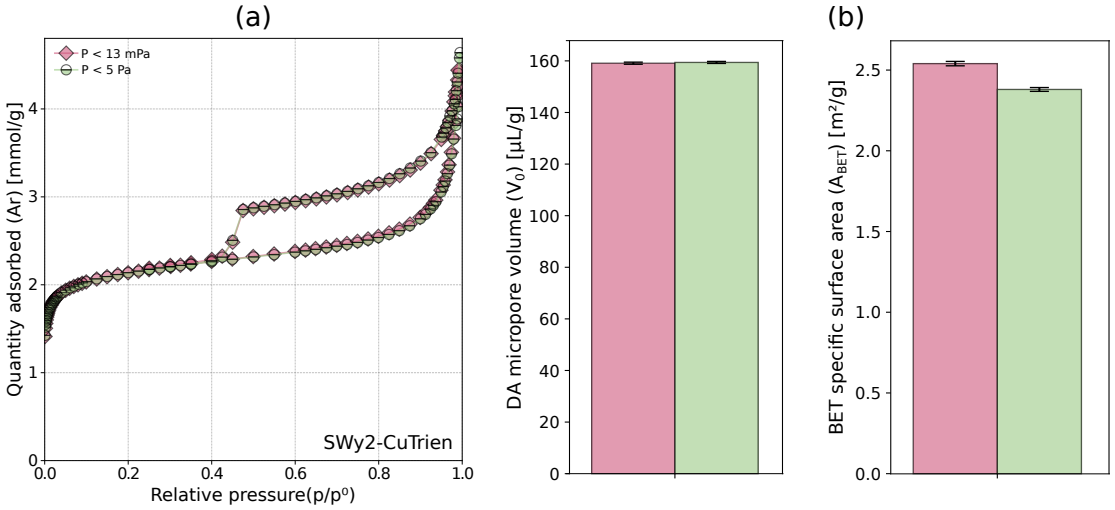

Figure 5.2: (a) Argon physisorption isotherms of Cu-Trien exchanged montmorillonite outgassed at $P < 5\,\mathrm{Pa}$ and $P < 13\,\mathrm{mPa}$ at $T = 378\,\mathrm{K}$ for 24 h; (b) Bar plots of micropore volume and specific surface area; error bars represent uncertainties of the fit.

The differences in isotherms, micropore volume and BET specific surface area are minor for both samples, but detectable. The microporous Cu-Trien exchanged montmorillonite revealed

[1]Personal communication with C. Weber.

a difference of $< 0.2\%$, whereas for the lower Jurassic mudrock an approximated difference of 7% was identified (Figure 5.1, Figure 5.2). On an absolute scale, the discrepancy of the lower Jurassic mudrock is negligibly small with $0.17\,\mathrm{m}^2/\mathrm{g}$ for the specific surface area and $2.3\,\mu\mathrm{L/g}$ for the micropore volume.

The lack of significant difference leads to the conclusion that micropores contributing to the computed textural parameters are mostly accessible to argon for the given samples. Consequently, the micropore volumes seem to be not substantially underestimated as a result of extensive water blockage in micropores because of insufficient low vacuum.

For future experiments it should be considered to couple sample outgassing with, for example, thermogravimetry (or similar) in order to apply the mildest outgassing procedure possible, especially when a broad variety of mudrocks is considered.

Helium entrapment relates to the adsorption of helium in micropores at cryogenic temperatures occurring during the free-space measurement before the actual isotherm measurement. The phenomenon has been explicitly mentioned in the IUPAC guide for physisorption analysis and it is based on the observations of Silvestre-Albero et al. (2013) who detected He entrapment in ultra-tight activated carbons with pores below 7 Å at liquid nitrogen temperature. He entrapment impedes not only the accessibility to ultra-small micropores and connected compartments, but also results in a false free-space volume used for the calculation of the isotherm (important at high p/p^0). To avoid this, either a free-space measurement followed by elevated temperature He removal is recommended or the free-space should be determined after the actual isotherm measurement.

To estimate the impact of He entrapment for an average mudrock and frequently used texture parameters (V_0, A_{BET}), the free space was measured separately for the lower Jurassic mudrock and the Cu-Trien exchanged montomorillonite. The potentially trapped helium was removed after the free-space measurement under ultra-low vacuum at $T = 378\,\mathrm{K}$ for 24 h (Figure 5.3, Figure 5.4).[2]

Similar to the vacuum tests, the differences in textural parameters were not substantial. Slightly larger values of micropore volume and BET specific surface area were observed when the high-temperature removal was applied. In absolute terms, the difference was approximately $0.1\,\mathrm{m}^2/\mathrm{g}$ for A_{BET} and $3.9\,\mu\mathrm{L/g}$ for V_0 (lower Jurassic mudrock) and $2.9\,\mathrm{m}^2/\mathrm{g}$ for A_{BET} and $1.3\,\mu\mathrm{L/g}$ for V_0 (SWy2-CuTrien). In fact, this difference is also minor with respect to the actual sizes of the BET specific surface area and the micropore volume as the deviations are one to two orders of magnitude lower than the parameter values themselves. Pore size distributions consistently indicate a growing deviation for both preparation procedures which can be a result of the false free-space calculation due to helium entrapment. However, the severe discrepancy shown by the lower Jurassic mudrock is rather considered as an artefact of insufficient liquid argon supply during the measurement, since the dewar ran empty and low levels of cooling agent make the measurement very susceptible to atmospheric pressure fluctuations (cf. *chapter 2*).

[2]The Ar physisorption isotherm with He removal at high temperature is incomplete because no more liquid argon was available making a remeasurement under similar conditions impossible.

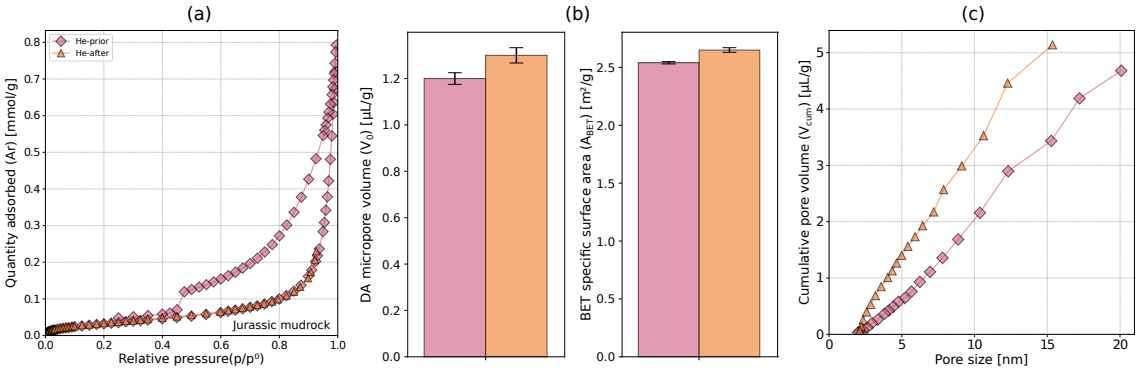

Figure 5.3: (a) Argon physisorption isotherms of a lower Jurassic mudrock measured with (isotherm incomplete due to empty dewar) and without helium removal at elevated temperature ($T = 378\,\mathrm{K}$) prior to the physisorption measurement; (b) Bar plots of micropore volume and specific surface area; error bars represent uncertainties of the fit; (c) Pore size distributions calculated via BJH theory.

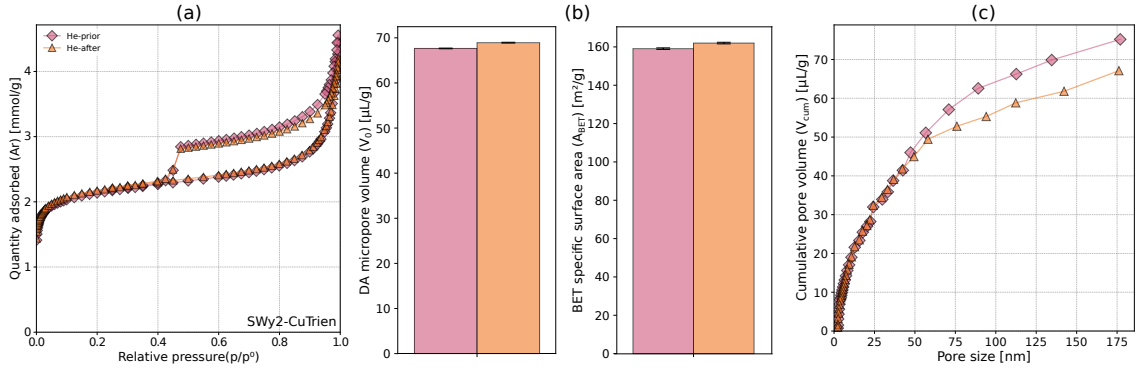

Figure 5.4: (a) Argon physisorption isotherms of Cu-Trien exchanged montmorillonite measured with and without helium removal at elevated temperature ($T = 378\,\mathrm{K}$) prior to the physisorption measurement; (b) Bar plots of micropore volume and specific surface area; error bars represent uncertainties of the fit; (c) Pore size distributions calculated via BJH theory, severely affects by low argon levels during measurement.

The preliminary tests suggest a detectable but low effect of He entrapment on the common textural parameters of the tested samples, rendering the importance of He entrapment for traditional texture descriptors negligible. This agrees with the results of Silvestre-Albero et al. (2013) for activated carbons. But it is noted, that due to the utilisation of the *Gemini VII 2390t* instrument, the ultra-low-pressure region could not be covered. Therefore, the potential influence of He entrapment in the ultra-low p/p^0 region could not be detected, despite its interest in micropore size distributions. In turn, this p/p^0 region needs to be tested in the future, because marked effects of He entrapment were only detected in this region by Silvestre-Albero et al. (2013). However, adequate models for the description of micropore size distributions are currently not available for mudrocks which will force a generic interpretation with respect to the difference in uptake as a function of partial pressure rather than pore size.

With respect to application, the importance of He entrapment is considered minor since pressure-driven transport is typically associated with larger pores while gas storage is relevant in the field of oil- and gas but not as much for mudrock barriers in nuclear waste storage repositories. Furthermore,

fluids stored in such small pores are very unlikely to be removed in any applications at an industrial scale. Nonetheless, future systematic testing may help to conclusively evaluate the importance of He entrapment on the microstructure characterisation of mudrocks, especially when the ultra-low pressure region is investigated and advanced models become available for the microporosity description. For now, integrating a high-temperature He removal step or the free-space measurement after the actual isotherm measurement appears to be the most adequate way to tackle the potential issue of He entrapment.

5.2 The future of water vapour sorption in mudrocks

In *chapter 3* and *4* the distribution, mechanisms and controls of water vapour sorption in mudrocks were at the centre of attention. The data highlighted the primary importance of smectite and the cation exchange capacity for the studied samples. Both parameters were predominantly responsible for the governing sorption mechanisms and modifications of the pore network in mudrocks. The classical picture of capillary condensation (high p/p^0) followed by capillary evaporation via a receding meniscus and finally cavitation could be established for non-expandable sorbents treated by Cu-Trien exchange. However, with regard to water vapour sorption, solo (single gas) sorption has nearly reached its limits, except when it comes to sorption kinetics and temperature effects on uptake.

Water vapour uptake kinetics of mudrocks have not been treated in this scientific contribution, even though the gravimetric raw data (mass vs. time) allow to obtain information about uptake rates when an appropriate evaluation model is used.

Recently Sang et al. (2020a) and Yang et al. (2021) made the first attempts at studying water vapour sorption kinetics of mudrocks. These authors obtained apparent diffusion coefficients from dynamic vapour sorption experiments on overmature Ordovician and Silurian mudrocks by applying an analytical solution to Fick's law provided by Crank (1975). Sang et al. (2020a) employed an early time solution for diffusion in a semi-infinite plane where only the initial part of the uptake is fitted, whereas Yang et al. (2021) used a multiphase transport model coupling concomitant liquid- and vapour transfer based on a mass-balance equation. Apparent diffusion coefficients ranged from 10^{-10} to $10^{-12}\,m^2/s$ which is below the apparent diffusion coefficients of gases in saturated media reported by Busch et al. (2018). In addition, Dang et al. (2021) provided a collection of kinetic adsorption models like pseudo-first and second-order models or double-exponential models, which were tested on organic-rich mudrocks of different particle sizes from the Ordos Basin. Thereby, the double-exponential model provided the best fit from which a kinetic, two-stage sorption process was concluded (Dang et al., 2021).

Here, apparent diffusion coefficients were modelled based on the analytical solution of Fick's law for a spherical particle shape and the boundary conditions outlined by Crank (1975)(*pp. 91*). To assess the apparent water vapour diffusivity, a dual diffusion model was applied based on a weighted linear combination of Crank's analytical solution of diffusion in a sphere. The motivation for a dual diffusion model was the hypothesis that a fast and a slow uptake process dominate at

different times during a partial pressure stage, similar to Dang et al. (2021). The weights of each contribution were included in the fitting process. Diffusion into the centre of a spherical particle is described by Equation 5.1:

$$\frac{M_t}{M_\infty} = 1 - \frac{6}{\pi^2} \times \sum_{n=1}^{\infty} \frac{1}{n^2} \exp(-Dn^2\pi^2 t/r^2) \tag{5.1}$$

where M denotes the diffused mass at time t [s] and at infinity (∞). D [m^2/s] is the apparent diffusion coefficient and r [m] is the radius of the sphere. Here, a nominal particle size of 300 µm was assumed.

Figure 5.5 displays the quantity adsorbed as a function of time at three partial pressures ($p/p^0 = 0.1, 0.4, 0.8$) for the Boom Clay and the Tournemire argillite studied in *chapter 3*. Apparent diffusivities are in the order of 10^{-11} to 10^{-12} m^2/s for the fast process. The fast process is in fair agreement with the reported data which is conceivable since the first part of the uptake curve represents the fast process where also the early time solution is fitted by Sang et al. (2020a). The slow process shows significantly lower apparent diffusion coefficients between 10^{-14} m^2/s and 10^{-17} m^2/s. The secondary process is very slow and needs to be scrutinised in more detail to obtain a physical or chemical explanation and to reliably rule out a mathematical fitting mistake.

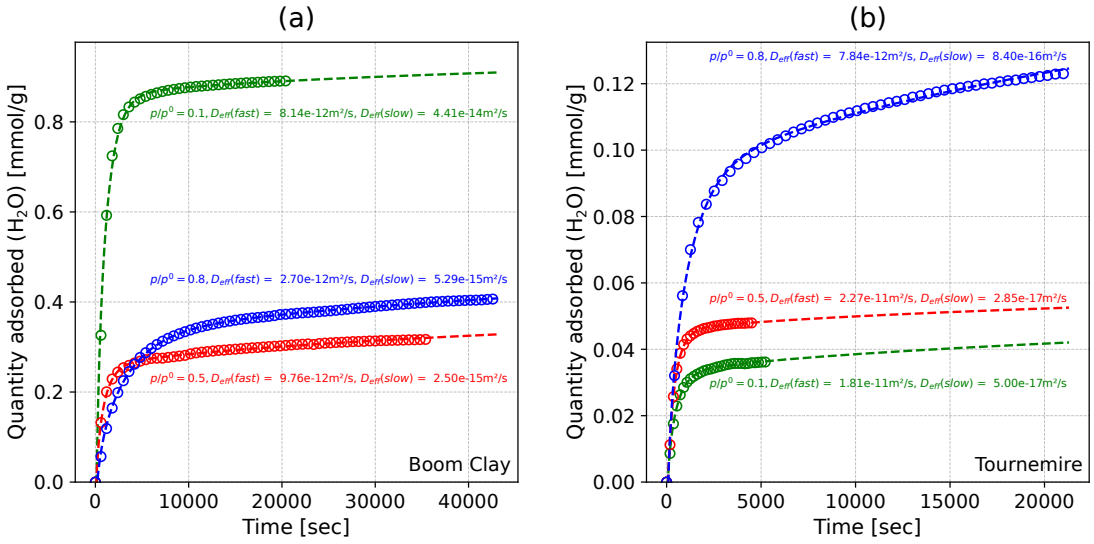

Figure 5.5: Amount adsorbed as a function of time, measured (open circles) at constant partial pressure, on the Boom Clay (a) and Tournemire argillite (b). The dashed lines represent fits to the data points, of the analytical solution of Fick's Law (1000 summation terms) for the weighted dual diffusion model, for diffusion into a sphere (r = 300 µm). The apparent diffusion coefficients (D) are shown for the individual fits.

By studying uptake rates as a function of partial pressure it may be possible to obtain further insight into dominant sorption mechanisms and the compartmentalisation of the pore network of mudrocks, because it may be hypothesised that uptake rates will slow down once capillary condensation occurs. In this case, pore network-internal concentration gradients will be present and diffusion might locally be impeded by menisci slowing down the diffusion rates substantially

which could be a tentative explanation for the low secondary diffusion coefficients. Additionally, such an analysis strategy might help in extending the study of hysteresis phenomena and pore network modification by swelling during water vapour sorption in mudrocks, especially in the low-pressure hysteresis range.

It is, however, remarked that the apparent diffusion coefficients obtained here are not "*real*" diffusion coefficients like those determined for non-sorbing gases through diffusion measurements (cf. e.g., Jacops et al., 2021). The computed coefficients are rather conceived as bulk-rate descriptors of water vapour uptake into the pore network of mudrocks. The reason is that transport into the aggregate particle and surface adsorption occur simultaneously, hence both processes contribute to the rate of mass increase as a function of time. For future applications, it is desirable to deconvolute the rate of adsorption from the rate of transport. Such a deconvolution is, however, anticipated to be complex because processes like swelling, pore network modification and changes in dominant sorption mechanisms need to be factored in.

Temperature has a profound influence on water vapour sorption in mudrocks which differs for ad- and desorption branches because of the distinct sensitivity of active sorption processes (Tang et al., 2017, Sang et al., 2019, Chen et al., 2021). Studying water vapour sorption as function of temperature provides the opportunity to obtain an idea about the energy involved when a water molecule bounds to the surface of a mudrock. Published enthalpies of adsorption vary from 48 to 55 kJ/mol (Tang et al., 2017), 44 to 54 kJ/mol (Sang et al., 2019), and 39 to 45 kJ/mol (Chen et al., 2021) implying an expectable mudrock-specific behaviour but a fairly small variability. The variability in enthalpy of adsorption has mostly been discussed from a qualitative perspective and within the framework of sorption mechanisms. Establishing a relation between enthalpy of adsorption and sorption mechanism is interesting, because it may help to tie a specific sorption mechanism to a particular partial pressure range. Furthermore, it aids in distinguishing the transition from one mechanism to another. In particular, such a strategy might be relevant at (very) low p/p^0 in order to discriminate between external surface hydration and the onset of interlayer cation hydration which, however, demands precise measurements and stable experimental conditions.

Moreover, attempts to correlate the enthalpy of adsorption with composition (mineralogy, organic matter, thermal maturity) have not been found in literature, except a qualitative mention by Chen et al. (2021). A correlation between composition and water vapour uptake as a function of p/p^0 may, however, help to obtain information on the uptake-dominating component. Furthermore, the enthalpy of adsorption may serve as an additional parameter to characterise the surface chemistry of the mudrock in an experimentally easy manner.

5.3 Future prospects and developments of (physi-) sorption

The future of sorption studies will be outside of single probe and solo technique analysis. On a comparative level, single probe analysis will continue to serve well for industrial applications like for quality control of solids or for the textural characterisation of the pore network of synthesised

sorbents. But, from a scientific and mechanistic perspective, the combination of (i) techniques, like water vapour sorption with small angle X-ray and neutron scattering, high-resolution nuclear magnetic resonance or Fourier transformed infrared spectroscopy, or (ii) of fluids, like alkanes, is considered as the way forward. This is believed to be of special importance to make progress in the in-depth understanding of heterogeneous and disordered sorbent systems like mudrocks since data are not always straightforward in interpretation and solo techniques may not deliver enough information to study the parameter in question.

A limited number of studies have already combined gas- or water sorption with the listed techniques (e.g., Iiyama et al., 1997, Thomas et al., 1998, 2014, Baumgartner et al., 2019, Sang et al., 2020b, Marreiros et al., 2021). These investigations emphasise the large potential of such combinations in order to decipher particular mechanisms because a particular feature such as condensation or surface chemical effects can be investigated in more detail with a physically independent principle and technique. At the same point, it is clear that also the combination of techniques may not always provide straightforward data, especially when properties like surface chemistry and pore structure compete with each other like in water vapour sorption. Hence, interpretation and the acquisition of statistically relevant (sample size) data sets remain challenging, particularly when correlations and causal relationships towards lithological parameters want to be established.

A straightforward insight into pore networks might be obtained from clever fluid-fluid combinations which are particularly interesting for the commonly requested, but most difficult to assess, microporosity of mudrocks. Mudrocks have a highly variable degree of microporosity, for which classical theories like Dubinin's volume filling theory provide only a fingerprint and derived micropore size distributions represent at best averaged distributions whose actual shape is dictated by the underlying mathematical model. To overcome these limitations, the molecular sieving effect can be employed to evaluate the microporosity independent of any model. Described by Rouquerol et al. (2014) as a molecule-size-based deconvolution of the micropore size distribution, the approach may involve the sequential measurement of isotherms with, at best, apolar molecules of equivalent structure but different size such as alkanes with increasing chain length (e.g., methane to decane). Theoretically, this enables a gradual reduction in the accessible micropore size and -volume from which an independent frequency distribution of pore sizes can be derived. Alternatively, employing temperature-controlled desorption of a preadsorbed molecule with high interaction energy (e.g., nonane, as suggested by Gregg & Langford (1969) and picked up by Rouquerol et al. (2014)), in combination with a traditional adsorptive (similar to the earlier combination of water and nitrogen), may offer a different but complementary analysis strategy. This method, initially devised by Gregg & Langford (1969), has been successfully applied to engineered materials (e.g., Velasco et al., 2017) and clays (e.g., Ribeiro Carrott et al., 2016), but it has not been explored in the context of mudrocks to the best of knowledge. Thus, such a fluid combination might provide an opportunity for progress in the microporosity assessment of mudrocks.

Despite advanced analysis strategies and technical progress, the model reliance will persist, if data cannot be interpreted generically. Consequently, advanced sorption models based on density functional theory and molecular simulations need to be advanced and developed with a particular

focus on mudrocks. Until recently, the application of advanced models for mudrocks was often performed without any justification, despite that experts clearly state that data are meaningless if no adequate model-kernel with regard to geometry and surface chemistry is available for the studied material (Thommes et al., 2015, Bertier et al., 2016). For obvious reasons, the complexity of mudrocks with respect to composition and pore network make the general development of such models extremely difficult and time-consuming. Nevertheless, such a development is necessary when predictive models need to be fed with such textural data; e.g., for the long-term risk assessment in nuclear waste repositories. To initiate such a process, a systematic comparison of advanced and classical methods on mineralogically, chemically and microstructurally very well-characterised samples (e.g., mudrocks, clays and clay minerals) can be a valuable base to scrutinise the sensitivity of a particular model towards specific parameters like scale dependent wettability. It is believed that such development will remain challenging for chemically and structurally heterogeneous materials but with the support of powerful artificial intelligence such developments are considered possible in the near future.

Bibliography

Alcañiz-Monge, J., Linares-Solano, A. & Rand, B. (2001) Water Adsorption on Activated Carbons: Study of Water Adsorption in Micro- and Mesopores. The Journal of Physical Chemistry B, **105**, 7998–8006.

Alcañiz-Monge, J. & Lozano-Castelló, D. (2002) Water Adsorption on Micro and Mesoporous Silicas. In: Studies in Surface Science and Catalysis, volume 144, 291–298. Elsevier.

Alcañiz-Monge, J., Pérez-Cadenas, M. & Lozano-Castelló, D. (2010) Influence of Pore Size Distribution on Water Adsorption on Silica Gels. Journal of Porous Materials, **17**, 409–416.

Amann-Hildenbrand, A., Krooss, B., Harrington, J., Cuss, R., Davy, C., Skoczylas, F., Jacops, E. & Maes, N. (2015a) Gas Transfer Through Clay Barriers. In: Developments in Clay Science, volume 6, 227–267. Elsevier.

Amann-Hildenbrand, A., Krooss, B. M., Bertier, P. & Busch, A. (2015b) Laboratory Testing Procedure for CO2 Capillary Entry Pressures on Caprocks. In: Carbon Dioxide Capture for Storage in Deep Geological Formations (K. F. Gerdes, editor), volume 4, 355–384. CPL Press.

Anovitz, L. M. & Cole, D. R. (2015) Characterization and Analysis of Porosity and Pore Structures. Reviews in Mineralogy and Geochemistry, **80**, 61–164.

Aplin, A. C., Matenaar, I. F., McCarty, D. K. & Van Der Pluijm, B. A. (2006) Influence of Mechanical Compaction and Clay Mineral Diagenesis on the Microfabric and Pore-Scale Properties of Deep-Water Gulf of Mexico Mudstones. Clays and Clay Minerals, **54**, 500–514.

Arthur, E., Tuller, M., Moldrup, P. & De Jonge, L. W. (2020) Clay Content and Mineralogy, Organic Carbon and Cation Exchange Capacity Affect Water Vapour Sorption Hysteresis of Soil. European Journal of Soil Science, **71**, 204–214.

Arthur, E., Tuller, M., Moldrup, P., Greve, M. H., Knadel, M. & de Jonge, L. W. (2018) Applicability of the Guggenheim-Anderson-Boer Water Vapour Sorption Model for Estimation of Soil Specific Surface Area: Soil Specific Surface Area Derived from GAB Model. European Journal of Soil Science, **69**, 245–255.

Arthur, E., Tuller, M., Moldrup, P., Jensen, D. K. & De Jonge, L. W. (2015) Prediction of Clay Content from Water Vapour Sorption Isotherms Considering Hysteresis and Soil Organic Matter Content: Clay Content Prediction from Water Vapour Sorption. European Journal of Soil Science, **66**, 206–217.

Bai, J., Kang, Y., Chen, M., Chen, Z., You, L., Li, X. & Chen, G. (2020) Impact of Surface Chemistry and Pore Structure on Water Vapor Adsorption Behavior in Gas Shale. Chemical Engineering Journal, **402**, 126238.

Barrer, R. M. (1978) Zeolites and Clay Minerals as Sorbents and Molecular Sieves. Academic Press London ; New York.

Barrer, RM. & Reay, JSS. (1957) Sorption and Intercalation by Methyl-Ammonium Montmorillonites. Transactions of the Faraday Society, **53**, 1253–1261.

Barrett, E. P., Joyner, L. G. & Halenda, P. P. (1951) The Determination of Pore Volume and Area Distributions in Porous Substances. I. Computations from Nitrogen Isotherms. Journal of the American Chemical Society, **73**, 373–380.

Baumgartner, B., Hayden, J., Loizillon, J., Steinbacher, S., Grosso, D. & Lendl, B. (2019) Pore Size-Dependent Structure of Confined Water in Mesoporous Silica Films from Water Adsorption/Desorption Using ATR–FTIR Spectroscopy. Langmuir, **35**, 11986–11994.

Behar, F., Beaumont, V. & De B. Penteado, H. L. (2001) Rock-Eval 6 Technology: Performances and Developments. Oil & Gas Science and Technology, **56**, 111–134.

Bérend, I. (1995) Mechanism of Adsorption and Desorption of Water Vapor by Homoionic Montmorillonites: 2. The Li^+, Na^+, K^+, Rb^+, and Cs^+-Exchanged Forms. Clays and Clay Minerals, **43**, 324–336.

Bergaya, F. & Lagaly, G. (2013) Handbook of Clay Science. Newnes.

Bergaya, F., Lagaly, G. & Vayer, M. (2006) Chapter 12.10 Cation and Anion Exchange. In: Handbook of Clay Science (F. Bergaya, B. K. Theng and G. Lagaly, editors), Developments in Clay Science, volume 1, 979–1001. Elsevier.

Bertier, P., Schweinar, K., Stanjek, H., Ghanizadeh, A., Clarkson, C. R., Busch, A., Kampman, N., Prinz, D., Amann-Hildebrand, A., Krooss, B. M. & Pipich, V. (2016) On the Use and Abuse of N2 Physisorption for the Characterization of the Pore Structure of Shales. In: Filling the Gaps – from Microscopic Pore Structures to Transport Properties in Shales, The Clay Minerals Society Workshop Lectures, volume 21, 151–161. The Clay Mineral Society.

Bossart, P., Bernier, F., Birkholzer, J., Bruggeman, C., Connolly, P., Dewonck, S., Fukaya, M., Herfort, M., Jensen, M., Matray, J.-M., Mayor, J. C., Moeri, A., Oyama, T., Schuster, K., Shigeta, N., Vietor, T. & Wieczorek, K. (2017) Mont Terri Rock Laboratory, 20 Years of Research: Introduction, Site Characteristics and Overview of Experiments. Swiss Journal of Geosciences, **110**, 3–22.

Bourg, I. C. & Tournassat, C. (2015) Chapter 6 - Self-Diffusion of Water and Ions in Clay Barriers. In: Natural and Engineered Clay Barriers (C. Tournassat, C. I. Steefel, I. C. Bourg and F. Bergaya, editors), Developments in Clay Science, volume 6, 189–226. Elsevier.

Bridgeman, O. C. & Aldrich, E. W. (1964) Vapor Pressure Tables for Water. Journal of Heat Transfer, **86**, 279–286.

Brigatti, M., Galan, E. & Theng, B. (2006) Chapter 2 Structures and Mineralogy of Clay Minerals. In: Handbook of Clay Science (F. Bergaya, B. K. Theng and G. Lagaly, editors), Developments in Clay Science, volume 1, 19–86. Elsevier.

Brovchenko, I. & Geiger, A. (2002) Water in Nanopores in Equilibrium with a Bulk Reservoir — Gibbs Ensemble Monte Carlo Simulations. Journal of Molecular Liquids, **96–97**, 195–206.

Brovchenko, I., Geiger, A. & Oleinikova, A. (2004) Water in Nanopores: II. The Liquid–Vapour Phase Transition near Hydrophobic Surfaces. Journal of Physics: Condensed Matter, **16**, S5345–S5370.

Brovchenko, Ivan. & Oleinikova, Alla. (2008) 3 - Surface Critical Behavior of Water. In: Interfacial and Confined Water (Ivan. Brovchenko and Alla. Oleinikova, editors), 67–89. Elsevier, Amsterdam.

Brunauer, S., Emmett, P. H. & Teller, E. (1938) Adsorption of Gases in Multimolecular Layers. Journal of the American chemical society, **60**, 309–319.

Busch, A., Bertier, P., Gensterblum, Y., Rother, G., Spiers, C. J., Zhang, M. & Wentinck, H. M. (2016) On Sorption and Swelling of CO2 in Clays. Geomechanics and Geophysics for Geo-Energy and Geo-Resources, **2**, 111–130.

Busch, A., Kampman, N., Bertier, P., Pipich, V., Feoktystov, A., Rother, G., Harrington, J., Leu, L., Aertens, M. & Jacops, E. (2018) Predicting Effective Diffusion Coefficients in Mudrocks Using a Fractal Model and Small-Angle Neutron Scattering Measurements. Water Resources Research, **54**, 7076–7091.

Busch, A., Schweinar, K., Kampman, N., Coorn, A., Pipich, V., Feoktystov, A., Leu, L., Amann-Hildenbrand, A. & Bertier, P. (2017) Determining the Porosity of Mudrocks Using Methodological Pluralism. Geological Society, London, Special Publications, **454**, 15–38.

Cao, T., Song, Z., Wang, S. & Xia, J. (2015) A Comparative Study of the Specific Surface Area and Pore Structure of Different Shales and Their Kerogens. Science China Earth Sciences, **58**, 510–522.

Cases, J. (1997) Mechanism of Adsorption and Desorption of Water Vapor by Homoionic Montmorillonite: 3. the Mg^{2+}, Ca^{2+}, Sr^{2+} and Ba^{2+} Exchanged Forms. Clays and Clay Minerals, **45**, 8–22.

Cases, J. M., Berend, I., Besson, G., Francois, M., Uriot, J. P., Thomas, F. & Poirier, J. E. (1992) Mechanism of Adsorption and Desorption of Water Vapor by Homoionic Montmorillonite. 1. The Sodium-Exchanged Form. Langmuir, **8**, 2730–2739.

Cazorla-Amorós, D., Alcañiz-Monge, J., de la Casa-Lillo, M. A. & Linares-Solano, A. (1998) CO_2 As an Adsorptive To Characterize Carbon Molecular Sieves and Activated Carbons. Langmuir, **14**, 4589–4596.

Chalmers, G. R. & Bustin, R. M. (2007) The Organic Matter Distribution and Methane Capacity of the Lower Cretaceous Strata of Northeastern British Columbia, Canada. International Journal of Coal Geology, **70**, 223–239.

Chalmers, G. R. & Bustin, R. M. (2008) Lower Cretaceous Gas Shales in Northeastern British Columbia, Part I: Geological Controls on Methane Sorption Capacity. Bulletin of Canadian Petroleum Geology, **56**, 1–21.

Chen, F., Liu, D., Ding, X., Zheng, Q. & Lu, S. (2022) Pore Size Distributions Contributed by Various Components in the Upper Ordovician Wufeng Shale from Southeast Chongqing, China. Journal of Petroleum Science and Engineering, **208**, 109230.

Chen, J., Gai, H. & Xiao, Q. (2021) Effects of Composition and Temperature on Water Sorption in Overmature Wufeng-Longmaxi Shales. International Journal of Coal Geology, **234**, 103673.

Chen, J. & Xiao, X. (2014) Evolution of Nanoporosity in Organic-Rich Shales during Thermal Maturation. Fuel, **129**, 173–181.

Cheng, P., Tian, H., Xiao, X., Gai, H., Li, T. & Wang, X. (2017) Water Distribution in Overmature Organic-Rich Shales: Implications from Water Adsorption Experiments. Energy & Fuels, **31**, 13120–13132.

Chiou, C. T. (1997) Effects of Exchanged Cation and Layer Charge on the Sorption of Water and EGME Vapors on Montmorillonite Clays. Clays and Clay Minerals, **45**, 867–880.

Choma, J., Górka, J. & Jaroniec, M. (2008) Mesoporous Carbons Synthesized by Soft-Templating Method: Determination of Pore Size Distribution from Argon and Nitrogen Adsorption Isotherms. Microporous and Mesoporous Materials, **112**, 573–579.

Cimino, R., Cychosz, K. A., Thommes, M. & Neimark, A. V. (2013) Experimental and Theoretical Studies of Scanning Adsorption–Desorption Isotherms. Colloids and Surfaces A: Physicochemical and Engineering Aspects, **437**, 76–89.

Claes, H., Miranda, T., Falcão, T. C., Soete, J., Mohammadi, Z., Zieger, L., Erthal, M. M., Aguillar, J., Schmatz, J., Busch, A. & Swennen, R. (2021) Model for Calcite Spherulite Formation in Organic, Clay-Rich, Lacustrine Carbonate Shales (Barbalha Formation, Aptian, Araripe Basin, NE Brazil). Marine and Petroleum Geology, **128**, 104988.

Clarkson, C., Freeman, M., He, L., Agamalian, M., Melnichenko, Y., Mastalerz, M., Bustin, R., Radliński, A. & Blach, T. (2012) Characterization of Tight Gas Reservoir Pore Structure Using USANS/SANS and Gas Adsorption Analysis. Fuel, **95**, 371–385.

Clarkson, C. & Haghshenas, B. (2016) Characterization of Multi-Fractured Horizontal Shale Wells Using Drill Cuttings: 1. Fluid-in-place Estimation. Journal of Natural Gas Science and Engineering, **32**, 574–585.

Clarkson, C., Solano, N., Bustin, R., Bustin, A., Chalmers, G., He, L., Melnichenko, Y., Radliński, A. & Blach, T. (2013) Pore Structure Characterization of North American Shale Gas Reservoirs Using USANS/SANS, Gas Adsorption, and Mercury Intrusion. Fuel, **103**, 606–616.

Clarkson, C. R. & Haghshenas, B. (2013) Modeling of Supercritical Fluid Adsorption on Organic-Rich Shales and Coal. In: All Days, SPE–164532–MS. SPE, The Woodlands, Texas, USA.

Clarkson, C. R. & Solano, N. A. (2016) Combined Use of Neutron-Scattering, Fluid-Invasion, and Image-Analysis Techniques to Assess Pore Structure, Accessibility, and Connectivity in Tight Rock. In: Filling the Gaps – from Microscopic Pore Structures to Transport Properties in Shales, number 21 in The Clay Minerals Society Workshop Lectures, 15–31. The Clay Minerals Society.

Coasne, B. (2016) Multiscale Adsorption and Transport in Hierarchical Porous Materials. New Journal of Chemistry, **40**, 4078–4094.

Crank, J. (1975) The Mathematics of Diffusion. Clarendon Press, Oxford, [Eng], 2d ed edition.

Cychosz, K. A., Guillet-Nicolas, R., García-Martínez, J. & Thommes, M. (2017) Recent Advances in the Textural Characterization of Hierarchically Structured Nanoporous Materials. Chemical Society Reviews, **46**, 389–414.

Cychosz, K. A. & Thommes, M. (2018) Progress in the Physisorption Characterization of Nanoporous Gas Storage Materials. Engineering, **4**, 559–566.

Dang, W., Jiang, S., Zhang, J., Li, P., Nie, H., Liu, Y., Li, F., Sun, J., Tao, J., Shan, C., Tang, X., Wang, R. & Yin, Y. (2021) A systematic experimental and modeling study of water adsorption/desorption behavior in organic-rich shale with different particle sizes. Chemical Engineering Journal, **426**, 130596.

Dazas, B., Lanson, B., Breu, J., Robert, J.-L., Pelletier, M. & Ferrage, E. (2013) Smectite Fluorination and Its Impact on Interlayer Water Content and Structure: A Way to Fine Tune the Hydrophilicity of Clay Surfaces? Microporous and Mesoporous Materials, **181**, 233–247.

Delle Piane, C., Ansari, H., Li, Z., Mata, J., Rickard, W., Pini, R., Dewhurst, D. N. & Sherwood, N. (2021) Influence of Organic Matter Type on Porosity Development in the Wufeng-Longmaxi Shale: A Combined Microscopy, Neutron Scattering and Physisorption Approach. International Journal of Coal Geology, 103880.

DENKA (2023) Fused Silica (DF) SphericalL (FB, FBX). https://www.denka.co.jp/eng/product/ detail_00032/.

Derkowski, A. & Kuligiewicz, A. (2017) Rehydroxylation in Smectites and Other Clay Minerals Observed In-Situ with a Modified Thermogravimetric System. Applied Clay Science, **136**, 219–229.

Derkowski, A. & Kuligiewicz, A. (2022) Thermal Analysis and Thermal Reactions of Smectites: A Review of Methodology, Mechanisms, and Kinetics. Clays and Clay Minerals, **70**, 946–972.

Desbois, G., Hemes, S., Laurich, B., Houben, M., Klaver, J., Höhne, N., Urai, J. L., Viggiani, G. & Bésuelle, P. (2016) Investigation of Microstructures in Naturally and Experimentally Deformed Reference Clay Rocks Using Innovative Methods in Scanning Electron Microscopy. In: Filling the Gaps – from Microscopic Pore Structures to Transport Properties in Shales. Clay Minerals Society.

Deutsche Institut für Normung e.V. (2012) Bestimmung der spezifischen Oberfläche von Festkörpern mittels Gasadsorption - BET-Verfahren (DIN ISO 9277:2010).

Dewhurst, D. N., Aplin, A. C., Sarda, J.-P. & Yang, Y. (1998) Compaction-driven Evolution of Porosity and Permeability in Natural Mudstones: An Experimental Study. Journal of Geophysical Research: Solid Earth, **103**, 651–661.

Dewhurst, D. N., Yang, Y. & Aplin, A. C. (1999) Permeability and Fluid Flow in Natural Mudstones. Geological Society, London, Special Publications, **158**, 23–43.

Do, D. & Do, H. (2000) A Model for Water Adsorption in Activated Carbon. Carbon, **38**, 767–773.

Do, D., Junpirom, S. & Do, H. (2009) A New Adsorption–Desorption Model for Water Adsorption in Activated Carbon. Carbon, **47**, 1466–1473.

Dobruskin, V. K. (1998) Micropore Volume Filling. A Condensation Approximation Approach as a Foundation to the Dubinin-Astakhov Equation. Langmuir, **14**, 3840–3846.

Doebelin, N. & Kleeberg, R. (2015) Profex : A Graphical User Interface for the Rietveld Refinement Program BGMN. Journal of Applied Crystallography, **48**, 1573–1580.

Drain, LE. (1953) Permanent Electric Quadrupole Moments of Molecules and Heats of Adsorption. Transactions of the Faraday Society, **49**, 650–654.

Dubinin, M. (1975) Physical Adsorption of Gases and Vapors in Micropores. In: Progress in Surface and Membrane Science (D. Cadenhead, J. Danielli and M. Rosenberg, editors), Progress in Surface and Membrane Science, volume 9, 1–70. Elsevier.

Dubinin, M. M., Zaverina, E. D. & Serpinsky, V. V. (1955) The Sorption of Water Vapour by Active Carbon. Journal of The Chemical Society, 1760–1766.

Dubinin, MM. & Astakhov, VA. (1971) Development of the Concepts of Volume Filling of Micropores in the Adsorption of Gases and Vapors by Microporous Adsorbents-Communication 1. Carbon Adsorbents. Bulletin of the Academy of Sciences of the USSR. Division of Chemical Sciences, **20**, 3–7.

Dubinin, MM. & Serpinsky, W. (1981) Isotherm Equation for Water Vapor Adsorption by Microporous Carbonaceous Adsorbents. Carbon, **5**, 402–403.

Dudek, L. (2016) Pore Size Distribution in Shale Gas Deposits Based on Adsorption Isotherm Analyses. Nafta-Gaz, **8**, 603–609.

Emmerich, K. (1999) Dehydroxylation Behavior of Heat-Treated and Steam-Treated Homoionic Cis-Vacant Montmorillonites. Clays and Clay Minerals, **47**, 591–604.

Everett, D. H. & Powl, J. C. (1976) Adsorption in Slit-like and Cylindrical Micropores in the Henry's Law Region. A Model for the Microporosity of Carbons. J. Chem. Soc., Faraday Trans. 1, **72**, 619–636.

Feng, D., Li, X., Wang, X., Li, J., Sun, F., Sun, Z., Zhang, T., Li, P., Chen, Y. & Zhang, X. (2018) Water Adsorption and Its Impact on the Pore Structure Characteristics of Shale Clay. Applied Clay Science, **155**, 126–138.

Feng, D., Wu, K., Bakhshian, S., Hosseini, S. A., Li, J. & Li, X. (2020) Nanoconfinement Effect on Surface Tension: Perspectives from Molecular Potential Theory. Langmuir, **36**, 8764–8776.

Fernandez-Colinas, J., Denoyel, R. & Rouquerol, J. (1989) Adsorption of Iodine from Aqueous Solutions on to Activated Carbons: Correlation with Nitrogen Adsorption at 77K. Adsorption Science & Technology, **6**, 18–26.

Ferrage, E. (2005) Investigation of Smectite Hydration Properties by Modeling Experimental X-ray Diffraction Patterns: Part I. Montmorillonite Hydration Properties. American Mineralogist, **90**, 1358–1374.

Ferrage, E. (2016) Investigation of the Interlayer Organization of Water and Ions In Smectite from the Combined Use of Diffraction Experiments And Molecular Simulations. a Review of Methodology, Applications, And Perspectives. Clays and Clay Minerals, **64**, 348–373.

Ferrage, E., Lanson, B., Malikova, N., Plançon, A., Sakharov, B. A. & Drits, V. A. (2005) New Insights on the Distribution of Interlayer Water in Bi-Hydrated Smectite from X-ray Diffraction Profile Modeling of 00 l Reflections. Chemistry of Materials, **17**, 3499–3512.

Ferrage, E., Lanson, B., Michot, L. J. & Robert, J.-L. (2010) Hydration Properties and Interlayer Organization of Water and Ions in Synthetic Na-Smectite with Tetrahedral Layer Charge. Part 1. Results from X-ray Diffraction Profile Modeling. The Journal of Physical Chemistry C, **114**, 4515–4526.

Ferrage, E., Lanson, B., Sakharov, B. A., Geoffroy, N., Jacquot, E. & Drits, V. A. (2007) Investigation of Dioctahedral Smectite Hydration Properties by Modeling of X-ray Diffraction Profiles: Influence of Layer Charge and Charge Location. American Mineralogist, **92**, 1731–1743.

Fink, R. (2017) Experimental Investigation of Gas Transport and Storage Processes in the Matrix of Gas Shales. Ph.D. thesis, RWTH Aachen University, Aachen.

Fink, R., Amann-Hildenbrand, A., Bertier, P. & Littke, R. (2018) Pore Structure, Gas Storage and Matrix Transport Characteristics of Lacustrine Newark Shale. Marine and Petroleum Geology, **97**, 525–539.

Fink, R., Frohn, V., Froidl, F., Littke, R. & Uffmann, A. K. (2019) Impact of Burial History on Petrophysical Properties of Jurassic and Lower Cretaceous Mudstones as Potential Nuclear Waste Storage Sites in the Lower Saxony Basin, Northern Germany. Zeitschrift der Deutschen Gesellschaft für Geowissenschaften, **170**, 339–355.

Fink, R., Krooss, B. M., Gensterblum, Y. & Amann-Hildenbrand, A. (2017) Apparent Permeability of Gas Shales – Superposition of Fluid-Dynamic and Poro-Elastic Effects. Fuel, **199**, 532–550.

Furmann, A., Mastalerz, M., Bish, D., Schimmelmann, A. & Pedersen, P. K. (2016) Porosity and Pore Size Distribution in Mudrocks from the Belle Fourche and Second White Specks Formations in Alberta, Canada. AAPG Bulletin, **100**, 1265–1288.

Garcia-Martinez, J., Xiao, C., Cychosz, K. A., Li, K., Wan, W., Zou, X. & Thommes, M. (2014) Evidence of Intracrystalline Mesostructured Porosity in Zeolites by Advanced Gas Sorption, Electron Tomography and Rotation Electron Diffraction. ChemCatChem, **6**, 3110–3115.

Gasparik, M., Ghanizadeh, A., Bertier, P., Gensterblum, Y., Bouw, S. & Krooss, B. M. (2012) High-Pressure Methane Sorption Isotherms of Black Shales from The Netherlands. Energy & Fuels, **26**, 4995–5004.

Gasparik, M., Rexer, T. F., Aplin, A. C., Billemont, P., De Weireld, G., Gensterblum, Y., Henry, M., Krooss, B. M., Liu, S., Ma, X., Sakurovs, R., Song, Z., Staib, G., Thomas, K. M., Wang, S. & Zhang, T. (2014) First International Inter-Laboratory Comparison of High-Pressure CH_4, CO_2 and C_2H_6 Sorption Isotherms on Carbonaceous Shales. International Journal of Coal Geology, **132**, 131–146.

Ghanizadeh, A., Gasparik, M., Amann-Hildenbrand, A., Gensterblum, Y. & Krooss, B. (2013) Lithological Controls on Matrix Permeability of Organic-rich Shales: An Experimental Study. Energy Procedia, **40**, 127–136.

Ghanizadeh, A., Gasparik, M., Amann-Hildenbrand, A., Gensterblum, Y. & Krooss, B. M. (2014) Experimental Study of Fluid Transport Processes in the Matrix System of the European Organic-Rich Shales: I. Scandinavian Alum Shale. Marine and Petroleum Geology, **51**, 79–99.

Gowrishankar, A., Jacops, E., Maes, N., Verboven, P. & Janssen, H. (2023) An Experimental Methodology to Assess the Impact of Desaturation on Gas Diffusion in Clay Based Materials. E3S Web of Conferences, **382**, 20001.

Greenspan, L. (1977) Humidity Fixed Points of Binary Saturated Aqueous Solutions. Journal of Research of the National Bureau of Standards Section A: Physics and Chemistry, **81A**, 89.

Gregg, S. J. & Langford, J. F. (1969) Evaluation of microporosity, with special reference to a carbon black. Trans. Faraday Soc., **65**, 1394–1400.

Grekov, D., Montavon, G., Robinet, J.-C. & Grambow, B. (2019) Smectite Fraction Assessment in Complex Natural Clay Rocks from Interlayer Water Content Determined by Thermogravimetric and Thermoporometry Analysis. Journal of Colloid and Interface Science, **555**, 157–165.

Groen, J. C., Peffer, L. A. & Pérez-Ramírez, J. (2003) Pore Size Determination in Modified Micro- and Mesoporous Materials. Pitfalls and Limitations in Gas Adsorption Data Analysis. Microporous and Mesoporous Materials, **60**, 1–17.

Grohmann, S., Fietz, S. W., Littke, R., Bou Daher, S., Romero-Sarmiento, M. F., Nader, F. H. & Baudin, F. (2018) Source Rock Characterization of Mesozoic to Cenozoic Organic Matter Rich Marls and Shales of the Eratosthenes Seamount, Eastern Mediterranean Sea. Oil & Gas Science and Technology – Revue d'IFP Energies nouvelles, **73**, 49.

Grohmann, S., Littke, R., Abu-Mahfouz, I., Gaus, G., Klaver, J., Thüns, N., Schulte, P., Patzek, T. & Vahrenkamp, V. (2023) The Deposition of Type II-S Jordan Oil Shale in the Context of Late Cretaceous Source Rock Formation in the Eastern Mediterranean Realm. Insights from Organic and Inorganic Geochemistry and Petrography. Marine and Petroleum Geology, **148**, 106058.

Grosman, A. & Ortega, C. (2005) Nature of Capillary Condensation and Evaporation Processes in Ordered Porous Materials. Langmuir, **21**, 10515–10521.

Grosman, A. & Ortega, C. (2008) Capillary Condensation in Porous Materials. Hysteresis and Interaction Mechanism without Pore Blocking/Percolation Process. Langmuir, **24**, 3977–3986.

Gu, Y., Wan, Q. & Li, X. (2021) The Selection of Outgas Temperature for Shale in Low-Pressure N $_2$ Adsorption: An Evidence from Thermogravimetry. Energy Exploration & Exploitation, **39**, 1685–1696.

Guha Roy, D., Singh, T. N., Kodikara, J. & Das, R. (2017) Effect of Water Saturation on the Fracture and Mechanical Properties of Sedimentary Rocks. Rock Mechanics and Rock Engineering, **50**, 2585–2600.

Gurvich, LG. (1915) Acerca de La Fuerza de Atracción Fisicoquímica. Journal of Russian Physical and Chemical Society, **47**, 805–27.

Hagymassy, J., Brunauer, S. & Mikhail, R. (1969) Pore Structure Analysis by Water Vapor Adsorption: I. t-Curves for Water Vapor. Journal of Colloid and Interface Science, **29**, 485–491.

Harkins, W. D. & Jura, G. (1944a) The Decrease (π) of Free Surface Energy (γ) as a Basis for the Development of Equations for Adsorption Isotherms; and the Existence of Two Condensed Phases in Films on Solids. The Journal of Chemical Physics, **12**, 112–113.

Harkins, W. D. & Jura, G. (1944b) Surfaces of Solids. XIII. A Vapor Adsorption Method for the Determination of the Area of a Solid without the Assumption of a Molecular Area, and the Areas Occupied by Nitrogen and Other Molecules on the Surface of a Solid. Journal of the American Chemical Society, **66**, 1366–1373.

Hartmann, M. & Vinu, A. (2002) Mechanical Stability and Porosity Analysis of Large-Pore SBA-15 Mesoporous Molecular Sieves by Mercury Porosimetry and Organics Adsorption. Langmuir, **18**, 8010–8016.

HEGLA boraident GmbH (2013) Porous Glass Membranes (VYCOR).
URL:http://www.boraident.de/index.php?url=%2FSeiten%2FProdukte%2FNanopor%C3%B6ses+Glas%2Findex&state=page&action=default.

Hendricks, S. B., Nelson, RA. & Alexander, L. T. (1940) Hydration Mechanism of the Clay Mineral Montmorillonite Saturated with Various Cations1. Journal of the American Chemical Society, **62**, 1457–1464.

Henry, P. & Bourlange, S. (2004) Smectite and Fluid Budget at Nankai ODP Sites Derived from Cation Exchange Capacity. Earth and Planetary Science Letters, **219**, 129–145.

Hildenbrand, A., Krooss, B., Busch, A. & Gaschnitz, R. (2006) Evolution of Methane Sorption Capacity of Coal Seams as a Function of Burial History — a Case Study from the Campine Basin, NE Belgium. International Journal of Coal Geology, **66**, 179–203.

Hildenbrand, A., Krooss, B. & Schlömer, S. (2020) N2 and CO2 Gas Breakthrough Experiments on Fine-Grained Sediments. In: Poromechanics II (J.-L. Auriault, C. Geindreau, P. Royer, J.-F. Bloch, C. Boutin and J. Lewandowska, editors), 445–451. CRC Press, 1 edition.

Holmes, R., Aljamaan, H., Vishal, V., Wilcox, J. & Kovscek, A. R. (2019) Idealized Shale Sorption Isotherm Measurements To Determine Pore Capacity, Pore Size Distribution, and Surface Area. Energy & Fuels, **33**, 665–676.

Holmes, R., Rupp, E. C., Vishal, V. & Wilcox, J. (2015) Characterization and Adsorption Investigations of the Nanostructure of Gas Shales. In: Day 1 Tue, October 27, 2015, D011S003R002. OTC, Rio de Janeiro, Brazil.

Holmes, R., Rupp, E. C., Vishal, V. & Wilcox, J. (2017) Selection of Shale Preparation Protocol and Outgas Procedures for Applications in Low-Pressure Analysis. Energy & Fuels, **31**, 9043–9051.

Horikawa, T., Do, D. & Nicholson, D. (2011a) Capillary Condensation of Adsorbates in Porous Materials. Advances in Colloid and Interface Science, **169**, 40–58.

Horikawa, T., Sakao, N. & Do, D. (2013) Effects of Temperature on Water Adsorption on Controlled Microporous and Mesoporous Carbonaceous Solids. Carbon, **56**, 183–192.

Horikawa, T., Sekida, T., Hayashi, J., Katoh, M. & Do, D. D. (2011b) A New Adsorption–Desorption Model for Water Adsorption in Porous Carbons. Carbon, **49**, 416–424.

Horikawa, T., Tan, S. J., Do, D., Sotowa, K.-I., Alcántara-Avila, J. R. & Nicholson, D. (2017) Temperature

Dependence of Water Adsorption on Highly Graphitized Carbon Black and Highly Ordered Mesoporous Carbon. Carbon, **124**, 271–280.

Hou, C., Yu, B., Liu, L., Xu, Y., Zhang, Y., Zhang, L., Zhao, J., Zhao, X., Zuo, Q. & Sun, M. (2021) Water Uptake Behavior and Influence Factors of Longmaxi Shale: Implications from Water Physisorption and Imbibition Measurements. Energy & Fuels, **35**, 11958–11975.

Hu, Z., Gaus, G., Seemann, T., Zhang, Q., Littke, R. & Fink, R. (2021) Pore Structure and Sorption Capacity Investigations of Ediacaran and Lower Silurian Gas Shales from the Upper Yangtze Platform, China. Geomechanics and Geophysics for Geo-Energy and Geo-Resources, **7**, 1–26.

Iiyama, T., Nishikawa, K., Suzuki, T. & Kaneko, K. (1997) Study of the Structure of a Water Molecular Assembly in a Hydrophobic Nanospace at Low Temperature with in Situ X-ray Diffraction. Chemical Physics Letters, **274**, 152–158.

Iiyama, T., Ruike, M. & Kaneko, K. (2000) Structural Mechanism of Water Adsorption in Hydrophobic Micropores from in Situ Small Angle X-ray Scattering. Chemical Physics Letters, **331**, 359–364.

Jacops, E., Phung, Q. T., Frederickx, L. & Levasseur, S. (2021) Diffusive Transport of Dissolved Gases in Potential Concretes for Nuclear Waste Disposal. Sustainability, **13**, 10007.

Jacops, E., Swennen, R., Janssens, N., Seemann, T., Amann-Hildenbrand, A., Krooss, B., Littke, R., Maes, N. & Bruggeman, C. (2020) Linking Petrographical and Petrophysical Properties to Transport Characteristics: A Case from Boom Clay and Eigenbilzen Sands. Applied Clay Science, **190**, 105568.

Janssen, M. & Van Oorschot, C. (1989) The Characterization of Zeolites by Gas Adsorption. In: Studies in Surface Science and Catalysis, volume 49, 633–642. Elsevier.

Jaroniec, M. & Kaneko, K. (1997) Physicochemical Foundations for Characterization of Adsorbents by Using High-Resolution Comparative Plots. Langmuir, **13**, 6589–6596.

Jaroniec, M., Kruk, M. & Olivier, J. P. (1999) Standard Nitrogen Adsorption Data for Characterization of Nanoporous Silicas. Langmuir, **15**, 5410–5413.

Jelinek, L. & Kovats, E. (1994) True Surface Areas from Nitrogen Adsorption Experiments. Langmuir, **10**, 4225–4231.

Johansen, R. T. & Dunning, H. N. (1957) Water-Vapor Adsorption on Clays. Clays and Clay Minerals, **6**, 249–258.

Johnston, CT., Sposito, G. & Erickson, C. (1992) Vibrational Probe Studies of Water Interactions with Montmorillonite. Clays and Clay Minerals, **40**, 722–730.

Kaneko, K., Hanzawa, Y., Iiyama, T., Kanda, T. & Suzuki, T. (1999) Cluster-Mediated Water Adsorption on Carbon Nanopores. Adsorption-journal of The International Adsorption Society, **5**, 7–13.

Kaufhold, S., Dohrmann, R. & Gröger-Trampe, J. (2023) About the Possibility to Liberate Naturally Present Fixed Cations from Dioctahedral Smectites by Hydrothermal Treatment. Applied Clay Science, **244**, 107115.

Kaufhold, S., Dohrmann, R., Klinkenberg, M., Siegesmund, S. & Ufer, K. (2010) N_2-BET Specific Surface Area of Bentonites. Journal of Colloid and Interface Science, **349**, 275–282.

Kaufhold, S., Dohrmann, R., Ufer, K., Kleeberg, R. & Stanjek, H. (2011) Termination of Swelling Capacity of Smectites by Cutrien Exchange. Clay Minerals, **46**, 411–420.

Keller, J. U. & Staudt, R. (2005) Gas adsorption equilibria: experimental methods and adsorptive isotherms. Springer Science & Business Media.

Keller, L. M., Holzer, L., Schuetz, P. & Gasser, P. (2013) Pore Space Relevant for Gas Permeability in Opalinus Clay: Statistical Analysis of Homogeneity, Percolation, and Representative Volume Element. Journal of Geophysical Research: Solid Earth, **118**, 2799–2812.

Keren, R. & Shainberg, I. (1975) Water Vapor Isotherms and Heat of Immersion of Na/Ca-montmorillonite Systems—I: Homoionic Clay. Clays and Clay Minerals, **23**, 193–200.

Kierlik, E., Rosinberg, M. L., Tarjus, G. & Viot, P. (2001) Equilibrium and Out-of-Equilibrium (Hysteretic) Behavior of Fluids in Disordered Porous Materials: Theoretical Predictions. Physical Chemistry Chemical Physics, **3**, 1201–1206.

Klank, D. (2021) Adsorption Studies of Porous and Nonporous Materials with Various Adsorptives in the Entire Temperature Range from 77 K up to 323 K. Partikelwelt, **14**, 1–7.

Klaver, J., Desbois, G., Urai, J. L. & Littke, R. (2012) BIB-SEM Study of the Pore Space Morphology in Early Mature Posidonia Shale from the Hils Area, Germany. International Journal of Coal Geology, **103**, 12–25.

Klobes, P., Meyer, K. & Munro, R. G. (2006) Porosity and Specific Surface Area Measurements for Solid Materials.

KMI-Industrial-Materials (2022) Muscovite HLM3. **URL:**https://kmi.at/de/produktuebersicht/muscovite-mica-hlm.

KMI-Industrial-Minerals (2023) Eisenglimmer MIOX. **URL:**https://kmi.at/de/produktuebersicht/eisenglimmer-miox.

Kruk, M. & Jaroniec, M. (2000) Accurate Method for Calculating Mesopore Size Distributions from Argon Adsorption Data at 87 K Developed Using Model MCM-41 Materials. Chemistry of Materials, **12**, 222–230.

Kruk, M., Jaroniec, M. & Choma, J. (1997) Critical Discussion of Simple Adsorption Methods Used to Evaluate the Micropore Size Distribution. Adsorption, **3**, 209–219.

Kuila, U., McCarty, D. K., Derkowski, A., Fischer, T. B., Topór, T. & Prasad, M. (2014) Nano-Scale Texture and Porosity of Organic Matter and Clay Minerals in Organic-Rich Mudrocks. Fuel, **135**, 359–373.

Kuila, U. & Prasad, M. (2013) Application of Nitrogen Gas-Adsorption Technique for Characterization of Pore Structure of Mudrocks. The Leading Edge, **32**, 1478–1485.

Kuligiewicz, A. & Derkowski, A. (2017) Tightly Bound Water in Smectites. American Mineralogist, **102**, 1073–1090.

Küster, D., Kaufhold, S., Limam, E., Jatlaoui, O., Ba, O., Mohamed, A. M. Z., Pohlmann-Lortz, M., Ranneberg, M. & Ufer, K. (2021) Investigation of Unexplored Kaolin Occurrences in Southern Mauritania and Preliminary Assessment of Possible Applications. Clay Minerals, **56**, 126–139.

Lahn, L., Bertier, P., Seemann, T. & Stanjek, H. (2020) Distribution of Sorbed Water in the Pore Network of Mudstones Assessed from Physisorption Measurements. Microporous and Mesoporous Materials, **295**, 109902.

Laird, D. A. (1999) Layer Charge Influences on the Hydration of Expandable 2:1 Phyllosilicates. Clays and Clay Minerals, **47**, 630–636.

Laird, D. A., Shang, C. & Thompson, M. L. (1995) Hysteresis in Crystalline Swelling of Smectites. Journal of Colloid and Interface Science, **171**, 240–245.

Landers, J., Gor, G. Y. & Neimark, A. V. (2013) Density Functional Theory Methods for Characterization of Porous Materials. Colloids and Surfaces A: Physicochemical and Engineering Aspects, **437**, 3–32.

Lashkaripour, G. R. (2002) Predicting Mechanical Properties of Mudrock from Index Parameters. Bulletin of Engineering Geology and the Environment, **61**, 73–77.

Lazar, O. R., Bohacs, K. M., Macquaker, J. H., Schieber, J. & Demko, T. M. (2015) Capturing Key Attributes of Fine-Grained Sedimentary Rocks in Outcrops, Cores, and Thin Sections: Nomenclature and Description Guidelines. Journal of Sedimentary Research, **85**, 230–246.

Leu, L., Bertier, P., Georgiadis, A., Busch, A., Diaz, A., Klaver, J., Schmatz, J., Lutz-Bueno, V., Ihli, J., Ott, H. & Blunt, M. (2019) SAXS and WAXS Microscopy Applied to Mudrocks: A New Method for Systematic Multiscale Studies of Porosity, Pore Orientation and Mineralogy. In: Sixth EAGE Shale Workshop, 1–4. European Association of Geoscientists & Engineers, Bordeaux, France,.

Leu, L., Georgiadis, A., Blunt, M. J., Busch, A., Bertier, P., Schweinar, K., Liebi, M., Menzel, A. & Ott, H. (2016) Multiscale Description of Shale Pore Systems by Scanning SAXS and WAXS Microscopy. Energy & Fuels, **30**, 10282–10297.

Li, J., Li, X., Wang, X., Li, Y., Wu, K., Shi, J., Yang, L., Feng, D., Zhang, T. & Yu, P. (2016a) Water Distribution Characteristic and Effect on Methane Adsorption Capacity in Shale Clay. International Journal of Coal Geology, **159**, 135–154.

Li, J., Li, X., Wu, K., Feng, D., Zhang, T. & Zhang, Y. (2017) Thickness and Stability of Water Film Confined inside Nanoslits and Nanocapillaries of Shale and Clay. International Journal of Coal Geology, **179**, 253–268.

Li, J., Li, X., Wu, K., Wang, X., Shi, J., Yang, L., Zhang, H., Sun, Z., Wang, R. & Feng, D. (2016b) Water Sorption and Distribution Characteristics in Clay and Shale: Effect of Surface Force. Energy & Fuels, **30**, 8863–8874.

Li, J., Wang, S., Lu, S., Zhang, P., Cai, J., Zhao, J. & Li, W. (2019a) Microdistribution and Mobility of Water in Gas Shale: A Theoretical and Experimental Study. Marine and Petroleum Geology, **102**, 496–507.

Li, J., Wu, K., Chen, Z., Wang, W., Yang, B., Wang, K., Luo, J. & Yu, R. (2019b) Effects of Energetic Heterogeneity on Gas Adsorption and Gas Storage in Geologic Shale Systems. Applied Energy, **251**, 113368.

Li, J., Wu, K., Shi, J., Li, X., Li, Y., Feng, D., Zhang, T., Xu, M. & Bai, Y. (2015a) Water Distribution Characteristic and Effect on Methane Adsorption Capacity in Shale Clays. In: All Days, SPE–176965–MS. SPE, Brisbane, Australia.

Li, J., Yin, J., Zhang, Y., Lu, S., Wang, W., Li, J., Chen, F. & Meng, Y. (2015b) A Comparison of Experimental

Methods for Describing Shale Pore Features — A Case Study in the Bohai Bay Basin of Eastern China. International Journal of Coal Geology, **152**, 39–49.

Li, P., Zhang, J., Rezaee, R., Dang, W., Tang, X., Nie, H. & Chen, S. (2021) Effect of Adsorbed Moisture on the Pore Size Distribution of Marine-Continental Transitional Shales: Insights from Lithofacies Differences and Clay Swelling. Applied Clay Science, **201**, 105926.

Li, X. & Krooss, B. M. (2017) Influence of Grain Size and Moisture Content on the High-Pressure Methane Sorption Capacity of Kimmeridge Clay. Energy & Fuels, **31**, 11548–11557.

Likos, W. J. & Lu, N. (2006) Pore-Scale Analysis of Bulk Volume Change from Crystalline Interlayer Swelling in Na^{+}- and Ca^{2+}-Smectite. Clays and Clay Minerals, **54**, 515–528.

Lindholm, J., Boily, J.-F. & Holmboe, M. (2019) Deconvolution of Smectite Hydration Isotherms. ACS Earth and Space Chemistry, **3**, 2490–2498.

Liu, T. & Yu, Q. (2022) Experimental Investigation into the Permeability of Water Vapor in Shales. Journal of Hydrology, **609**, 127697.

Loganathan, N., Bowers, G. M., Yazaydin, A. O., Schaef, H. T., Loring, J. S., Kalinichev, A. G. & Kirkpatrick, R. J. (2018) Clay Swelling in Dry Supercritical Carbon Dioxide: Effects of Interlayer Cations on the Structure, Dynamics, and Energetics of CO_2 Intercalation Probed by XRD, NMR, and GCMD Simulations. The Journal of Physical Chemistry C, **122**, 4391–4402.

Loucks, R. G., Reed, R. M., Ruppel, S. C. & Hammes, U. (2012) Spectrum of Pore Types and Networks in Mudrocks and a Descriptive Classification for Matrix-Related Mudrock Pores. AAPG Bulletin, **96**, 1071–1098.

Lowell, S., Shields, J. E., Thomas, M. A. & Thommes, M. (2006) Characterization of Porous Solids and Powders: Surface Area, Pore Size and Density, volume 16. Springer Science & Business Media.

Ma, X., Shen, W., Li, X., Hu, Y., Liu, X. & Lu, X. (2020) Experimental Investigation on Water Adsorption and Desorption Isotherms of the Longmaxi Shale in the Sichuan Basin, China. Scientific Reports, **10**, 13434.

Maheshwari, P., Dutta, D., Muthulakshmi, T., Chakraborty, B., Raje, N. & Pujari, P. K. (2017) Desorption of Water from Hydrophilic MCM-41 Mesopores: Positron Annihilation, FTIR and MD Simulation Studies. Journal of Physics: Condensed Matter, **29**, 055003.

Majda, D., Ikonen, T., Krupa, A., Lehto, V.-P. & Makowski, W. (2018) Application of Thermoporometry for Characterization of Mesoporous Silicon: In Search for Probe Liquid Aimed at Large Pores. Microporous and Mesoporous Materials, **264**, 1–7.

Marreiros, J., de Oliveira-Silva, R., Iacomi, P., Llewellyn, P. L., Ameloot, R. & Sakellariou, D. (2021) Benchtop In Situ Measurement of Full Adsorption Isotherms by NMR. Journal of the American Chemical Society, **143**, 8249–8254.

Marschall, P., Horseman, S. & Gimmi, T. (2005) Characterisation of Gas Transport Properties of the Opalinus Clay, a Potential Host Rock Formation for Radioactive Waste Disposal. Oil & Gas Science and Technology, **60**, 121–139.

Martin, R. T. (1957) Water-Vapor Sorption on Kaolinite: Hysteresis. Clays and Clay Minerals, **6**, 259–278.

Maruyama, I., Rymeš, J., Vandamme, M. & Coasne, B. (2018) Cavitation of Water in Hardened Cement Paste under Short-Term Desorption Measurements. Materials and Structures, **51**, 159.

Mastalerz, M., He, L., Melnichenko, Y. B. & Rupp, J. A. (2012) Porosity of Coal and Shale: Insights from Gas Adsorption and SANS/ USANS Techniques. Energy Fuels, 12.

Mastalerz, M., Schimmelmann, A., Drobniak, A. & Chen, Y. (2013) Porosity of Devonian and Mississippian New Albany Shale across a Maturation Gradient: Insights from Organic Petrology, Gas Adsorption, and Mercury Intrusion. AAPG bulletin, **97**, 1621–1643.

McKee, D. W. (1959) The Sorption of Hydrocarbon Vapors by Silica Gel. The Journal of Physical Chemistry, **63**, 1256–1259.

Medek, J. (1977) Possibility of Micropore Analysis of Coal and Coke from the Carbon Dioxide Isotherm. Fuel, **56**, 131–133.

Medina-Rodriguez, B. X. & Alvarado, V. (2021) Use of Gas Adsorption and Inversion Methods for Shale Pore Structure Characterization. Energies, **14**, 2880.

Melnichenko, Y., Radlinski, A., Mastalerz, M., Cheng, G. & Rupp, J. (2009) Characterization of the CO_2 Fluid Adsorption in Coal as a Function of Pressure Using Neutron Scattering Techniques (SANS and USANS). International Journal of Coal Geology, **77**, 69–79.

Merkel, A., Fink, R. & Littke, R. (2015) The Role of Pre-Adsorbed Water on Methane Sorption Capacity of Bossier and Haynesville Shales. International Journal of Coal Geology, **147–148**, 1–8.

Michot, L. & Villiéras, F. (2006) Chapter 12.9 Surface Area and Porosity. In: Handbook of Clay Science (F. Bergaya, B. K. Theng and G. Lagaly, editors), Developments in Clay Science, volume 1, 965–978. Elsevier.

Michot, L. J. (2018) Determination of Surface Areas and Textural Properties of Clay Minerals. In: Developments in Clay Science, volume 9, 23–47. Elsevier.

Michot, L. J., Bihannic, I., Pelletier, M., Rinnert, E. & Robert, J.-L. (2005) Hydration and Swelling of Synthetic Na-saponites: Influence of Layer Charge. American Mineralogist, **90**, 166–172.

Micromeritics-Instrument-Corporation (2012) SiAl-pellets Datasheet. Datasheet Lot:A-501-49.

Milliken, K. L. & Hayman, N. W. (2019) Mudrock Components and the Genesis of Bulk Rock Properties. In: Shale, chapter 1, 1–25. American Geophysical Union (AGU).

Miocic, J. M., Heinemann, N., Alcalde, J., Edlmann, K. & Schultz, R. A. (2023) Enabling Secure Subsurface Storage in Future Energy Systems: An Introduction. Geological Society, London, Special Publications, **528**, 1–14.

Momma, K. & Izumi, F. (2008) VESTA: A Three-Dimensional Visualization System for Electronic and Structural Analysis. Journal of Applied Crystallography, **41**, 653–658.

Mooney, R. W., Keenan, A. G. & Wood, L. A. (1952a) Adsorption of Water Vapor by Montmorillonite. I. Heat of Desorption and Application of BET Theory. Journal of the American Chemical Society, **74**, 1367–1371.

Mooney, RW., Keenan, AG. & Wood, LA. (1952b) Adsorption of Water Vapor by Montmorillonite. II. Effect of Exchangeable Ions and Lattice Swelling as Measured by X-ray Diffraction. Journal of the American Chemical Society, **74**, 1371–1374.

Moore, D. M. & Reynolds, J., R. C. (1989) X-ray diffraction and the identification and analysis of clay minerals. Oxford University Press (OUP), Oxford.

Morishige, K., Tateishi, M., Hirose, F. & Aramaki, K. (2006) Change in Desorption Mechanism from Pore Blocking to Cavitation with Temperature for Nitrogen in Ordered Silica with Cagelike Pores. Langmuir : the ACS journal of surfaces and colloids, **22**, 9220–9224.

Neimark, A. V. & Ravikovitch, P. I. (2001) Capillary Condensation in MMS and Pore Structure Characterization. Microporous and Mesoporous Materials, **44–45**, 697–707.

Neimark, A. V., Ravikovitch, P. I., Grün, M., Schüth, F. & Unger, K. K. (1998) Pore Size Analysis of MCM-41 Type Adsorbents by Means of Nitrogen and Argon Adsorption. Journal of Colloid and Interface Science, **207**, 159–169.

Neimark, A. V., Ravikovitch, P. I. & Vishnyakov, A. (2000) Adsorption Hysteresis in Nanopores. Physical Review E, **62**, R1493–R1496.

Neuzil, C. E. (1994) How Permeable Are Clays and Shales? Water Resources Research, **30**, 145–150.

Newman, A. (1983) The Specific Surface of Soils Determined by Water Sorption. Journal of Soil Science, **34**, 23–32.

Ng, E.-P. & Mintova, S. (2008) Nanoporous Materials with Enhanced Hydrophilicity and High Water Sorption Capacity. Microporous and Mesoporous Materials, **114**, 1–26.

Nguyen, P. T. M., Do, D. D. & Nicholson, D. (2011) On The Cavitation and Pore Blocking in Cylindrical Pores with Simple Connectivity. The Journal of Physical Chemistry B, **115**, 12160–12172.

NIST, N. I. o. S. a. T. (2023) Saturation Properties for Water — Temperature Increments.
URL: https://webbook.nist.gov/cgi/fluid.cgi?TLow=298&THigh=308&TInc=1&Digits=5&ID=C7732185&Action=Load&Type=SatP&TUnit=K&PUnit=bar&DUnit=mol%2Fl&HUnit=kJ%2Fmol&WUnit=m%2Fs&VisUnit=uPa*s&STUnit=N%2Fm&RefState=DEF.

Nolte, S. (2021) Experimental Investigation of Gas Transport and Storage Processes in Tight Porous Media. Ph.D. thesis, RWTH Aachen University.

Norrish, K. (1954) The Swelling of Montmorillonite. Discussions of the Faraday Society, **18**, 120.

Nunn, J. A., Xiang, Y. & Al, T. A. (2018) Investigation of Partial Water Saturation Effects on Diffusion in Shale. Applied Geochemistry, **97**, 93–101.

Payne, D., Sing, K. & Turk, D. (1973) Comparison of Argon and Nitrogen Adsorption Isotherms on Porous and Nonporous Hydroxylated Silica. Journal of Colloid and Interface Science, **43**, 287–293.

Pellenard, P. & Deconinck, J.-F. (2006) Mineralogical Variability of Callovo-Oxfordian Clays from the Paris Basin and the Subalpine Basin. Comptes Rendus Geoscience, **338**, 854–866.

Peng, S. (2019) Gas Relative Permeability and Its Evolution During Water Imbibition in Unconventional Reservoir Rocks: Direct Laboratory Measurement and a Conceptual Model. SPE Reservoir Evaluation & Engineering, **22**, 1346–1359.

Peters, K. E. & Cassa, M. R. (1994) Applied Source Rock Geochemistry: Chapter 5: Part II. Essential Elements. AAPG Special Volumes.

Peyaud, J.-B., Pagel, M., Cabrera, J. & Pitsch, H. (2006) Mineralogical, Chemical and Isotopic Perturbations Induced in Shale by Fluid Circulation in a Fault at the Tournemire Experimental Site (Aveyron, France). Journal of Geochemical Exploration, **90**, 9–23.

Potter, P. E. (2003) Mudrocks. In: Encyclopedia of Sediments and Sedimentary Rocks (G. V. Middleton, M. J. Church, M. Coniglio, L. A. Hardie and F. J. Longstaffe, editors), 451–459. Springer Netherlands, Dordrecht.

Potter, P. E., Maynard, J. B. & Pryor, W. A. (1977) Geology or Argillaceous Sediments: An Annotated and Illustrated Bibliography.

Prinz, D. & Littke, R. (2005) Development of the Micro- and Ultramicroporous Structure of Coals with Rank as Deduced from the Accessibility to Water. Fuel, **84**, 1645–1652.

Prost, R., Koutit, T., Benchara, A. & Huard, E. (1998) State and Location of Water Adsorbed on Clay Minerals: Consequences of the Hydration and Swelling-Shrinkage Phenomena. Clays and clay minerals, **46**, 117–131.

Psarras, P., Holmes, R., Vishal, V. & Wilcox, J. (2017) Methane and CO_2 Adsorption Capacities of Kerogen in the Eagle Ford Shale from Molecular Simulation. Accounts of Chemical Research, **50**, 1818–1828.

Qi, Y., Ju, Y., Cai, J., Gao, Y., Zhu, H., Hunag, C., Wu, J., Meng, S. & Chen, W. (2019) The Effects of Solvent Extraction on Nanoporosity of Marine-Continental Coal and Mudstone. Fuel, **235**, 72–84.

Quirk, J. P. & Murray, R. S. (1999) Appraisal of the Ethylene Glycol Monoethyl Ether Method for Measuring Hydratable Surface Area of Clays and Soils. Soil Science Society of America Journal, **63**, 839–849.

Quirk, JP. (1955) Significance of Surface Areas Calculated from Water Vapor Sorption Isotherms by Use of the BET Equation. Soil Science, **80**, 423–430.

Rathouský, J. & Thommes, M. (2007) Adsorption Properties and Advanced Textural Characterization of Novel Micro/Mesoporous Zeolites. In: Studies in Surface Science and Catalysis, volume 170, 1042–1047. Elsevier.

Ravikovitch, P. I. & Neimark, A. V. (2002a) Density Functional Theory of Adsorption in Spherical Cavities and Pore Size Characterization of Templated Nanoporous Silicas with Cubic and Three-Dimensional Hexagonal Structures. Langmuir, **18**, 1550–1560.

Ravikovitch, P. I. & Neimark, A. V. (2002b) Experimental Confirmation of Different Mechanisms of Evaporation from Ink-Bottle Type Pores: Equilibrium, Pore Blocking, and Cavitation. Langmuir, **18**, 9830–9837.

Reichenbach, C. & Klank, D. (2014) Vollautomatisierte Adsorptionsvolumetrie Bei Variablen Messtemperaturen Teil 1: Untersuchungen von Sorptions-phänomenen in Zeolithe. Partikelwelt, **15**, 17–21.

Rejeb, A., Stephansson, O., Millard, A., Ziefle, G., Kohlmeier, M., Massmann, J., Zielke, W., Uehara, S., Kobayashi, A., Chijimatsu, M. & Fujita, T. (2007) DECOVALEX-THMC Project. Task C. Excavation Damaged Zone (EDZ) in Argillaceous Rock at Tournemire Site (France). Report of Task C1. Technical Report SKI-R–07-09, Swedish Nuclear Power Inspectorate.

Rezaeyan, A., Kampman, N., Pipich, V., Barnsley, L. C., Rother, G., Magill, C., Ma, J. & Busch, A. (2023) Evolution of Pore Structure in Organic-Lean and Organic-Rich Mudrocks. Energy & Fuels, **37**, 16446–16460.

Rezaeyan, A., Kampman, N., Pipich, V., Barnsley, L. C., Rother, G., Magill, C., Ma, J. & Busch, A. (2024) Compaction and Clay Content Control Mudrock Porosity. Energy, **289**, 129966.

Ribeiro Carrott, M., Cansado, I., Carrott, P., Russo, P., Castilho, P., Fernandes, C., Catrinescu, C. & Breen, C. (2016) Porosity in Ion-Exchanged and Acid Activated Clays Evaluated Using n-Nonane Pre-Adsorption. Microporous and Mesoporous Materials, **232**, 238–247.

Rinnert, E., Carteret, C., Humbert, B., Fragneto-Cusani, G., Ramsay, J. D. F., Delville, A., Robert, J.-L., Bihannic, I., Pelletier, M. & Michot, L. J. (2005) Hydration of a Synthetic Clay with Tetrahedral Charges: A Multidisciplinary Experimental and Numerical Study. The Journal of Physical Chemistry B, **109**, 23745–23759.

Ross, D. J. & Bustin, M. R. (2009) The Importance of Shale Composition and Pore Structure upon Gas Storage Potential of Shale Gas Reservoirs. Marine and Petroleum Geology, **26**, 916–927.

Rother, G., Krukowski, E. G., Wallacher, D., Grimm, N., Bodnar, R. J. & Cole, D. R. (2012) Pore Size Effects on the Sorption of Supercritical CO_2 in Mesoporous CPG-10 Silica. The Journal of Physical Chemistry C, **116**, 917–922.

Rother, G., Stack, A. G., Gautam, S., Liu, T., Cole, D. R. & Busch, A. (2020) Water Uptake by Silica Nanopores: Impacts of Surface Hydrophilicity and Pore Size. The Journal of Physical Chemistry C, **124**, 15188–15194.

Rouquerol, F., Rouquerol, J. & Sing, K. (1999) Chapter 13 - General Conclusions and Recommendations. In: Adsorption by Powders and Porous Solids (F. Rouquerol, J. Rouquerol and K. Sing, editors), 439–447. Academic Press, London.

Rouquerol, F., Rouquerol, J., Sing, K. S. W., Llewellyn, P. L. & Maurin, G. (2014) Adsorption by Powders and Porous Solids: Principles, Methodology and Applications. Elsevier/AP, Amsterdam, second edition edition.

Rouquerol, J., Llewellyn, P. & Rouquerol, F. (2007) Is the Bet Equation Applicable to Microporous Adsorbents? In: Studies in Surface Science and Catalysis, volume 160, 49–56. Elsevier.

Rutter, E., Mecklenburgh, J. & Taylor, K. (2017) Geomechanical and Petrophysical Properties of Mudrocks: Introduction. Geological Society, London, Special Publications, **454**, 1–13.

Saliba, S., Ruch, P., Volksen, W., Magbitang, T. P., Dubois, G. & Michel, B. (2016) Combined Influence of Pore Size Distribution and Surface Hydrophilicity on the Water Adsorption Characteristics of Micro- and Mesoporous Silica. Microporous and Mesoporous Materials, **226**, 221–228.

Salles, F., Beurroies, I., Bildstein, O., Jullien, M., Raynal, J., Denoyel, R. & Damme, H. V. (2008) A Calorimetric Study of Mesoscopic Swelling and Hydration Sequence in Solid Na-montmorillonite. Applied Clay Science, **39**, 186–201.

Sang, G., Liu, S. & Elsworth, D. (2019) Water Vapor Sorption Properties of Illinois Shales Under Dynamic Water Vapor Conditions: Experimentation and Modeling. Water Resources Research, **55**, 7212–7228.

Sang, G., Liu, S., Elsworth, D., Yang, Y. & Fan, L. (2020a) Evaluation and Modeling of Water Vapor Sorption and Transport in Nanoporous Shale. International Journal of Coal Geology, **228**, 103553.

Sang, G., Liu, S., Elsworth, D., Zhang, R. & Bleuel, M. (2020b) Pore-Scale Water Vapor Condensation Behaviors in Shales: An Experimental Study. Transport in Porous Media, **135**, 713–734.

Savoye, S., Beaucaire, C., Fayette, A., Herbette, M. & Coelho, D. (2012) Mobility of Cesium through the Callovo-Oxfordian Claystones under Partially Saturated Conditions. Environmental Science & Technology, **46**, 2633–2641.

Savoye, S., Goutelard, F., Beaucaire, C., Charles, Y., Fayette, A., Herbette, M., Larabi, Y. & Coelho, D. (2011) Effect of Temperature on the Containment Properties of Argillaceous Rocks: The Case Study of Callovo–Oxfordian Claystones. Journal of Contaminant Hydrology, **125**, 102–112.

Savoye, S., Page, J., Puente, C., Imbert, C. & Coelho, D. (2010) New Experimental Approach for Studying Diffusion through an Intact and Unsaturated Medium: A Case Study with Callovo-Oxfordian Argillite. Environmental Science & Technology, **44**, 3698–3704.

Schieber, J. (2003) Black Shales. In: Encyclopedia of Sediments and Sedimentary Rocks (G. V. Middleton, M. J. Church, M. Coniglio, L. A. Hardie and F. J. Longstaffe, editors), 83–85. Springer Netherlands, Dordrecht.

Schlömer, S. & Krooss, BM. (1997) Experimental Characterisation of the Hydrocarbon Sealing Efficiency of Cap Rocks. Marine and Petroleum Geology, **14**, 565–580.

Schlömer, S. & Krooss, BM. (2004) Molecular Transport of Methane, Ethane and Nitrogen and the Influence of Diffusion on the Chemical and Isotopic Composition of Natural Gas Accumulations. Geofluids, **4**, 81–108.

Schlumberger, C. & Thommes, M. (2021) Characterization of Hierarchically Ordered Porous Materials by Physisorption and Mercury Porosimetry—A Tutorial Review. Advanced Materials Interfaces, **8**, 2002181.

Schoen, M. & Thommes, M. (1995) Microscopic Structure of a Pure Near-Critical Fluid Confined to a Mesoscopic Slit-Pore. Physical Review E, **52**, 6375–6386.

Schoen, M., Thommes, M. & Findenegg, G. H. (1997) Aspects of Sorption and Phase Behavior of Near-Critical Fluids Confined to Mesoporous Media. The Journal of Chemical Physics, **107**, 3262–3266.

Schoonheydt, R. A., Johnston, C. T. & Bergaya, F. (2018) Clay Minerals and Their Surfaces. In: Developments in Clay Science, volume 9, 1–21. Elsevier.

Seemann, T., Bertier, P., Krooss, B. M. & Stanjek, H. (2017) Water Vapour Sorption on Mudrocks. Geological Society, London, Special Publications, **454**, 201–233.

Shabani, M., Krooss, B. M., Hallenberger, M., Amann-Hildenbrand, A., Fink, R. & Littke, R. (2020) Petrophysical Characterization of Low-Permeable Carbonaceous Rocks: Comparison of Different Experimental Methods. Marine and Petroleum Geology, **122**, 104658.

Silvestre-Albero, A. M., Juárez-Galán, J. M., Silvestre-Albero, J. & Rodríguez-Reinoso, F. (2012) Low-Pressure Hysteresis in Adsorption: An Artifact? The Journal of Physical Chemistry C, **116**, 16652–16655.

Silvestre-Albero, J., Silvestre-Albero, A. M., Llewellyn, P. L. & Rodríguez-Reinoso, F. (2013) High-Resolution N $_2$ Adsorption Isotherms at 77.4 K: Critical Effect of the He Used During Calibration. The Journal of Physical Chemistry C, **117**, 16885–16889.

Sing, K. S. & Williams, R. T. (2005) Empirical Procedures for the Analysis of Physisorption Isotherms. Adsorption Science & Technology, **23**, 839–853.

Singh, D. P., Chandra, D., Vishal, V., Hazra, B. & Sarkar, P. (2021) Impact of Degassing Time and Temperature on the Estimation of Pore Attributes in Shale. Energy & Fuels, **35**, 15628–15641.

Sircar, S. (2006) Basic Research Needs for Design of Adsorptive Gas Separation Processes. Industrial & Engineering Chemistry Research, **45**, 5435–5448.

Smith, D. W. (1977) Ionic Hydration Enthalpies. Journal of Chemical Education, **54**, 540.

Šolcová, O., Matějová, L., Topka, P., Musilová, Z. & Schneider, P. (2011) Comparison of Textural Information from Argon (87 K) and Nitrogen (77 K) Physisorption. Journal of Porous Materials, **18**, 557–565.

Song, Y., Davy, C., Bertier, P., Skoczylas, F. & Talandier, J. (2017) On the Porosity of COx Claystone by Gas Injection. Microporous and Mesoporous Materials, **239**, 272–286.

Sonwane, C. G. & Bhatia, S. K. (2000) Characterization of Pore Size Distributions of Mesoporous Materials from Adsorption Isotherms. The Journal of Physical Chemistry B, **104**, 9099–9110.

Sotomayor, F. J., Cychosz, K. A. & Thommes, M. (2018) Characterization of Micro/Mesoporous Materials by Physisorption: Concepts and Case Studies. Accounts of Materials and Surface Research, 17.

Sposito, G. & Babcock, K. (1966) Equilibrium Theory of the Kaolinite-Water System at Low Moisture Contents, with Some Remarks Concerning Adsorption Hysteresis. In: Clays and Clay Minerals (S. Bailey, editor), 133–147. Pergamon.

Sposito, G. & Prost, R. (1982) Structure of Water Adsorbed on Smectites. Chemical Reviews, **82**, 553–573.

Środoń, J. (2003a) Illite Group Clay Minerals. In: Encyclopedia of Sediments and Sedimentary Rocks (G. V. Middleton, M. J. Church, M. Coniglio, L. A. Hardie and F. J. Longstaffe, editors), 369–371. Springer Netherlands, Dordrecht.

Środoń, J. (2003b) Mixed-Layer Clays. In: Encyclopedia of Sediments and Sedimentary Rocks (G. V. Middleton, M. J. Church, M. Coniglio, L. A. Hardie and F. J. Longstaffe, editors), 447–450. Springer Netherlands, Dordrecht.

Środoń, J. (2006) Chapter 12.2 Identification and Quantitative Analysis of Clay Minerals. Developments in Clay Science, **1**, 765–787.

Środoń, J. & MaCarty, D. K. (2008) Surface Area and Layer Charge of Smectite from CEC and EGME/H_2O-retention Measurements. Clays and Clay Minerals, **56**, 155–174.

Stanjek, H. & Künkel, D. (2016) CEC Determination with Cu-triethylenetetramine: Recommendations for Improving Reproducibility and Accuracy. Clay Minerals, **51**, 1–17.

Stoeckli, F. (1998) Recent Developments in Dubinin's Theory. Carbon, **36**, 363–368.

Stoeckli, F. & Huguenin, D. (1992) Water Adsorption in Active Carbon Characterized by Adsorption and Immersion Techniques. Journal of the Chemical Society, Faraday Transactions, **88**, 737.

Sun, M., Yu, B., Hu, Q., Zhang, Y., Li, B., Yang, R., Melnichenko, Y. B. & Cheng, G. (2017) Pore Characteristics of Longmaxi Shale Gas Reservoir in the Northwest of Guizhou, China: Investigations Using Small-Angle Neutron Scattering (SANS), Helium Pycnometry, and Gas Sorption Isotherm. International Journal of Coal Geology, **171**, 61–68.

Tan, J., Weniger, P., Krooss, B., Merkel, A., Horsfield, B., Zhang, J., Boreham, C. J., van Graas, G. & Tocher, B. A. (2014) Shale Gas Potential of the Major Marine Shale Formations in the Upper Yangtze Platform, South China, Part II: Methane Sorption Capacity. Fuel, **129**, 204–218.

Tang, X., Ripepi, N., Luxbacher, K. & Pitcher, E. (2017) Adsorption Models for Methane in Shales: Review, Comparison, and Application. Energy & Fuels, **31**, 10787–10801.

Thomas, J. J., Jennings, H. M. & Allen, A. J. (1998) Determination of the Neutron Scattering Contrast of Hydrated Portland Cement Paste Using H2O/D2O Exchange. Advanced Cement Based Materials, **7**, 119–122.

Thomas, J. J., Valenza, J. J., Craddock, P. R., Bake, K. D. & Pomerantz, A. E. (2014) The Neutron Scattering Length Density of Kerogen and Coal as Determined by CH_3OH/CD_3OH Exchange. Fuel, **117**, 801–808.

Thommes, M. (2004) Physical Adsorption Characterization of Ordered and Amorphous Mesoporous Material, volume 4, 317–364. Published by Imperial College Press and Distributed by World Scientific Publishing Co.

Thommes, M. (2007) Chapter 15 - Textural Characterization of Zeolites and Ordered Mesoporous Materials by Physical Adsorption. In: Introduction to Zeolite Science and Practice (J. Čejka, H. van Bekkum, A. Corma and F. Schüth, editors), Studies in Surface Science and Catalysis, volume 168, 495–XIII. Elsevier.

Thommes, M. & Cychosz, K. A. (2014) Physical Adsorption Characterization of Nanoporous Materials: Progress and Challenges. Adsorption, **20**, 233–250.

Thommes, M. & Findenegg, G. H. (1994) Pore Condensation and Critical-Point Shift of a Fluid in Controlled-Pore Glass. Langmuir, **10**, 4270–4277.

Thommes, M., Kaneko, K., Neimark, A. V., Olivier, J. P., Rodriguez-Reinoso, F., Rouquerol, J. & Sing, K. S. (2015) Physisorption of Gases, with Special Reference to the Evaluation of Surface Area and Pore Size Distribution (IUPAC Technical Report). Pure and Applied Chemistry, **87**, 1051–1069.

Thommes, M., Köhn, R. & Fröba, M. (2002a) Characterization of Mesoporous Solids: Pore Condensation and Sorption Hysteresis Phenomena in Mesoporous Molecular Sieves. In: Studies in Surface Science and Catalysis, volume 142, 1695–1702. Elsevier.

Thommes, M., Köhn, R. & Fröba, M. (2002b) Sorption and Pore Condensation Behavior of Pure Fluids in Mesoporous MCM-48 Silica, MCM-41 Silica, SBA-15 Silica and Controlled-Pore Glass at Temperatures above and below the Bulk Triple Point. Applied Surface Science, **196**, 239–249.

Thommes, M., Mitchell, S. & Pérez-Ramírez, J. (2012) Surface and Pore Structure Assessment of Hierarchical MFI Zeolites by Advanced Water and Argon Sorption Studies. The Journal of Physical Chemistry C, **116**, 18816–18823.

Thommes, M., Morell, J., Cychosz, K. A. & Fröba, M. (2013) Combining Nitrogen, Argon, and Water Adsorption for Advanced Characterization of Ordered Mesoporous Carbons (CMKs) and Periodic Mesoporous Organosilicas (PMOs). Langmuir, **29**, 14893–14902.

Thommes, M., Morlay, C., Ahmad, R. & Joly, J. P. (2011) Assessing Surface Chemistry and Pore Structure of Active Carbons by a Combination of Physisorption (H_2O, Ar, N_2, CO_2), XPS and TPD-MS. Adsorption, **17**, 653–661.

Thommes, M., Smarsly, B., Groenewolt, M., Ravikovitch, P. I. & Neimark, A. V. (2006) Adsorption Hysteresis of Nitrogen and Argon in Pore Networks and Characterization of Novel Micro- and Mesoporous Silicas. Langmuir, **22**, 756–764.

Tompsett, G. A., Krogh, L., Griffin, D. W. & Conner, W. C. (2005) Hysteresis and Scanning Behavior of Mesoporous Molecular Sieves. Langmuir, **21**, 8214–8225.

Tóth, J., editor (2002) Adsorption: Theory, Modeling, and Analysis. Number v. 107 in Surfactant Science Series. Marcel Dekker, New York.

Tournassat, C., Bourg, I. C., Steefel, C. I. & Bergaya, F. (2015a) Chapter 1 - Surface Properties of Clay Minerals. In: Natural and Engineered Clay Barriers (C. Tournassat, C. I. Steefel, I. C. Bourg and F. Bergaya, editors), Developments in Clay Science, volume 6, 5–31. Elsevier.

Tournassat, C., Steefel, C. I., Bourg, I. C. & Bergaya, F. (2015b) Natural and Engineered Clay Barriers. Elsevier.

Ufer, K. & Kleeberg, R. (2015) Parametric Rietveld Refinement of Coexisting Disordered Clay Minerals. Clay Minerals, **50**, 287–296.

Ufer, K., Stanjek, H., Roth, G., Dohrmann, R., Kleeberg, R. & Kaufhold, S. (2008) Quantitative Phase Analysis of Bentonites by the Rietveld Method. Clays and Clay Minerals, **56**, 272–282.

Van Olphen, H. (1965) Thermodynamics of Interlayer Adsorption of Water in Clays. I.—Sodium Vermiculite. Journal of Colloid Science, **20**, 822–837.

Vandenberghe, N., De Craen, M. & Wouters, L. (2014) The Boom Clay Geology From Sedimentation to Present-Day Occurrence A Review, volume 60. Geological Survey of Belgium.

Velasco, L. F., Berezovska, I., Boutillara, Y. & Lodewyckx, P. (2017) The use of organic vapour preadsorption to understand water adsorption on activated carbons. Microporous and Mesoporous Materials, **241**, 21–27.

Vranjes-Wessely, S., Misch, D., Issa, I., Kiener, D., Fink, R., Seemann, T., Liu, B., Rantitsch, G. & Sachsenhofer, R. (2020) Nanoscale Pore Structure of Carboniferous Coals from the Ukrainian Donets Basin: A Combined HRTEM and Gas Sorption Study. International Journal of Coal Geology, **224**, 103484.

Wang, G. & Ju, Y. (2015) Organic Shale Micropore and Mesopore Structure Characterization by Ultra-Low Pressure N_2 Physisorption: Experimental Procedure and Interpretation Model. Journal of Natural Gas Science and Engineering, **27**, 452–465.

Whitley, H. D. & Smith, D. E. (2004) Free Energy, Energy, and Entropy of Swelling in Cs–, Na–, and Sr–Montmorillonite Clays. The Journal of Chemical Physics, **120**, 5387–5395.

Wong, L. N. Y., Maruvanchery, V. & Liu, G. (2016) Water Effects on Rock Strength and Stiffness Degradation. Acta Geotechnica, **11**, 713–737.

Woo, H.-J., Sarkisov, L. & Monson, P. (2002) Understanding Adsorption Hysteresis in Porous Glasses and Other Mesoporous Materials. In: Studies in Surface Science and Catalysis, volume 144, 155–162. Elsevier.

Woodruff, W. F. & Revil, A. (2011) CEC-normalized Clay-Water Sorption Isotherm. Water Resources Research, **47**.

Worden, R., Griffiths, J., Wooldridge, L., Utley, J., Lawan, A., Muhammed, D., Simon, N. & Armitage, P. (2020) Chlorite in Sandstones. Earth-Science Reviews, **204**, 103105.

Xie, W., Wang, H., Chen, S., Gan, H., Vandeginste, V. & Wang, M. (2023) Water Adsorption and Its Pore Structure Dependence in Shale Gas Reservoirs. Langmuir, **39**, 10576–10592.

Xue, B., Zhang, J., Tang, X., Yang, C., Chen, Q., Man, X. & Dang, W. (2016) Micro-Pore Structure and Gas Accumulation Characteristics of Shale in the Longmaxi Formation, Northwest Guizhou. Petroleum Research, **1**, 191–204.

Yang, F., Lyu, B. & Xu, S. (2021) Water Sorption and Transport in Shales: An Experimental and Simulation Study. Water Resources Research, **57**.

Yang, R., Jia, A., He, S., Hu, Q., Dong, T., Hou, Y. & Yan, J. (2020a) Water Adsorption Characteristics of Organic-Rich Wufeng and Longmaxi Shales, Sichuan Basin (China). Journal of Petroleum Science and Engineering, **193**, 107387.

Yang, R., Jia, A., Hu, Q., Guo, X. & Sun, M. (2020b) Particle Size Effect on Water Vapor Sorption Measurement of Organic Shale: One Example from Dongyuemiao Member of Lower Jurassic Ziliujing Formation in Jiannan Area of China. Advances in Geo-Energy Research, **4**, 207–218.

Yang, Y. & Aplin, A. C. (1998) Influence of Lithology and Compaction on the Pore Size Distribution and Modelled Permeability of Some Mudstones from the Norwegian Margin. Marine and Petroleum Geology, **15**, 163–175.

Yang, Y. & Aplin, A. C. (2007) Permeability and Petrophysical Properties of 30 Natural Mudstones. Journal of Geophysical Research: Solid Earth, **112**, 2005JB004243.

Zhang, C., Czaikowski, O., Rothfuchs, T. & Zhang, C.-L. (2010) Thermo-Hydro-Mechanical Behaviour of the Callovo-Oxfordian Clay Rock: Within the Framework of GRS/ANDRA Cooperation Programme and the EC TIMODAZ Project ; Final Report. Number 266 in GRS. GRS, Köln Garching b. München Berlin Braunschweig.

Zhang, C., Yao, Y., Swennen, R. & Wu, H. (2022) Combined Effects of the Chemical Structure and Nanopore Development on Water Vapor/Liquid Adsorption in Shale Kerogen. Colloids and Surfaces A: Physicochemical and Engineering Aspects, **653**, 129920.

Zhang, L., Xiong, Y., Li, Y., Wei, M., Jiang, W., Lei, R. & Wu, Z. (2017) DFT Modeling of CO_2 and Ar Low-Pressure Adsorption for Accurate Nanopore Structure Characterization in Organic-Rich Shales. Fuel, **204**, 1–11.

Zhang, M., Hu, M., Wei, S., Cai, Q., Fu, W., Shi, F., Zhang, L. & Ding, H. (2023) Factors Controlling the Pore Development of Low-Mature Marine–Continental Transitional Shale: A Case Study of the Upper Permian Longtan Shale, Western Guizhou, South China. Journal of Marine Science and Engineering, **11**, 1862.

Ziemiański, P. P., Derkowski, A., Szczurowski, J. & Kozieł, M. (2020) The Structural versus Textural Control on the Methane Sorption Capacity of Clay Minerals. International Journal of Coal Geology, **224**, 103483.

Zolfaghari, A. & Dehghanpour, H. (2015) Pore Size Distribution from Water Adsorption Isotherm. In: Day 3 Wed, September 30, 2015, D031S036R008. SPE, Houston, Texas, USA.